

Ralf Schneider

## **Plasma edge physics for tokamaks**

IPP 12/1  
Februar 2001

# Plasma edge physics for tokamaks

Ralf Schneider

Max-Planck-Institut für Plasmaphysik, EURATOM Association, Teilinstitut Greifswald,  
17489 Greifswald, Germany

## Abstract

The aim of this work was to give insight into the physics in the scrape-off layer (SOL) of magnetised plasmas, which is defined as the region of open fieldlines intersecting walls. It is characterised by the competition of parallel and perpendicular transport. The description of the plasma-wall interaction due to the existence of walls and atomic processes are necessary ingredients for an understanding of the scrape-off layer. This work mainly focussed on divertor tokamaks, but most of the arguments and principles can be easily adapted also to other concepts like island divertors in stellarators or limiter devices. Results from the 2D SOL transport code B2-Eirene as well as simplified models were used as tools to identify the basic physics mechanisms and apply this knowledge for design optimisation of the ASDEX-Upgrade divertor.

The first part introduced, after a short motivation, the basic concepts for power and particle exhaust in the SOL. The discussion of the different length scales involved in the SOL physics followed, including sheath physics. The second major part covered the physics of the pure hydrogen plasma based on a fluid description. Starting from simple models, the influence of neutral transport and the characteristics of the different operation regimes was there the main topic. This part finished with time-dependent phenomena for the pure plasma, so-called Edge Localised Modes (ELMs), and their effect on the SOL. The next part discussed the influence of impurities on the SOL plasma. For the understanding of impurity physics in the SOL one needs a rather complex combination of different aspects. The impurity production process has to be understood, then the effects of impurities in terms of radiation losses have to be included and finally the impurity transport is necessary. This was introduced with rising complexity starting with simple estimates, analysing then the detailed parallel force balance and the flow pattern of impurities. Using this, impurity compression and radiation instabilities were discussed. This part ended, combining all the elements introduced before, with specific, detailed results from ASDEX-Upgrade (especially for the optimized new divertor configuration). The predictive capability of the 2D-SOL code B2-Eirene was demonstrated for this new design based on transport calculations.

The effect of drifts and currents was addressed in the next part, including the derivation of the basic equations and some examples. This was necessary to get closer insight into the physics of the formation of large radial electric fields close to the separatrix as well as in-out asymmetry between the divertor legs and influence of the toroidal momentum input on this asymmetry. A specific topology effect appears for the (toroidally averaged) island divertor of a stellarator due to the existence of an additional region of closed fieldlines in the island. The resulting potential and current profile is quite sensitive to the effect of drifts. Finally, some work on deriving scaling laws for the anomalous turbulent transport based on automatic edge transport code fitting procedures was described. Looking forward, the

necessary work to achieve a self-consistent SOL model including the anomalous turbulent transport was discussed.

The necessary ingredients for a model being able to describe the SOL are shown in Fig. 0.1. Elements from quite different physics fields have to be combined. The knowledge

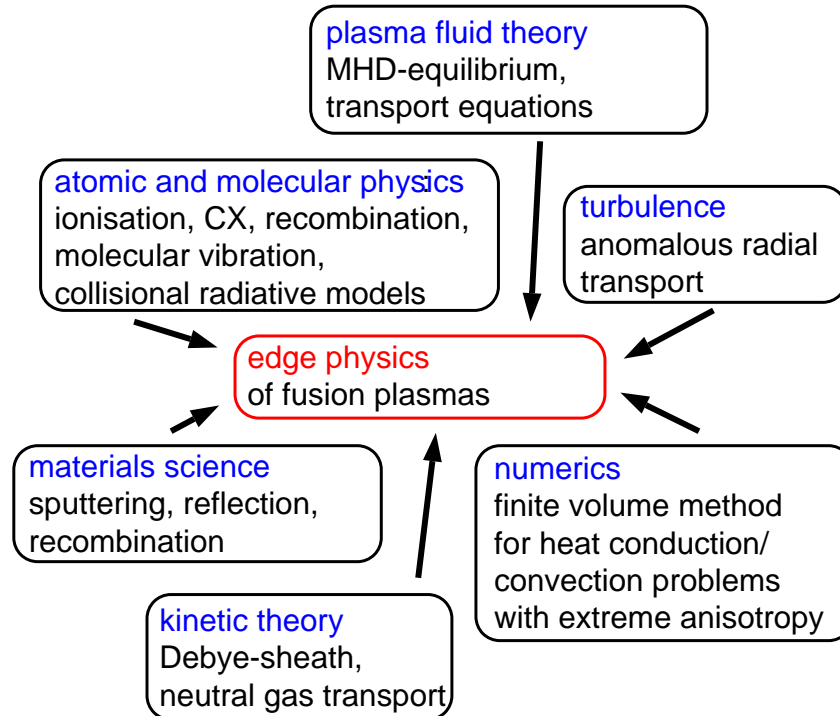


Figure 0.1:

of the experimental magneto-hydrodynamical equilibrium is a necessary prerequisite for any work in this area. Plasma fluid theory in a general sense is needed to obtain the transport equations governing the transport in the edge of a plasma. Kinetic theory is necessary to deliver the correct description of the sheath forming in front of a wall which is in contact with the plasma. This defines boundary conditions for the fluid models used in the transport codes. The interaction of plasma with walls also introduces the need for detailed understanding of processes creating neutrals or ions at surfaces (sputtering, reflection, recombination, ...). Atomic and molecular processes affect strongly the plasma through ionisation and recombination, thus collisional-radiative models are used (even accounting for vibrationally excited molecules). The classical transport of neutrals strongly determines the operational regime. To be able to optimize existing designs the complete kinetic transport equation has to be solved in full geometry. Due to the existence of the turbulent radial transport in fusion devices, either scaling laws or direct coupling to turbulence codes are necessary for a full predictive quality. Last but not least, the numerical problems of solving the extremely anisotropic transport equations (very strong parallel heat conduction of electrons) and combining all the elements to a usable code for producing results based on a rather complete physics description within reasonable run-time has to be solved. All these elements together defines this working field as a fascinating one with inputs from many areas.

## **Plasma edge physics for tokamaks**

Ralf Schneider,  
Max-Planck-Institut für Plasmaphysik,  
EURATOM association,  
Garching, Germany





# Contents

<b>1. Introduction</b>	<b>9</b>
<b>2. Motivation</b>	<b>11</b>
<b>3. Power and particle exhaust concepts</b>	<b>13</b>
3.1. Limiter . . . . .	13
3.2. Divertor . . . . .	14
3.3. Stellarator island divertor . . . . .	14
3.4. Ergodic limiter . . . . .	15
<b>4. Scrape-off layer length scales</b>	<b>17</b>
4.1. Transport along fieldlines . . . . .	17
4.2. Interaction with neutrals . . . . .	19
4.3. Brief summary of sheath physics . . . . .	21
4.3.1. Plasma-wall contact without magnetic field . . . . .	22
4.3.2. Plasma-wall contact with an electron emitting wall . . . . .	27
4.3.3. Plasma-wall contact in presence of a magnetic field . . . . .	34
4.4. Summary of SOL length scales . . . . .	36
4.5. Problems for a fluid description of the SOL . . . . .	37
<b>5. Fluid equations</b>	<b>39</b>
5.1. Braginskii equations . . . . .	39
5.2. B2 equations . . . . .	41
5.2.1. Radial ion-electron heat exchange term . . . . .	43
5.2.2. Kinetic corrections . . . . .	44
<b>6. Neutral transport, surface reflection, recycling</b>	<b>45</b>
6.1. Neutral losses . . . . .	45
6.1.1. Charge exchange losses . . . . .	45
6.1.2. Neutral hydrogen radiation . . . . .	46
6.2. Neutral transport . . . . .	47
6.2.1. Simple neutral diffusion model . . . . .	47
6.2.2. Neutral transport in Monte-Carlo codes . . . . .	47
6.2.3. Neutral hybrid model . . . . .	49

<b>7. The two-point model</b>	<b>51</b>
7.1. Basic equations . . . . .	51
7.2. Divertor operation regimes . . . . .	52
7.2.1. Low recycling (Linear or Sheath-limited regime) . . . . .	52
7.2.2. High recycling (Conduction-limited regime) . . . . .	54
7.2.3. Layer detachment . . . . .	55
7.2.4. Flame detachment . . . . .	58
<b>8. Detachment</b>	<b>59</b>
8.1. Simple model for momentum loss by neutrals . . . . .	59
8.2. Divertor balances in the attached and detached regime . . . . .	61
8.3. Transition from layer to flame detachment . . . . .	63
8.4. Volume recombination . . . . .	64
8.5. Importance of volume recombination for the divertor . . . . .	65
8.6. Characterisation of gas target . . . . .	67
8.7. Strong onset of recombination radiation . . . . .	68
8.8. Effect of vibrationally excited molecules . . . . .	73
<b>9. Radial midplane profiles</b>	<b>77</b>
9.1. Radial midplane temperature profile . . . . .	77
9.2. Radial midplane density profile . . . . .	78
<b>10. Hydrogen flow reversal, geometry effects</b>	<b>81</b>
10.1. Hydrogen flow reversal . . . . .	81
10.2. Geometry effects . . . . .	81
10.2.1. Radial plasma profile . . . . .	81
10.2.2. Detachment properties . . . . .	83
10.2.3. Main chamber baffling . . . . .	85
10.2.4. Pumping properties . . . . .	85
10.2.5. Geometry effects on volume recombination . . . . .	87
<b>11. Time-dependent phenomena: ELMs</b>	<b>91</b>
<b>12. Impurity physics: sputtering, radiation losses</b>	<b>97</b>
12.1. Impurity production . . . . .	97
12.2. Radiation loss on closed field lines . . . . .	100
<b>13. Extension of the 2-point model</b>	<b>103</b>
13.1. Basic equations . . . . .	103
13.2. Coronal estimate . . . . .	104
13.3. Non-coronal effects . . . . .	105
13.3.1. Effect of transport . . . . .	105
13.3.2. Charge exchange recombination . . . . .	106

13.4. Influence of perpendicular transport . . . . .	106
13.5. Advanced 2-point model including radiation losses . . . . .	108
<b>14.SOL density limit</b>	<b>111</b>
14.1. Basic idea . . . . .	111
14.2. Scaling considerations . . . . .	111
14.3. Detailed analysis of density limit scenarios . . . . .	112
<b>15.Impurity flow pattern, flow reversal</b>	<b>115</b>
15.1. Parallel force balance . . . . .	115
15.2. Impurity regimes and corrections to the fluid model . . . . .	118
15.3. Impurity flow pattern . . . . .	119
15.4. Impurity ion flow in the divertor . . . . .	121
<b>16.Compression, helium pumping</b>	<b>123</b>
16.1. Experimental characterization of compression . . . . .	123
16.2. Importance of helium compression for a reactor . . . . .	123
16.3. Impurity compression at ASDEX-Upgrade . . . . .	126
16.4. Consequences for ITER . . . . .	128
<b>17.Time-dependent phenomena: Type III ELMs, MARFEs</b>	<b>133</b>
17.1. Type III ELMs . . . . .	133
17.1.1. Edge operational diagram . . . . .	133
17.1.2. Completely detached H-mode at ASDEX Upgrade . . . . .	134
17.2. MARFEs . . . . .	137
17.3. Characterisation of a stable MARFE . . . . .	140
<b>18.ASDEX-Upgrade DivII results</b>	<b>143</b>
18.1. Divertor configurations . . . . .	143
18.2. Detachment properties . . . . .	144
18.3. Divertor power load . . . . .	149
18.4. Pumping and helium exhaust . . . . .	155
18.5. Target power load reduction . . . . .	157
18.6. A simple model of the detached or nearly detached regime . . . . .	159
18.7. Role of divertor inclination . . . . .	161
18.8. Replacement of carbon . . . . .	161
<b>19.Drifts and currents</b>	<b>163</b>
19.1. General treatment . . . . .	163
19.2. Numerics . . . . .	164
19.3. Model equations . . . . .	164
19.4. Boundary conditions with drifts and currents . . . . .	173
19.5. Structure of the radial electric field close to the edge . . . . .	174

19.6. Drift effects in the SOL . . . . .	178
19.7. Effect of neutral beam injection . . . . .	180
19.8. Topology effects: Stellarator island divertor . . . . .	184
<b>20. Anomalous transport</b>	<b>189</b>
20.1. Fit procedure . . . . .	191
20.2. First database on ASDEX-Upgrade . . . . .	193
20.3. Preliminary multiple regression fit to $\chi$ . . . . .	194
20.4. Including an inward pinch . . . . .	195
20.5. Self-consistent coupling of turbulence and transport models . . . . .	197
<b>21. Summary</b>	<b>199</b>
<b>A. Scrape-off layer diagnostics</b>	<b>201</b>
A.1. Langmuir probes (M. Weinlich, A. Carlson) . . . . .	201
A.1.1. Single probe without magnetic field . . . . .	201
A.1.2. Double probe without magnetic field . . . . .	203
A.1.3. Triple probe without magnetic field . . . . .	204
A.1.4. Single probe with magnetic field . . . . .	205
A.1.5. Multitip probes . . . . .	205
A.1.6. Thermal load . . . . .	206
A.1.7. Derived quantities . . . . .	206
A.1.8. Sophisticated probes . . . . .	207
A.1.9. Modifications of the simplest models . . . . .	208
A.1.10. Langmuir probes at ASDEX-Upgrade . . . . .	208
A.2. $H_\alpha$ . . . . .	212
A.3. Fast Lithium-beam spectroscopy (J. Schweinzer) . . . . .	212
A.3.1. Li-Beam modeling and related atomic data base . . . . .	213
A.3.2. Spectroscopical observation systems on ASDEX-Upgrade . . . . .	214
A.3.3. Neutral lithium beam production . . . . .	216
A.4. Thermography (A. Herrmann) . . . . .	217
A.4.1. Principles of measurement and problems . . . . .	217
A.4.2. Contribution of bremsstrahlung . . . . .	219
A.4.3. Principles of measurement . . . . .	220
A.4.4. Accuracy and calibration . . . . .	221
A.4.5. Heat flux calculation . . . . .	223
A.4.6. Design considerations . . . . .	224
A.5. Calorimetry (P. Franzen) . . . . .	225
A.5.1. Experiment . . . . .	225
A.6. Spectroscopy . . . . .	227
A.6.1. Spectroscopy with the VUV survey spectrometer SPRED (R. Dux) . . . . .	227
A.6.2. Spectroscopic particle influx measurements (A. Kallenbach) . . . . .	230

---

A.6.3. Spectroscopic temperature measurements (R. Neu) . . . . .	231
A.7. Neutral pressure gauges (G.Haas) . . . . .	235
A.7.1. Design of the ASDEX gauge . . . . .	235
A.7.2. Operation and discussion of physical processes . . . . .	237
A.8. Bolometers (K.F. Mast, J.C. Fuchs) . . . . .	240
A.9. Energy-resolved neutral fluxes (J. Stober) . . . . .	242
A.10. Microwave reflectometry (B. Kurzan) . . . . .	249
A.10.1. Principle of reflectometry . . . . .	249
A.10.2. Classification of the reflectometry techniques with respect to the cut-off used . . . . .	249
A.10.3. Principle setup . . . . .	250
A.10.4. Measurement of electron density profiles . . . . .	250
A.10.5. Measurement of the motion of the reflecting layer . . . . .	252
A.11. Electron cyclotron emission (W. Suttrop) . . . . .	252
A.12. DCN-Interferometer (O. Gehre) . . . . .	256
A.13. Thomson scattering (H. Salzmann) . . . . .	258



# 1. Introduction

The concept of magnetic confinement fusion uses the possibility to confine a hot plasma by the appropriate design of magnetic coils to optimize the conditions for the fusion reaction of deuterium and tritium to helium [1]. The basic idea is that the plasma particles (electrons and ions) are strongly magnetized and follow the magnetic field lines such that the radial losses are rather small to sustain the conditions for fusion for steady-state reactors. The plasma particles have very large transport along the magnetic field-lines, but rather small perpendicular to it. By proper shaping of the coils, configurations are possible with very good confinement properties. The two most promising candidates for this concept are the tokamak (which is toroidally symmetric, see Fig 1.1) and the stellarator (a full 3D system, see Fig 1.2). All these devices have areas where magnetic fieldlines (and therefore plasma) gets in contact with walls.

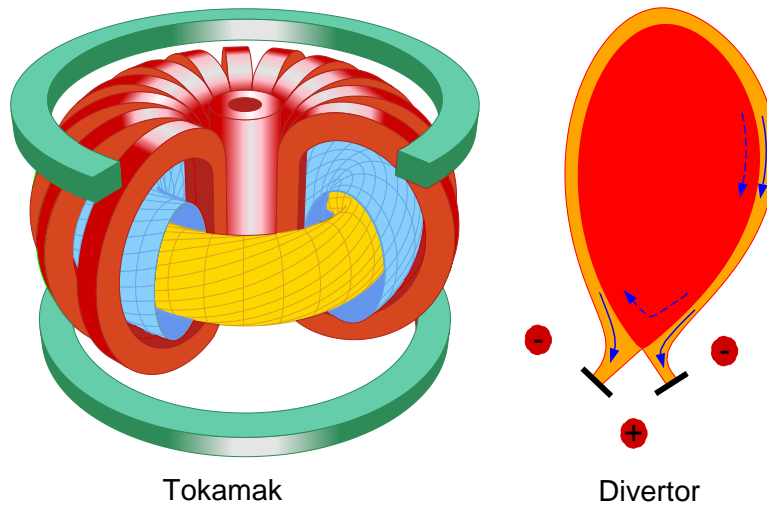


Figure 1.1.: Schematic view of a tokamak. The magnetic field lines create flux surfaces due to the action of poloidal and toroidal field components, either through external coils or due to the generation of magnetic field by the plasma current itself. The plasma current is created by using the transformer in the centre of the machine and inducing the current in the plasma as the secondary winding. Usage of additional coils can create a divertor with X-point.

The aim of this work is to give insight into the physics in the scrape-off layer (SOL), which is defined as the region of open fieldlines intersecting walls. It is characterised by the competition of parallel and perpendicular transport. The description of the plasma-wall interaction due to the existence of walls and atomic processes are necessary ingredients for



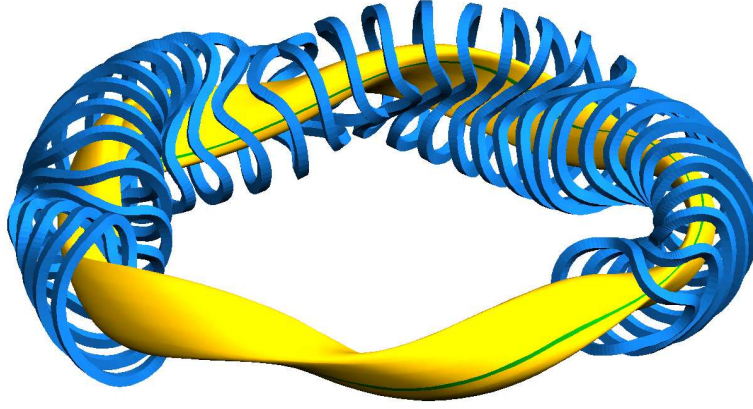


Figure 1.2.: Schematic view of a stellarator (W7-X). Here, the plasma is nearly current-free and all field components for the plasma confinement are created by 3D, external magnetic coils.

an understanding of the scrape-off layer. This introduction will mainly focus on divertor tokamaks, but most of the arguments and principles can be easily adapted also to other concepts like island divertors in stellarators or limiter devices. Results from 2D SOL transport codes will be used as a tool to identify the basic physics mechanisms. Most of the discussion will be done for ASDEX-Upgrade results.

The work is structured as follows: the first part introduces, after a short motivation, the basic concepts for power and particle exhaust in the SOL. The discussion of the different length scales involved in the SOL physics follows, including sheath physics. The second major part covers the physics of the pure hydrogen plasma on the basis of a fluid description. The influence of neutral transport on the different operation regimes will be the main topic. This part will finish with time-dependent phenomena for the pure plasma, so-called Edge Localised Modes (ELMs). The next part discusses the influence of impurities on the SOL plasma. For the understanding of impurity physics in the SOL one needs a rather complex combination of different aspects. The impurity production process has to be understood, then the effects of impurities in terms of radiation losses have to be included and finally the impurity transport is necessary. This will be introduced with rising complexity starting with simple estimates, analysing then the detailed parallel force balance and the flow pattern of impurities. Using this, impurity compression and radiation instabilities will be discussed. This part ends, combining all the elements introduced before, with specific, detailed results from ASDEX-Upgrade (especially for the optimized new divertor configuration). The effect of drifts and currents is addressed in the next part, including the derivation of the basic equations and some examples. Finally, some work on deriving scaling laws of the anomalous turbulent transport based on automatic edge transport code fitting procedures will be described. Looking forward, the necessary work to achieve a self-consistent SOL model including the anomalous turbulent transport will be discussed.

## 2. Motivation

The scrape-off layer region gets very important in any fusion reactor, because it is directly related to the requirements for power and particle exhaust compatible with the core confinement. One major problem is that the thickness of the layer where the heat flux from the core is transported onto walls is rather small (typically about 1 cm, which is the size of the poloidally projected ion gyro-radius) due to the very strong parallel transport, especially for the required enhanced confinement modes necessary for ignition. This results in severe engineering problems due to exceedingly large power loads on the walls, illustrated here for ITER and motivating the need for a detailed understanding of the scrape-off layer physics.

In ITER the amount of power carried by the alpha-particles  $P_\alpha$  has to be exhausted in a controlled way. Doing a simple estimate for the ITER target plate power load  $q_{\perp,tp}$ , one gets

$$q_{\perp,tp} = \frac{P_\alpha}{2\pi \cdot R_{X-point} \cdot 2 \cdot \Delta_e}, \quad (2.1)$$

where  $\Delta_e$  is the energy decay length at the target plate and  $R_{X-point}$  is the major radius at the X-point. For this estimate one assumes the deposition of the power in a strip of  $\Delta_e$  on 2 divertor plates on a ring with length  $2\pi R_{X-point}$ .

This gives for the planned ITER [2]

$$q_{\perp,tp} = \frac{300 \text{ MW}}{4\pi \cdot 7 \text{ m} \cdot 0.02 \text{ m}} = 175 \text{ MW/m}^2. \quad (2.2)$$

Introducing further reduction factors due to bulk radiation losses (0.8) and poloidal tilting of target plates (0.5-0.25) one still get values of about  $q_{\perp,tp} = 35 \text{ MW/m}^2$ . Realistic values for steady-state operation are below about  $5 \text{ MW/m}^2$ . This means that additional losses are required to spread the target power load over a wider area. It is important to note here that the final concept has to be compatible then also with the necessity of particle exhaust (helium ash removal) and core confinement.



## 3. Power and particle exhaust concepts

In the following the different concepts of exhaust will be shortly presented.

### 3.1. Limiter

The first concept is the limiter, where the plasma volume of closed fieldlines is limited by direct contact of hot core plasma with a “Limiter”, e.g. the ALT-II, TEXTOR (see Fig. 3.1).

Its advantage is its direct influence onto the core and its principal simplicity. However, it

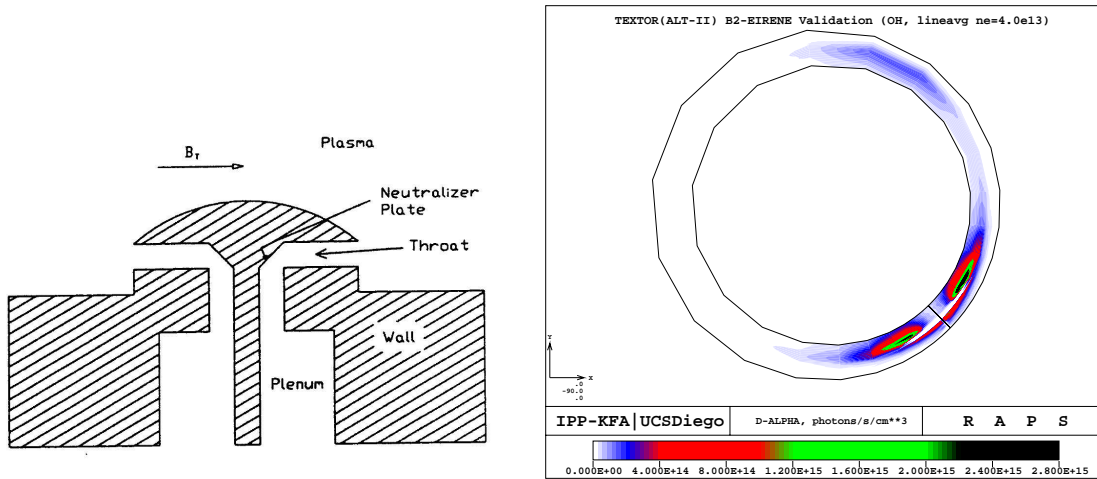


Figure 3.1.: Schematic view of the ALT-II pump limiter of TEXTOR (left side, M. Baelmans, Forschungszentrum Jülich).

Plasma entering the throat is neutralized at the neutralizer plate and the neutrals are directed through the plenum into a pump duct. On the right side, the calculated  $D_\alpha$  emission for an ohmic shot with a line-averaged density of  $4.0 \cdot 10^{19} m^{-3}$  is shown (D. Cray, UC San Diego).

has severe problems due to this direct contact with the hot plasma: this can produce too high limiter power loads, resulting in hot spots and thus generating large erosion problems and difficult impurity control situations (carbon blooms). For larger input powers combination with radiation losses of extrinsic impurities (such as noble gases) on closed field lines (photosphere) is required for this concept.

### 3.2. Divertor

The second concept is the divertor, where additional coils produce a divertor by creating a separatrix intersecting in the X-point (Figs. 1.1 and 3.2). Here, the basic idea is to move the interaction zone away from the core to so-called divertor plates, e.g. ASDEX-Upgrade.

It is hoped to get a better impurity control due to very good divertor retention and to achieve a reduction of the heat flux to target plates due to radiation losses. A potential problem is the fact that it is dominated by more non-linear reactions than the limiter. Here, the problem of radiation instabilities (so-called MARFES) has to be addressed.

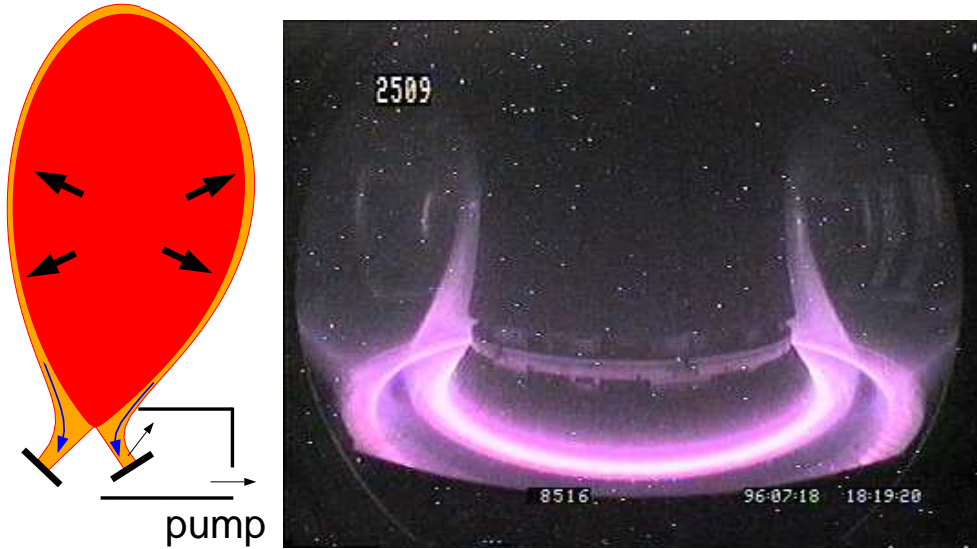


Figure 3.2.: Schematic view of a divertor (left side). Energy and particles flow over the separatrix into the divertor and hit there target plates. Neutrals created at the target plates can escape into a pumping duct. On the right side, a toroidal view from a CCD camera is shown for an ASDEX Upgrade divertor plasma (K. Büchl). The enhanced  $D_{\alpha}$  emission at the target plates is seen, showing the location of the interaction zone between plasma and walls, which has now moved away from the main plasma into the divertor compared to the limiter configuration.

### 3.3. Stellarator island divertor

The third concept is the island divertor of the stellarator [3] (Fig. 3.3), which has similar properties to the tokamak divertor, but is much more complex due to its 3D characteristics, e.g. W7-AS and W7-X.

Eventually, one has the chance to operate at higher density without the danger of disruptions, because the stellarator is internally current-free. Also, there is the potential to use the three-dimensionality for impurity and neutral screening. Potential problems are the

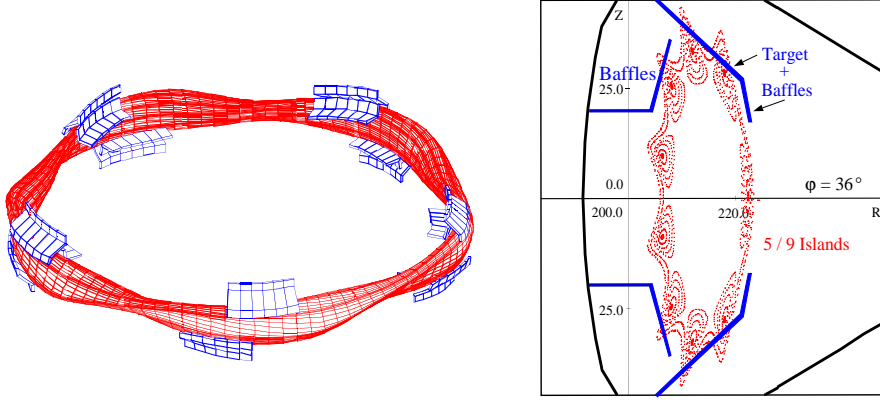


Figure 3.3.: Possible stellarator island divertor geometry for W7A-S with targetplates and baffles. 3D-view of plasma, targetplates and baffles on the left, 2D-Poincare plot for one poloidal plane on the right (Y. Feng, IPP Garching)

danger to produce local instabilities (hot spots, MARFES) even earlier than in the 2D tokamak divertor and much more difficult baffling and pumping, due to the 3D structure.

### 3.4. Ergodic limiter

The fourth concept is the ergodic limiter [4], where modulation coils produce an ergodic edge by magnetic error-fields resulting in an magnetic field diffusion by a random walk of field-lines at every turn-around, e.g. Tore Supra (Fig. 3.4). Due to this ergodic zone with enhanced radial transport this is combined with the limiter to reduce the power load on the limiter by radiation losses and to benefit from a better impurity shielding. However, this concept is not effective for open field-lines, because the field-lines do not make enough turns (since they soon intersec wall structures) to experience the error-field and by this the field diffusion.

The possible advantage of this concept is to overcome the problems of limiters with a 3D SOL structure. Also, for a concept relying on radiation losses on closed field lines (photosphere), the enhanced radial transport in this zone might maximize these losses and thus reduce the necessary amount of additional extrinsic impurities (like noble gases) to be injected. Its potential problems (like for the stellarator) is that the 3D structure might produce local instabilities (hot spots, MARFES) and baffling and pumping gets more difficult.

The prospects of all concepts have to be evaluated to define the optimised concept for a reactor. If a kind of photosphere close to the edge by radiation of extrinsic impurities like argon or neon can be realised compatible with good core confinement then all four concepts are possible candidates. However, if the edge region has to be kept hot to guarantee good confinement for ignition then the concept of a divertor is favoured, because it has the best chance to reduce the power load by spreading the power by impurity radiation and neutral losses from the midplane down to the divertor plates.

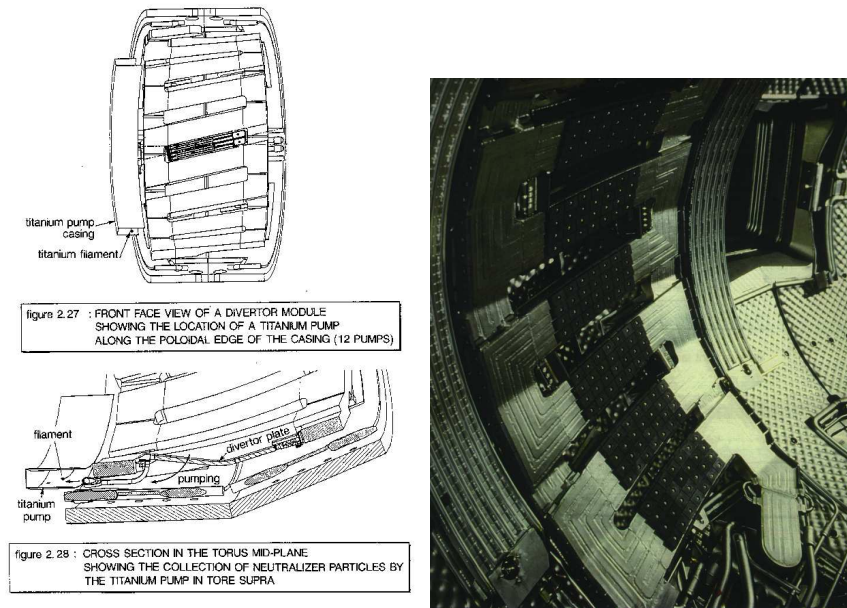


Figure 3.4.: Front face view of a divertor module for Tore Supra (left upper side). Modulation coils and windings for magnetic error-fields can be seen. Plasma should be neutralized at divertor plates (in a 3D fan structure, left lower side). The neutrals are directed to a titanium getter through this 3D structure. On the right side a view into Tore Supra shows the realisation of this in the machine. (All pictures from Tore Supra EURATOM phase I proposal for a new ergodic divertor)

## 4. Scrape-off layer length scales

In this chapter the different length scales defined by transport (i.e. heat conduction) and relaxation (i.e. Maxwellization, temperature equilibration) of plasma particles and by their interaction with neutrals will be discussed to address the physics in the scrape-off layer (following [5]).

### 4.1. Transport along fieldlines

The first important process is the transport along fieldlines, which is governed by Coulomb collisions. The electron mean-free path length  $\lambda_e = v\tau_e = \sqrt{3}v_{th,e}\tau_e$  for a test particle with energy  $mv^2/2 = 3/2kT$  and a thermal speed  $v_{th} = (kT/m)^{1/2}$  is

$$\lambda_e \cong 1.5 \cdot 10^{16} T^2 / n, \quad (4.1)$$

with temperature  $T$  in electron Volts (eV) and the rest in MKS-units. This is the sum of small angle scattering events producing a  $90^\circ$  deflection. According to the Rutherford scattering formula the mean free path scales with  $v^4$ .

The ion-ion and electron-ion mean free paths are practically identical to the electron-electron mean free path (within a factor of  $1/\sqrt{2}$ ).

The electron heat conduction along the magnetic field is

$$q_{e,\parallel} = -\chi_{e,\parallel} \nabla_{\parallel} T_e, \quad (4.2)$$

with  $q_{e,\parallel}$  and  $T_e$  being the electron heat flux and temperature respectively.

Heat conductivity  $\chi_{e,\parallel}$  is given by:

$$\chi_{e,\parallel} \cong 1.8 \cdot 10^3 T_e^{5/2} \quad (4.3)$$

The ion parallel heat conduction is smaller by a factor of the order of  $\sqrt{m_e/M_i}$ , therefore less important.

One can define an electron temperature gradient length  $\lambda_{\nabla T}$  along the fieldline

$$\lambda_{\nabla T} = \chi_{e,\parallel} T_e / q_{e,\parallel} \cong 1.8 \cdot 10^3 T_e^{7/2} / q_{e,\parallel} \quad (4.4)$$

with  $T_e$  in electron Volts (eV) and  $q_{e,\parallel}$  in  $W/m^2$ .

One gets typical values for the SOL ( $T_e=50$  eV)  $q_{e,\parallel} = P_{heat}/(2\pi \cdot R \cdot \lambda_{perp})$  for ASDEX Upgrade:  $q_{e,\parallel} = 10 MW/(2\pi \cdot 1.65m \cdot 1cm) = 1 \cdot 10^8 W/m^2$



and for ITER:  $q_{e,\parallel} = 300 \text{ MW} / (2\pi \cdot 8.0 \text{ m} \cdot 1 \text{ cm}) = 6 \cdot 10^8 \text{ W/m}^2$ .

However, heat conduction is done mostly by the tail electrons with velocities of  $\geq 3.7v_{th,e}$ . For the heat conduction equation to be applicable, these must have a mean free path  $\lambda_{hce}$  smaller than the temperature gradient length  $\lambda_{\nabla T}$ .

The mean free path of a test particle and Maxwellian target particles of the same species with mean energy  $mv_{test}^2/2 = 3/2kT$  is given by  $\lambda_{hce} = (v/v_{test})^4 \lambda_e = (v/(\sqrt{3}v_{th,e}))^4 \lambda_e$ . This gives

$$\lambda_{hce} = 21\lambda_e \quad (4.5)$$

For steeper gradients the heat flux is non-locally determined by a weighted mean of the temperature profile over a radius of about  $5\lambda_e$ .

The different characteristic lengths are plotted in Fig 4.1 for two densities ( $1.0 \cdot 10^{20} \text{ m}^{-3}$  and  $3.0 \cdot 10^{19} \text{ m}^{-3}$ ), a magnetic field of 2T and an angle of incidence of the field-line of  $3^\circ$ .

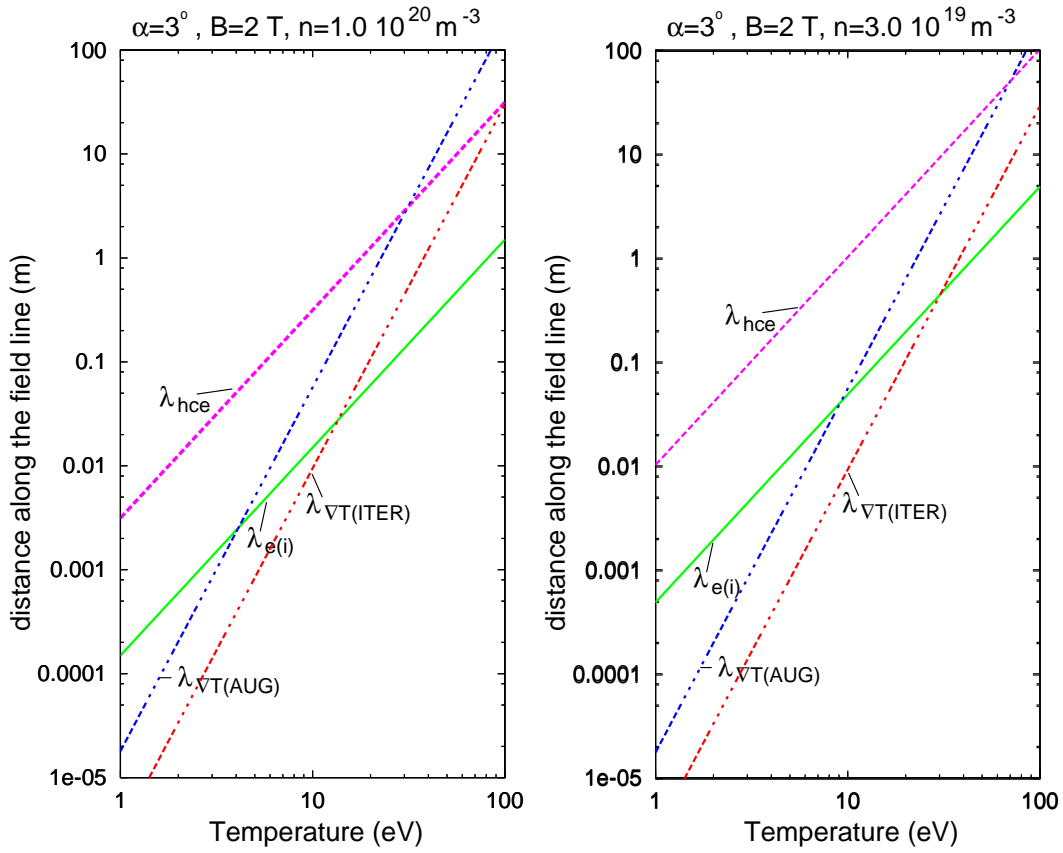


Figure 4.1.: Scrape-off layer length scales for an angle of incidence of the field-line of  $3^\circ$ , a magnetic field of 2 T and a density of  $1.0 \cdot 10^{20} \text{ m}^{-3}$  (left) and  $3.0 \cdot 10^{19} \text{ m}^{-3}$  (right) as a function of temperature

## 4.2. Interaction with neutrals

Ions hitting a surface get neutralized after acceleration in the sheath. Due to their ionization, they set up a recycling cycle resulting in a large flux amplification (at low temperatures) of the target particle flux compared to the throat ion flux at the divertor entrance. Recycling enhances density at the plate and therefore reduces the temperature and by consequence the sputtering. Additionally, radiation losses by hydrogen and impurities spread the divertor target load over a larger area.

Neutral hydrogen molecules from the wall create a population of neutral hydrogen atoms by dissociation of about  $m_i v_0^2/2 = 2 - 3\text{eV}$  (Franck-Condon energy). They have a mean free path of  $\lambda_{ion}$  before being ionized by collisions with electrons of velocity  $v_e$

$$\lambda_{ion} = v_0 / (n_e < \sigma_{ion} v_e >). \quad (4.6)$$

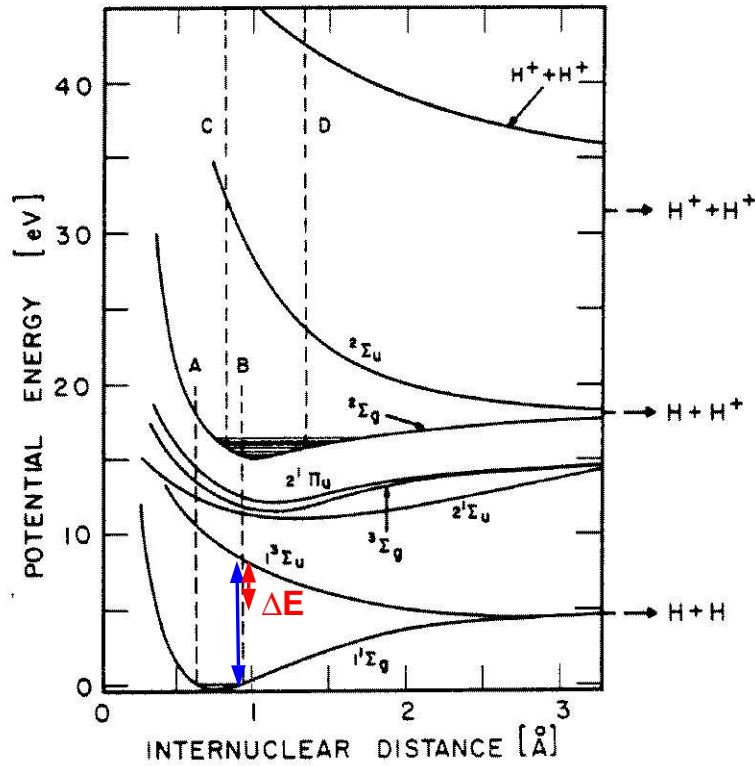


Figure 4.2.: Potential energy of  $H_2$  and  $H_2^+$  molecules as a function of internuclear separation. The Franck-Condon region of  $H_2$  is shown by the vertical lines A and B [6].

The Franck-Condon energy is derived from the Franck-Condon principle for the intensity of vibrational transitions of molecules. In the classical formulation by Franck this means, that the jump of an electron from one state to another ( $10^{-16}s$ ) is so fast compared with

the period of nuclear vibrations ( $10^{-14}s$ ) that these nuclei keep the same positions and velocities before and after this electron transition (vertical paths in the potential energy curve, i.e. interaction energy as a function of inter-nuclear separation, Fig. 4.2). Condon formulated this for quantum mechanics.

If, like in  $H_2$ , the potential energy curve of the upper level is shifted away from the ground state to higher energies then the Franck-Condon region also includes a part of continuous levels above the dissociation threshold.

In the Fig. 4.2, the range of inter-nuclear separation associated with the lowest vibrational state of  $H_2$  is indicated by the vertical lines A and B. An incident electron is most likely to encounter the nuclei at the turning points in their motion (A or B). To describe the effects of electron collisions with molecular hydrogen let us consider the scenario in which the energy of the incident electron is progressively increased. The first transition from the ground state occurs at about 8.5 eV (see line B). This state is repulsive and dissociates into two ground state H atoms. At the Franck-Condon-edge (B) the potential energy of the upper state is about 4 eV higher than the ground state curve at infinite internuclear separation. Therefore, two H atoms are created with about 4/2 eV kinetic energy.

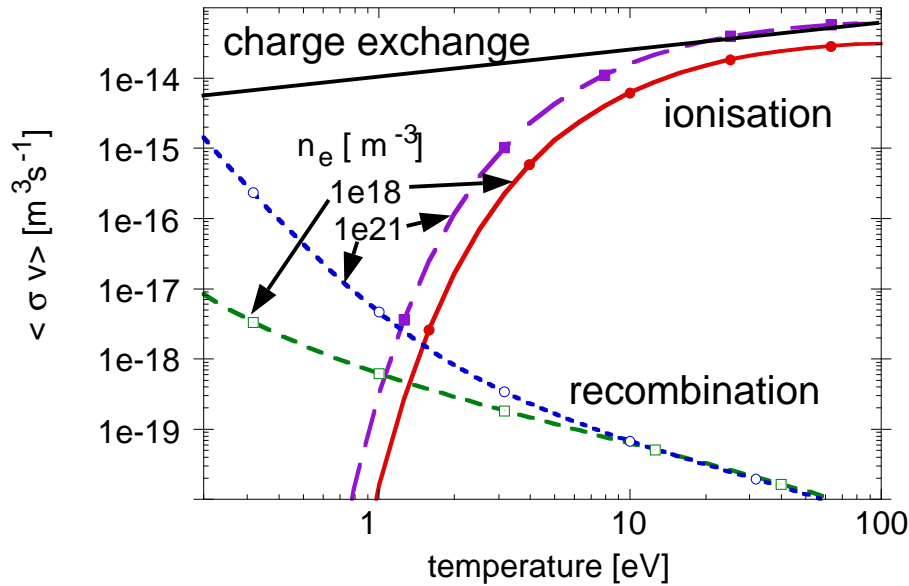


Figure 4.3.: Reaction rates for charge-exchange, ionisation and recombination for hydrogen (in  $m^3 s^{-1}$ ) versus temperature (in eV).

The second important process for neutral hydrogen is the charge-exchange of neutrals with ions (see also Fig. 4.3).

The mean free path of a neutral H atom  $\lambda_{CX}$  before exchanging charge with an  $H^+$  ion of velocity  $v_i$  is

$$\lambda_{CX} = v_0 / (n_i \langle \sigma_{CX} v_i \rangle). \quad (4.7)$$

$\sigma_{CX} \approx 5 \cdot 10^{-19} m^2$ ,  $v_i = v_0 = \sqrt{2kT_0/m_0} = 1.4 \cdot 10^4 m/s$  for hydrogen with a temperature  $T_0$  of 1 eV.

For the detachment physics below about 2 eV volume recombination gets important (Fig. 4.3). Recombination of an electron and an ion to a neutral atom needs a third body to account for the conservation laws. This is possible in two ways: in the process of radiative recombination a photon takes care of energy and momentum transfer. This process shows up in the recombination rate plot as the lower envelope of the different density values. The second process is three-body recombination where an additional electron is necessary. The recombination rate for this process gives below about 2 eV the strong rise (especially for high densities above  $10^{20}m^{-3}$ ) in the plot of the effective hydrogenic recombination rate.

The penetration of neutrals into a plasma can be divided into three regimes (Fig. 4.3): For  $T > 10eV$  one gets a kinetic regime with a small number of CX events before ionisation ( $\lambda_0 \approx \lambda_{CX} \approx \lambda_{ion}$ ).

For  $T \ll 10eV$  (and larger than 2 eV) the neutral transport is diffusive in a random walk process, where many CX collisions occur before the neutral is ionized ( $\lambda_{ion} \gg \lambda_{CX}$ ,  $\lambda_0 \approx \sqrt{\lambda_{CX} \lambda_{ion}}$ ). Below 2 eV the plasma recombines in the volume and gets stopped before it reaches the wall.

For a comparison of the characteristic neutral lengths with the parallel transport lengths the mean free paths for CX and ionisation are plotted (projected onto the fieldline by the field-line angle sine) in Fig. 4.4.

A more detailed discussion of the atomic physics of neutrals can be found in [6, 7].

### 4.3. Brief summary of sheath physics

In this chapter a brief summary of the physics of the sheath is presented. More complete discussion of this can be found in [5].

To analyse the physics of the sheath some additional definitions are necessary:

The simplest situation in a plasma is characterized by equilibrated Maxwellian distribution functions

$$f(\vec{v}) = (m/(2\pi kT))^{3/2} \exp(-mv^2/(2kT)). \quad (4.8)$$

For these, a root-mean-square velocity

$$\overline{v^2} = \sqrt{3kT/m}, \quad (4.9)$$

an average velocity

$$\overline{|v|} = \sqrt{8kT/(\pi m)} \quad (4.10)$$

and a random flux onto a plane

$$j_{Random} = 1/2n\overline{|v_{Random}|} = 1/4n\overline{|v|} \quad (4.11)$$

can be derived.

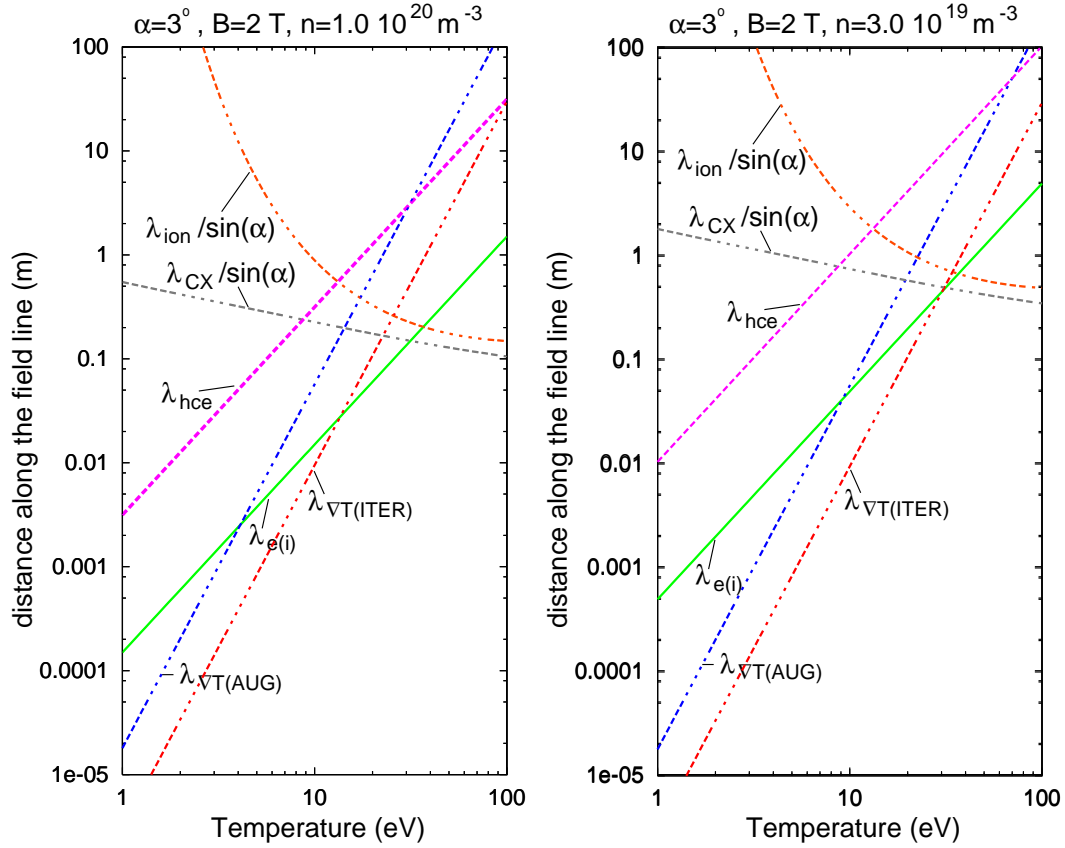


Figure 4.4.: Scrape-off layer length scales for an angle of incidence of the field-line of  $3^\circ$ , a magnetic field of 2 T and a density of  $1.0 \cdot 10^{20} m^{-3}$  (left) and  $3.0 \cdot 10^{19} m^{-3}$  (right) as a function of temperature

#### 4.3.1. Plasma-wall contact without magnetic field

Assuming ideally reflecting walls and Maxwell distribution functions  $f(v)$ , one gets a much larger electron than ion current due to the much smaller electron mass compared to the ion mass  $j_e = (m_i/m_e)^{1/2} j_i$  and a constant wall potential ( $\Phi = const$ ).

$$j_e = 1/4 n_e \overline{|v|}_e, j_i = 1/4 n_i \overline{|v|}_i, n_e = n_i = n. \quad (4.12)$$

A much more realistic scenario is complete wall recombination, because ions and electrons get completely neutralised at the (conducting) wall.

The different regions (sheath and presheath) in front of this wall can be characterised rather qualitatively regarding the properties of the plasma in this region (see Fig. 4.5). The recycling neutrals get ionized at distance  $\lambda_{ion}$  in the presheath, where ions are accelerated to sound speed at the sheath edge  $x_s$  as described by the Bohm criterion ([8, 9] see later).

The sheath is characterized by free outstreaming ions and no interaction with neutrals. The coupling with electrons is done by the electric field. In this region collisions can be neglected. Due to their much smaller mass, electrons are moving faster than ions. Therefore, a higher potential relative to the wall develops to reflect some electrons and achieve

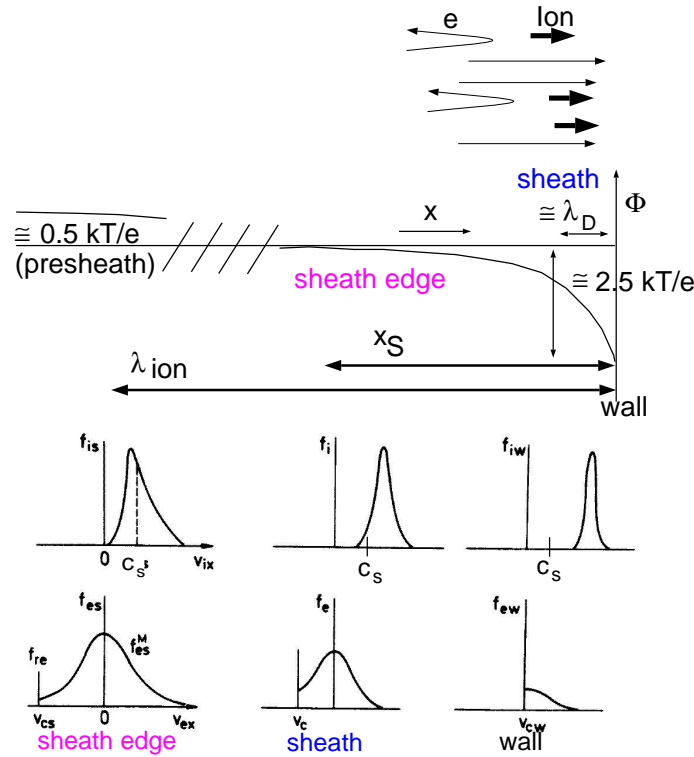


Figure 4.5.: Schematics of the sheath potential in front of the wall without magnetic field (top). The relevant length scales are shown: Debye-length  $\lambda_D$ , sheath edge position  $x_S$  and ionisation length for neutrals  $\lambda_{ion}$ . In the bottom, the velocity distribution functions for ions  $f_i$  and electrons  $f_e$  are shown at the sheath edge, in the sheath and at the wall. The electrons have a cut-off Maxwellian (with a cut-off velocity  $v_{cs}$  at the sheath edge). At the wall no electrons are going back (half -Maxwellian). The ions have already at the sheath edge a Non-Maxwellian distribution function as they are accelerated to  $c_S$  or larger because of the Bohm criterion. (Figure from R. Chodura)

zero net current on the length scale of a Debye length.

At the wall ions are neutralised completely. The electrons have a half-Maxwellian velocity (energy) distribution.

Consequently, electrons impinging from the plasma onto a wall contribute less to the energy deposition at the wall than ions, because electrons are partly reflected whereas ions are accelerated in the sheath.

The sheath introduces additional length scales: first the Debye length, which is defined as the length-scale for charge separation and shielding of electric potentials (Fig. 4.6)

$$\lambda_D = \sqrt{\epsilon_0 k T_e / (n_e e^2)} \cong 2.35 \cdot 10^5 (T_e / 1000.0 / n_e)^{1/2}. \quad (4.13)$$

All regions of the SOL with length scales larger than the Debye length may be treated as

being quasineutral. Thus only the electrostatic part of the sheath deviates from neutrality.

Second is the Maxwellian relaxation length, describing the isotropization and Maxwellization of the electron distribution function by electron-electron and electron-ion collisions. The electron distribution ahead of the sheath is depleted for  $v > v_c$ , where  $m_e v_c^2/2 \cong 3kT_e$  due to losses to the wall. With increasing distance from the wall this loss region is filled up by collisions, i.e. electron distribution is isotropized by electron-electron and electron-ion collisions and Maxwellized by electron-electron collisions on a length scale  $\lambda_{re}$  (Fig. 4.6)

$$\lambda_{re} \cong 4\lambda_e. \quad (4.14)$$

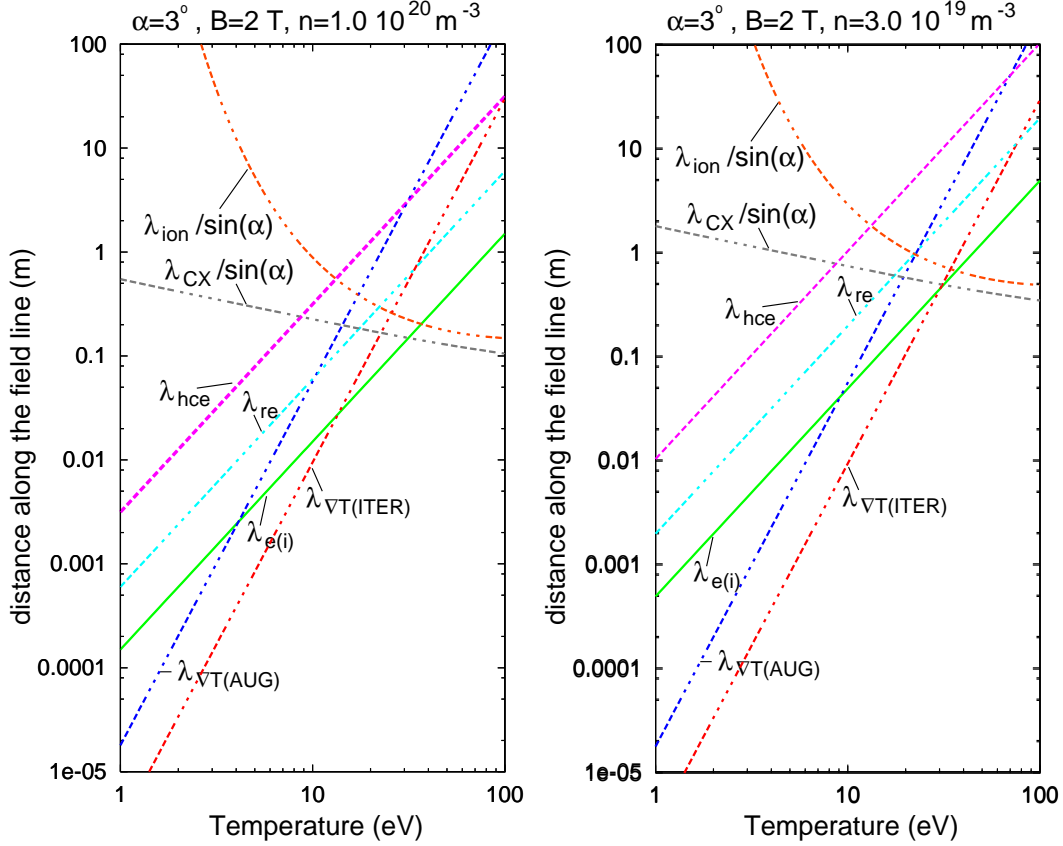


Figure 4.6.: Scrape-off layer length scales for an angle of incidence of the field-line of  $3^\circ$ , a magnetic field of 2 T and a density of  $1.0 \cdot 10^{20} \text{ m}^{-3}$  (left) and  $3.0 \cdot 10^{19} \text{ m}^{-3}$  (right) as a function of temperature

### Bohm criterion at the sheath edge

In the region ( $x_s > x > \lambda_D$ ) charge separation is still small:  $\Delta\Phi \ll kT_e$ . Therefore, one can calculate the change of charge density for electrons and ions (with velocity  $v_{i0}$ ) for small variations of the potential  $\Delta\Phi$  in a linearized form.

For electrons which have a Boltzmann distribution:

$$n_e = n_{e,plasma} * \exp(-e\Delta\Phi/(kT_e)) \approx n_{e,plasma}(1 - \frac{e\Delta\Phi}{kT_e}) \quad (4.15)$$

and for ions, where one applies the energy conservation (cold ions):

$$\frac{1}{2}mv_i^2 - e\Delta\Phi = \frac{1}{2}mv_{i,plasma}^2, \quad (4.16)$$

which gives:

$$v_i^2 = v_{i,plasma}^2 + \frac{2e}{m_i}\Delta\Phi. \quad (4.17)$$

Taking into account ion current density conservation:

$$n_{i,plasma}v_{i,plasma} = n_iv_i \quad (4.18)$$

and combining both:

$$n_i = n_{i,plasma} \sqrt{\frac{v_{i,plasma}^2}{v_{i,plasma}^2 + 2e/m_i\Delta\Phi}} \approx n_{i,plasma}(1 - \frac{e\Delta\Phi}{m_iv_{i,plasma}^2}). \quad (4.19)$$

This gives a net charge density:

$$n_i - n_e = n_{plasma}e\Delta\Phi(\frac{1}{kT_e} - \frac{1}{m_iv_{i,plasma}^2}). \quad (4.20)$$

In the sheath the electron density is decaying faster than the ion density. Therefore, for a monotonic potential  $n_i - n_e \geq 0$  is required, defining the Bohm condition at the sheath edge:

$$v_{i,plasma} \geq \sqrt{\frac{kT_e}{m_i}}, \quad (4.21)$$

where the r.h.s. is the unity Mach number  $M = \frac{v_{i,plasma}}{c_s} = 1$ .

The necessary acceleration is done in the presheath, where additional forces (ionisation, friction) build up an electric field for this (potential drop  $\frac{1}{2}kT_e$ ). This potential drop can be calculated from the necessary energy at the sheath edge of  $\frac{m}{2}c_s^2 = e\Phi_{presheath}$ . The expansion energy of the electrons builds up there due to their larger velocity a (weak) electric field, accelerating the ions to  $c_s$ .

One can also explain this in a different picture: ions and electrons are streaming out of the plasma and get neutralised completely at the wall. The created neutrals ionize far away from the wall. Therefore, no information is coming back (only characteristics pointing onto the wall). To transport information (this is done at the sound speed) the flow has to be at the sound speed (or faster).



### Calculation of potential drop

The electron current density at the wall is (for plasma potential = 0, wall potential  $\Phi_W < 0$ ):

$$j_e = -e/4n_e \overline{v}_e \exp(-e|\Phi_W|/(kT_e)). \quad (4.22)$$

From the Bohm criterion the ion density at the sheath entrance can be calculated:

$$j_i = Zen_i \sqrt{\frac{kT_e}{m_i}}. \quad (4.23)$$

In the sheath, the ions are accelerated due to the potential drop (with constant ion current density).

For zero net current at the wall ( $j_e = j_i$ ) and quasi-neutrality ( $Zn_i = n_e = n_0$ ), the wall potential (cold ions) follows as:

$$e\Phi_W = -kT_e \ln\left(\sqrt{\frac{m_i}{2\pi m_e}}\right). \quad (4.24)$$

For a hydrogen plasma one gets

$$e\Phi_W = -2.8kT_e. \quad (4.25)$$

Taking into account also warm ions modifies this somewhat to

$$e\Phi_W = -kT_e \ln\left(\sqrt{\frac{m_i}{2\pi m_e}} / \left(1 + \frac{T_i}{T_e}\right)\right), \quad (4.26)$$

resulting in (for a hydrogen plasma with  $T = T_i = T_e$ )

$$e\Phi_W = -2.5kT_e. \quad (4.27)$$

### Langmuir probe

This analysis of the sheath physics can be used to measure temperature and density in the scrape-off layer with so-called Langmuir probes (see also Appendix). For this, the Langmuir characteristic is used, where, for a probe pin in the plasma, current vs. potential is measured.

The electric current to a probe of area A is

$$I_{probe} = -I_{i,sat} + I_e \quad (4.28)$$

with

$$I_e = I_{e,sat} * \exp(e(\Phi_{probe} - \Phi_{plasma})/(kT_e)) \quad (4.29)$$

At net zero current  $j = 0$ , the probe sits at the floating potential  $V_{floating}$ , which is typically  $3kT_e$  below the potential of the undisturbed plasma. For homogenous plasmas this is identical to the vessel potential (standard sheath).

For large negative voltage one gets more and more electrons reflected, for constant ion current density

$$j_{i,sat} = Z e n_i \sqrt{\frac{kT_e}{m_i}}. \quad (4.30)$$

The maximum current, when no electrons can reach the probe, is called the ion saturation current

$$I_{i,sat} = A j_{i,sat}. \quad (4.31)$$

For large positive voltage ions are reflected. The maximum current is the electron saturation current

$$I_{e,sat} = A j_{e,sat}. \quad (4.32)$$

From the slope of the Langmuir characteristic one can derive the plasma temperature:

$$T_e = e/k(V_{probe} - V_{floating})(\ln(1 + \frac{I_{probe}}{I_{i,sat}}))^{-1}. \quad (4.33)$$

Knowing the temperature, the density can be calculated from ion saturation current

$$I_{sat,i} = n_e c_s e. \quad (4.34)$$

### 4.3.2. Plasma-wall contact with an electron emitting wall

Very often the plasma-wall contact is modified by the fact that the wall material is emitting electrons (or ions) ([10]). Then, the potential drop is reduced, since, to reach zero net current with an emitting wall having an electron emission coefficient  $\gamma$ , more electrons from the plasma have to reach the wall.

This gives a modification of the potential at the wall [11]:

$$e\Phi_W = -kT_e \ln((1 - \gamma)\sqrt{\frac{m_i}{2\pi m_e/m_i}}). \quad (4.35)$$

Nevertheless, there is a limit for very strong emission, because with reduced potential drop, the electric field at the wall also drops and reaches zero for a critical emission coefficient

$$\gamma_C = 1 - 8.3\sqrt{m_e/m_i}. \quad (4.36)$$

A higher emission leads to field reversal and the creation of an electrostatic double layer at the wall, such that emitted electrons are partly reflected back to the wall and are directly reabsorbed (space-charge limit of emission current). In the case of a pure hydrogen plasma one has there

$$\gamma_C = 0.86, e\Phi_W = -0.8kT_e. \quad (4.37)$$

In the following the different emission processes will be shortly discussed. More details can be found in [12].

## Electron emission processes

### Photoelectric emission

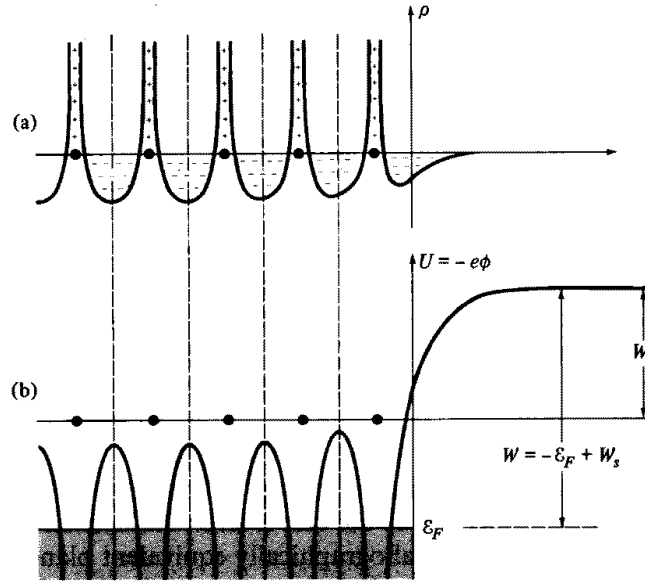


Figure 4.7.: Schematic charge distribution  $\rho$  and energy levels in a solid including the surface layer [12].

Electrons in a solid occupy energy levels according to the Fermi-Dirac distribution, where the Fermi-energy  $\epsilon_F$  is the highest occupied energy level (at zero temperature). Due to the existence of a surface the workfunction  $W$  (typically several eV) is modified by the contribution of a surface layer  $W_s$  (net electrical dipole moment and/or surface charge: displacement of surface atoms, missing neighbours)  $W = W_s - \epsilon_F$  (see Fig. 4.7). For photoemission, an electron gets the energy from a photon hitting the surface (energy  $h\nu$ ) and is emitted with energy  $h\nu - W$ .

This process is only important for satellite measurements in cosmic plasmas (see Fig. 4.8 for photoelectron emission coefficients).

### Thermionic emission

Electrons from the high-energy tail of the Fermi function

$$f(E) = \left( \exp\left(\frac{E - \epsilon_F}{kT}\right) + 1 \right)^{-1} \quad (4.38)$$

electrons can leave the solid, if they are able to overcome the workfunction (energies greater than  $\epsilon_F + W$ ). One gets the thermionic emission current from the (temperature

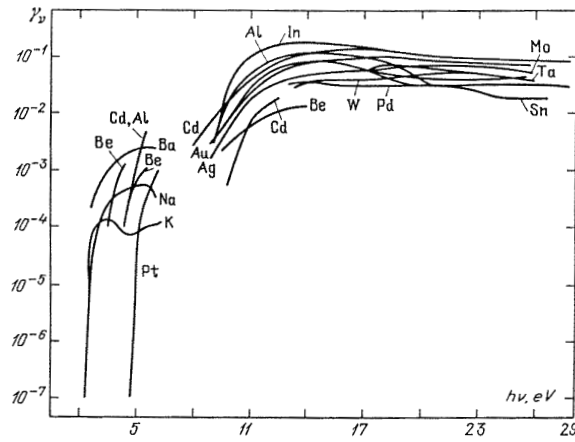


Fig. 4.16. Photoelectron emission coefficients (quantum yield) for various metals as functions of photon energy. From [4.2]

Figure 4.8.: Photoelectron emission coefficients for various metals as functions of photon energy [13].

dependent) number of electrons in these energy levels (Richardson-Dushman formula):

$$j_{th} = A T_{Wall}^2 \exp\left(-\frac{W}{kT_{Wall}}\right), \quad (4.39)$$

with

$$A \approx 1.2 \cdot 10^6 \frac{A}{m^2 K^2}. \quad (4.40)$$

The velocity distribution of the emitted electrons is Maxwellian, because they are thermalised by collisions in the solid.

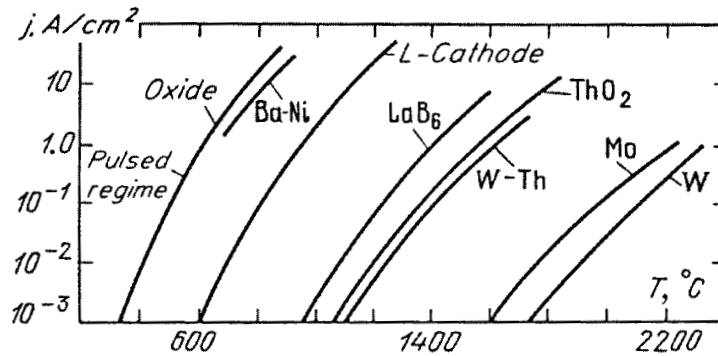


Fig. 4.14. Current density of thermionic emission as a function of cathode temperature for a of materials. From [4.16]

Figure 4.9.: Current density of thermionic emission as a function of cathode temperature for different materials [13].

Thermionic emission is quite important in arcs and hot spots (see Fig. 4.9). For example, graphite has a workfunction of 4.6 eV. Therefore, about 2500 K is needed for thermionic emission (which is very close to the melting temperature of carbon). Also, impurities on the surface can reduce the workfunction.

### Field emission

The effective workfunction can be reduced by electric fields (Schottky effect). However, this is usually unimportant for fusion plasmas, except for arcs.

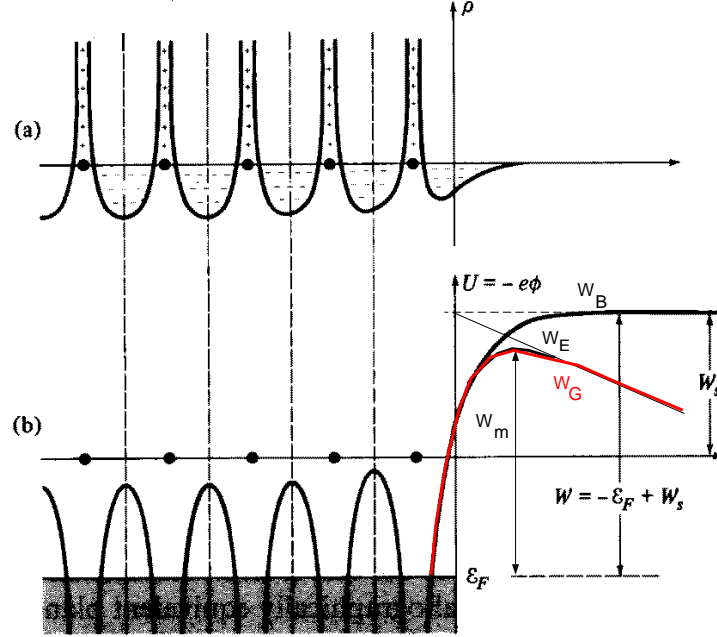


Figure 4.10.: Influence of external applied electric fields  $W_E$  on effective workfunction  $W_G$  [12].

An additional emission enhancement can be reached by tunneling of electrons through the potential wall created by the electric field. This process is especially important for creation of arcs in fusion plasmas (Fig. 4.10). High fields of order  $10^8 \text{ V/m}$  are required for this effect. The field emission electron microscope relies on this phenomenon.

### Secondary electron emission

Electrons hitting a surface are either reflected elastically (usually a small amount) or ejected due to inelastic collisions with other electrons (Fig. 4.11).

The energy distribution of the electron-induced secondary electrons has two peaks: one at low energies and one close to the energy of the impinging electrons.

The secondary electron emission coefficient  $\gamma_e$  has a maximum at 200 to 1000 eV. For fusion plasmas  $\gamma_e$  is between 0.4 and 0.6 (maximum estimate, [15]). However, this value is very uncertain because the measured data have to be extrapolated to lower energies.

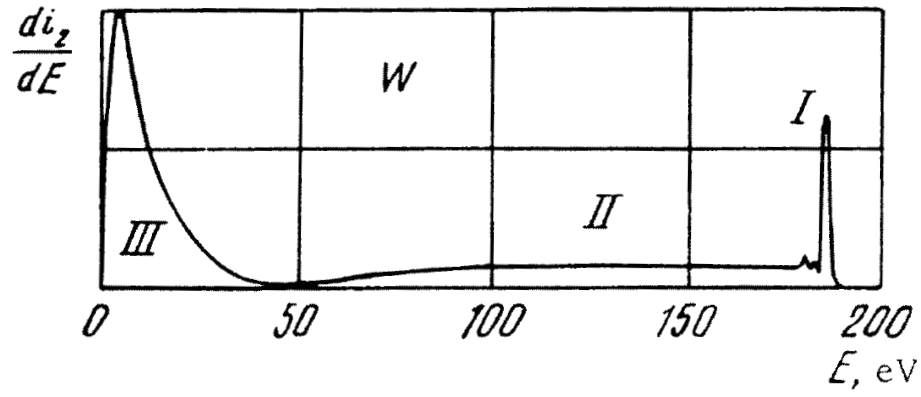


Figure 4.11.: Energy distribution of electrons hitting a surface [14].

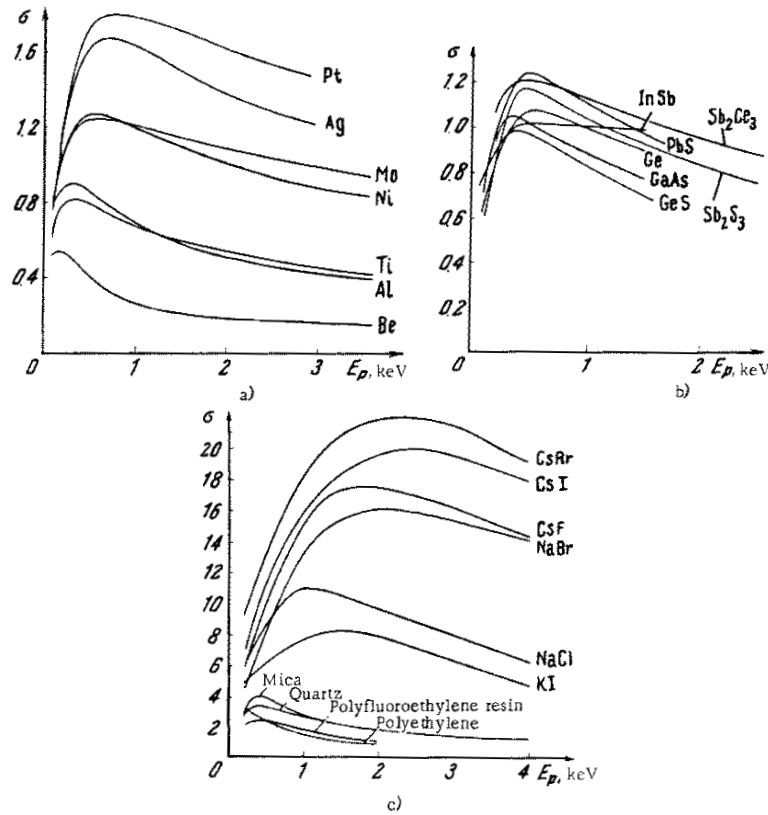


Figure 4.12.: Secondary electron emission coefficient for different materials [14].

The emission coefficient  $\gamma_i$  for ion-induced secondary electrons is rather small for fusion plasmas (about 0.07, [13]) and can therefore usually be neglected. Ions produce a large electric field in front of the surface and create a potential wall (like in the field emission, see Fig. 4.10), through which electrons can tunnel and neutralize the ions. If the difference between the energy of the electrons and the ionisation energy of the ion is larger than the

workfunction secondary electrons can be emitted.

### Total emission coefficient

The total emission coefficient

$$\gamma = \frac{\gamma_e + \gamma_i + j}{1 + \gamma_e + j} \quad (4.41)$$

is summarising all possible emission processes with the normalised (to the ion current density) emission current  $j$  (thermionic, field and photoelectric emission):

$$j = \frac{J}{n_e \sqrt{kT_e/m_i}} \quad (4.42)$$

### Arcs

The emission processes discussed before can result locally in strongly varying electric potential conditions at a surface. For example, fieldemission at a tip, one can get locally a smaller potential drop: a positive current at this position is flowing into the surface. The current can melt the material and a unipolar arc is created stabilised by thermo-electrons, where the vessel is the cathode and the plasma the anode (Fig. 4.13). Typical time-scales for unipolar arcs are  $\leq 1\mu s$  with plasma densities of about  $10^{20}m^{-3}$  and temperatures between  $3eV$  and  $10eV$  (this means voltages of  $3kT \approx 10$  to  $30$  eV)

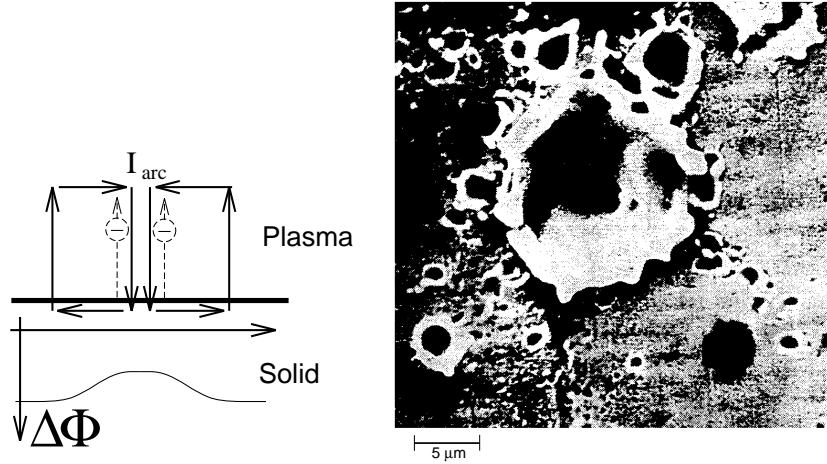


Figure 4.13.: Scheme of an arc (left). Arcing on a first wall material (right) [16].

The arc current  $I_{arc}$  (1 to 10 A) closes through a current from the wall into the plasma. After the creation of an arc, which can melt the wall material due to the arc current flowing into the surface, droplets can be released from the melted area (Fig. 4.14). Surprisingly the unipolar arc is moving opposite to the  $\vec{I}_{arc} \times \vec{B}$  Lorentz force (retrograde motion), when the magnetic field is parallel to the surface (see Fig. 4.15).

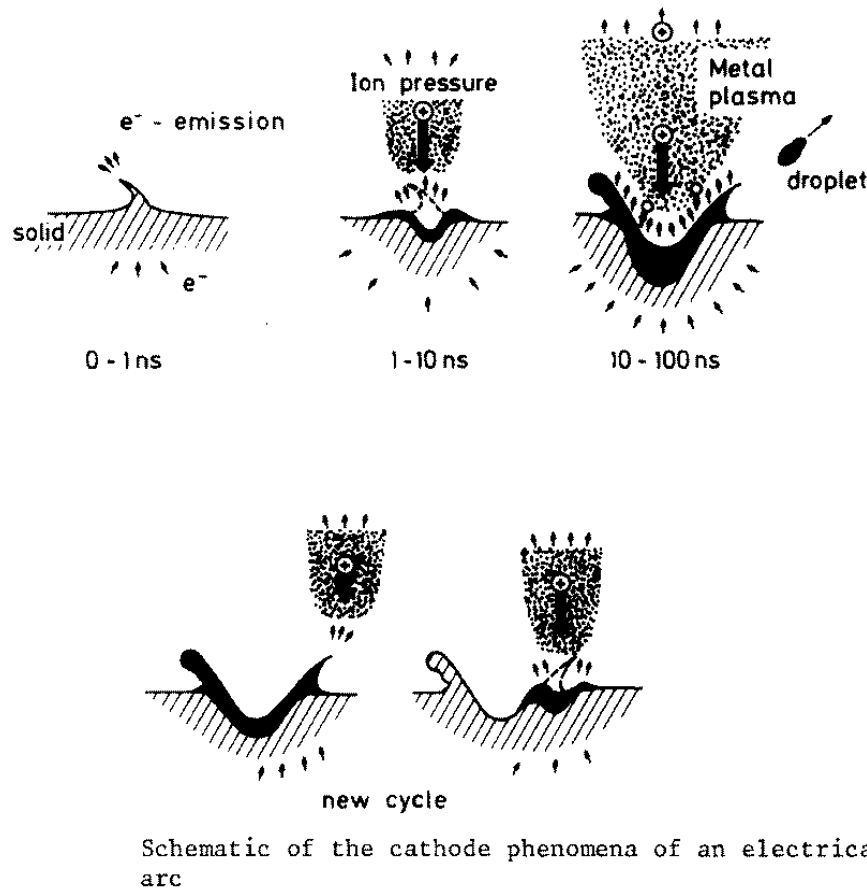


Figure 4.14.: Schematic sketch of the development of an electrical arc [16]. Due to enhanced secondary electron emission or fieldemission at a tip one gets locally a smaller potential drop and a positive current flowing at this position into the surface. This current can melt the material and a metal plasma is created (eventually droplets are also released), which is moving due to the interaction with the magnetic field (Lorentz force). At positions where one has additional tips the process can continue and melt additional areas.

This retrograde arc motion can be understood as an effect of the interaction of radial electric field and magnetic field (see Fig. 4.15). At the edge of the positively charged cloud of ionized metallic vapour in front of the cathode an additional radial electric field builds up directed towards the anode. The direction of the drift from the interaction of this field and the external magnetic field depends on the direction of this radial electric field. At the  $\vec{E} \times \vec{B}$  side the plasma moves away from the surface, whereas in the other direction it moves towards the surface. By this enhanced power flux onto the wall in the retrograde direction because of the enhanced electric field in the Debye sheath (due to the larger plasma density) the arc moves against the field.



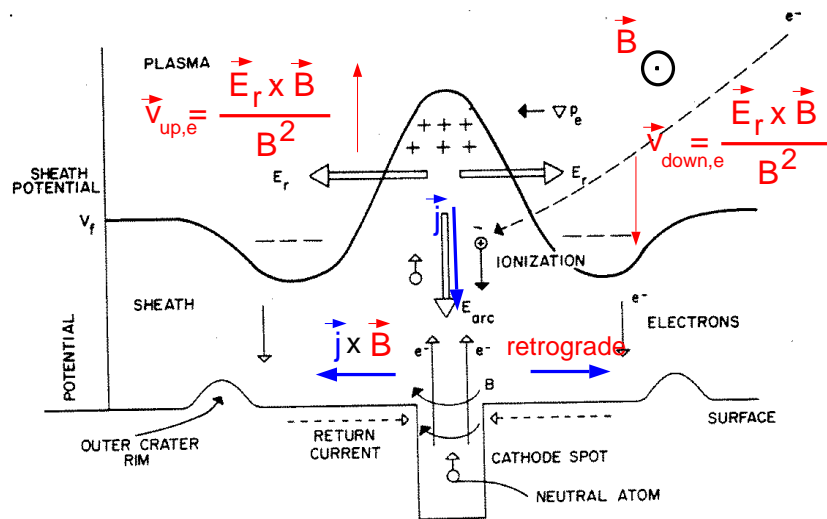


Figure 4.15.: Schematic sketch of an unipolar arc. (original Figure from [17])

There are other explanations for this retrograde motion:

Due to the large arc current the magnetic field of the arc can be larger the external one. When the current to the anode is deflected in the  $\vec{E} \times \vec{B}$  direction a kink instability can develop driving the arc into the retrograde direction.

Also, it is possible that, due to the strong erosion, surface material can get expelled (like pellets) into the plasma and get ionized there. These penetrate deeper into the plasma on the  $\vec{E} \times \vec{B}$  side, whereas on the retrograde side they drift back to the wall, creating a rough surface patch which can act as a new arc trigger.

In contrast to arcs hot spots (which do not create their own plasma due to ionization of eroded neutrals) move (experimentally and in simulations) in  $\vec{E} \times \vec{B}$  direction, because hot spots do not show the effects which are candidates for retrograde motion: strong self-induced magnetic field or positive cloud of ionized gas in front of the surface.

### 4.3.3. Plasma-wall contact in presence of a magnetic field

Due to the magnetic field electrons and ions gyrate with frequency  $\omega_C = |q|B/m$  and radius  $v_\perp/\omega_C$ , where  $v_\perp$  is the component of the velocity perpendicular to the magnetic field. In thermal equilibrium and a system with two degrees of freedom, one has  $v_\perp = \sqrt{2}v_{th}$ . The gyration or Larmor radius is proportional to  $\sqrt{m}$ . With a magnetic field perpendicular to the wall, one gets the same results as without field, because the gyration is perpendicular to the electric field. For the sheath physics, only the dimension perpendicular to the wall, e.g. parallel field-lines is important. For an inclined magnetic field, in the presheath ions are confined to the field-lines by the weak electric field in the presheath, whereas they experience a strong electric field with a force perpendicular to the wall in the electrostatic sheath. In contrast, electrons stay more strongly coupled to the fieldlines due to their much smaller gyroradius. A magnetic sheath is formed in which ions experience

both electric and magnetic forces (see Fig. 4.16). The magnetic sheath has a width of up to 3 ion gyroradii. Here, the ions are accelerated to sound velocity perpendicular to the wall (Bohm condition), which cools them, reduces their density, and enhances the local Debye length because of the smaller inclination angle  $\alpha$  between magnetic field and wall  $\lambda_{D,local} = \lambda_D / \sqrt{\sin \alpha}$  [5].

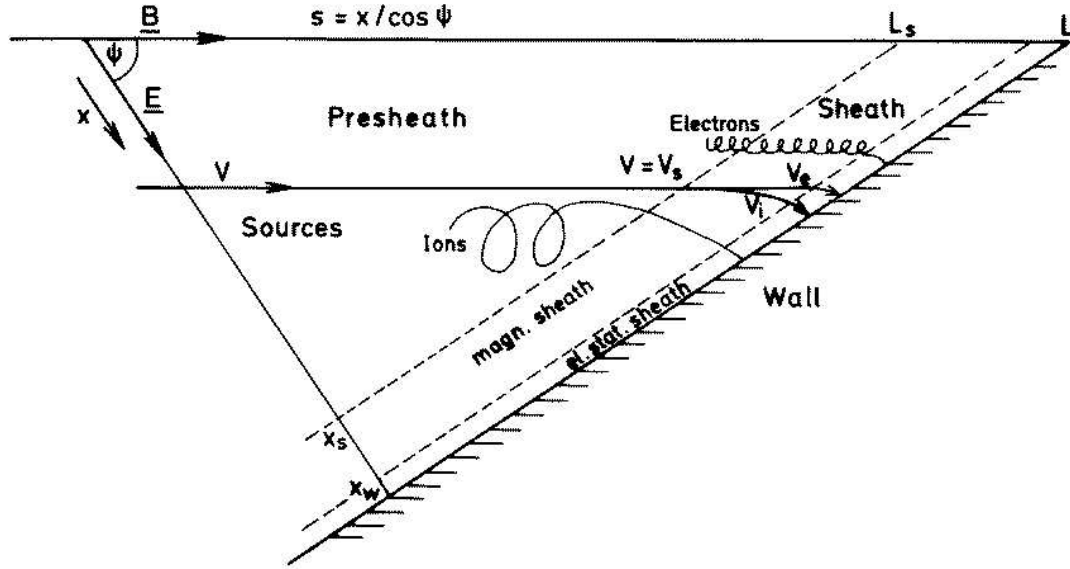


Figure 4.16.: Schematics of the sheath with inclined magnetic field (Figure from R. Chodura)

The magnetic field introduces two more characteristic length scales. The first is the thickness of the magnetic sheath. The magnetic sheath determined by a magnetic field  $B$  has a characteristic thickness  $\lambda_m$  (computed at sound speed  $C_s = \sqrt{2kT/m_i}$ ) of the order of the ion gyroradius at sound speed perpendicular to the wall. Here, the ions are deflected from the direction along the field-line towards the wall. For oblique angles one gets

$$\lambda_m \cong 4C_s / \omega_{ci}, \quad (4.43)$$

where  $\omega_{ci}$  is the ion gyrofrequency for the ions,  $\omega_{ci} = ZeB/m_i$ . The relevant length along  $B$  is then  $\lambda_m / \sin \psi$ , where  $\psi$  is the angle between  $\vec{B}$  and the wall.

The second length scale is the electrostatic Debye sheath thickness (see Fig. 4.17). The electrons experience a deflection from the direction along the field-line towards the wall only in this region, which extends over about 10 Debye lengths  $\lambda_D$  perpendicular to the wall

$$\lambda_{es} \cong 10\lambda_D = 10 \cdot 2.35 \cdot 10^5 (T_e/1000.0/n_e)^{1/2}. \quad (4.44)$$

## 4.4. Summary of SOL length scales

This chapter discussing the scrape-off layer length scales is summarized in the following 2 figures, where, for two densities ( $1.0 \cdot 10^{20} m^{-3}$  and  $3.0 \cdot 10^{19} m^{-3}$ ), a magnetic field of 2T and an angle of incidence of the field-line of  $3^\circ$ , the different characteristic lengths are plotted (projected onto the field line with the sine of the angle of incidence). Additionally, typical values for the parallel field-line length  $L_{||}$  are shown (Fig. 4.17).

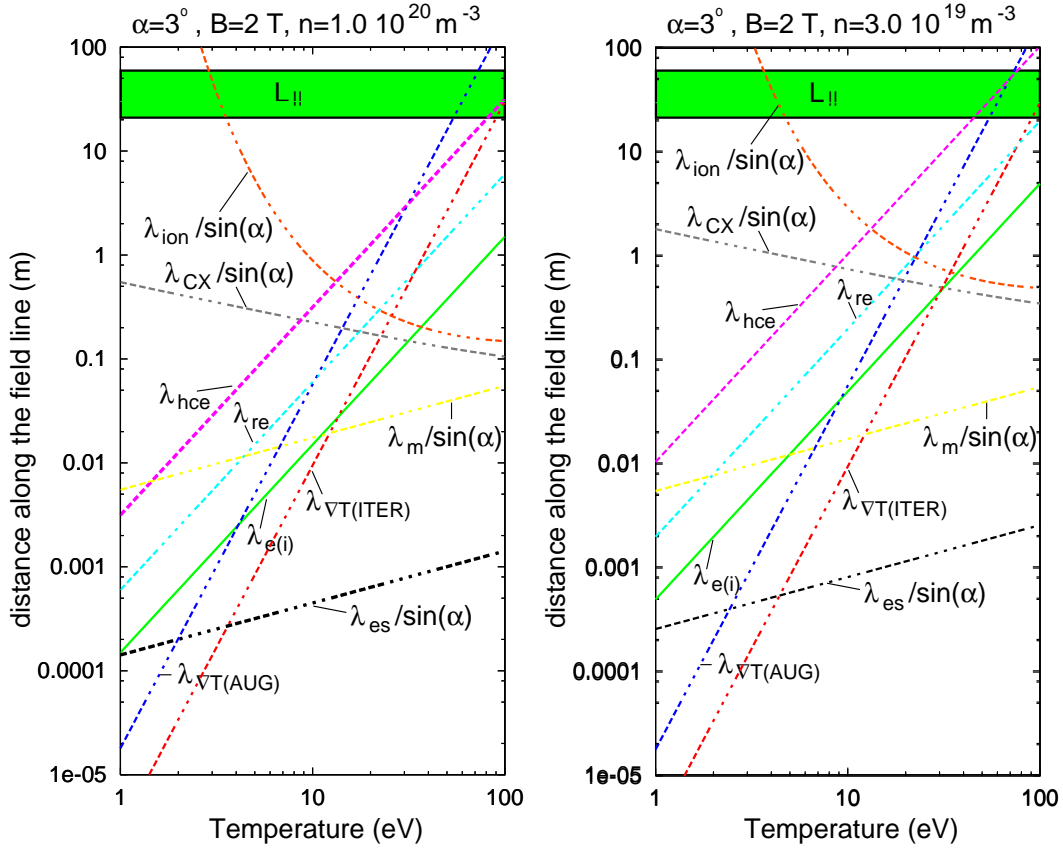


Figure 4.17.: Scrape-off layer length scales for an angle of incidence of the field-line of  $3^\circ$ , a magnetic field of 2 T and a density of  $1.0 \cdot 10^{20} m^{-3}$  (left) and  $3.0 \cdot 10^{19} m^{-3}$  (right) as a function of temperature

To complete the discussion of characteristic SOL length scales, the length scales of the anomalous radial (turbulent) transport are shortly discussed. The basic picture is that, due to turbulent eddies, particle and energy transport are largely enhanced over their classical values. The correlation length parallel fieldlines is typically the connection length, whereas in the radial direction the eddies along measure only 0.5 to 1 cm.

## 4.5. Problems for a fluid description of the SOL

Problems for the (standard) fluid description of the edge become obvious looking at the final summary of the SOL length scales (Fig. 4.17). To apply a fluid model for the description of the SOL, a specific ordering of lengths is necessary. The necessary condition that all characteristic lengths should be smaller than the parallel connection length is usually fulfilled:  $\lambda_e, \lambda_{es}, \lambda_m, \lambda_0 \ll L_{||}$ .

However, three problems appear:

1)  $\lambda_{hce} > \lambda_{\nabla T}$  at low temperatures, e.g. near the target in the divertor. Steeper gradients result in non-local heat flux (no longer local temperature gradient, but weighted mean of temperature profile over  $\pm 5\lambda_e$ ).

2)  $\lambda_{hce} > L_{||}$  at high temperatures (midplane, near separatrix). Corrections for flux limit and for periodic systems on closed field lines are necessary.

3) the sheath cannot be resolved by a fluid model and is represented by kinetic boundary conditions at the sheath entrance (for simplicity given here for hydrogenic plasma) and for zero total current at the wall:  $j_e = j_i$ :

At the Debye sheath most of the electrons are reflected. The Bohm-criterion is necessary to obtain a monotonic potential drop across the sheath:

$$M \geq 1, v_{wall} \geq c_s = \sqrt{\gamma/m_i \cdot k(T_e + T_i)}, \quad (4.45)$$

with ratio of specific heats  $\gamma$  ( $=5/3$  adiabatic,  $=1$  isothermal).

Potential drop:

$$\Phi_O - \Phi = -kT_e/e \cdot \ln(2\pi m_e/m_i(1 + T_i/T_e)/(1 - \gamma)^2) \approx 3kT_e/e. \quad (4.46)$$

Particle fluxes:

$$\Gamma = n \cdot V_{poloidal} = n \cdot \frac{B_{poloidal}}{B} \cdot M \cdot c_s \text{ with } M \geq 1. \quad (4.47)$$

At this point, the boundary conditions for electron and ion heat flux at the sheath have to be defined. For this, firstly the particle fluxes and sources in the sheath have to be analysed: since the sheath dimension is small compared to the mean free path for ionization, the source terms from neutrals are zero. Within the sheath, the ion flux is preferentially turned from the direction parallel B towards the wall normal (in x-direction) and twisted to some extent. So a current parallel to the wall arises in the sheath.

$$Z\Gamma_{i,x} = \Gamma_{e,x} = \Gamma_x = const = \Gamma, S_{q,i} = S_{q,e} = 0. \quad (4.48)$$

Also, the energy flux of the ions is bent more strongly towards the wall normal than that of the electrons. Ions gain energy flux in the x-direction due to their acceleration in the sheath

$$\nabla Q_{i,x} = \frac{dQ_{i,x}}{dx} = Ze\Gamma_{i,x}E \quad (4.49)$$

or the electrons

$$\nabla Q_{e,x} = \frac{dQ_{e,x}}{dx} = -e\Gamma_{e,x}E \quad (4.50)$$

This gives for the energy fluxes of ions and electrons

$$Q_{i,x} = Ze\Gamma_{i,x}(\Phi_{sheath} - \Phi) + Q_{i,x}(x_{sheath}) \quad (4.51)$$

$$Q_{e,x} = -e\Gamma_{e,x}(\Phi_{sheath} - \Phi) + Q_{e,x}(x_{sheath}) \quad (4.52)$$

and therefore (see particle flux discussion before)

$$Q_{i,x} + Q_{e,x} = Q_{i,x}(x_{sheath}) + Q_{e,x}(x_{sheath}) = const. \quad (4.53)$$

The energy flux of ions at the sheath edge depends on their acceleration and thermalization in the presheath. The Bohm condition defines a lower bound for their kinetic energy at  $x_{sheath}$ . The convective energy flux  $\gamma_i/(\gamma_i - 1)T_{i,sheath}\Gamma_{i,x}$  can be estimated using a shifted Maxwellian. Additionally, the heat conduction flux  $q_{i,x}$  contributes

$$Q_{i,x}(x_{sheath}) = \delta_i T_{i,sheath} \Gamma_{i,x} = \left( \frac{m_i v_{sheath}^2}{2} + \frac{\gamma_i T_{i,sheath}}{\gamma_i - 1} \right) \Gamma_{i,x} + q_{i,x}(x_{sheath}). \quad (4.54)$$

The electron energy flux at the sheath edge

$$Q_{e,x}(x_{sheath}) = \delta_e T_{e,sheath} \Gamma_{e,x} \quad (4.55)$$

is mainly determined by the electron reflection properties of the sheath and the wall, i.e. by the sheath potential and electron reflection coefficient  $\gamma_e$ . One gets [9]

$$\delta_e = 2/(1 - \gamma_e) + (\Phi_{sheath} - \Phi_{wall}) \cdot e/(kT_{e,s}) \approx 5 \quad (4.56)$$

For collisional ions in an isothermal model, so with no  $T_i$  gradient and assuming that ions are not influenced before the sheath, one calculates [5]

$$\delta_i = 3.5. \quad (4.57)$$

The acceleration of ions in the sheath before hitting the wall by the potential drop has to be accounted for in the creation of neutrals. The ion energy may also be partly reflected as energy of recycled neutral atoms, while electrons in general deposit all their energy at the wall.

After this analysis, the sheath can be represented by proper boundary conditions in fluid models which will be used extensively in the following.

## 5. Fluid equations

Calculating from the kinetic equations the different moments of the distribution functions of electrons and ions, one gets the common fluid equations for the plasma as already derived by Braginskii [18]. These will be shortly summarized in this chapter. Also, the discussion will start with clean plasmas, adding later the effect of impurities. A more detailed discussion can be found in [19].

### 5.1. Braginskii equations

The continuity equations for ions:

$$\frac{\partial}{\partial t} + \vec{\nabla} \cdot (n_i \vec{V}_i) = S_{n_i} \quad (5.1)$$

and electrons:

$$\frac{\partial}{\partial t} + \vec{\nabla} \cdot (n_e \vec{V}_e) = S_{n_e} \quad (5.2)$$

are balancing the total derivative (time-derivative and divergence) of the particle fluxes by the particle source terms on the right hand side of the equations.

The momentum equations for ions:

$$\frac{\partial}{\partial t}(m_i n_i \vec{V}_i) + \vec{\nabla} \cdot (m_i n_i \vec{V}_i \vec{V}_i) = -\vec{\nabla} p_i - \vec{\nabla} \Pi_i^{\leftrightarrow} + Z_i e n_i (\vec{E} + \vec{V}_i \times \vec{B}) + \vec{R}_i + \vec{S}_{m_i \vec{V}_i} \quad (5.3)$$

and electrons (neglecting inertia, often called the generalized Ohm's law):

$$-\vec{\nabla} p_e - e n_e (\vec{E} + \vec{V}_e \times \vec{B}) + \vec{R}_e = 0 \quad (5.4)$$

with

$$\vec{R}_e = -\vec{R}_i = e n_e \left( \frac{\vec{j}_{\parallel}}{\sigma_{\parallel}} + \frac{\vec{j}_{\perp}}{\sigma_{\perp}} \right) - 0.71 n_e \vec{\nabla}_{\parallel} T_e - \frac{3}{2} \frac{e n_e^2}{\sigma_{\perp} B^2} \vec{B} \times \vec{\nabla} T_e \quad (5.5)$$

( $Z_i = 1$ , single ion species) include losses due to ohmic heating (very small due to the high conductivities), losses due to deflection of electrons at temperature gradients perpendicular to  $B$  (factor  $\omega\tau \geq 1000$  smaller than the ohmic losses) and losses due to friction of electrons with different temperature parallel to  $B$  and thus different thermal velocities,

which is the most important term.

The total electric current density is defined as:

$$\vec{j} = e(Z_i n_i \vec{V}_i - n_e \vec{V}_e). \quad (5.6)$$

Summing over all species one gets the total momentum equation:

$$\frac{\partial}{\partial t}(m_i n_i \vec{V}_i) + \vec{\nabla} \cdot (m_i n_i \vec{V}_i \vec{V}_i) = -\vec{\nabla} p - \vec{\nabla} \Pi_i + \vec{j} \times \vec{B} + \vec{S}_{m_i \vec{V}_i} \quad (5.7)$$

This can be used to discuss momentum conservation along field lines. This momentum conservation equation, for stationary cases, can be formally written in the form

$$d/ds(\rho v^2 + p) = S_{CX} + \text{viscosity} + \text{convect. mom. transp. across flux surface}, \quad (5.8)$$

with  $\rho = m_i n_i$ .

Neglecting the right-hand side, this would lead to  $p(1 + \gamma M^2) = \text{const}$ , with the definition of the Mach number  $M = \sqrt{\rho v^2 / (\gamma p)}$  and momentum sink (or source) terms due to charge exchange  $S_{CX}$ . The other terms on the right hand side will just spread momentum across the scrape-off layer and hence drop out, if appropriate averages are taken. Charge exchange, on the other hand, can transport momentum from the plasma directly to the walls, provided the mean free path for the neutrals is sufficiently large. The criterion for this is  $n_i \delta_E \leq \sigma_{i-n}^{-1}$ , getting important especially at low temperatures. Here, ionization becomes unimportant, and, as the characteristic decay length of neutrals in the plasma is given by  $\sqrt{\lambda_{CX} \cdot \lambda_{ion}}$ , neutrals can freely interpenetrate the plasma flow. Net momentum loss from the plasma through charge exchange, however, will remain confined to a boundary layer with thickness  $(n_i \sigma_{i-n})^{-1}$ , with the effect of CX in the deeper layers being only an enhancement of perpendicular viscosity (and ion-energy cross-diffusion). Momentum removal from the plasma will therefore always proceed in a relatively thin layer in front of the target plates and at the boundaries of the divertor plasma fan.

The total energy equations for ions:

$$\begin{aligned} \frac{\partial}{\partial t} \left( \frac{3}{2} n_i T_i + \frac{m_i n_i}{2} \vec{V}_i^2 \right) + \vec{\nabla} \cdot \left[ \left( \frac{5}{2} n_i T_i + \frac{m_i n_i}{2} \vec{V}_i^2 \right) \vec{V}_i + \vec{\Pi}_i \cdot \vec{V}_i + \vec{q}_i \right] = \\ (Z_i e n_i \vec{E} - \vec{R}) \cdot \vec{V}_i - Q_{ei} + S_{E_i} \end{aligned} \quad (5.9)$$

and electrons (simplified):

$$\frac{\partial}{\partial t} \left( \frac{3}{2} n_e T_e \right) + \vec{\nabla} \cdot \left[ \left( \frac{5}{2} n_e T_e \vec{V}_i + \vec{q}_e \right) \right] = -e n_e \vec{E} \cdot \vec{V}_e + \vec{R} \cdot \vec{V}_i + Q_{ei} + S_{E_e} \quad (5.10)$$

defines the full set of equations for the plasma description. The set of equations is closed by the energy fluxes for ions

$$\vec{q}_i = -\kappa_{\parallel}^i \nabla_{\parallel} T_i - \kappa_{\perp}^i \nabla_{\perp} T_i + \kappa_{\wedge}^i \frac{\vec{B}}{B} \times \vec{\nabla}_{\perp} T_i \quad (5.11)$$

and electrons (if  $Z_i = 1$ )

$$\begin{aligned} \vec{q}_e = -\kappa_{\parallel}^e \nabla_{\parallel} T_e - \kappa_{\perp}^e \nabla_{\perp} T_e + \kappa_{\wedge}^e \frac{\vec{B}}{B} \times \vec{\nabla}_{\perp} T_e \\ - 0.71 \frac{T_e}{e} \vec{j}_{\parallel} - \frac{3}{2} \frac{T_e}{e \omega_e \tau_e B} \vec{B} \times \vec{j}_{\perp}, \end{aligned} \quad (5.12)$$

the energy exchange term between electrons and ions

$$Q_{ei} = \frac{3m_e n_e}{m_i \tau_e} (T_i - T_e). \quad (5.13)$$

and the transport coefficients.

## 5.2. B2 equations

Based on the Braginskii equations, SOL fluid equations can be derived, e.g. those used in the standard B2 code. The B2 code is a 2D multifluid transport code for SOL modelling.

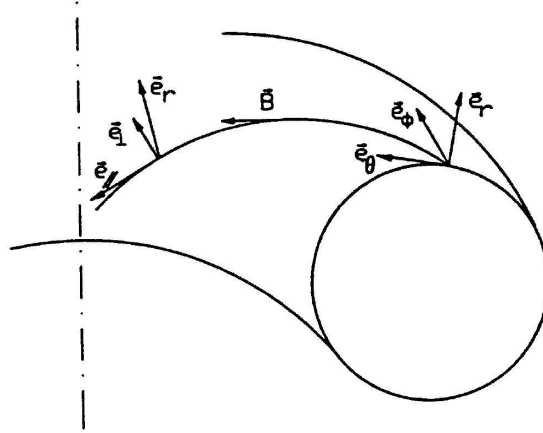


Figure 5.1.: Sketch of the two basic coordinate systems for Tokamak SOL transport studies.

Usually, a poloidal and a radial coordinate is used in SOL transport codes. For a tokamak the toroidal coordinate can be ignored due to axis-symmetry.

Additional assumptions are used in the formulation of the original B2 equations:

- 1) Plasma is quasineutral and ambipolar flow is assumed  
 $\Rightarrow \vec{j} = 0$ , no separate electron momentum equation
- 2) Ion velocity in diamagnetic direction is neglected  
 $\Rightarrow$  one component of the ion momentum equation is eliminated
- 3) Anomalous radial transport assumed, which is much stronger than the classical terms  
 $\Rightarrow$  radial diffusion equations, no classical terms for radial fluxes
- 4) One ion temperature assumed for all ionic species  
 $\Rightarrow$  only one ion temperature equation
- 5) Viscosity tensor simplified  
 $\Rightarrow$  cross-field derivative terms neglected

This defines the SOL set of equations in the standard B2 form [20].

Continuity of species  $a$  ( $1 \leq a \leq N$ ):

$$\frac{\partial n_a}{\partial t} + \frac{1}{\sqrt{g}} \frac{\partial}{\partial x} \left( \frac{\sqrt{g}}{h_x} n_a (u_a + v_{p,a}) \right) + \frac{1}{\sqrt{g}} \frac{\partial}{\partial y} \left( \frac{\sqrt{g}}{h_y} n_a v_a \right) = S_n^a. \quad (5.14)$$



Momentum balance of species  $a$  ( $1 \leq a \leq N$ ):

$$\begin{aligned}
 & \frac{\partial}{\partial t}(m_a n_a u_{\parallel a}) + \frac{1}{\sqrt{g}} \frac{\partial}{\partial x} \left( \frac{\sqrt{g}}{h_x} m_a n_a (u_a + v_{p,a}) u_{\parallel a} - \frac{\sqrt{g}}{h_x^2} \eta_x^a \frac{\partial u_{\parallel a}}{\partial x} \right) \\
 & + \frac{1}{\sqrt{g}} \frac{\partial}{\partial y} \left( \frac{\sqrt{g}}{h_y} m_a n_a v_a u_{\parallel a} - \frac{\sqrt{g}}{h_y^2} \eta_y^a \frac{\partial u_{\parallel a}}{\partial y} \right) \\
 & = \frac{B_\theta}{B} \frac{1}{h_x} \left[ -\frac{\partial p_a}{\partial x} - \frac{Z_a n_a}{n_e} \frac{\partial p_e}{\partial x} + c_e \left( \frac{Z_a}{Z_{eff}} - 1 \right) Z_a n_a \frac{\partial T_e}{\partial x} \right. \\
 & \quad \left. + c_i \left( \frac{Z_a}{Z_{eff}} - 1 \right) Z_a n_a \frac{\partial T_i}{\partial x} \right] + \sum_{b=1}^N F_{ab} + S_{mu_{\parallel}}^a. \tag{5.15}
 \end{aligned}$$

Diffusion of species  $a$  ( $1 \leq a \leq N$ ):

$$v_a = -\frac{1}{h_y} \frac{D_n^a}{n_a} \frac{\partial n_a}{\partial y} - \frac{1}{h_y} \frac{D_p^a}{n_a} \frac{\partial p_a}{\partial y}, \tag{5.16}$$

$$v_{p,a} = -\frac{1}{h_x} \frac{D_n^a}{n_a} \frac{\partial n_a}{\partial x} - \frac{1}{h_x} \frac{D_p^a}{n_a} \frac{\partial p_a}{\partial x}. \tag{5.17}$$

Electron energy balance:

$$\begin{aligned}
 & \frac{\partial}{\partial t} \left( \frac{3}{2} n_e T_e \right) + \frac{1}{\sqrt{g}} \frac{\partial}{\partial x} \left( \frac{\sqrt{g}}{h_x} \frac{5}{2} n_e u_e T_e - \frac{\sqrt{g}}{h_x^2} \kappa_x^e \frac{\partial T_e}{\partial x} \right) \\
 & + \frac{1}{\sqrt{g}} \frac{\partial}{\partial y} \left( \frac{\sqrt{g}}{h_y} \frac{5}{2} n_e v_e T_e - \frac{\sqrt{g}}{h_y^2} \kappa_y^e \frac{\partial T_e}{\partial y} \right) \\
 & = \frac{u_e}{h_x} \frac{\partial p_e}{\partial x} + \frac{v_e}{h_y} \frac{\partial p_e}{\partial y} - k (T_e - T_i) + S_E^e. \tag{5.18}
 \end{aligned}$$

Ion energy balance:

$$\begin{aligned}
 & \frac{\partial}{\partial t} \left( \frac{3}{2} n_i T_i + \sum_a \frac{1}{2} \rho_a u_{\parallel a}^2 \right) \\
 & + \frac{1}{\sqrt{g}} \frac{\partial}{\partial x} \left[ \frac{\sqrt{g}}{h_x} \left( \sum_a \frac{5}{2} n_a (u_a + v_{p,a}) T_i + \sum_a \frac{1}{2} m_a n_a (u_a + v_{p,a}) u_{\parallel a}^2 \right) \right. \\
 & \quad \left. - \frac{\sqrt{g}}{h_x^2} \left( \kappa_x^i \frac{\partial T_i}{\partial x} + \sum_a \frac{1}{2} \eta_x^a \frac{\partial u_{\parallel a}^2}{\partial x} \right) \right] \\
 & + \frac{1}{\sqrt{g}} \frac{\partial}{\partial y} \left[ \frac{\sqrt{g}}{h_y} \left( \sum_a \frac{5}{2} n_a v_a T_i + \sum_a \frac{1}{2} m_a n_a v_a u_{\parallel a}^2 \right) \right. \\
 & \quad \left. - \frac{\sqrt{g}}{h_y^2} \left( \kappa_y^i \frac{\partial T_i}{\partial y} + \sum_a \frac{1}{2} \eta_y^a \frac{\partial u_{\parallel a}^2}{\partial y} \right) \right] \\
 & = -\frac{u_e}{h_x} \frac{\partial p_e}{\partial x} - \frac{v_e}{h_y} \frac{\partial p_e}{\partial y} + k (T_e - T_i) + S_E^i. \tag{5.19}
 \end{aligned}$$

$$\begin{aligned}
n_i &= \sum_a n_a \\
n_e &= \sum_a Z_a n_a \\
\rho_a &= m_a n_a \\
p_a &= n_a T_i \\
p_e &= n_e T_e \\
u_a &= (B_\theta/B) u_{\parallel a} \\
u_e &= (\sum_a Z_a n_a (u_a + v_{p,a}))/n_e \\
v_e &= (\sum_a Z_a n_a v_a)/n_e \\
Z_{eff} &= (\sum_a Z_a^2 n_a)/(\sum_a Z_a n_a)
\end{aligned}$$

Due to the geometrical transformation metric coefficients enter. The parallel transport is treated classically, whereas the radial transport is assumed anomalous and described by empirical diffusion coefficients (and possibly pinch velocities).

Especially for the study of the effect of drifts and currents, extended equations are needed and some of the simplifying assumptions mentioned above are dropped.

### 5.2.1. Radial ion-electron heat exchange term

A problem arising from the *ad-hoc* description of anomalous transport is the uncertainty of the choice of the radial ion-electron heat exchange term.

To reproduce measured  $T_i$  profiles it is necessary to use different radial electron-ion heat exchange coupling terms than in the original B2.

Classical energy equations include a contribution to heat transfer from ions to electrons  $\vec{j} \cdot (\vec{V}_i \times \vec{B}) = \vec{V}_i \cdot (-\vec{j} \times \vec{B})$ . The dominant term of the normal contribution (no radial current considered) is  $(\vec{j} \times \vec{B})_r = (\vec{\nabla} p)_r$ . Therefore, the ion-electron heat transfer term in B2 changes from  $V_r \cdot \frac{\partial p_e}{\partial u^r}$  to  $-V_r \cdot \frac{\partial p_i}{\partial u^r}$  for this classical ansatz. However, anomalous transport could still change this description. For ASDEX, the classical ansatz seem to reproduce quite well the experimental data.

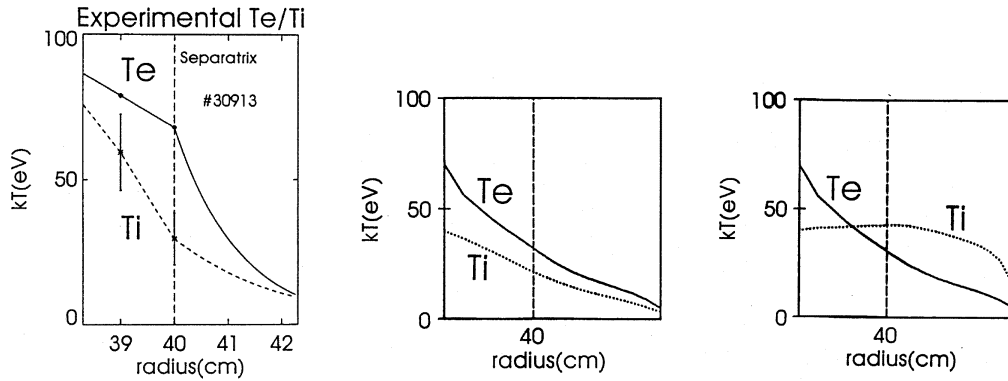


Figure 5.2.: Radial ion temperature midplane profiles from experiment (left) and modelling using for the ion-electron heat transfer term either  $-V_r \cdot \frac{\partial p_i}{\partial u^r}$  (middle) or  $V_r \cdot \frac{\partial p_e}{\partial u^r}$  (right).

### 5.2.2. Kinetic corrections

As a consequence of the limits of the fluid description in some cases (high temperatures in the midplane, ...), kinetic corrections are applied in B2. Simple heat flux and momentum flux (viscosity) limits are available. The heat flux limit is formulated as

$$\kappa_{||} = \frac{\kappa_{SH}}{1 + |q_{SH}/q_{fl}|}, \quad (5.20)$$

with the classical Spitzer-Härm heat flux

$$q_{SH} = -\kappa_{||,SH} \cdot \frac{\partial T_e}{\partial x} \quad (5.21)$$

and the flux limit

$$q_{fl} = \alpha n_e T_e^{3/2} \sqrt{m_e} \quad (5.22)$$

( $\alpha = 0.2$  from comparison with kinetic calculations). The momentum flux limit is done the same way

$$\eta_{||} = \frac{\eta_{cl,ion\ i}}{1 + |q_{cl,ion\ i}/q_{fl,ion\ i}|}, \quad (5.23)$$

with the classical momentum flux

$$q_{cl,ion\ i} = -\eta_{||,ion\ i} \cdot \frac{\partial u_{||,ion\ i}}{\partial x} \quad (5.24)$$

and the flux limit

$$q_{fl,ion\ i} = \alpha p_{ion\ i} \quad (5.25)$$

(with  $\alpha = 0.5$ ).

Additionally, long mean free path corrections of classical heat conduction and viscosity (in the core) are applied. For periodic systems and small perturbations one gets [21]:

$$q_{||,eff} = q_{SH} / (h_{||}^2 \lambda_{HC}^2 + 1) \quad (5.26)$$

with wavenumber of periodicity

$$h_{||} = 2\pi / \lambda_{||} \quad (5.27)$$

$$\lambda_{||} = 2\pi R q \quad (5.28)$$

and mean free path of tail electrons [5]

$$\lambda_{HC}(m) = 7.5 \cdot 10^{16} \cdot T_e^2(eV) / n_e(m^{-3}) \quad (5.29)$$

Fokker-Planck computer simulations of electron heat transport in laser plasmas [22] show that a better description is obtained for a linear correction:

$$q_{||,eff} = q_{SH} / (h_{||} \lambda_{HC} + 1). \quad (5.30)$$

Applying these limits for the core, convergence behaviour of the code improves significantly.

A more correct kinetic limit would imply a non-local heat transport (and viscosity,...) description. The parallel heat-flux at a point should be determined by classical fluxes at points up to one mean-free path away. As an additional feature, one would get pre-heating effects by fast electrons, maybe important for the ELMs. Work is necessary to generalize this to the SOL [23, 24] and this has to be cross-checked with kinetic calculations [25]. Also, numerical problems due to this non-local description have to be solved [26].

## 6. Neutral transport, surface reflection, recycling

The second important transport process in the SOL besides plasma transport is neutral transport. The effect of neutrals will be estimated regarding their potential for relaxing the power exhaust problem at the target plate, spreading the divertor target load over a larger area. Afterwards, neutral transport will be discussed. This needs to be included in any SOL model, because neutral sources are important for the plasma, whereas neutral transport (and by this the neutral source distribution) is determined by the plasma background. Therefore, plasma and neutral transport together define self-consistently the SOL properties.

### 6.1. Neutral losses

To lower the maximum power load and to broaden the energy deposition profile on the target plates, one has to use loss channels which are not constricting the energy flow to follow magnetic field lines. The ideal scenario would be one where these energy losses would be created without additional impurities. For hydrogen two energy loss channels - CX losses and atomic radiation - are in principle available.

#### 6.1.1. Charge exchange losses

Charge exchange (CX) losses are already used experimentally with great success to convert high energy fluxes of charged particles into neutral through neutralizer sections in neutral injector beam lines. It requires, however, that the plasma be sufficiently thin, so that neutrals can interpenetrate it, i.e. that  $n_i \delta_E \leq \sigma_{i-n}^{-1}$  with  $\delta_E$  being the width of the CX energy loss region (maximum size is the energy decay length) [27]. The energy that can be carried into such a scrape-off region by ions is limited by  $\gamma_i n_i v_i k T_i (B_p/B_t) (4\pi R_X \delta_E)$ , where the coefficient  $\gamma_i$  (of order one) depends on the splitting of the energy between conduction (where the above expression corresponds to a heat flux limit) and convection. This power amounts to a fraction  $f_{CX}$  of the total power  $P_{heat,s}$  crossing the separatrix as particle energy, which can be written as

$$f_{CX} = 4\pi \gamma_i (n_i \delta_E) v_i k T_i \frac{B_p}{B_t} \frac{R_X}{P_{heat,s}} \leq 4\pi \gamma_i \sigma_{i-n}^{-1} v_i k T_i \frac{B_p}{B_t} \frac{R_X}{P_{heat,s}}. \quad (6.1)$$

For nominal ITER parameters ( $P_{heat,s} = 300$  MW,  $\frac{B_p}{B_t} = 0.1$  (in the divertor channel),  $R_X = 7$  m) and  $\gamma_i = 1$ ,  $\sigma_{i-n}^{-1} = 5 \cdot 10^{19} m^{-2}$ , this gives  $f_{CX} = 1$  at 660 eV, but only 0.06 at

100 eV and 0.002 at 10 eV. That means, that CX energy losses are only effective at high temperatures. Moreover, CX neutrals from the hot regions pose erosion problems in the main chamber and the transition region from the divertor to the main chamber (baffles, etc.).

### 6.1.2. Neutral hydrogen radiation

For neutral hydrogen radiation above about 8 eV, the ratio of an enhanced 'effective' ionization loss  $\epsilon_{ion,eff}$  to the ionization energy  $\epsilon_{ion}$ , which is again deposited along field lines at the target plate (without volume recombination) is around 2-3 (Fig. 6.1).

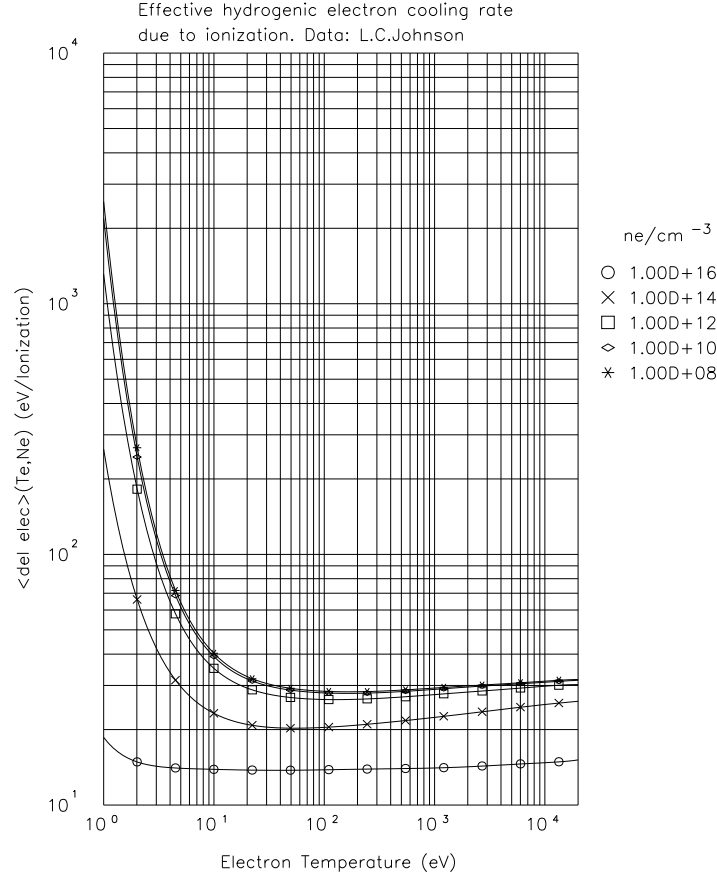


Figure 6.1.: Effective hydrogenic electron cooling rate due to ionization (in eV/ ionization) versus temperature (in eV) for various densities (in  $cm^{-3}$ ) (D. Reiter)

Only the fraction  $(\epsilon_{ion,eff} - \epsilon_{ion})/\epsilon_{ion,eff}$  constitutes a true volumetric loss. Below about 8 eV  $(\epsilon_{ion,eff} - \epsilon_{ion})$  increases significantly [27]. The characteristics of the parallel electron heat conduction ( $q_{\parallel} \sim T^{5/2} \nabla T \sim T^{7/2}$ ) imply, however, that the volume over which the temperature can be below a certain value at a certain heat flux density is proportional to  $T^{7/2}$  along field lines, and hence dramatically decreases with temperature. Therefore, the low temperature region is very small and cannot contribute to the integral radiation loss.

Summarizing this discussion of energy losses from hydrogen, it is obvious that for ITER additional radiation losses from impurities are necessary.

## 6.2. Neutral transport

In the following, after the discussion of the neutral losses, the question of neutral transport will be addressed. As already discussed, the penetration of neutrals into a plasma is characterized by two different regimes.

For  $T > 10\text{eV}$  (upstream, midplane), one has a kinetic regime, where after some (0-2) CX collisions the neutrals get ionized ( $\lambda_0 \approx \lambda_{CX} \approx \lambda_{ion}$ ).

For  $T \ll 10\text{eV}$  (divertor), one has a diffusive process with a very large number of CX events resulting in a random walk before ionization occur ( $\lambda_{ion} \gg \lambda_{CX}$ ,  $\lambda_0 \approx \sqrt{\lambda_{CX} \lambda_{ion}}$ ).

### 6.2.1. Simple neutral diffusion model

Neutrals do not experience fieldlines (they are not charged). Therefore, a simple neutral diffusion model where CX gives rise to diffusion and ionisation to the loss of neutrals can be set up, with a coordinate  $x$  perpendicular to the plate.

$$\frac{d}{dx} \lambda_{CX} v_{th,0} \frac{dn_0}{dx} = n_e \langle \sigma_{ion} v_{th,e} \rangle n_0 \quad (6.2)$$

This gives the well known result for the spatial distribution of neutrals

$$n_0(x) = n_{0,d} e^{-\xi / \sqrt{\lambda_{ion} \lambda_{CX}}} \quad (6.3)$$

in terms of CX and ionisation mean-free paths

$$\lambda_{ion} = v_{th,0} / (n_e \langle \sigma_{ion} v_{th,e} \rangle). \quad (6.4)$$

$$\lambda_{CX} = v_{th,0} / (n_i \langle \sigma_{CX} v_i \rangle). \quad (6.5)$$

at a reference electron density in the divertor  $n_{ed}$  in terms of the coordinate

$$\xi = \int_0^x n_e / n_{ed} dx. \quad (6.6)$$

The total ionisation rate (per unit area and for an optically thick SOL) becomes

$$\int_0^\infty n_e \langle \sigma_{ion} v_{th,e} \rangle n_0 dx = n_{0,d} v_{th,0} \sqrt{\frac{\lambda_{CX}}{\lambda_{ion}}} \quad (6.7)$$

### 6.2.2. Neutral transport in Monte-Carlo codes

For a proper description of neutral transport Monte-Carlo neutral transport codes are normally used (like EIRENE [28, 29, 30]) solving the full 3D Boltzmann transport equations for the neutral distribution function

$$\frac{\partial f(\vec{x}, \vec{v}, t)}{\partial t} + \vec{v} \cdot \nabla f(\vec{x}, \vec{v}, t) = C(f(\vec{x}, \vec{v}, t)) \quad (6.8)$$

. The collision term  $C$  can include also neutral-neutral collisions, creating a nonlinear problem.

In addition to the atomic physics data surface reflection data are necessary, and are also provided by Monte-Carlo codes like TRIM [31], where, using a binary collision model, surface reflection of ions and neutrals can be calculated (Fig. 6.2).

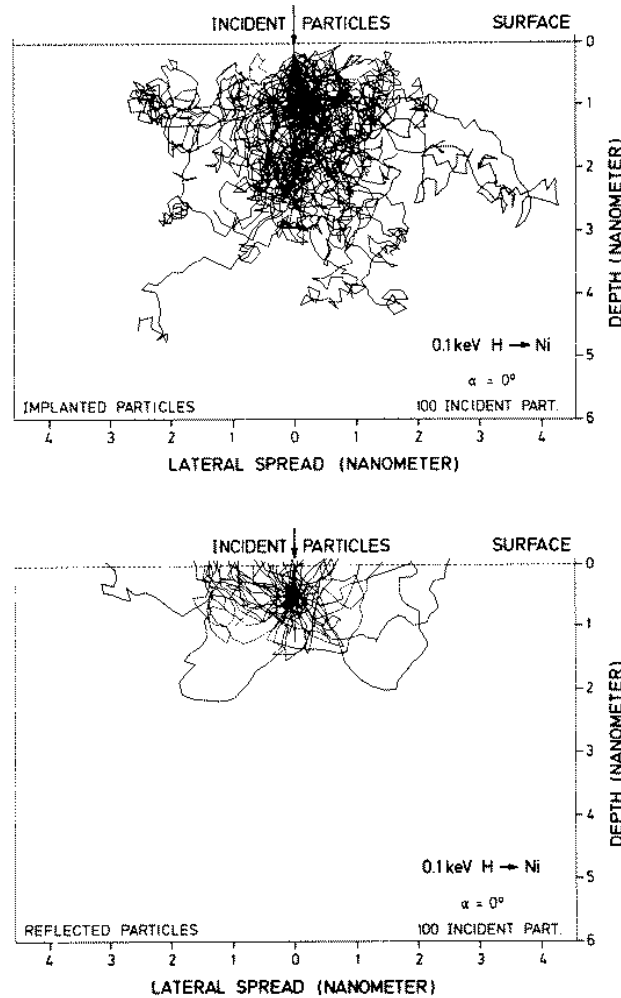


Figure 6.2.: Calculated trajectories from TRIM for implanted (top) and reflected (bottom) particles for normal incidence 100 eV hydrogen on nickel (W.Eckstein).

These results can then be used to get energy and particle reflection coefficients depending on surface/projectile combination, energy, angle of incidence,.... (see Fig. 6.3)

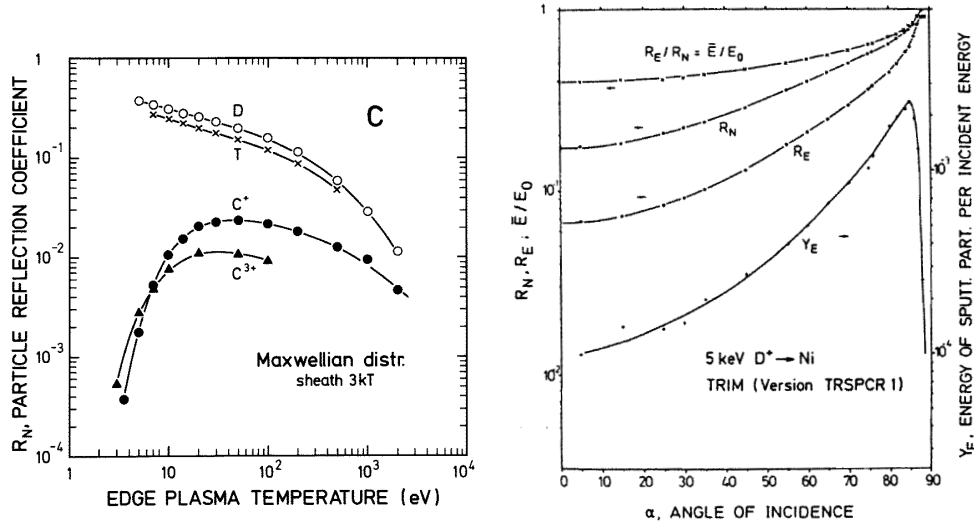


Figure 6.3.: Calculated particle reflection coefficients from TRIM for deuterium, tritium,  $C^+$  and  $C^{3+}$  on carbon as a function of the plasma temperature (in eV), assuming Maxwellian distributions and accounting for the sheath acceleration by a factor of  $3kT$  (left side). Calculated particle ( $R_N$ ) and energy ( $R_E$ ) reflection coefficients and energy of the sputtered particle ( $Y_E$ ) per incident energy from TRIM for 5 keV deuterium onto nickel (W. Eckstein).

### 6.2.3. Neutral hybrid model

With both a fluid neutral model (similar to [32]) as well as a Monte-Carlo neutral model (EIRENE [30]), the possibility of implementing a hybrid neutral model is now available. The idea would be to add a new pair of reactions to the Monte-Carlo code that would “ionize” fluid neutrals to Monte-Carlo neutrals and “recombine” Monte-Carlo neutrals to fluid neutrals. Plasma recombining at a surface would start off as Monte-Carlo neutrals as done in the present B2-Eirene code. However a new loss mechanism would be added so that in addition to being lost from the Monte-Carlo calculation by ionization, neutrals could also be lost by the new reaction converting Monte-Carlo neutrals to fluid neutrals. In the case of ionization, the particles become sources of particles, energy and momentum for the plasma code; in the case of Monte-Carlo/fluid neutral conversion, the particles become sources of particles, energy and momentum for the fluid neutrals. The paired reaction rates for Monte-Carlo/fluid neutral conversion would be chosen so that particles whose mean free path (for charge exchange or neutral-neutral collisions) becomes smaller than the cell size are treated by the fluid code, and neutrals for which the mean free path is larger than the cell size are treated by the Monte-Carlo code. This should achieve the goals of first-flight/last-flight Monte-Carlo treatment of the neutrals (which leverages the advantage of the Monte-Carlo codes in allowing for the appropriate physics to be preserved) while speeding up the treatment of neutrals undergoing thousands of charge exchange reactions before an ionization event — a process that is expensive to model with the Monte-Carlo code but cheap for the fluid code.





## 7. The two-point model

Now, a first model will be introduced to describe the SOL properties: the 2-point model uses very simplified conservation relations between the flow stagnation point on a field line (usually taken in outer midplane) and the target plate (Fig. 7.1) [33, 34]. It is very useful to understand many of the basic physics mechanisms and the different operational regimes in the SOL.

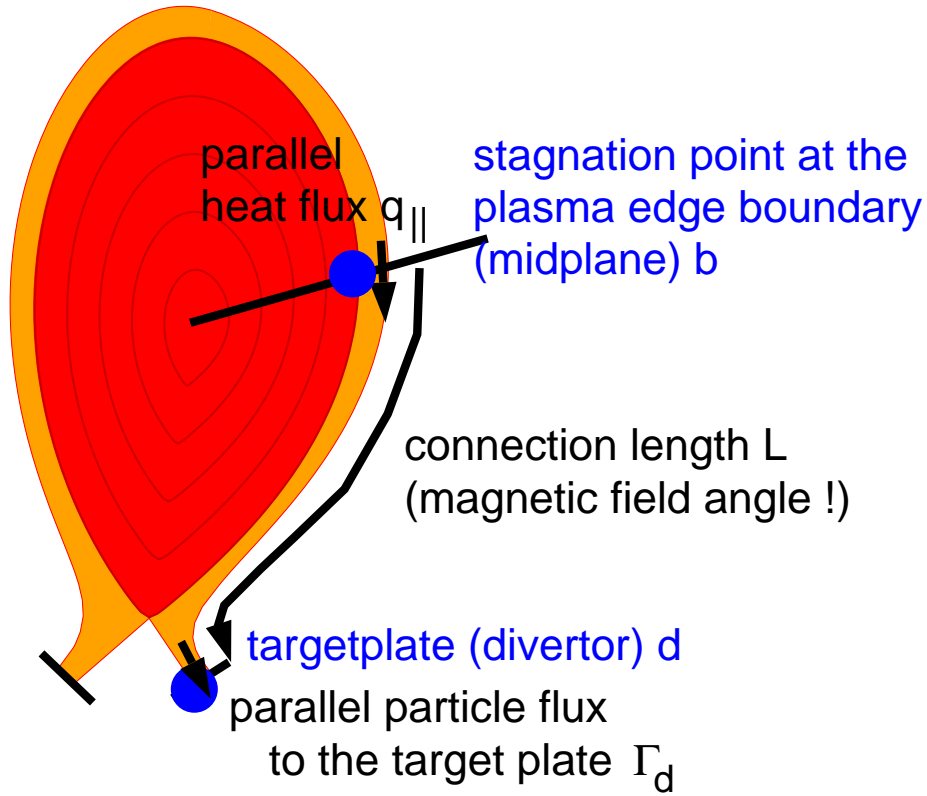


Figure 7.1.: Schematics of the 2-point model

### 7.1. Basic equations

Momentum balance between the flow stagnation point on a field line (usually taken in outer mid-plane) and the target plate gives (Bernoulli equation):

$$n_d T_d (1 + \gamma M_d^2) = (1 - f_{mom}) n_b T_b, \quad (7.1)$$

where index b indicates the midplane quantities at the separatrix and index d the divertor plate quantities at the separatrix,  $\gamma$  the adiabatic coefficient,  $M$  the mach number and  $f_{mom}$  the momentum loss factor.

Energy balance obtained by the solution of the parallel heat conduction equation along fieldlines results in:

$$T_b^{7/2} - T_d^{7/2} = 4.6 \cdot 10^{-14} q_{\parallel} L \quad (7.2)$$

for a parallel heat flux  $q_{\parallel}$  and a field line length from separatrix midplane to the target plate  $L$ .

Additionally, the relation between target particle and energy fluxes completes the set of equations:

$$\underbrace{\delta_e T_D \Gamma_D}_{(targetload)} + \underbrace{\epsilon_{ion} \frac{\Gamma_D}{1 - f_{rec}}}_{(hydrogen)} = \underbrace{(1 - f_{rad}) q_{\parallel}}_{(impurities)}, \quad (7.3)$$

where the sheath transmission factor  $\delta_e$  consists of a kinetic factor  $\tilde{\delta}_e$  plus  $(5/2) + (\gamma M_d^2/2)$  due to convective factor and acceleration due to the Bohm condition.

The first term represent the targetload, the second the hydrogenic recycling losses by ionisation (with effective ionisation loss  $\epsilon_{ion}$  and possible recombination  $f_{rec}$ ). In addition, radiation losses by impurities have to be taken into account by the radiation loss factor  $f_{rad}$ .

## 7.2. Divertor operation regimes

Based on the 2-point model the different divertor operation regimes can be discussed. Experimentally, one can think of operating at a fixed input power and then doing a density ramp-up, passing through all these different regimes. The different regimes are not really separated from each other, but one goes smoothly from one regime to the other (including regimes with mixed character). These different regimes are not only observed in Tokamak divertors but also in the W7-AS (island) divertor.

### 7.2.1. Low recycling (Linear or Sheath-limited regime)

The first operational regime is the low recycling regime (Fig. 7.3). In this regime, the midplane separatrix density is quite low, so that recycling losses (and radiation losses from impurities) can be neglected (small particle flux to the plate).

The high temperatures give practically constant plasma profiles along the fieldline, because the parallel heat conduction is dominating all other processes (see also Fig. 7.2). The total pressure is constant along field-lines (corrected for the acceleration to Mach=1 at the sheath entrance due to the Bohm condition), because momentum loss from CX is uneffective. The flux of potential energy can be neglected due to the high plasma temperature. Due to the fact that the target density rises linearly with upstream density this regime is also called the linear regime. The transmission of heat through the sheath ( $\delta_e$ )

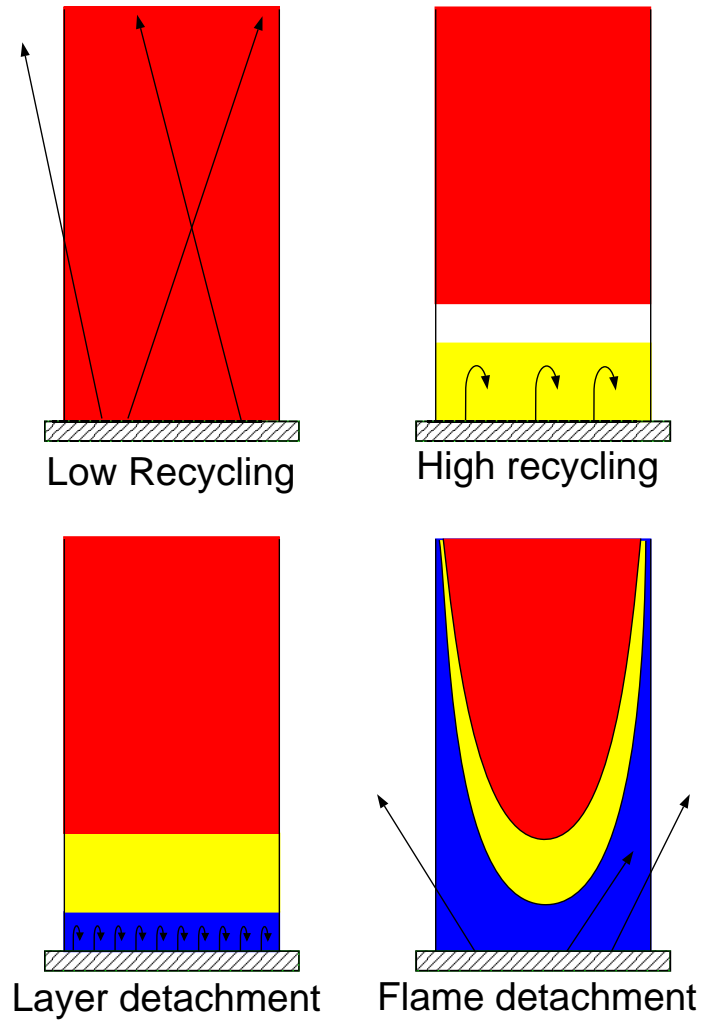


Figure 7.2.: Schematic sketch of the different divertor operating regimes with different plasma temperature profiles and neutral trajectories in front of the target plate. Starting from a low-recycling situation with practically transparent divertor fan and nearly constant temperatures along the fieldlines, one gets for fixed input power with increasing midplane density other regimes. First, a strong temperature gradient in front of the target develops with neutrals confined to this area. Then, even lower temperatures develop, where neutrals start removing effectively momentum from the plasma. Finally, a flame-like temperature profile develops with reduced plasma densities close to the plate due to plasma recombination at rather low temperatures (about 1-2 eV) allowing the neutrals to escape to the side and maximizing the neutral losses.

limits the heat loss rather than parallel thermal conductivity (Sheath-limited regime). The mean free path of neutrals is much larger than the SOL width ( $\lambda_0 \gg \text{SOL width}$ ). It is radially 1-D, because the radial gradients (SOL width) are much larger than parallel gradients, resulting in much larger radial flows than parallel flows.

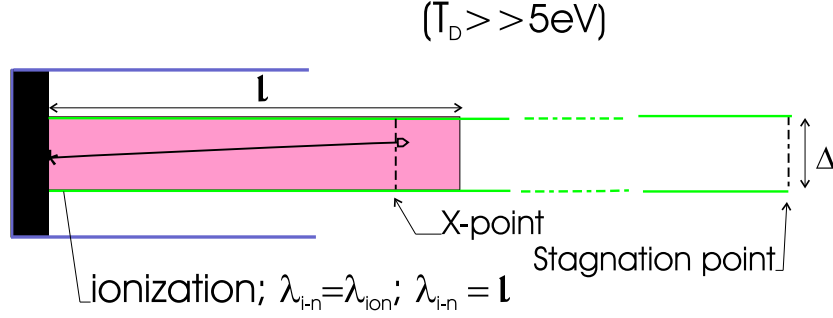


Figure 7.3.: Low recycling regime: the ionization mean free path is longer than the divertor length, because the divertor density is rather low and neutrals can penetrate rather far away from the target plate.

The power balance simplifies to:

$$q_{||b} \approx q_{||d} \approx \delta_e \Gamma_d T_{ed} \quad (7.4)$$

The Mach profile along the field line rises from 0 at the stagnation point in the midplane to 1 at the target plate (Bohm condition at the sheath entrance) in a square-root dependence from the distance away from the stagnation point along the field line. As a consequence, one gets relatively large flows in the main chamber and at the divertor entrance (up to about Mach=0.3).

The temperature at the plate is given by the sheath limit:

$$T_b \cong T_d \cong (2m)^{1/3} q_{||b}^{2/3} / (\delta_e n_{eb})^{2/3} \quad (7.5)$$

### 7.2.2. High recycling (Conduction-limited regime)

Rising the midplane density, one gets into the high recycling regime. The particle flows to the target plates reach very high values due to the intrinsic recycling of neutrals getting ionized closer to the plate (due to higher densities). The finite plasma conductivity results in significant parallel temperature gradients (Conduction-limited regime), e.g. the mean free path of neutrals is now much smaller than the SOL width (see Figs. 7.2 and 7.4).

The radial gradients (SOL width) are now much smaller than parallel gradients (especially in front of the target plate), e.g. radial flows are much smaller than parallel flows (parallel 1-D). The intrinsic divertor recycling fluxes are much larger than all other particle fluxes (pumping, separatrix flux). Close to the plate, due to the strong ionization sources from recycling neutrals, one gets a high density and therefore a low temperature.

For small energy losses and no momentum loss, one gets:

$$T_d = 0.98 \frac{m q_{||b}^{10/7} \kappa_0^{4/7}}{\delta_e^2 n_{eb}^2 L^{4/7}} \quad (7.6)$$

and

$$n_d = 0.73 \frac{n_{eb}^3 \delta_e^2 L^{6/7}}{m q_{||b}^{8/7} \kappa_0^{6/7}}. \quad (7.7)$$

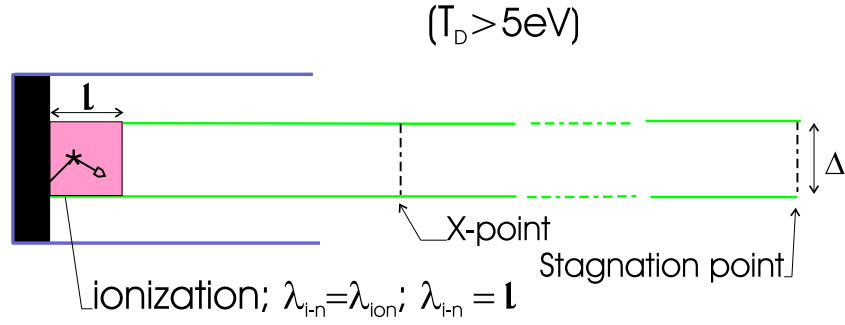


Figure 7.4.: High recycling regime: the ionization mean free path is much shorter than the divertor length, because the divertor density is now rather high. Neutrals make only several CX collisions before they get ionized.

The Mach profile rises from practically stagnant flow ( $\approx 0$ ) to 1 just in the zone close to the target plate, where the neutral losses appear (very short mean free path of neutrals  $\lambda_0$ ). Therefore, the particle flows in the main chamber and at the divertor entrance are very small (well below Mach=0.1). Momentum losses (momentum loss factor at the target plate  $f_{mom} \approx 0.5$ -0.6) start at temperatures below about 5 eV, where CX momentum losses start.

The experimental determination of  $f_{mom}$  is complicated by the fact that, for low densities, the upstream temperatures of ions and electrons are not coupled (with usually a higher ion than electron temperature), whereas in the divertor (due to much higher densities there because of recycling) both are practically equal. Only a limited number of machines have reliable ion temperature information in the SOL. Therefore, high density operation machines (like Alcator C-Mod, see also Fig. 7.5) have the advantage that this problem is less severe due to the stronger equilibration of ion and electron temperatures upstream. Then, the measurement of electron temperatures and densities is sufficient to derive the momentum factor.

### 7.2.3. Layer detachment

Pushing the upstream density further, one gets into layer detachment, which is similar to high recycling, but already much colder (below about 3 eV). The mean free path of neutrals  $\lambda_0$  is still much smaller than the SOL width. As in high recycling, radial gradients (SOL width) are much smaller than parallel gradients and therefore radial flows much larger than parallel flows (1-D). The difference to high recycling is the effect of energy detachment, e.g. energy losses are so high that the energy flux to the target plates is strongly reduced (by one order of magnitude). The momentum loss factor from midplane to the target plate is about 0.7-0.8, e.g. momentum flow is still appearing and therefore one also still has particle flow to the plate (maybe reduced by a factor of about 4 compared to the maximum particle flux). The density maximum along the field line is still close to the plate (see Figs. 7.2 and 7.7).

This cold divertor regime simplifies the parallel heat conduction equation: (SI-units,

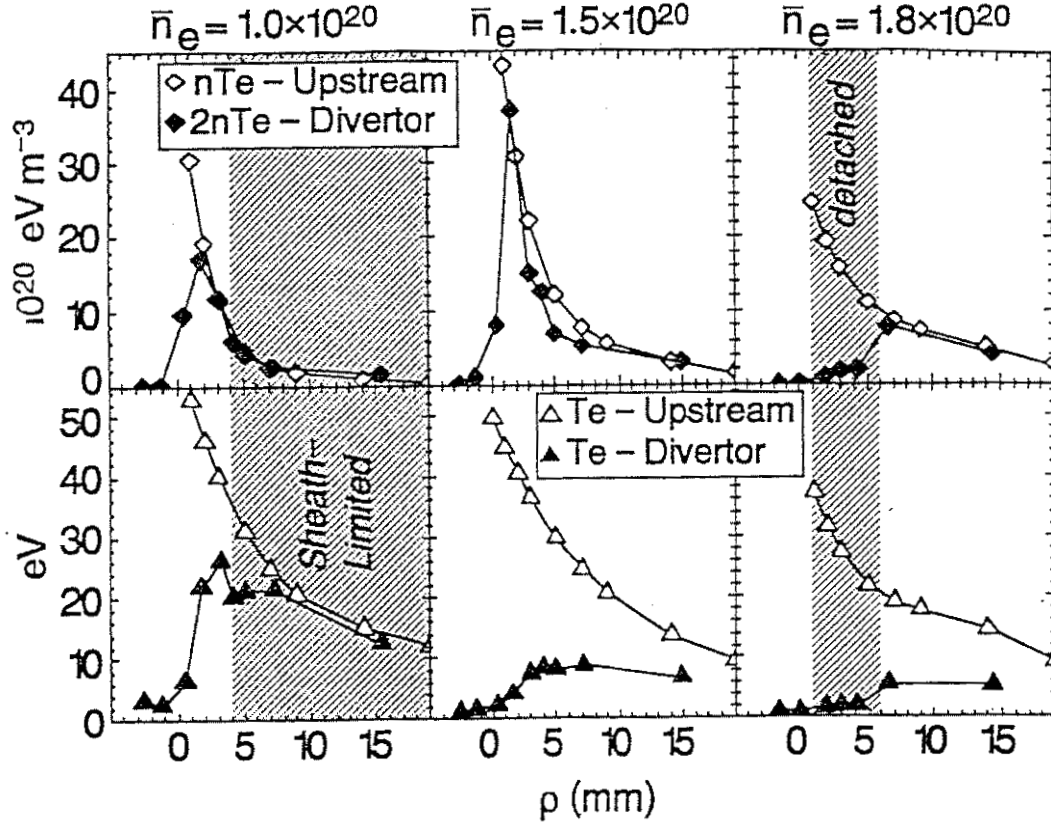


Figure 7.5.: Experimental midplane and divertor profiles from Alcator C-Mod for different divertor regimes. The top row shows a comparison of the electron pressures, the bottom row compares the electron temperatures. In the sheath-limited regime pressure and temperature upstream and downstream coincide, whereas in high recycling conditions temperatures downstream are much colder but still without pressure loss. In the detached regime, one has quite cold divertor conditions (below 3 eV) and momentum loss is observed [35].

temperatures in keV)

$$T_b^{7/2} \gg T_d^{7/2}. \quad (7.8)$$

Therefore:

$$T_b = 1.55 \cdot 10^{-4} (q_{||} L)^{2/7}. \quad (7.9)$$

This gives:

$$n_b = 2.1 \cdot 10^{-2} \frac{(1 - f_{rad})}{(1 - f_{mom})} \cdot \frac{q_{||}^{5/7}}{L^{2/7}} \cdot F(M_d, T_d), \quad (7.10)$$

with

$$F(M_d, T_d) = \frac{(1 + \gamma M_d^2)}{M_d \sqrt{\gamma/\mu}} \cdot \frac{\sqrt{T_d}}{\delta_e k T_d + \epsilon_{ion,eff}/(1 - f_{rec})}. \quad (7.11)$$

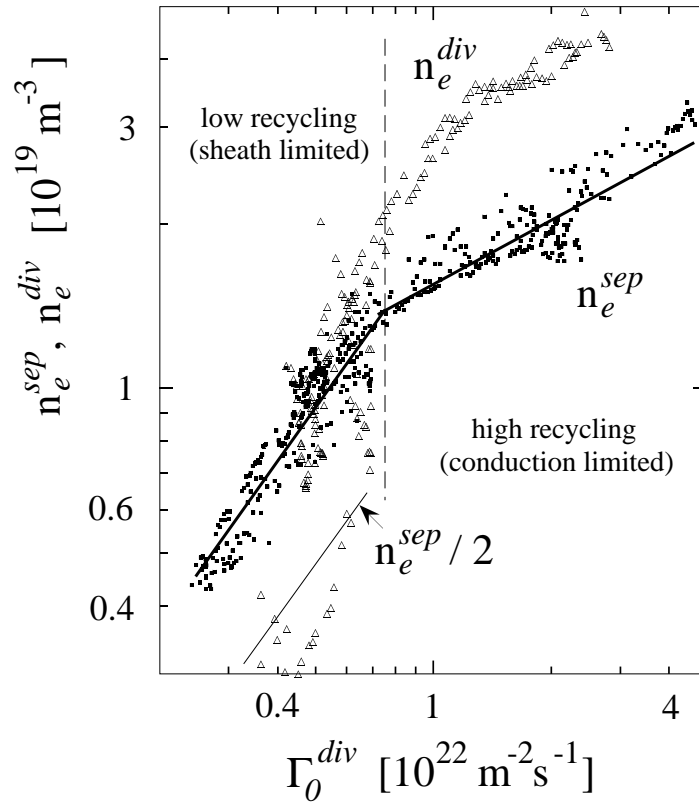


Figure 7.6.: Separatrix outer midplane and divertor densities (in  $m^{-3}$ ) as a function of neutral divertor particle flux densities in ASDEX Upgrade (in  $m^{-2}s^{-1}$ ). The transition from the linear (low-recycling) regime to the non-linear regimes (high recycling and detachment) can be seen by the higher values of divertor to midplane densities and the change in the slope from a linear dependence of the neutral divertor particle flux densities from the outer midplane separatrix density to a  $n^3$  dependence [36].

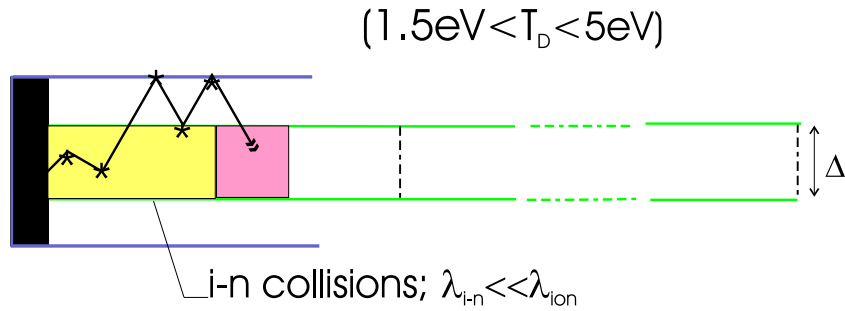


Figure 7.7.: Partial detachment: below 5 eV a zone with a lot of CX collisions for neutrals establish (here also the plasma flow slows down due to these collisions). The neutrals can diffuse out of this region or pass through until they reach the hotter zone in upstream direction where they are ionized.



This equation shows, that the momentum loss ( $f_{mom}$ ) from the plasma is coupled with its radiation loss capability ( $f_{rad}$ ).

#### 7.2.4. Flame detachment

The last scenario is flame detachment (or complete detachment), where one gets not only energy detachment, but also complete momentum detachment (momentum loss factor of about 1.0) and therefore a reduction of particle flux to the plate by at least a factor of 10 (particle detachment). Due to this strong reduction of the particle flux, the density maximum along the field line shifts away from the plate and the divertor gets more transparent for neutrals again, e.g. the mean free path of neutrals gets equal or greater than the SOL width (see 7.2 and 7.8).

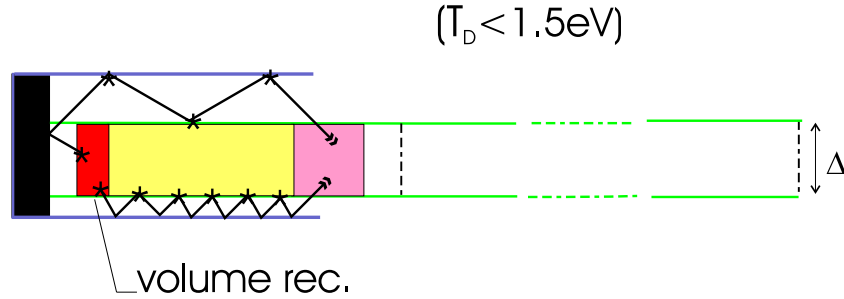


Figure 7.8.: Flame detachment: below 1.5 eV a zone and due to the quasi-stagnant plasma flow (large CX friction for temperatures below 5 eV) the plasma has enough time to recombine in front of the target plate. It forms a virtual target and shields by this the material target (large drop of the plasma particle flow to this). Neutrals created in the volume recombination zone can diffuse out until they reach the hotter zone in upstream direction either directly or versus reflection between walls and cold plasma where they are finally ionized.

Also, the radial gradients (SOL width) are comparable to parallel gradients and radial flows are comparable with parallel flows. Therefore, this situation is intrinsically a 2-D situation with a complicated flow structure.

## 8. Detachment

As already shortly mentioned in the previous chapter, momentum loss by neutrals gets very efficient in the temperature range below 5 eV and unavoidably will drive the system towards detachment. This will be discussed in this chapter in terms of the momentum factor  $f_{mom}$ .

### 8.1. Simple model for momentum loss by neutrals

Pitcher [37] uses a simple model of Self and Ewald [38] for the pressure loss fraction defined as,

$$(1 - f_{mom}) = f_m = \frac{2n_d T_d}{n_b T_b}. \quad (8.1)$$

Self and Ewald analyse an isothermal plasma with both ionization and CX friction, assuming that one has only neutral atoms with uniform density  $n_H$  in the recycling region. Particle continuity along the field line coordinate  $x$  is then just the balance of the divergence of the parallel particle flux and the ionisation source by neutrals:

$$\frac{d(nv)}{dx} = S_i = nn_H \langle \sigma v \rangle_i. \quad (8.2)$$

The momentum equation has to include the pressure drop along field lines and the source terms from ionisation and CX:

$$mnv \frac{dv}{dx} = -\frac{dp}{dx} - mvS_i - mvS_{CX}, \quad (8.3)$$

with

$$S_{CX} = nn_H \langle \sigma v \rangle_{CX}. \quad (8.4)$$

$p$  is the static plasma pressure  $p_e + p_i$ . For isothermal conditions and  $T_i = T_e = T$ , one gets:

$$\frac{dp}{dn} = \frac{d(p_e + p_i)}{dn} = 2T, \quad (8.5)$$

and therefore

$$mnv \frac{dv}{dx} = -2T \frac{dn}{dx} - \frac{mvS_i}{\alpha}, \quad (8.6)$$

with

$$\alpha = \frac{\langle \sigma v \rangle_i}{\langle \sigma v \rangle_i + \langle \sigma v \rangle_{CX}}. \quad (8.7)$$

For sonic conditions at the plate, the plasma density can be expressed as a function of the Mach number ( $M = v/c_s$ ):

$$\frac{n(M)}{n_{target}} = \left( \frac{\alpha + 1}{\alpha + M^2} \right)^{\frac{\alpha+1}{2}}. \quad (8.8)$$

At the entrance of the recycling region ( $M=0$ ), one gets

$$\frac{n(M=0)}{n_{target}} = \left( \frac{\alpha + 1}{\alpha} \right)^{\frac{\alpha+1}{2}}. \quad (8.9)$$

This results in the expression for the momentum factor

$$f_m = 2 \left( \frac{\alpha}{\alpha + 1} \right)^{\frac{\alpha+1}{2}}. \quad (8.10)$$

Experimentally, the fact that momentum removal gets effective below about 5 eV was confirmed by many experiments. As an example, results from Alcator C-Mod are shown in Fig. 8.1, comparing experimental measurements with the expression from Pitcher. This

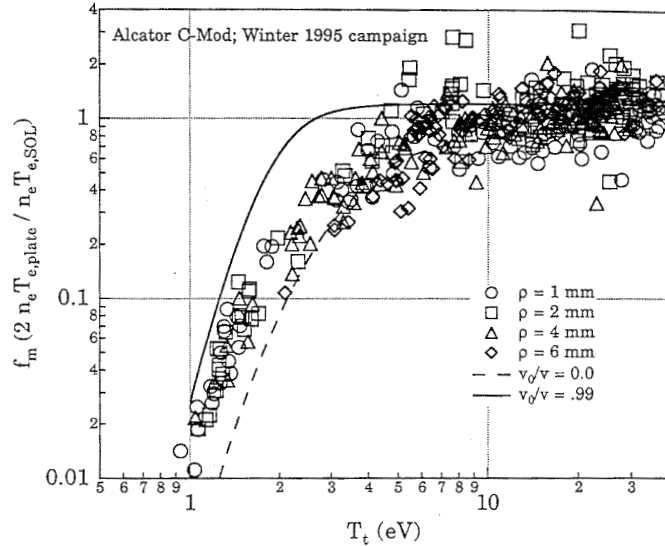


Figure 8.1.: Momentum factor  $f_m$  for Alcator C-Mod experimental data and comparison with Pitcher's formula for two extreme neutral conditions (full line: neutrals move with 0.99 of plasma velocity; broken line: neutrals at rest) [37].

effect can also be understood qualitatively, since, below 5 eV, ionisation gets unimportant, neutrals can freely interpenetrate the plasma flow. The CX momentum loss is still confined to a boundary layer with thickness  $\lambda_{CX,0}$ . In deeper layers, CX enhances perpendicular viscosity and ion-energy cross-diffusion. In the comparison between simple model and

experiment in Fig. 8.1, two curves are shown (full and broken line). This is due to the fact that the momentum loss from neutrals and therefore the pressure reduction is dependent on the regime of the neutrals, resulting, especially at very low temperatures (below 2 eV), in differences of the momentum loss factor of at least one order of magnitude. In the fluid regime, the neutral velocity is quite large (especially toroidally due to coupling to the ions by CX collisions), and neutrals have quite a short mean free path (high recycling, layer detachment). One gets small momentum loss factors (because the difference of neutral and ion velocities determine the CX momentum loss) and the divertor density is usually larger than the midplane density.

In the Knudsen regime, the neutral velocity is rather small and the divertor conditions are such that one has a rather long mean free path for neutrals (flame detachment). In this regime, one gets maximum momentum losses.

The transition between the two regimes can also be determined by e.g. SOL width in the divertor influencing strongly the neutral opacity and radial neutral collisionality.

## 8.2. Divertor balances in the attached and detached regime

B2-Eirene results for ASDEX-Upgrade are used to characterise the divertor solution for an attached (input power 20 MW) and a detached (input power 1 MW) case. This will illustrate the discussion of the different operating regimes. As expected, the attached hot 20 MW case is characterised by temperature gradients and density maximum close to the plate. In contrast, the detached cold case (1 MW) has already temperature gradients up to the X-point and density maximas well separated from the plate (Figs. 8.2 and 8.3).

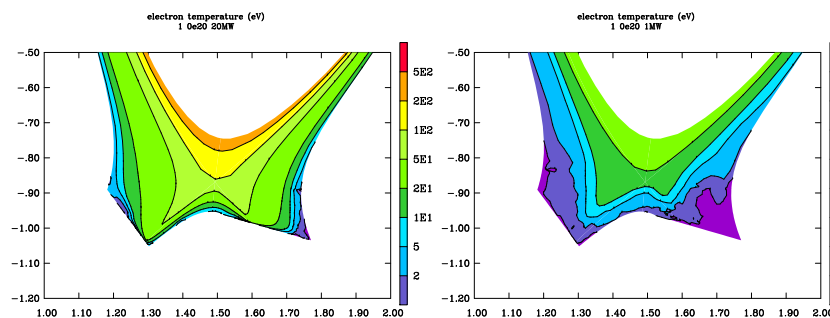


Figure 8.2.: Contours of electron temperature for a 20 MW (left) and a 1 MW (right) ASDEX-Upgrade case with a midplane separatrix density of  $1 \cdot 10^{20} \text{ m}^{-3}$

Divertor balances are shown in the Figs. 8.4 and 8.5 for the outer divertor: plotted are fluxes at the entrance of the divertor, at the target plate and integrated sources and integrated divergences of radial fluxes in this flux tube (starting from the target plate going backward to the X-point).

For the divertor particle balance (Fig. 8.4) for the attached case (20 MW), the particle flux hitting the target plate is practically identical to the particle sources from the neutrals in each radial flux tube, whereas for the detached case (1 MW) the radial fluxes (integrated from the target plate up to the divertor entrance) are also important and a rather complicated 2-D balance is setup.

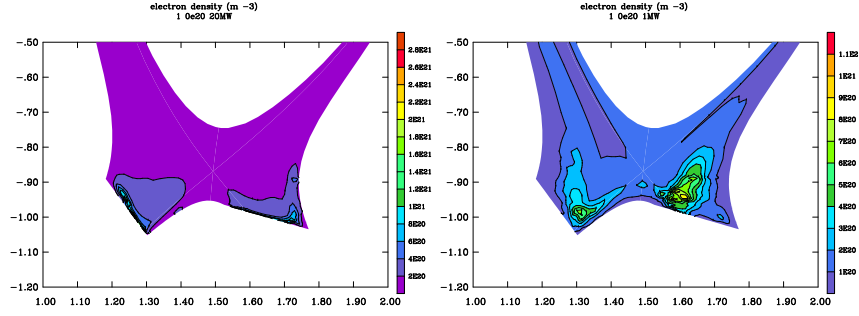


Figure 8.3.: Contours of electron density for a 20 MW (left) and a 1 MW (right) ASDEX-Upgrade case with a midplane separatrix density of  $1 \cdot 10^{20} m^{-3}$

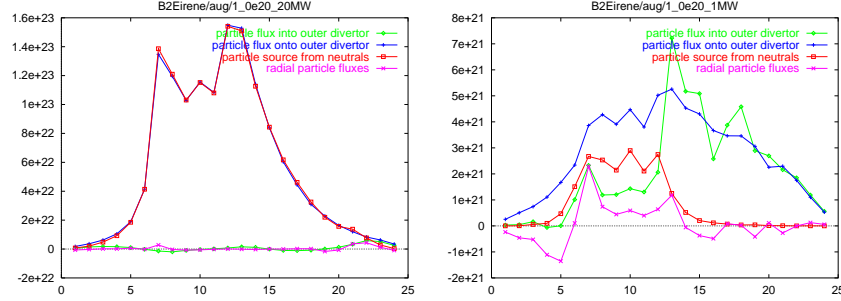


Figure 8.4.: Radial outer divertor particle flux balance for a 20 MW (left) and a 1 MW (right) ASDEX-Upgrade case with a midplane separatrix density of  $1 \cdot 10^{20} m^{-3}$ . Separatrix is between 6 and 7.

The same holds for the divertor energy balance, where, for the attached case (20 MW) (Fig. 8.5), the difference in each radial fluxtube between energy flux hitting the target plate and entering the fluxtube is practically identical to the energy sinks from the neutrals, whereas for the detached case (1 MW), again the radial fluxes (integrated from the target plate up to the divertor entrance) are important.

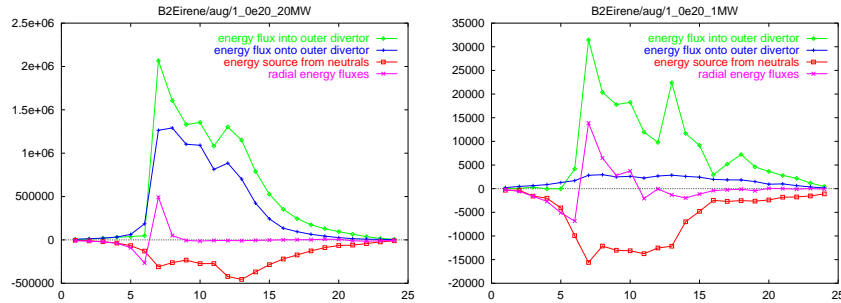


Figure 8.5.: Radial outer divertor energy flux balance for a 20 MW (left) and a 1 MW (right) ASDEX-Upgrade case with a midplane separatrix density of  $1 \cdot 10^{20} m^{-3}$ . Separatrix is between 6 and 7.

Major radial fluxes appear to the private flux (this is important for pumping scenarios).

### 8.3. Transition from layer to flame detachment

The detached case is characterised by a complicated 2-D balance. The transition of the system from layer to flame detachment is characterised by the ratio of the mean-free path of D atoms to the SOL width: as long as the D atoms have a shorter mean-free path than the typical SOL width, the system is 1-D dominated (radial gradients (SOL width)  $\ll$  parallel gradients, radial flows  $\ll$  parallel flows).

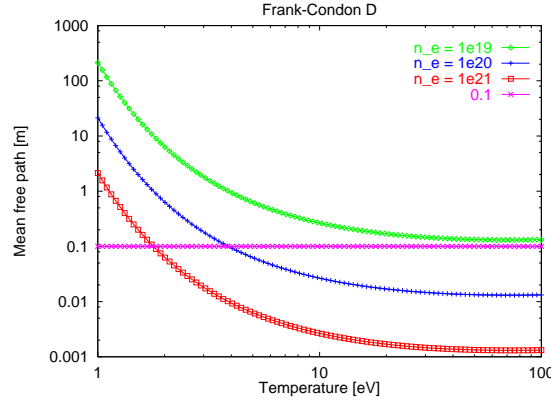


Figure 8.6.: Mean free path of Franck-Condon neutrals (in m) with an energy of 2 eV as a function of plasma temperature (in eV) for different electron densities (in  $m^{-3}$ ). Also shown is a typical SOL width in the divertor of 10 cm.

Using simple approximations for the CX and ionisation mean free path of neutrals

$$\langle \sigma_{ion} v_{th,e} \rangle_{ion} = 10^{-28} \sqrt{n_e} T_e^6 \quad (8.11)$$

(temperatures in eV, valid for the range between 1 and 3 eV),

$$\sigma_{CX} \sim 10^{-19} m^2. \quad (8.12)$$

For a random walk process one gets

$$\lambda_0 = \sqrt{\lambda_{ion} \cdot \lambda_{CX}}, \text{ with } \lambda_{ion} = \frac{v_0}{n_e \langle \sigma_{ion} v_{th,e} \rangle_{ion}}, \lambda_{CX} = \frac{1}{\sigma_{CX} n_e}. \quad (8.13)$$

For a (Frank-Condon) energy of 2 eV one gets a critical temperature, where this change appears

$$T_{e,c} = \sqrt[3]{\frac{3.8 \times 10^{25}}{n_{e,d}^{\frac{5}{4}} \lambda_0^{\text{crit}}}} \quad (8.14)$$

where  $\lambda_0^{\text{crit}}$  is taken as 0.08m (typically 4\*(SOL width) in the divertor). This gives for a divertor density of  $10^{19} m^{-3}$  a temperature of 9.5 eV, whereas for  $10^{21} m^{-3}$  one gets 1.4 eV. Avoiding the 2-D (flame) detachment therefore also means keeping the density high in front of the divertor.

## 8.4. Volume recombination

For the discussion of the detachment physics below about 2 eV, volume recombination becomes important.

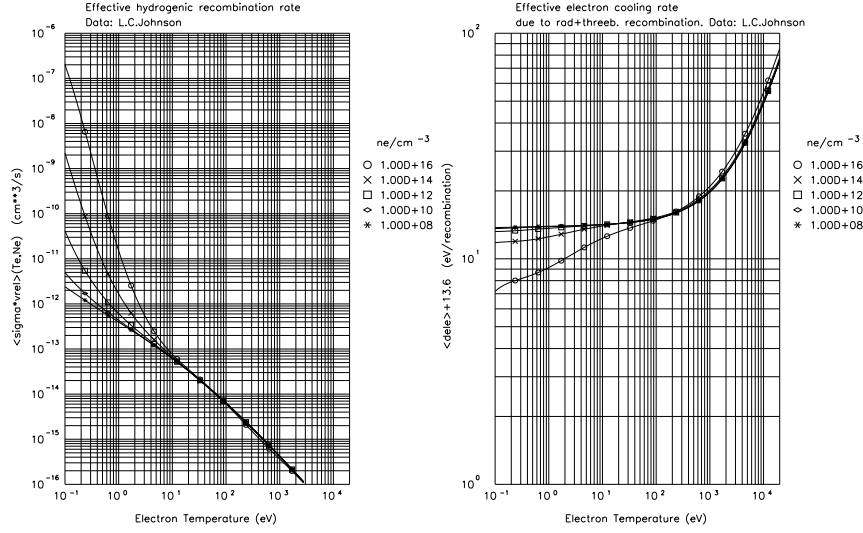


Figure 8.7.: Effective hydrogenic recombination rate (in  $\text{cm}^3/\text{s}$ ) as a function of electron temperature (in eV) for different electron densities (in  $\text{cm}^{-3}$ ) (left). Effective electron cooling rate (in  $\text{cm}^3/\text{s}$ ) due to radiation and three-body recombination as a function of electron temperature (in eV) for different electron densities (in  $\text{cm}^{-3}$ ) (right). Due to the logarithmic scale data are plotted with an offset of 13.6 eV for energy sink as well as energy source (D. Reiter).

Recombination of an electron and an ion into a neutral atom needs a third body to account for the conservation laws. This is possible in two ways: in the process of radiative recombination a photon takes care of energy and momentum transfer. This process shows up in the recombination rate plot (Fig. 8.7) as the lower envelope of the different density values. The second process is three-body recombination where an additional electron is necessary. The recombination rate for this process gives the strong rise below about 2 eV (especially for high densities above  $10^{20} \text{m}^{-3}$ ) in the plot of the effective hydrogenic recombination rate. This second process is responsible for the strong effects of volume recombination in the divertor affecting the whole character of the plasma state, whereas the first process is important for diagnosing the onset of strong volume recombination spectroscopically.

The effective electron cooling rate (Fig. 8.7) for the recombination rates shows that the absolute direct energy loss for electrons by volume recombination is usually small and can be even a heating term for high densities and low temperatures. That means that the process of volume recombination has the tendency to stabilize the temperature and avoid further cooling.

## 8.5. Importance of volume recombination for the divertor

Experimentally, in the JET discharge 30829, the ion saturation current drops by one order of magnitude even at constant net input power, while in parallel the neutral particle fluxes in the divertor and the  $D_\alpha$  signal rise (Fig. 8.8).

This seems to be contradictory, because from a drop of the ion particle flux to the plate

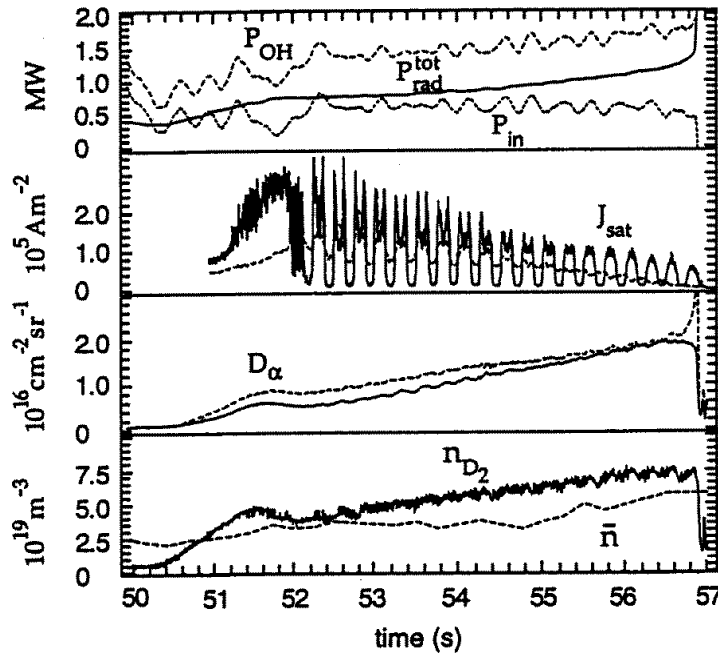


Figure 8.8.: Traces of various parameters for the detaching JET discharge 30829: (a) heating power  $P_{OH}$  (upper dashed line), total radiation power  $P_{rad}^{tot}$  (solid line) and net input power  $P_{OH} - P_{rad}^{tot}$  (lower dashed line), (b) ion saturation current  $J_{sat}$  for two near-separatrix inboard (dashed line) and outboard (solid line) probes, (c) the  $D_\alpha$  signals for an inboard (dashed line) and outboard (dotted line) channel, (d) neutral density in the private flux region  $n_{D_2}$  (solid line) and line-averaged (dashed line) density. The oscillations are due to X-point sweeping. [39]

one would expect a drop of the neutral recycling flux. Due to the fact that the net input power was constant, impurity driven (upstream, e.g. radiation in main chamber or SOL) effects can be ruled out for the observed behaviour, and the explanation has to address the physics of the formation of a gas target (complete detachment).

One has to generalize the relation between target particle and energy fluxes by introducing



the effect of volume recombination [39]

$$\delta_e \Gamma_d T_d (1 + M_d^2) + \frac{\Gamma_d \epsilon_{ion,eff}}{1 - f_{rec}} = (1 - f_{rad}) q_{||}, \quad (8.15)$$

where the ratio of number of volume recombination events to the number of ionization events per second is introduced as  $f_{rec}$ .

As mentioned before in the particular JET discharge, the net input power was practically constant, e.g.  $(1 - f_{rad}) q_{||} \approx const.$  Consistent modelling of drop of the ion saturation current by one order of magnitude, increase of  $D_\alpha$  and increase of the neutral divertor fluxes is only possible by a strong onset of volume recombination (Fig. 8.9).

Without volume recombination, one is unable to obtain the observed drop of ion saturation current.

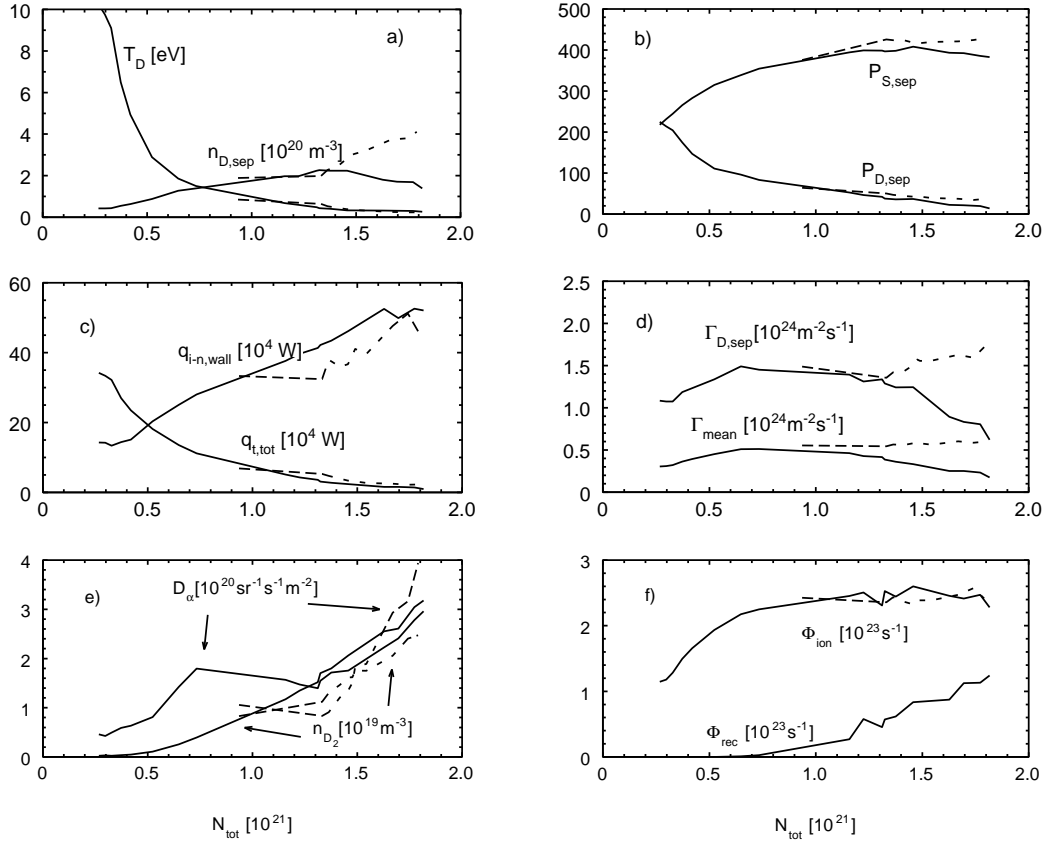


Figure 8.9.: Summary of  $N_{tot}$  (total number of particles) traces for a variety of inboard SOL quantities with (solid lines) and without (dotted lines) recombination.  $n_D$ ,  $T_D$ , and  $P_D$  are, respectively, the plasma density, electron temperature and plasma pressure at the plate. Subscript S denotes upstream quantities.  $n_{D_2}$  is the neutral density in the private flux region.  $q_{i-n,wall}$  is the power flux carried by neutrals to the walls and  $q_{t,tot}$  is the total power flux to the target.  $\Gamma_{D,sep}$  and  $\Gamma_{D,mean}$  are the separatrix and mean parallel particle flux densities at the plate.  $\Phi_{ion}$  and  $\Phi_{rec}$  are the total ionization and recombination rates [39].

## 8.6. Characterisation of gas target

The gas target which is formed in the detachment process is characterised by the removal of the remaining (small) energy by charge exchange to the walls. This is possible because the gas target itself has already a lower density than upstream (due to volume recombination and momentum loss). The volume recombination scenario forms a double layer: a recombination zone forms (radially and poloidally displaced) with its maximum in the outer SOL, because the drop of the temperature in the radial direction is faster than for density. This acts as a virtual target stopping the particle flux to the plate. The recombining neutrals can travel upstream to the hotter regions, where they are ionized. This is intrinsically a 2-D situation (flame detachment, see Fig. 8.10). The direct energy sink by volume recombination is not important (can even be a heating term). Only by the ionization of neutrals from the additional particle source in the divertor volume does one get the dominant energy sink from this process.

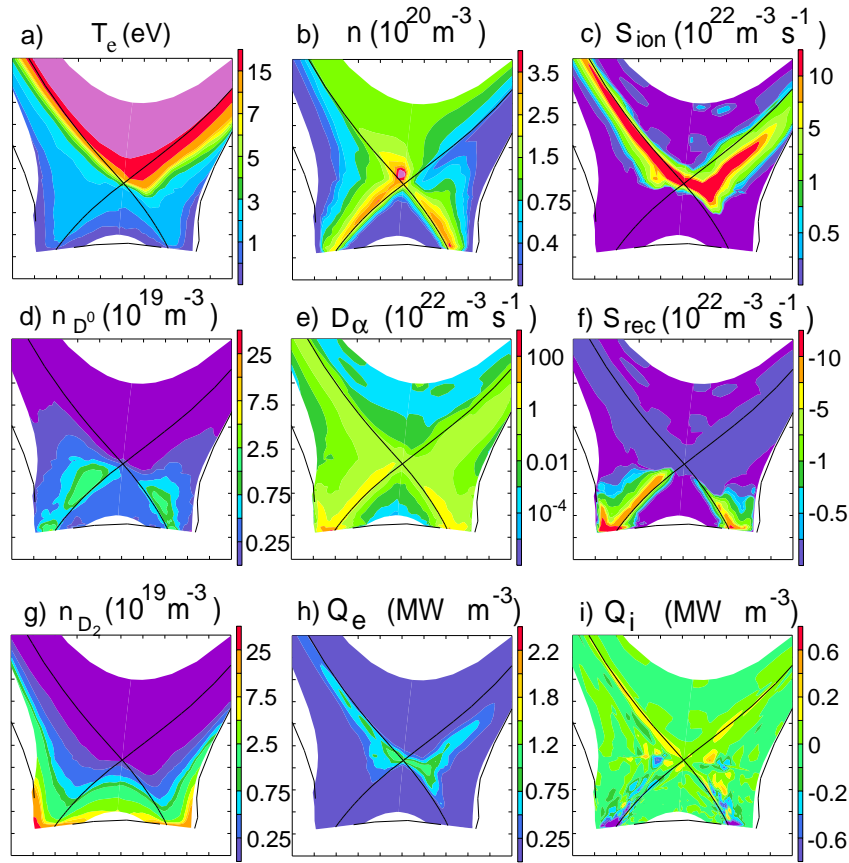


Figure 8.10.: Spatial distribution of relevant parameters for  $N_{tot} = 1.4 \cdot 10^{21}$ : (a) Electron temperature, (b) plasma density, (c) ionization source strength, (d) atom density, (e)  $D_\alpha$  emissivity, (f) recombination source, (g) molecule density, (h) total electron energy losses and (i) total ion energy losses.[39]

## 8.7. Strong onset of recombination radiation

In ASDEX-Upgrade this modelling prediction for L-mode density limit scenarios was proven by spectroscopic measurements [40].

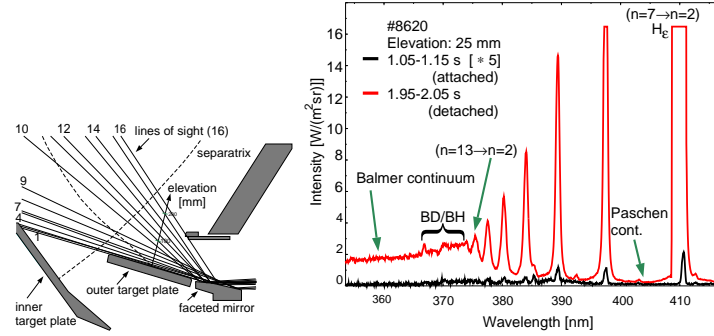


Figure 8.11.: Arrangement of the 16 poloidal sightlines of the divertor spectrometer. Another set of 30 sightlines views the plasma parallel to the outer target plate (left). Spectra around the Balmer series limit measured with the divertor spectrometer. The midplane density rises from  $4.1 \cdot 10^{19} m^{-3}$  (at 1.1 s) to  $6.7 \cdot 10^{19} m^{-3}$  (at 2.0 s) leading to full detachment (right). [40]

The divertor spectrometer system observed the plasma along several sightlines in the poloidal cross-section. There are 30 sightlines viewing the plasma parallel to the outer target plate in a distance of 1 to 90 mm, another set of 16 sightlines is arranged fan-wise. The collected light was fed via optical fibres to a Czerny-Turner or a Fastie-Ebert (Echelle grating) spectrometer with low and high spatial resolution, respectively. Several lines of sight were detected simultaneously by means of a fast CCD camera. For detached condition (close to the L-mode density limit), Balmer and Paschen continuum radiation and line radiation of the Balmer series up to transitions from level  $n=14$  are observed (Figs. 8.11 and 8.12).

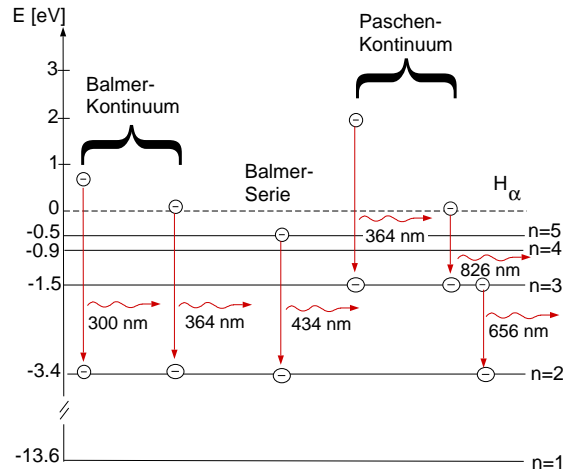


Figure 8.12.: Term scheme for hydrogen with Balmer and Paschen continua (B. Napi-ontek).

The detachment process results in a drop of electron temperature and an increase of electron density. Therefore, the rates for radiative and three-body recombination increase strongly, as discussed before, which leads to the strong increase in hydrogen radiation. The

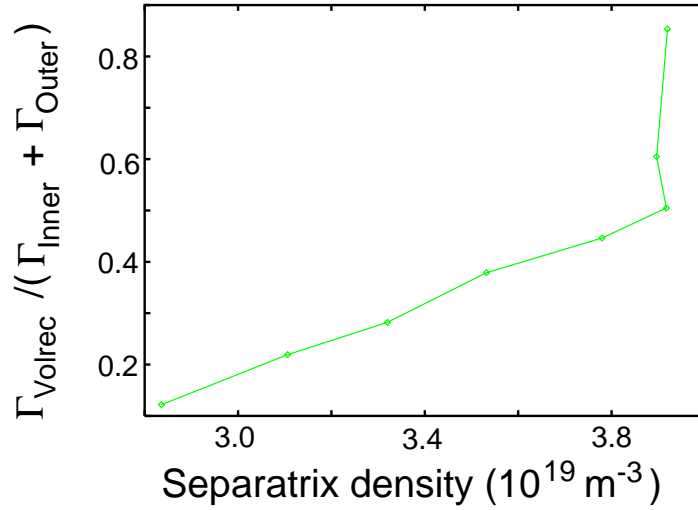


Figure 8.13.: Strong onset of the volume recombination source strength (expressed as flux of neutrals) normalised to the sum of inner and outer target fluxes. Due to the onset of volume recombination (and complete detachment) the separatrix upstream density clamps and a SOL density limit establishes.

continuum radiation is dominated by free-bound transitions. The energy of the emitted photons ( $h\nu$ ) is determined by the sum of the energy of the free electron ( $E_{el}$ ) and the difference of the binding energy  $E_n$  of level  $n$  into which the electron transfers and the ionization energy  $E_H$  of hydrogen:

$$h\nu = E_{el} + (E_H - E_n) = E_{el} + E_H(1 - (1 - 1/n^2)) = E_{el} + E_H/n^2 \quad (8.16)$$

The continuum radiation for a given photon energy is the sum of contributions from all levels  $n$ . The minimum energy for a transition into  $n=2$  is  $E_H/4$  (364 nm) (see Fig. 8.12). For larger wavelengths, the contribution from this transition to the continuum is missing, therefore one observes a drop in the spectrum. This can now be used to determine the temperature. The continuum radiation of the hydrogen atom is given by the emission coefficient as a function of frequency

$$\epsilon_\nu = 1.719 \cdot 10^{-46} \frac{n_e n_{Z,1} Z^4}{T_e^{3/2}} \exp\left(\frac{W_{i,Z-1} - h\nu}{kT_e}\right) \sum_n \frac{G_n(\nu)}{n^3} \exp\left(\frac{-W_n}{kT_e}\right), \epsilon_\lambda = \frac{c}{\lambda^2} \epsilon_\nu \quad (8.17)$$

in  $\frac{W}{\text{m}^3 \cdot \text{Hz} \cdot \text{sr}}$ ,  $T_e$  in K.  $n$  is the major quantum number (2 for Balmer, 3 for Paschen continuum),  $W_i$  is the ionization energy,  $W_n$  is the excitation energy for quantum number  $n$  ( $W_i - W_n = W_i/n^2$ ) and  $G_n$  are the Gaunt factors (about 1). At the Balmer limit, one has  $W_i - W_2 - h\nu = 0$  and  $T_e^{-3/2}$  is the only temperature dependence. For the Paschen limit, one has  $W_i - W_3 - h\nu \approx -1.9 \text{ eV}$ . From the ratio of both intensities, one gets the (line integrated) electron temperatures. The electron densities are determined from the absolutely calibrated Balmer continuum emission. The arrays of lines of sight of the

divertor spectrometer allow measurements of spatial  $T_e$  and  $n_e$  profiles. Spatial resolution is possible in the direction perpendicular to the target plates, whereas, along the line of sight, the emission is integrated. Due to the dependence of the emissivity on  $n_e^2$ , the region with the highest density dominates the intensity. The temperature measurements pickup the region with the highest temperature along the line of sight because of the steep dependence of Balmer to Paschen continuum intensities for  $T_e \leq 2\text{eV}$ . Therefore, one gets upper limits for  $T_e$  and  $n_e$  along the line of sight.

These experimental features are reproduced (and predicted) by B2-Eirene modelling (see Figs. 8.13, 8.15 and 8.16). This regime for ASDEX Upgrade is again characterised by a double layer of ionization sources from neutrals and recombination sinks for the plasma (Fig. 8.14).

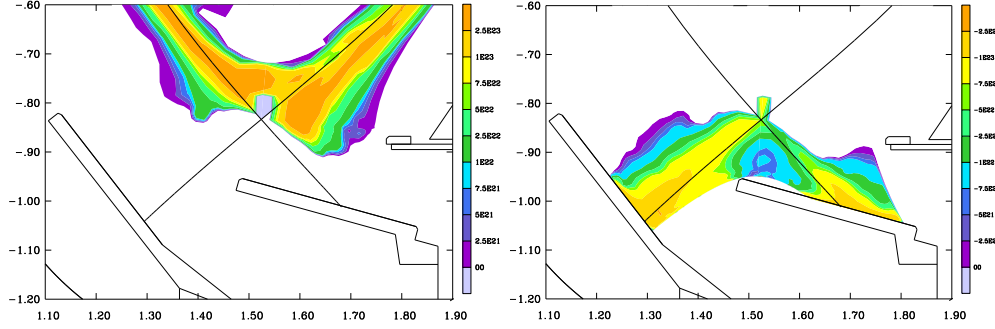


Figure 8.14.: B2-Eirene results for contours of ionization sources per volume (left) and recombination sink terms per volume (right) for the plasma due to neutrals for a strongly recombining case.

Using B2-Eirene, one can compare quantitatively modelling results and experimental measurements (Figs. 8.15 and 8.16).

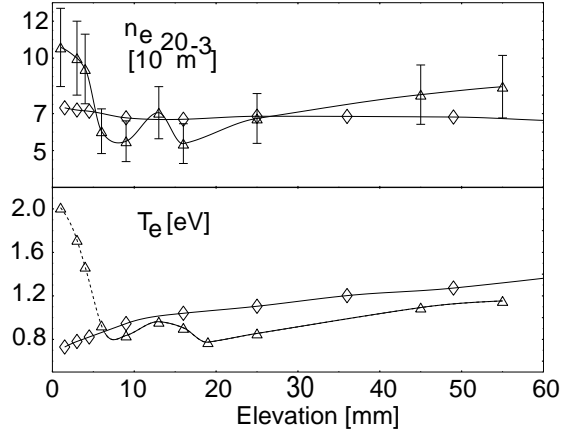


Figure 8.15.: Modelling (diamonds) and measurements (triangles, #8620 at 2.7 s) of electron temperature and density profiles. The rise of the measured electron temperature near the target plate is due to the effect of the inner divertor on line integrated intensity (see also the following figure) (B. Napiontek).

Near the outer target plate (within 10 mm), the modelled mean temperature decreases

due to the lower temperatures in the outer divertor. The spectroscopic temperature measurements are dominated by the inner divertor. Thus the measured spatial profiles

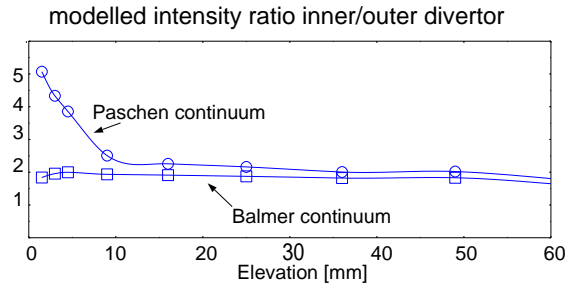


Figure 8.16.: Modelling results for the line integral measurements for Paschen and Balmer continuum. For line-of sights close to the plate the inner divertor is the dominating contribution.

can only be interpreted as profiles of mean values in the emission zone of the outer divertor at greater distances to the target plate. Therefore, qualitative differences between the modelled mean parameters and the measurements especially for  $T_e$  near the target, are to be expected. The agreement at greater distances to the target plates and for the electron density is quite good.

Under high density conditions in the divertor, one must also address the issue of optical thickness. In the experiment,  $L_\beta$  and  $H_\alpha$  were measured simultaneously with the boundary layer spectrometer, which is viewing from the top through the divertor plasma onto the target plates (Fig. 8.17).

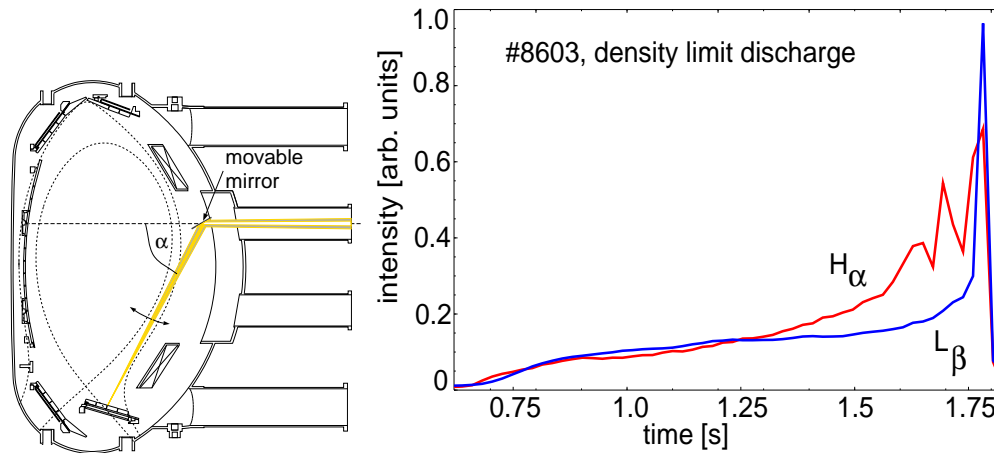


Figure 8.17.: Schematic view of the boundary layer spectrometer (left). Ratio of  $H_\alpha$  to  $L_\beta$  intensities during shot # 8603 measured with the boundary layer spectrometer (right) (B. Napiontek).

At moderate divertor densities the ratio of  $H_\alpha$  to  $L_\beta$  intensities starts to increase with density, indicating the effect of optical thickness. At higher densities and regarding  $L_\alpha$ , the effect must be even more pronounced. Thus in the region of high density plasmas, where the observed continuum radiation is preferentially emitted, recombination into the ground

state via excited states is reduced by reabsorption of photons emitted at recombination processes into ground state.

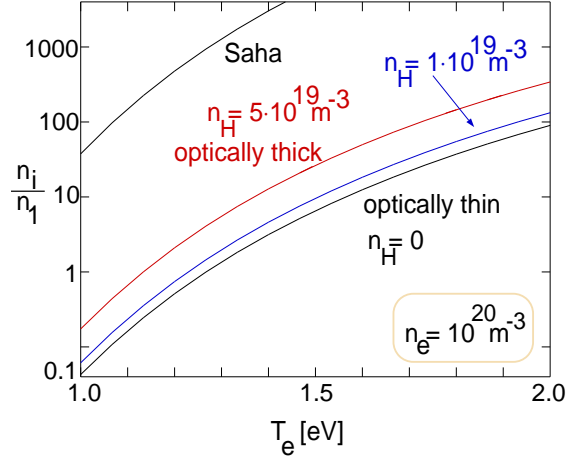


Figure 8.18.: Ionization degree  $n_i/n_1$  ( $n_1 = n_e$ ) as a function of electron temperature for a high electron density  $n_e = 10^{20} \text{ m}^{-3}$  for a variety of hydrogenic neutral densities showing the effect of optical thickness (K. Behringer).

DIII-D divertor Thomson scattering data also show low divertor temperatures consistent with strong onset of volume recombination [41]. Both experimental measurements demonstrate that the temperatures for detachment have to be in the range below about 2 eV. This proves the prediction of the modelling for detachment, while demonstrated

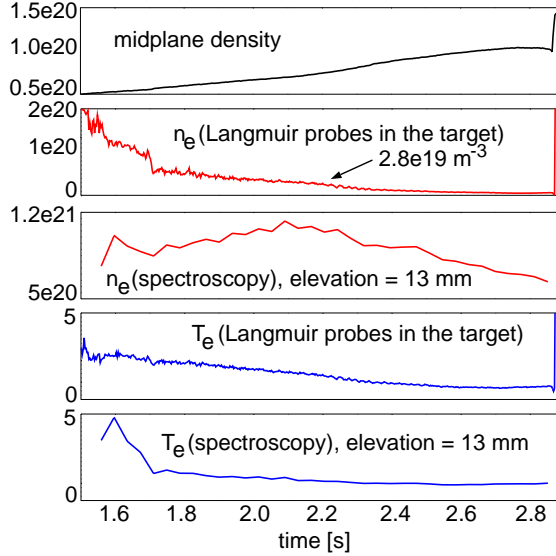


Figure 8.19.: Time evolution of plasma parameters at a density ramp (# 8620, L-mode, 600 kA,  $B_t = -2.0$  T,  $P_{NB}=5$  MW). Midplane density, spectroscopic electron density and temperature close to the plate as well as Langmuir target electron density and temperature are shown (B. Napiontek, M. Weinlich).

problems for Langmuir probe analysis give much lower electron densities (and without proper corrections also too high temperatures) (Fig. 8.19).

## 8.8. Effect of vibrationally excited molecules

A mechanism, possibly also important in the divertor, is recombination through vibrationally excited molecules. Two possible reaction paths exist. The first one is the creation of negative ions ( $e + H_2(v) \rightarrow H_2^-$ ), followed by dissociation ( $H_2^- \rightarrow H + H^-$  and  $H^+ + H^- \rightarrow H + H^*$ ). The second channel is ion conversion ( $H^+ + H_2(v) \rightarrow H + H_2^+$ ) and dissociation ( $e + H_2^+ \rightarrow H + H^*$ ).

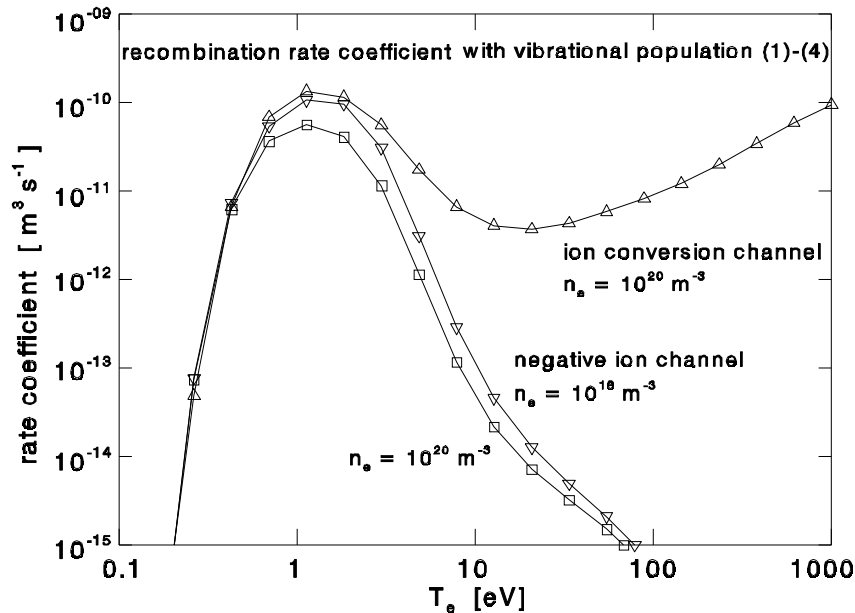


Figure 8.20.: Recombination rate coefficient with vibrational population taken into account as a function of electron temperature for ion conversion and negative ion channel (U. Fantz).

The rate coefficients of these two processes lead to a large increase of the total recombination rate coefficient (including also three-body and radiative recombination) by at least one order of magnitude for temperatures below about 5 eV (see Fig. 8.20 and Fig. 8.21). However, the rate coefficients for ionisation and dissociation increase also, reducing thus the mean free path of the molecules (Fig. 8.22). The recombination source depends on rate coefficient and electron density, but also on the molecular density. Therefore, a large recombination rate coefficient not necessarily leads to large recombination effects (sources). A detailed discussion of this can be found in [42, 43, 44].

However, the rate coefficients for ionisation and dissociation increase also, reducing by this the mean free path of the molecules. The recombination source depends on rate coefficient and electron density, but also on the molecular density. Therefore, a large recombination rate coefficient not necessarily leads to large recombination effects (sources). A detailed discussion of this can be found in [42, 43, 44].



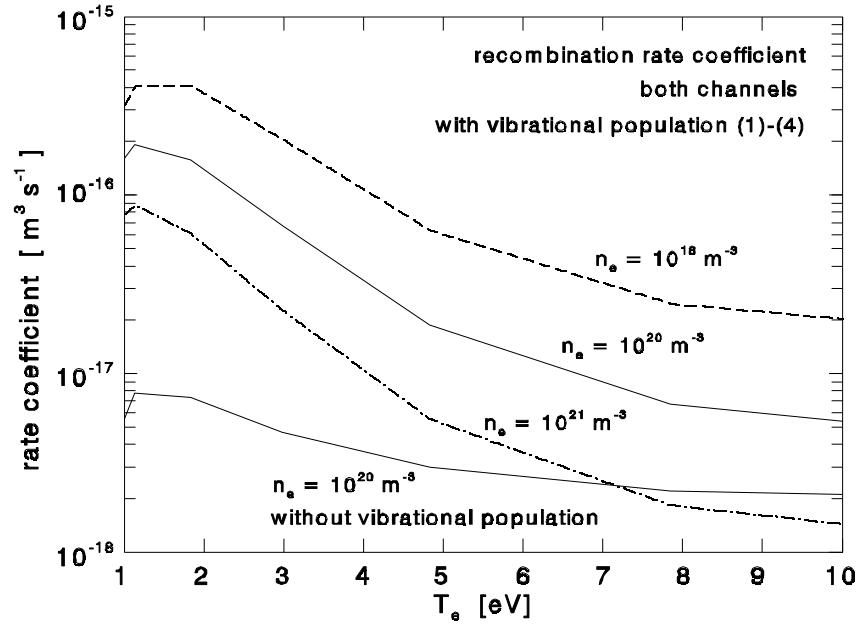


Figure 8.21.: Total recombination rate coefficient with effect of vibrational excitation of molecules and without as a function of electron temperature for different electron densities (U. Fantz).

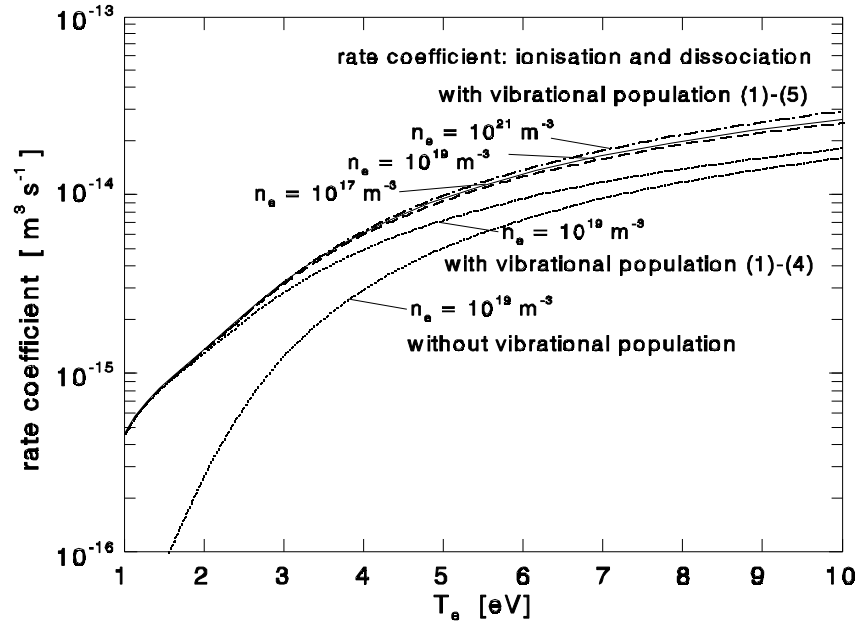


Figure 8.22.: Ionisation and dissociation rate coefficient with effect of vibrational excitation of molecules and without as a function of electron temperature for different electron densities (U. Fantz).

Introducing the different vibrational levels as separate species in the neutral Monte-Carlo-Code Eirene and doing a self-consistent B2-Eirene calculation this recombination channel

is only important in a rather thin surface layer close to the plasma boundary, because the neutral molecules do not penetrate as deep as for the case without taking into account the vibrational excitation (Fig. 8.23). The integral contribution to the total recombination rate is also a minor correction.

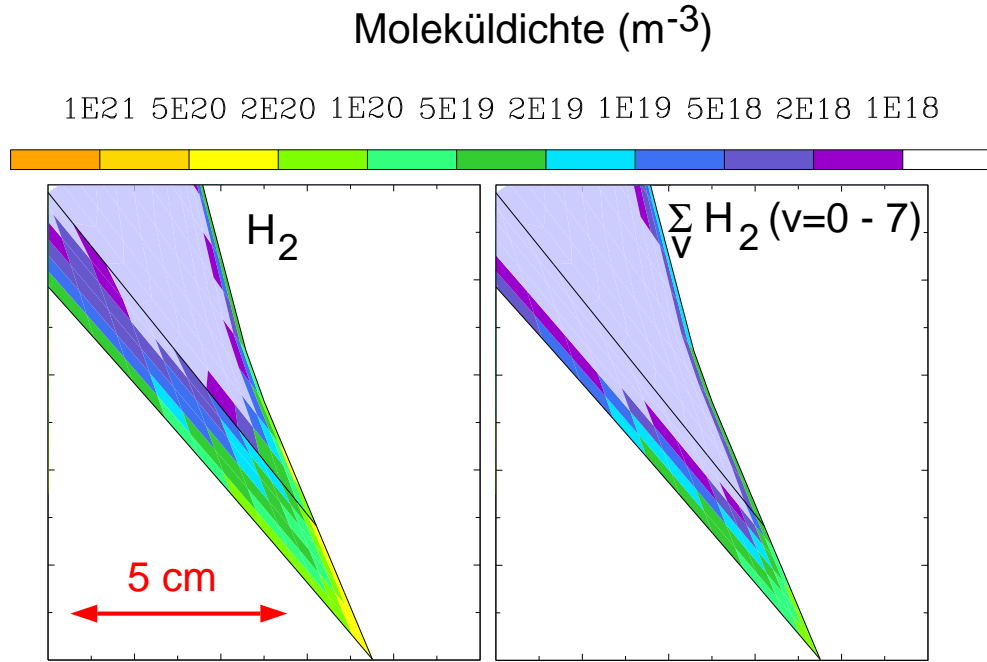


Figure 8.23.: Neutral molecular density from B2-Eirene with (right) and without (left) the effect of vibrational excitation of molecules.



## 9. Radial midplane profiles

After the rather detailed discussion of the divertor scenarios and processes, the SOL description will be extended also to more global features like flow patterns and main chamber effects. To start with, simple models for the SOL midplane profiles will be presented here.

### 9.1. Radial midplane temperature profile

The temperature profile is expected to follow relatively simple physics, because the parallel heat conduction is absolutely dominating on open fieldlines in the main chamber, whereas the influence of sources is relatively weak (only CX gives energy source or sink terms). Following [45, 46] one starts with the relation between perpendicular and parallel heat fluxes (projection onto perpendicular direction by factor  $\frac{B_p}{B_t}$ ). For simplicity a radially constant  $\kappa_\perp$  is assumed, e.g. the anomalous heat conductivity varies with  $1/n$ .

$$\kappa_\perp \cdot \frac{d^2 k_B T_e}{dx^2} = \frac{q_\parallel}{l} \cdot \frac{2B_p}{B_t} \quad (9.1)$$

with length of SOL (ring at separatrix radius a)  $l = 2\pi a$  for 2 divertors. The parallel heat flux equations is transformed into

$$q_\parallel = -\kappa_\parallel \frac{dT_e}{dz} = -\kappa_0 \cdot T_e^{5/2} \frac{dT_e}{dz} = -\kappa_0 \cdot \frac{2}{7} \cdot \frac{dT_e^{7/2}}{dz}, \quad (9.2)$$

because

$$\frac{dT_e^{7/2}}{dT_e} = \frac{7}{2} \cdot T_e^{5/2}. \quad (9.3)$$

With

$$\frac{dT_e^{7/2}}{dz} = -\frac{T_e^{7/2}}{L} \quad (9.4)$$

one gets

$$\kappa_\perp \cdot \frac{d^2 k_B T_e}{dx^2} = \frac{2}{7} \cdot \frac{B_p}{B_t} \cdot \frac{\kappa_0}{\pi a L} \cdot T_e^{7/2}. \quad (9.5)$$

The description is completed by the boundary condition at the inner boundary

$$\kappa_\perp \cdot \frac{dk_B T_e}{dx} = \frac{P_{electrons}}{4\pi^2 a R \sqrt{\kappa}}, \quad (9.6)$$

where  $P_{electrons}$  is the power deposited within the plasma and transported across the surface ( $2\pi a \cdot 2\pi R$ ) by electrons for a plasma with elongation  $\kappa$ .

The solution shows no exponential decay: one gets a sharp drop close to the separatrix with a long tail in the SOL (see Fig. 9.1).

$$T_e(x) = 1.9 \cdot \left( \frac{\kappa_{\perp} k_B \pi a B_t L}{B_p \kappa_0} \right)^{2/5} \cdot \frac{1}{(\lambda_T + x)^{4/5}}, \quad (9.7)$$

with

$$\lambda_T = 1.26 \cdot (\kappa_{\perp} k_B)^{7/9} \cdot \left( \frac{a \pi B_t L}{B_p \kappa_0} \right)^{2/9} \cdot \left( \frac{4 \pi^2 a R}{P_{electrons}} \right)^{5/9}. \quad (9.8)$$

Therefore, evolution of experimental profiles should take into account this behaviour: definition of an exponential decay length may not be the best description. For other kinds of radial transport laws, the behaviour is similar but with slightly different dependencies.

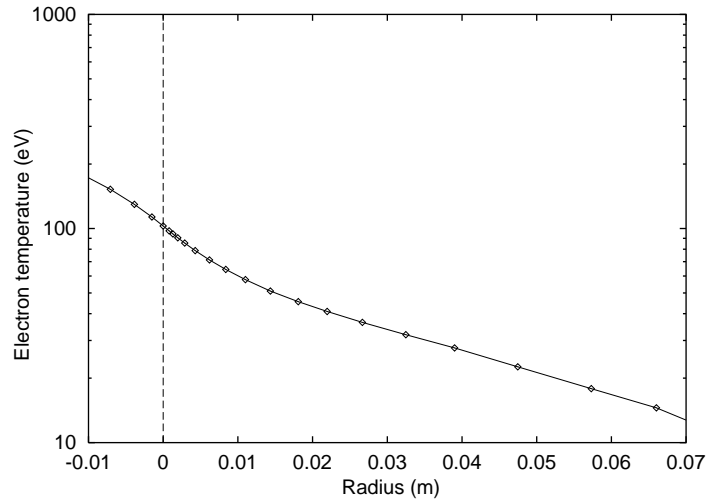


Figure 9.1.: Radial temperature midplane profiles from B2-Eirene simulations of JT-60U. As in the simple model, one gets a sharp drop close to the separatrix with a long tail in the SOL.

## 9.2. Radial midplane density profile

For the midplane density profile, the situation is more complicated. The simplest model is assuming that the radial variation of the (anomalous diffusive) particle flux is caused only by parallel losses.

$$D_{\perp} \frac{d^2 n_e}{dx^2} = \frac{n_e}{\tau_{\parallel}}, \quad (9.9)$$

where  $\tau_{\parallel}$  is a mean particle residence time in the SOL.

The solution gives an exponential decay in the SOL

$$n_e(x) = n_e(0) * \exp(-x/\sqrt{D_{\perp} \tau_{\parallel}}) \quad (9.10)$$

for  $x \geq 0$  ( $x = 0$  is the separatrix).

However, due to sources from neutrals (wall recycling and divertor leakage), and the influence of the flow pattern (flow reversal, variation of flow velocity, see discussion in the next chapter), the density profile cannot be described in this simple model (or the mean residence time entering this model would depend in a very complicated fashion on other parameters) (Fig. 9.2).

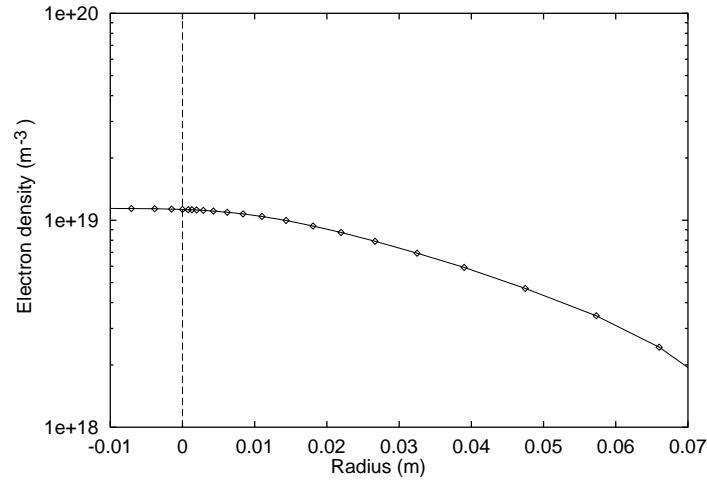


Figure 9.2.: Radial density midplane profiles from B2-Eirene simulations of JT-60U. One does not see the expected exponential decay from the simple model.



# 10. Hydrogen flow reversal, geometry effects

To improve the simple models, the effect of the divertor onto the midplane profiles has to be included. This will lead to the discussion of the global hydrogen flow pattern and effects of different divertor geometries.

## 10.1. Hydrogen flow reversal

Detachment physics (for clean plasmas) is also influenced and characterised by specific flow patterns. Here, especially the appearance of flow reversal near the separatrix for very high recycling conditions has to be discussed. The onset of this effect is strongly dependent on divertor geometry including baffles to the main chamber as will be shown soon.

For flow reversal, a flow pattern is created, where the flow out of the divertor near the separatrix is followed by outward cross-field diffusion and flow back towards the divertor further out in the SOL, e.g. a kind of convective cell is built. The divertor geometry is influencing the flow reversal by directing the recycling gas in the direction perpendicular to the plate, e.g. enhancing or reducing ionization near the separatrix. If ionization sources downstream are stronger than the flux supplied by upstream (midplane) conditions, flow reversal sets in (Fig. 10.1). Flow reversal is therefore characterised by the adaptation of the upstream pressure profile (dominated by anomalous radial transport) and the divertor pressure profile (determined by ionization and CX neutral losses).

## 10.2. Geometry effects

The target plate geometry strongly influences the plasma profiles by controlling the neutral recycling pattern, which in turn has a strong effect on the symmetry and stability of the divertor plasma and finally on the whole edge region. The design of the new divertor configuration for ASDEX-Upgrade (see Fig. 10.2) is a good example of this optimization strategy.

### 10.2.1. Radial plasma profile

The radial plasma profile is a consequence of two major contributions (which are coupled self-consistently, see e.g. a radially continuous two-chamber model [48]). In the midplane, the plasma particle transport is dominated by the anomalous radial diffusion coefficient



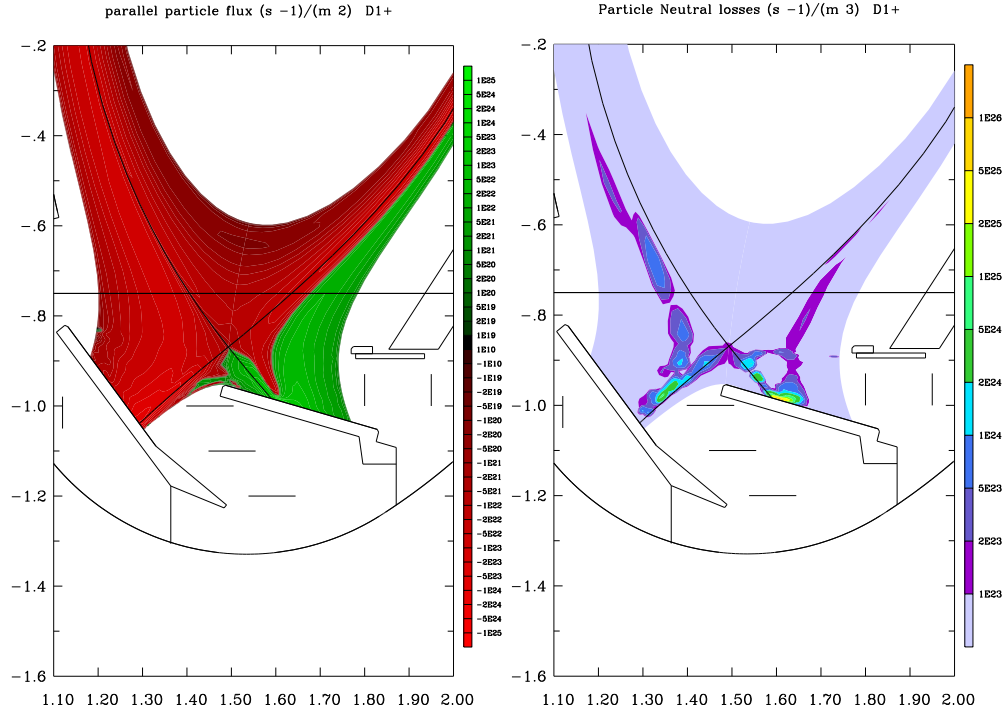


Figure 10.1.: Contours of parallel particle flux (left) and ionization sources from neutrals (right) for ASDEX-Upgrade Divertor I from B2-Eirene. In the outer divertor leg close to the separatrix flow reversal is observed, starting in the region with very large ionization sources.

(a number of the order of  $1 \text{ m}^2/\text{s}$ ), and a possible drift velocity. This plasma drift velocity has to be of the order of the radial diffusion coefficient divided by the SOL width giving a typical value of several  $10 \text{ m/s}$  to become important. The second major contribution is the neutral transport in the divertor, which can also be interpreted as a classical diffusion-drift-type process. The neutrals are created at the plate and do a random walk with a diffusion coefficient proportional to neutral thermal velocity times the mean free path. Neutrals are reflected perpendicular to the plate with a cosine-like distribution. Therefore, the target plate geometry acts as a radial drift term being proportional to the neutral thermal velocity times the sine of the target plate inclination.

For high recycling conditions the neutral diffusion coefficient becomes small. However, the target geometry has still a strong effect through its influence on the neutral drift velocity term. For highly inclined target plates (where the sine factor is close to 1), this drift velocity must only be larger than several  $\text{m/s}$  to be comparable to the plasma diffusion term, a condition that is usually fulfilled. Therefore, a strong profile effect for the density profile (and consequently for the temperature profile) is expected from a change of the target inclination, if other transport terms like plasma radial drift velocities or cross field transport driven by main chamber recycling (if e.g. toroidal gaps exist) are small.

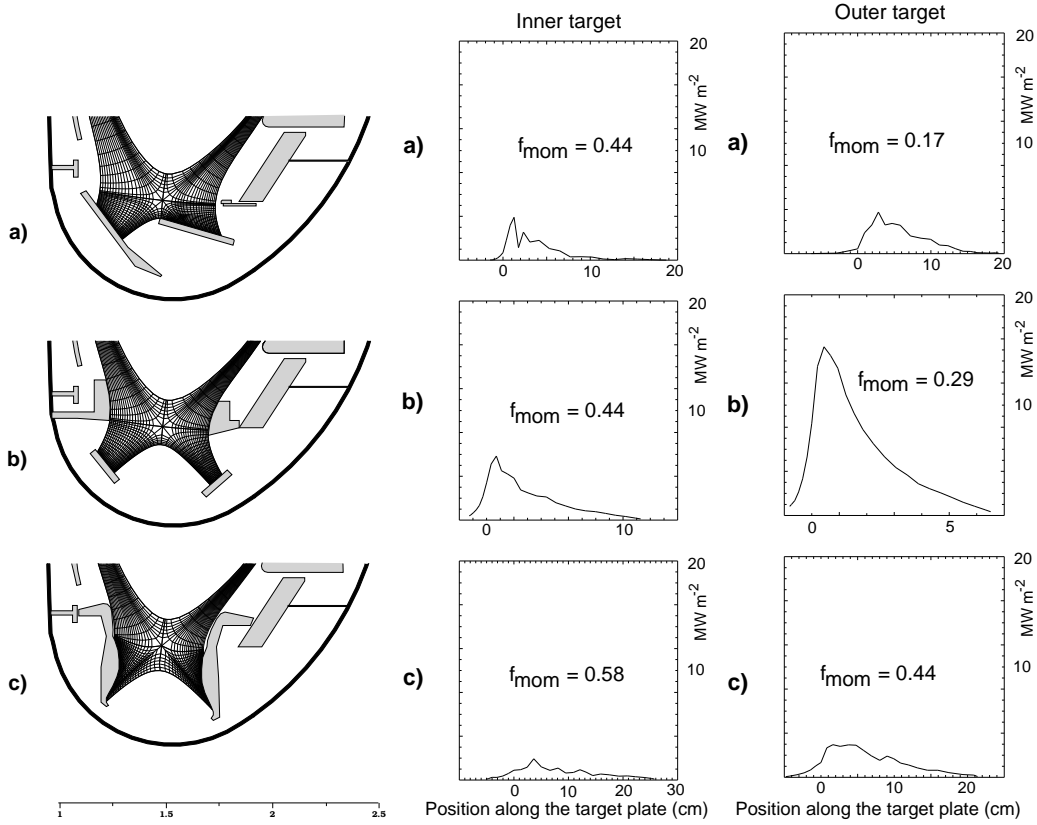


Figure 10.2.: Computational grids, target plate configurations (left column), inner target (middle column) and outer target (right column) total parallel energy flux density for a: Divertor I, b: Gasbag and c: Lyra. Total input power is 7.5MW and separatrix density is  $1.0 \cdot 10^{20} m^{-3}$ .  $f_{mom}$  is the integral momentum loss factor (see definition in the text) [47].

### 10.2.2. Detachment properties

Using B2-Eirene, the existing Divertor I is compared with the Lyra and gas bag configurations concerning their detachment properties. As a quantitative measure for detachment the integral momentum loss factor from midplane to target plate is used. It is calculated from the flux integrated ( $d\psi$ ) pressure profiles at the target plate and midplane:

$$f_{mom} = 1 - \frac{\int_{targetplate} p \cdot (1 + \gamma M^2) d\psi}{\int_{midplane} p \cdot (1 + \gamma M^2) d\psi}. \quad (10.1)$$

In this integral momentum loss factor ( $f_{mom} = 0$  means no momentum loss,  $f_{mom}$  values close to 1 means getting close to complete detachment), the effect of the acceleration at the sheath entrance appears as the factor  $\gamma M^2$  ( $\gamma$ = adiabatic coefficient; in this case 1;  $M$ =Mach number). For standard conditions (midplane  $M$  practically zero, target plate  $M = 1$ ) this results in an additional factor of 0.5 for the pressure drop.

For Divertor I, the outer divertor plate reflects the neutrals away from the energy-carrying zone close to the separatrix and thus blocks indirectly the detachment (see Fig. 10.3).

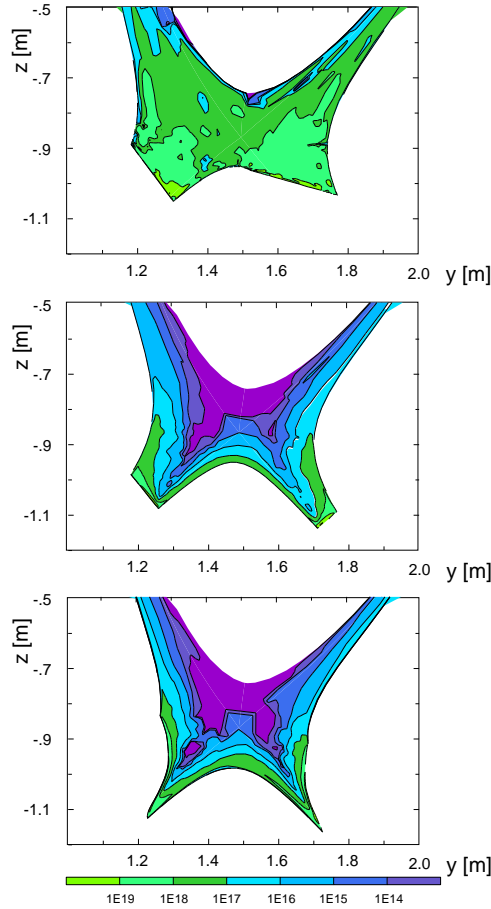


Figure 10.3.: Atomic density contours for Divertor I (top), gas bag (middle) and Lyra (bottom). Neutrals tend to be reflected perpendicular to the plates. Therefore, for Divertor I the neutral density in the outer divertor is enhanced in the outer SOL away from the separatrix, for the Gasbag it is very homogeneous and for the Lyra the neutral density in the outer divertor is enhanced close to the separatrix [27].

Therefore, Divertor I detaches strongly asymmetrically (preferentially on the inner divertor:  $f_{mom}^{inner} = 0.44$ ,  $f_{mom}^{outer} = 0.17$ , Fig. 10.2). Nevertheless, the power load on the outer target plate is reduced by the large flux expansion close to the X-point. The gas bag is already more symmetric ( $f_{mom}^{inner} = 0.44$ ,  $f_{mom}^{outer} = 0.29$ , Figs. 10.3 and 10.2), but has severe problems with power loadings in scenarios without additional external impurities — its perpendicular plates give maximum power loadings. The Lyra has, for the same density conditions, the largest and most symmetric momentum losses and lowest power loads ( $f_{mom}^{inner} = 0.58$ ,  $f_{mom}^{outer} = 0.44$  (Figs. 10.3 and 10.2), because it reflects the neutrals towards the high energy zone at the separatrix and is strongly tilted. Therefore, concerning the operational safety of the machine, it offers the best configuration to start with, allowing for scenarios without external impurities and the largest heating power.

### 10.2.3. Main chamber baffling

An additional geometry effect comes in through the main chamber baffling. Main chamber baffling is necessary to minimize the neutral leakage from the divertor to the main chamber. This is important, because experimentally a deterioration of high confinement for higher neutral fluxes in the main chamber is observed. Additionally, CX sputtering in the main chamber can be a concern (not for ASDEX-Upgrade, but probably for ITER). Divertor I of ASDEX-Upgrade is a very open gas-bag like divertor, where the neutrals can penetrate into the whole divertor fan: the baffling towards the main chamber is poor. It has only a small additional pumping baffle, which is not very efficient for the baffling of hydrogen neutrals. However, it gets quite important for the understanding of the compression of neon and helium (see discussion later). Lyra (and gas bag) have a much better reduction of divertor neutral leakage due to their tight baffling up to the X-point. The leakage is reduced by 2 to 3 orders of magnitude for attached or partially detached conditions (Fig. 10.4). Therefore, in contrast to Divertor I where main chamber recycling and divertor leakage are equal to each other, now the main chamber recycling is dominant. For the engineering realisation, one has to avoid toroidal gaps to the vessel which would produce indirect main chamber leakage.

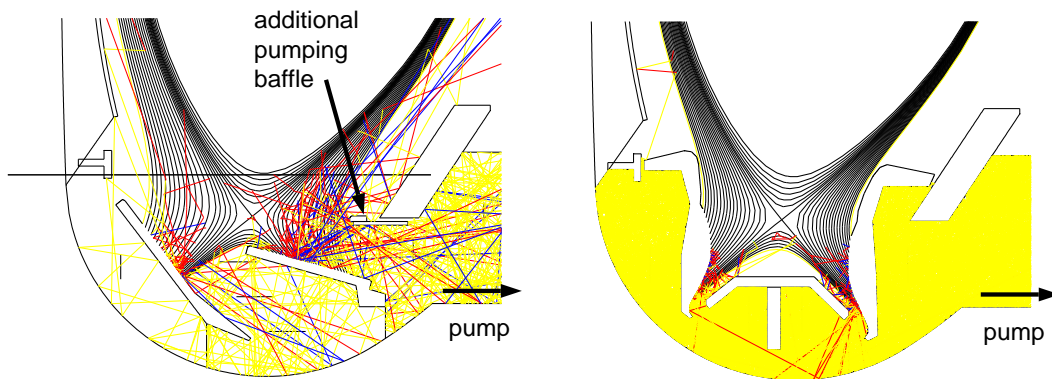


Figure 10.4.: 100 neutral trajectories for the Divertor I and the final Lyra configuration for deuterium atoms (red) and molecules (yellow). 50 particles are started from each plate. The midplane conditions were comparable for both cases: 7 MW input power, separatrix density of  $3 \cdot 10^{19} m^{-3}$ , similar amount of carbon and neon impurities [47].

### 10.2.4. Pumping properties

After having fixed the target geometry and main chamber baffling, the final step is the optimisation of the private flux baffles.

By changing the private flux baffling (Fig. 10.5), the neutral recirculation pattern — especially the neutral penetration to the X-point — is strongly affected and one is even able to suppress flow reversal zones in the hydrogenic flow pattern (Fig. 10.5). As discussed before, these occur usually for high recycling conditions due to strong local ionisation sources, resulting in incompatible divertor vs. midplane profiles and forcing backflow. This suppression of flow reversal may also lead to better impurity entrainment (to be

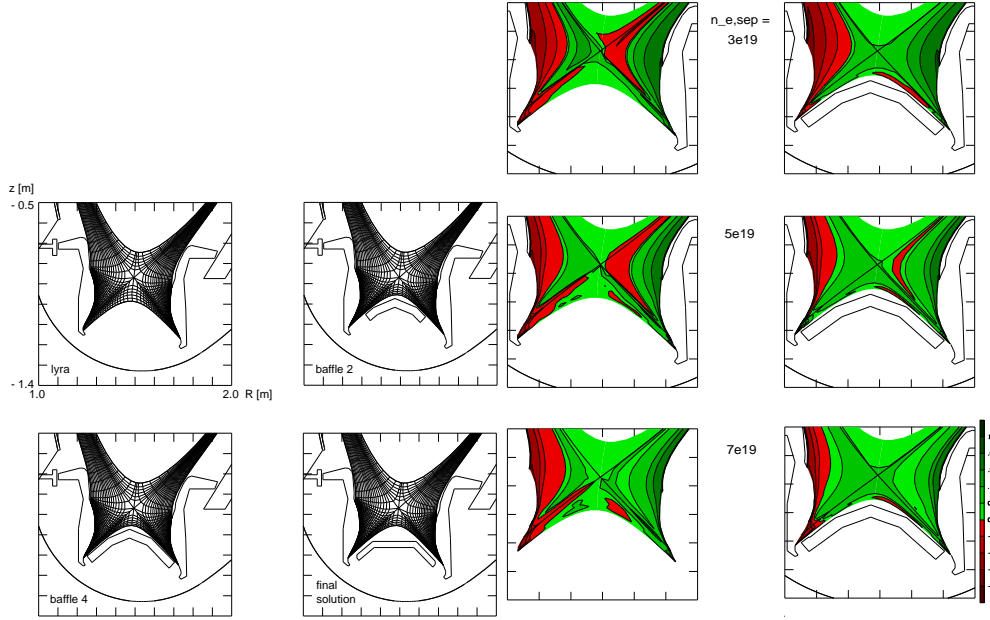


Figure 10.5.: Left: three different private flux baffle Lyra configurations used for pumping scan studies plus the final configuration [47].

Right: Comparison of flow patterns (contours of parallel particle fluxes) for open (left) and closed (right) Lyra configurations for  $n_{e,sep} = 3 \cdot 10^{19} m^{-3}$  (top),  $5 \cdot 10^{19} m^{-3}$  (middle) and  $7 \cdot 10^{19} m^{-3}$  (bottom). For the open Lyra configuration flow reversal appears in the outer divertor, which is absent in the closed configuration.

tested, see later discussion). Density scans for different private flux baffle configurations show little change of detachment properties, but much higher neutral divertor fluxes and therefore better pumping in the case of optimised baffle length (Baffle 4, Fig. 10.6). This can be easily understood, because by closing most of the private flux region with baffles the competing process of the (very effective) pumping (ionisation) by the plasma is strongly reduced. The distance of the baffle to the plate has to be long enough so that the hydrogen neutrals are still able to escape into the private flux area.

The detachment properties are not changed, because they are more determined by quasi-1D balances along the fieldlines close to the plate, which are not affected strongly by these private flux baffles.

For the realisation of the final geometry, the optimised baffle length (baffle 4) was used, however the top part (close to the X-point) no longer follows the field line geometry, but is horizontal. This way, it is possible in the experiments to use this private flux baffle (at least transiently or for reduced input power) as a target plate, a necessity for advanced scenarios with high triangularities. The flexibility for testing different neutral recirculations is still achieved by possible holes in the baffle structure for neutral recirculation or additional septum structures for separation of the inner and outer divertors. Also, one can move the plasma separatrix away from the baffle to do experimental scans with quite different private flux divertor baffling: an effective baffle along a fieldline has to be 3 to 4 mean free paths of the neutrals; opening a gap drastically reduces its baffling effect.

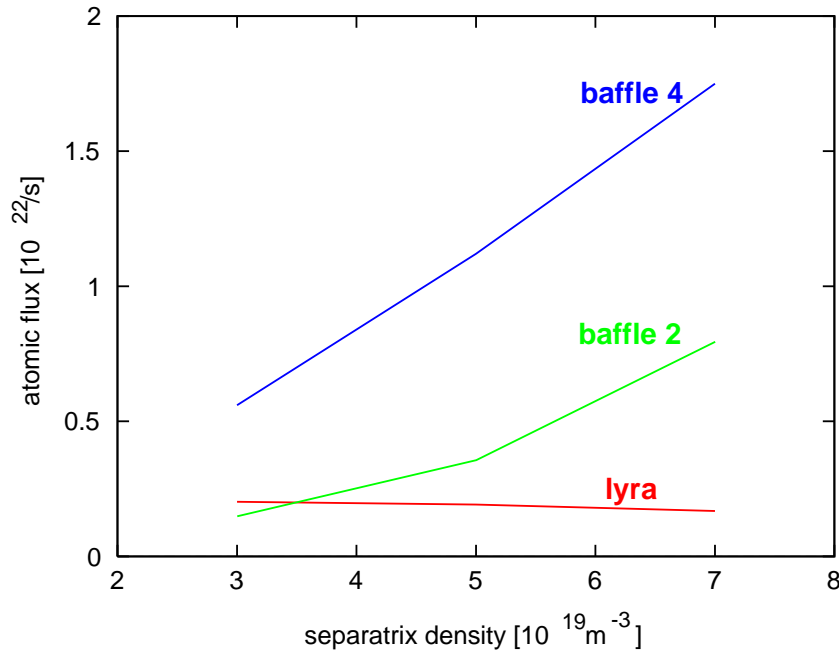


Figure 10.6.: B2-Eirene results for pumping flux vs. separatrix density for three different Lyra configurations (Lyra, Baffle2, Baffle4). Input power is 5 MW [47].

### 10.2.5. Geometry effects on volume recombination

To complete the discussion of geometry effects (for pure plasmas), one has to mention also the effect on onset, location and strength of volume recombination. This will be done for two JET divertor configurations (MARK I and II) [49]. Mark I was a fairly open unbaffled divertor, whereas Mark II operated on the bottom plate and because of side baffles was pretty good closed (Fig. 10.7).

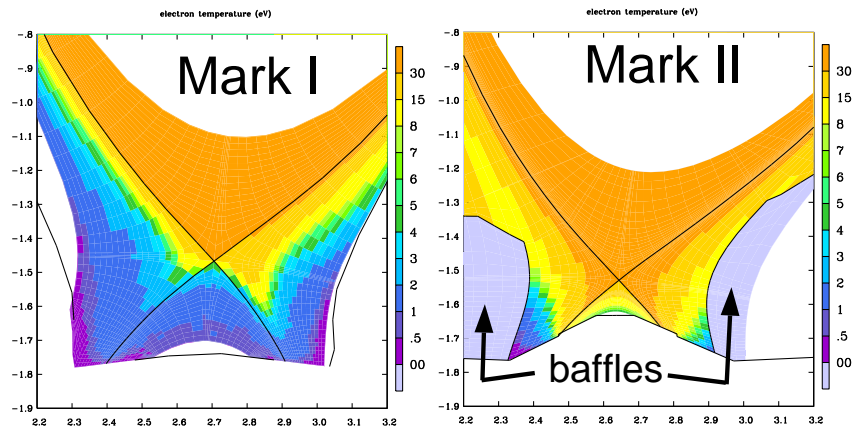


Figure 10.7.: B2-Eirene results for electron temperature contours of Mark I and Mark II configurations.

Doing with B2-Eirene a separatrix density scan for a fixed input power, one gets an earlier detachment of the MARK-II configuration compared to the MARK-I geometry as seen in

the experiment (Fig. 10.8).

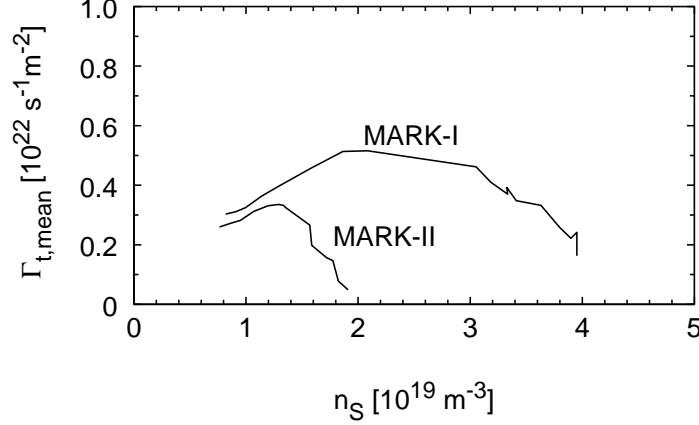


Figure 10.8.: B2-Eirene results for the mean inner target particle flux as a function of upstream separatrix density  $n_S$ .

The reason for this is the different onset of volume recombination in the two geometries.

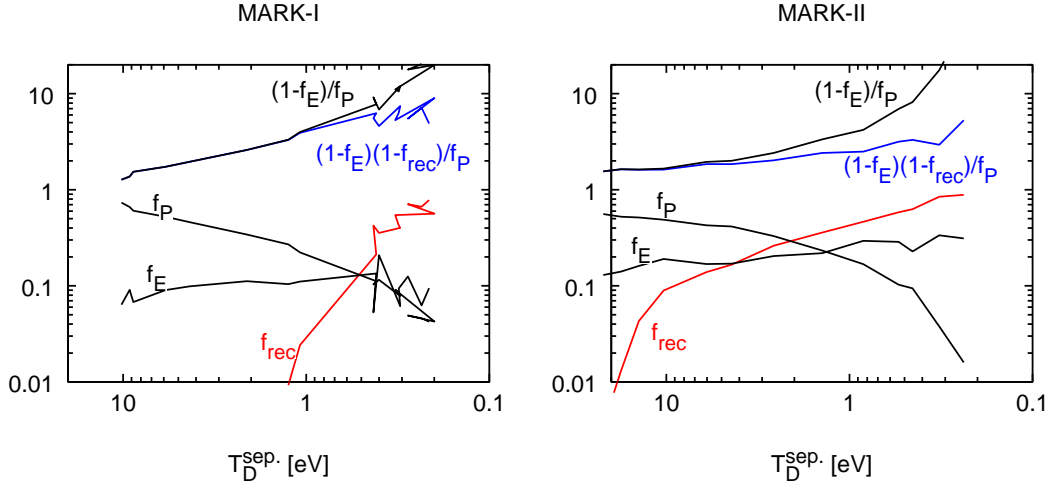


Figure 10.9.: B2-Eirene results for the pressure drop along B ( $f_P$ ), fraction of power into the gas target lost due to ion-neutral interactions, e.g. CX ( $f_E$ ) and ration of recombination to ionization rate ( $f_{\text{rec}}$ ) for MARK-I and II versus divertor separatrix temperature [49].

Due to the tilt of the target plates in Mark II one gets an much earlier onset of volume recombination (in the outer SOL away from the separatrix) compared with Mark I (Fig. 10.9).

The effect can be understood by doing a gedanken-experiment. Starting from an orthogonal plate one drives the system just to the onset of volume recombination (which then also starts in this configuration in the outer SOL away from the separatrix). Now tilting the plate into the Mark II orientation one gets a much larger recombination zone in this outer part. This is due to the fact that the temperature profile is pinned at the separatrix

(this is the hottest place) and in the outer SOL already for the orthogonal plate one has conditions of about 1 eV or lower (for the onset of strong volume recombination). The tilting therefore just increases this low temperature (and high density) region and by this pushes the recombination. A proof of this simple picture is found by overlaying the contours of the recombination sinks for Mark I and II for similar upstream conditions keeping the separatrix position fixed for this overlay (Fig. 10.10).

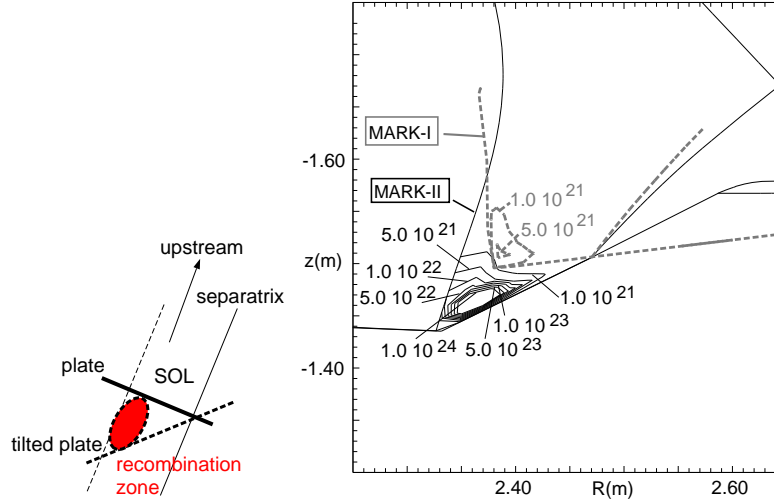


Figure 10.10.: Sketch of the geometry effect responsible for the earlier onset of volume recombination in Mark II (left). Overlay of recombination sinks per volume for Mark I and II for similar upstream conditions keeping the separatrix position fixed (right) [49].

The difference in the two divertor geometries for Mark I and II results then also in quite different changes of the ion saturation profiles during detachment (Fig. 10.11). In Mark I detachment appears as a quite homogenous drop of the ion saturation current

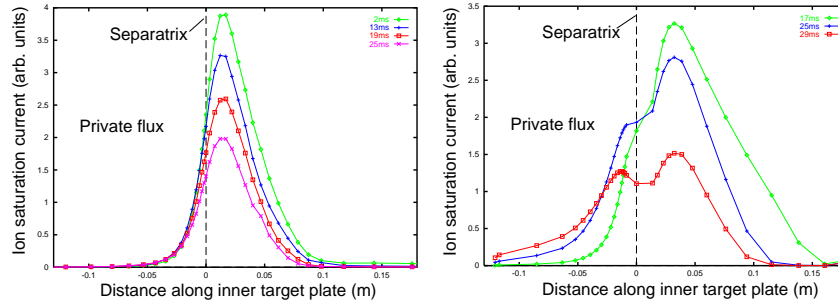


Figure 10.11.: Development of inner ion saturation current profiles for Mark I and II geometry during the detachment process.

over the whole profile, maybe even starting earlier at the separatrix. In contrast, the Mark II configuration is characterized by an earlier detachment and a larger drop of the ion saturation current in the outer SOL away from the separatrix. Also, the strong volume recombination can produce additional structures (especially in the private flux



region). These differences in behaviour were predicted by modelling and confirmed by experimental measurements. The same holds for the observation that, due to the strong volume recombination source of neutrals in the corner in Mark II, an anomalous high  $H_\alpha$  emission is observed there.

# 11. Time-dependent phenomena: ELMs

Up to now, only stationary situations have been discussed. In this chapter, the discussion of time-dependent phenomena (so-called ELMs) will be done for pure plasmas. ELMs (Edge Localised Modes) appear in H-mode and periodically expel particles and energy from a region inside the separatrix (of the order of several cm). Type I ELMs are experimentally observed as large, regular, isolated  $H_\alpha$  spikes. Their frequency increases with heating power and they are probably associated with an ideal ballooning instability (critical pressure gradient  $\alpha_{crit}$ ). This instability process (under the assumption that the transport in this unstable region is enhanced from  $D$  to a larger value  $\tilde{D}$ ) creates periodically a loss region (the ELM layer) [50, 51]. This kind of avalanche transport stops at the radial position, where the profile gets below the critical gradient condition (Fig. 11.1).

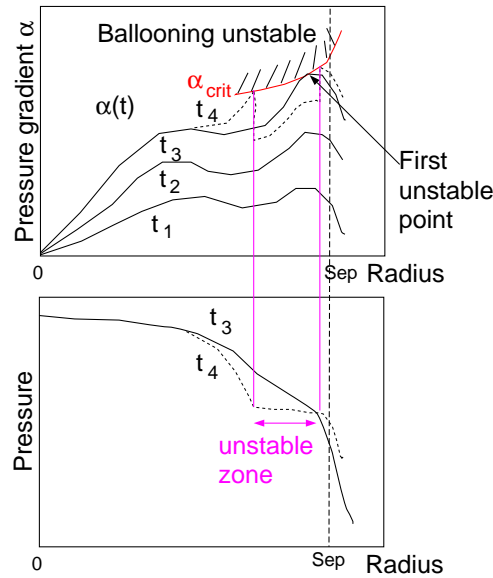


Figure 11.1.: Sketch of pressure gradient (top) and pressure (bottom) for type I ELMs. As soon as the pressure gradient reaches a critical value (MHD ballooning instability), the ELM starts. This kind of avalanche transport stops at the radial position, where the profile gets below the critical gradient condition (H. de Blank).

To analyse the effect of ELMs on the SOL and divertor properties, different time-scales have to be considered.

The time scales involved in ELMs are the characteristic ELM time scales for the active

ELM perturbation of about  $100 \mu s$  with a fine structure in the  $10 \mu s$  range. During this active phase, the hot core plasma gets in contact with the divertor (maybe due to ergodization of parts of the main plasma region). This ELM event results in enhanced transport (for 0.1 to 1 ms) and has a repetition time of 1 up to some 10 ms. These times have to be compared with parallel plasma transport times of electron heat conduction by tail electrons (0.001 to 0.01 ms) and for ions (0.1 to 1 ms). In addition, the flight times of neutrals have to be considered: atoms are flying typically at 10 m per ms. For a divertor dimension of about 1 m, this defines a crossing time of 0.1 ms. Molecules are about a factor of 10 slower than atoms, this gives typical flight times of some ms. Comparing these different time scales, it is evident that time-dependent modelling (not only for the plasma, but also for the neutrals) is necessary.

In B2-Eirene, an ELM is modelled by transient enhanced radial transport in the edge region. The transport coefficients are momentarily increased from equilibrium values (about  $0.1 m^2/s$ ) to large values ( $5 m^2/s$ ), repeated according to the measured ELM repetition time. This was also used in 1D (radial) modelling of ELMs, including ELMs triggered by pellets [52]. As a consequence for ITER one might use pellets as a tool to control the ELM frequency. Results of the modelling are compared with thermography profiles on divertor plates for ASDEX-Upgrade (Fig. 11.2). Best agreement of modelling

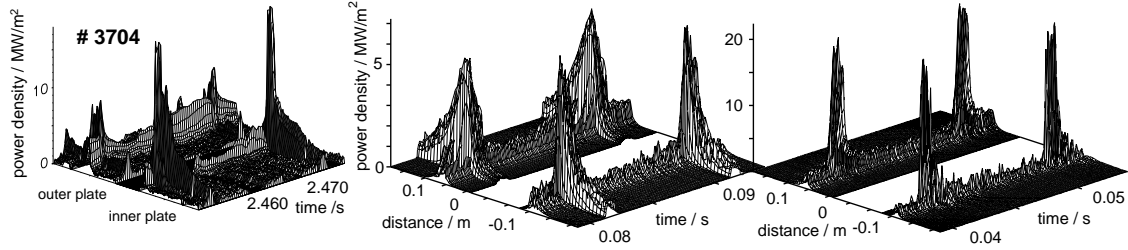


Figure 11.2.: Target power load as measured by thermography (left side), modelled with B2-Eirene with enhanced transport in the core and SOL (middle) and enhanced transport just in the core (right side).

with experimental thermography profiles on divertor profiles is obtained if radial particle diffusion coefficient as well as radial heat conduction coefficients are enhanced during the ELM [53]. The modelling results also indicate that the ELM effect of enhanced transport extends over the core region into the region of open field lines in the SOL. This result is consistent with calculated electron thermal diffusivities using the Rochester and Rosenbluth formula from fitted filamentary currents following field lines to match the measured magnetic perturbations picked up by Mirnov coils [54]. A problem still exists with the in-out asymmetry of the target plate power load during the ELM, which is much stronger in the experiment compared to the modelling. Applying instead of the standard model of radial diffusion according to the radial distance during the ELM a diffusion law based on the magnetic flux space overcomes this problem. As a consequence of this description, the turbulent transport during the ELM is no longer larger on the outer side than on the inner side (effect of the Shafranov shift), but is equal.

The experimental signatures of  $H_\alpha$  (Fig. 11.3), Langmuir probe and spectroscopy ELM resolved measurements are reproduced very well [55].

The global features are characterized by a fast response due to the fast change of the target

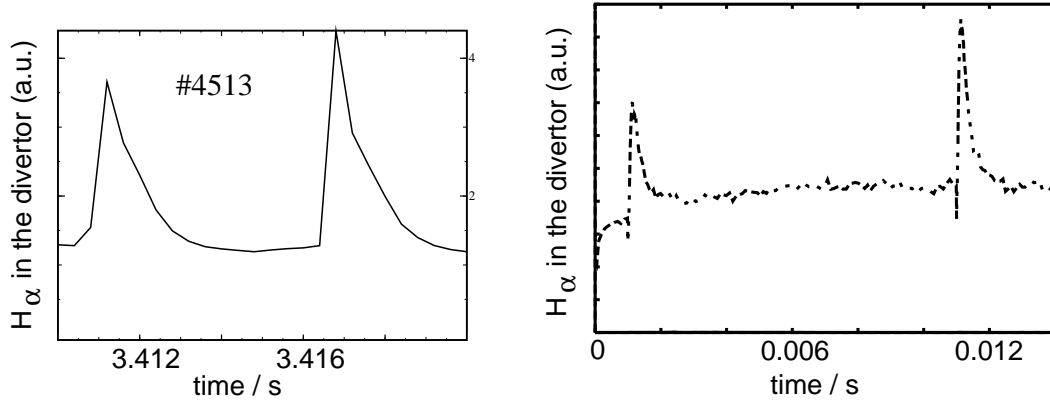


Figure 11.3.:  $H_\alpha$  in the divertor as measured (left side) and modelled (right side)

particle flux. This is driven by the electron heat conduction which changes the pressure in front of the plate and by this then the recycling. Results from kinetic modelling [56, 57] show that in this phase the distribution function is unable to equilibrate. One gets an elevated tail and a much larger heat conduction coefficient (factor of 10 compared with the Maxwellian value) in the region between the heat front and the target. At the midplane, the distribution function falls below Maxwellian, leading to a decrease in the heat conduction coefficient of about a factor of 2. The second feature is an asymmetric and slower decay, which is due to the ion particle and neutral transport.

2D divertor Langmuir probe measurements in ASDEX-Upgrade at the entrance of the outer divertor show deuterium backflow from the divertor into the main chamber during ELMs (Fig. 11.4).

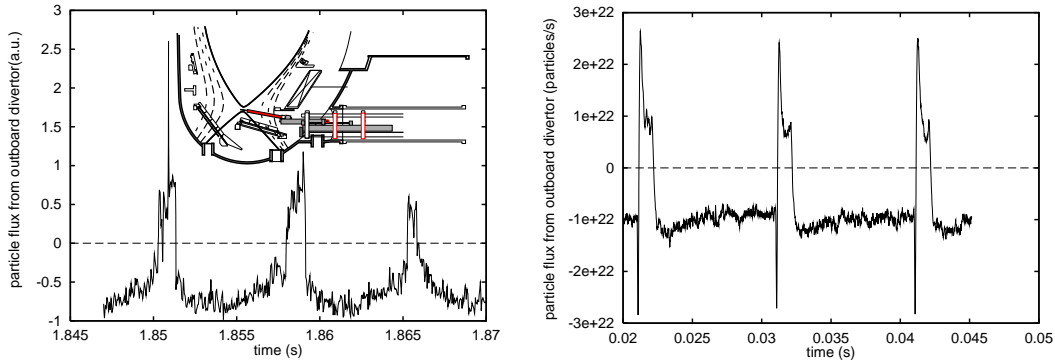


Figure 11.4.: Particle fluxes at the outer divertor entrance as measured with a movable langmuir probe (left side) and modelled (right side). Positive fluxes are fluxes going from the divertor into the main chamber [58].

The same signature shows up in the simulation. The enhanced pressure in front of the plate drives flow reversal as the system tries to achieve pressure equilibration. In addition, the neutral reservoir was ionized by the fast response of the target particle flux, which is also driving this backflow.

A special phenomenon is the appearance of negative ELMs for detached divertor con-

ditions. They are caused by the transition from recombining to ionising plasmas in the detached divertor. This can reduce the  $H_\alpha$  signals in the divertor, because the number of emitted photons per ionization event decreases strongly for temperatures above 1 eV and below 5 eV (Fig. 11.5). Therefore, a heating of a detached divertor results in a decrease of the  $H_\alpha$  signals in this temperature range. In this regime, the heating mechanism is the convective heat transport into the divertor, which happens on a much slower timescale (ion convection) than the very fast timescale of electron heat conduction. This extends considerably the time, where the ELM produces changes in the heat load for the detached divertor leg (Fig. 11.6).

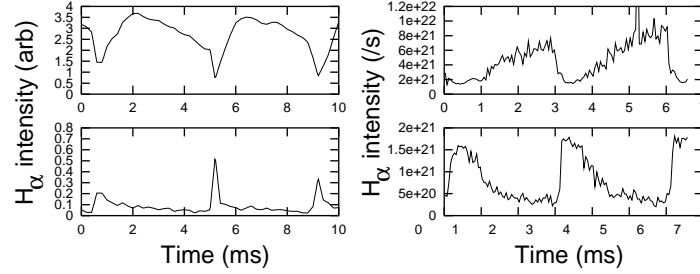


Figure 11.5.:  $H_\alpha$  signals for line-of-sights into the inner (left top figure) and outer (left bottom) divertor target plate as measured and as modelled (right) for three ELMs as a function of time. The detached inner divertor shows the typical signature of a negative ELM, whereas the hotter attached outer divertor has the standard signature.

10193 comparison, 20MW, ELMing H-mode

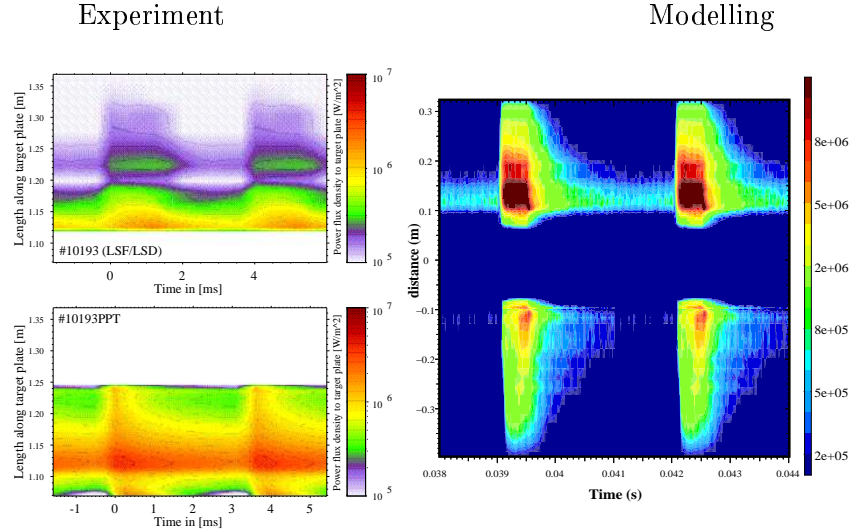


Figure 11.6.: Power flux density of the inner (left top) and outer (left bottom) divertor target plate as measured with thermography and as modelled (right) for two ELMs as a function of time.

As was shown before, type I ELMs produce additional power loading problems of the divertor due to the ELM bursts. These burn through any cold divertor necessary for safe

---

operation. Therefore, scenarios have to be studied with tolerable ELMs. This requires the use of extrinsic impurities. Therefore, the influence of impurities will be studied in the following chapter.



## 12. Impurity physics: sputtering, radiation losses

After the discussion of the clean plasma the effect of impurities has to be included in the description of the SOL. For the understanding of impurity physics in the SOL, one needs a rather complex combination of different aspects. The impurity production process has to be understood, then the effects of impurities in terms of radiation losses have to be included, and finally the impurity transport is necessary. In the following, this will be done with rising complexity starting with simple estimates and an improved 2-point model, analysing then the detailed parallel force balance and the flow pattern of impurities. This is then the basis for the discussion of impurity compression and radiation instabilities.

### 12.1. Impurity production

The radiation losses by impurities are necessary for relaxing the heat exhaust problem by spreading the heat deposition onto a larger surface by radiation. However, radiation losses in the main chamber can be a problem, because a minimum amount of power is necessary in order to sustain sufficient confinement (H-mode threshold) and one has to avoid too large fusion power losses to sustain ignition. Therefore, a scenario is needed where impurity losses (power as well as position) can be (feedback) controlled. Intrinsic impurities (C,W,Be,..) are produced through erosion (ions, CX neutrals, hot spots, arcs) and melting (disruptions). The physical sputtering process is a binary collision between surface or bulk atoms and impinging ions (after acceleration in the sheath) or neutrals. It is very well described by this binary collision model (see the discussion of neutral transport, where results of the Monte Carlo code TRIM also show sputtering yields, Fig. 6.3). Due to the binary collisions, one gets a threshold energy for the impinging particle below which the sputtering yield drops very fast to practically zero. This threshold is therefore higher for heavier particles. Seeded impurities for controlled impurity losses have to be recycling impurities (noble gases, e.g. Ne, Ar, Kr), because non-recycling impurities can not be pumped for feedback control but stick to the walls. For the choice of target (and main chamber) materials, one has several candidates representing either low Z (e.g. Be, C) or high Z (e.g. Mo, W) materials, which both have different advantages and disadvantages. Carbon has a very high thermal conductivity, high melting point and low vapour pressure. Concerning the sputtering by ions (after acceleration in the sheath) and high energy CX neutrals, tungsten has much lower effective sputtering yields than beryllium or carbon (Fig. 12.1). Beryllium has the problem of a low melting point and high toxicity.

The reason for the strongly reduced effective sputtering yield of tungsten is due to the advantageous ratio of ionization-length to ion gyro-radius [59] leading to prompt redepo-



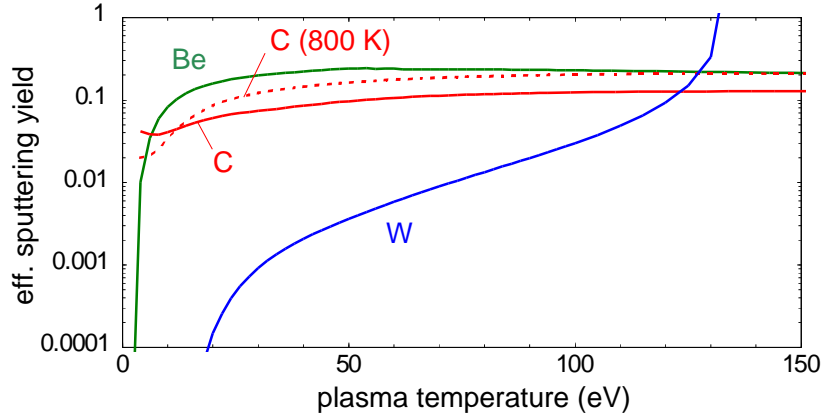


Figure 12.1.: Effective sputtering yields for room temperature carbon, carbon at 800 K, beryllium and tungsten as a function of plasma temperature (J. Roth).

sition within the first ion gyro-radius for tungsten (Fig. 12.2).

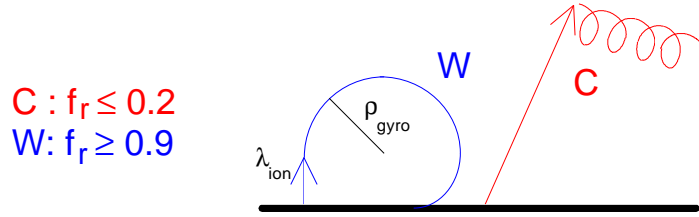


Figure 12.2.: Sketch of trajectories for carbon and tungsten, showing the large amount of promptly redeposited material  $f_r$  for tungsten (D. Naujoks)

The radiation losses for the low  $Z$  elements are dominated for temperatures below 100 eV by line radiation losses and above several keV by bremsstrahlung. Due to their radiation characteristics, low  $Z$  elements will contribute more to SOL and divertor radiation (temperatures below 100 eV), whereas with higher  $Z$  more and more radiation will move to the confinement region of closed field lines (Fig. 12.3). For tungsten, the radiation losses are 3 orders of magnitude larger than for carbon or beryllium. Therefore, one needs nearly perfect divertor retention for tungsten in contrast to carbon.

This gives a very strict limit for main chamber concentration ( $10^{-5}$ ) for ITER, and up to now it is not clear whether this is achievable.

For carbon one has a different problem to overcome: even at low plasma temperatures, where physical sputtering switches off, sputtering of carbon is still continuing [60] (Fig. 12.4).

The reason is chemical sputtering producing methane, which finally breaks up into carbon ions [63]. This process is a surface effect and has a strong temperature dependence with a maximum yield at about 600 K, characterised by the change of the carbon bonds at a sur-

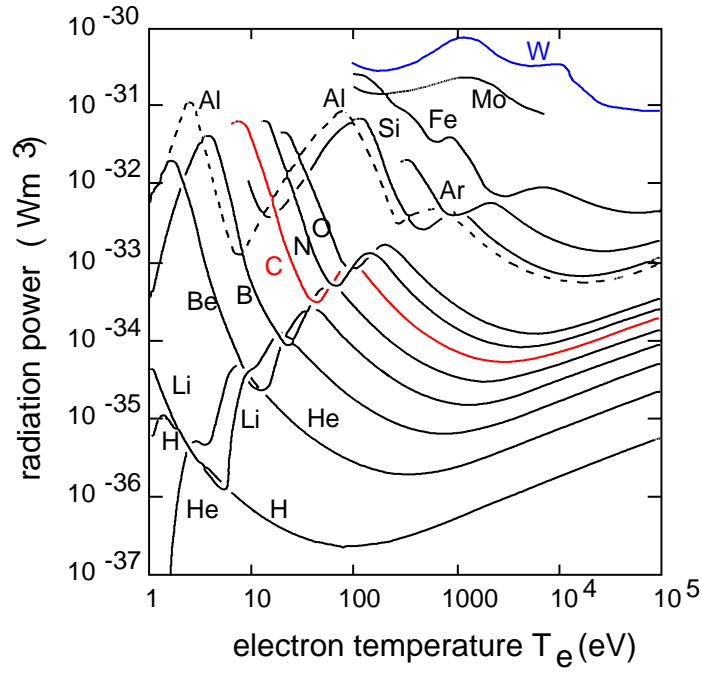


Figure 12.3.: Radiation power  $\frac{P_{rad}}{Vol \cdot n_e \cdot n_{imp}}$  as a function of electron temperature (D. Post).

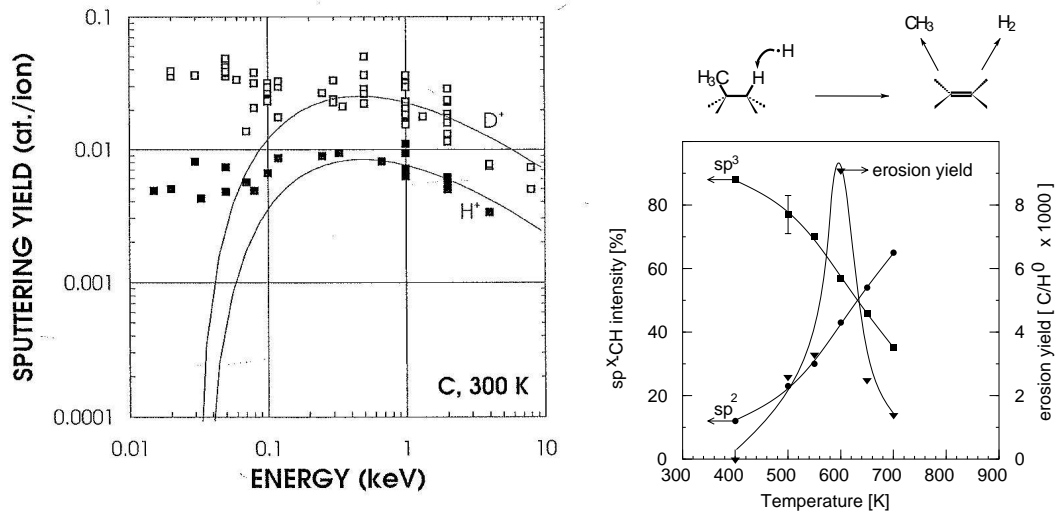


Figure 12.4.: Measured carbon sputtering yields for deuterium and hydrogen ions as a function of ion energy for room temperature conditions. The contribution from physical sputtering is shown as lines dropping at low energies, whereas the measurements stay at much higher values (left) [61]. Measured carbon erosion yield as a function of temperature. The strong temperature dependence with a maximum yield at about 600 K is characterized by the change of the carbon bonds at a surface from an  $sp^3$  to  $sp^2$  type. [62].

face from an  $sp^3$  to  $sp^2$  type (Fig. 12.4). This process gives large erosion rates for ITER, where the major problem for a reliable prediction is the experimentally very uncertain flux dependence of chemical sputtering yield. Possibilities to overcome this problem for carbon are proposed and tested by using titan (in small concentration) for suppression of the chemical erosion.

A more detailed discussion of the materials aspects for fusion, especially sputtering can be found in [64, 65, 66, 61].

## 12.2. Radiation loss on closed field lines

To account for the effect of impurities, the simplest model is to try to estimate their radiation losses. For the main chamber (on closed fieldlines), this was done in [67] by starting with the radial heat flow

$$q_{\perp} = \kappa_{\perp} \frac{\partial T}{\partial r}. \quad (12.1)$$

The radiation loss of impurity Z (radiation function  $L_Z(T_e)$ ) has to equal the divergence of  $q_{\perp}$ :

$$\frac{\partial q_{\perp}}{\partial r} = -n_e n_Z L_Z(T_e). \quad (12.2)$$

This gives for impurity concentration  $f_Z = n_Z/n_e$

$$q_{\perp} \frac{\partial q_{\perp}}{\partial r} = -n_e^2 f_Z L_Z(T_e) \kappa_{\perp} \frac{\partial T}{\partial r}. \quad (12.3)$$

Integration in the radial direction results in:

$$q_{\perp}^2 \approx 2 \int_0^{T_c} n_e^2 f_Z L_Z(T_e) \kappa_{\perp} dT_e. \quad (12.4)$$

To apply this formula the radiation function  $L_Z(T_e)$  has to be known. For this, the steady state balance of ionisation stage Z has to be evaluated

$$n_e n_{Z-1} S_{Z-1} - n_e n_Z S_Z + n_e n_{Z+1} \alpha_{Z+1} - n_e n_Z \alpha_Z - n_Z / \tau_Z = 0, \quad (12.5)$$

with ionisation rates  $S$  and recombination rates  $\alpha$ .

$n_Z$  is the ion density of the ground states and any contributions from the population of excited states are accommodated by the use of collisional radiative coefficients (temperature and density dependence). The time  $\tau_Z$  is the residence time of the ions in the plasma. If this transport term can be neglected (core region), one gets the coronal equilibrium. If the effect of collisions onto the radiative coefficients are neglected (only temperature dependence), this gives:

$$n_{Z+1}/n_Z = S_Z(T_e)/\alpha_{Z+1}(T_e). \quad (12.6)$$

The population ( $n_Z / \sum n_Z$ ) of a charge state  $Z$  is substantial, when  $S_Z(T_e) \cong \alpha_{Z+1}(T_e)$  and is only determined by the dependence on electron temperature. Using this, the radiation function  $L_Z(T_e)$  can be calculated (Fig. 12.3).

For ITER, there exists a rigid  $Z_{eff}$  limit. Only  $\Delta Z_{eff} = 0.2$  is available for seed impurities, otherwise due to too strong bremsstrahlung losses it is not possible to sustain ignition [68]. This results in a fatal fraction  $f_Z$  for Be (0.14), C (0.07), Ne(0.025), Ar(0.0054). From these values, 1/3 of the fatal fraction is used, because only part of the losses will originate from one single element. Using now the planned ITER parameter  $n_e \approx 1 \cdot 10^{20} \text{ m}^{-3}$ , one gets from the radiation estimates radiation losses expressed in perpendicular heat fluxes, which are compatible with sufficient power exhaust ( $q_{\perp} \approx 0.2 - 0.5 \text{ MW/m}^2$ ) only for higher  $Z$  and at temperatures already close to or inside the separatrix (Fig. 12.5).

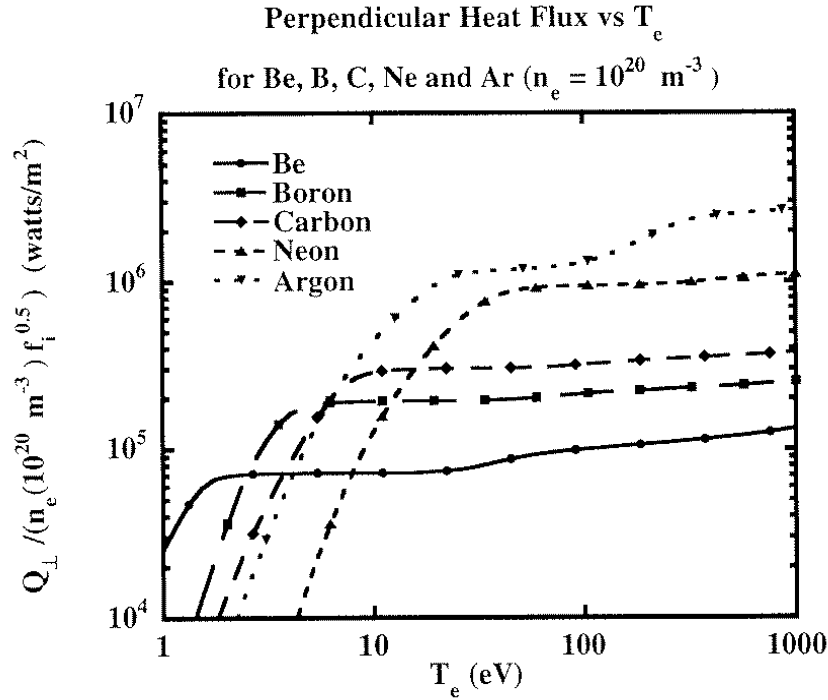


Figure 12.5.: Coronal radiation losses for ITER expressed as perpendicular heat fluxes as a function of electron temperature for 1/3 of the fatal fraction for Be, B, C, Ne and Ar (see text, D. Post)

This scenario is probably unrealistic, because for keeping a good confinement a minimum power flux crossing the separatrix seems to be necessary (H-mode power threshold predictions for ITER are between 70 and 300 MW).



# 13. Extension of the 2-point model

## 13.1. Basic equations

Following the same ideas as for the estimate of radiation losses on closed fieldlines, one starts with the energy balance along field lines with radiation loss rate  $l_Z$

$$\frac{d}{ds}q_{e,\parallel} = -\frac{d}{ds}\kappa_{e,\parallel}\frac{d}{ds}T_e = -\frac{1.2 \cdot 10^{15}}{ln\Lambda}\frac{d}{ds}T_e^{5/2}\frac{d}{ds}T_e = -f_Z n_e^2 l_Z. \quad (13.1)$$

Integration for constant impurity concentration  $f_Z$  and constant electron pressure  $n_e k T_e$  gives

$$q_{e,\parallel,b}^2 - q_{e,\parallel,d}^2 = \frac{2.4 \cdot 10^{15}}{ln\Lambda} f_Z \cdot (n_{e,b} T_{e,b})^2 \int_{T_{e,d}}^{T_{e,b}} \sqrt{T_e} l_Z dT_e \quad (13.2)$$

or

$$q_{e,\parallel,b}^2 - q_{e,\parallel,d}^2 = C_0 p_b^2 f_Z L_Z, \quad (13.3)$$

with

$$L_Z = \int_{T_{e,d}}^{T_{e,b}} \sqrt{T_e} l_Z dT_e \quad (13.4)$$

Rewriting the above equation with

$$q_{e,\parallel,b}^2 - q_{e,\parallel,d}^2 = (q_{e,\parallel,b} - q_{e,\parallel,d})(q_{e,\parallel,b} + q_{e,\parallel,d}) \quad (13.5)$$

and

$$q_{e,\parallel,b} - q_{e,\parallel,d} = (\delta q)_{rad,Z}, \quad (13.6)$$

$$q_{e,\parallel,b} + q_{e,\parallel,d} = q_{e,\parallel,b} + q_{e,\parallel,b} - (\delta q)_{rad,Z} \quad (13.7)$$

results in

$$(\delta q)_{rad,Z} = \frac{C_0 p_b^2 f_Z L_Z}{2q_{e,\parallel,b} - (\delta q)_{rad,Z}} \quad (13.8)$$

Defining as normalised variables

$$y = (\delta q)_{rad,Z} / \sqrt{C_0 p_b^2 f_Z L_Z} \quad (13.9)$$

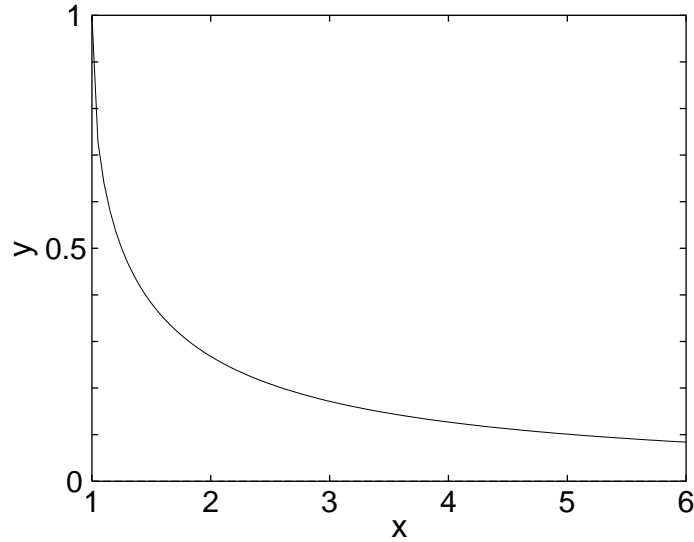


Figure 13.1.: Normalised radiation loss in a flux tube  $y$  as a function of the normalised parallel heat flux entering this flux tube.

and

$$x = q_{e,\parallel,b} / \sqrt{C_0 p_b^2 f_Z L_Z} \quad (13.10)$$

one gets the quadratic function  $y^2 - 2x \cdot y + 1 = 0$ . (Fig. 13.1) The synergy of radiation losses in series can be extracted from Fig. 13.1. Using different radiators (e.g. neon, carbon and hydrogen, which radiate most strongly at lower and lower temperatures) one moves in the curve to higher radiation fractions. Using several losses in series (different radiators, like neon, carbon and hydrogen) one gets larger losses, because after each loss the normalised input power gets smaller and this moves the operational point to larger relative losses. Due to the fact that a reduction in the heat flux density increases the spatial extent of the region between two fixed isotherms one gets enhanced total power radiated by a given impurity at given plasma pressure and impurity concentration.

This synergy for radiation losses in series [27] (reduction of upstream  $q_{e,\parallel,b}$  enhances downstream radiation losses) can in fact also act between any volumetric losses in series. By this, e.g. radiation from neutral hydrogen atoms can ultimately become significant (close to the target plate), once the major fraction of the total heating power has been radiated via other upstream loss channels.

## 13.2. Coronal estimate

Using the equations derived before, one gets an upper limit for the radiated power on open fieldlines

$$q_{e,\parallel,max} = \sqrt{\frac{2.4 \cdot 10^{15}}{\ln \Lambda}} \sqrt{f_Z} \cdot (n_{e,b} T_{e,b}) \sqrt{\int_{T_{ed}}^{T_{eb}} \sqrt{T_e} l_Z dT_e}. \quad (13.11)$$

This maximum radiated power is proportional to the mid-plane pressure and the square root of impurity concentration and temperature integral over radiation efficiency. As a consequence of parallel heat conduction, the spatial extent for a certain temperature drop  $\Delta T_e$  is proportional to  $T_e^{5/2}/q_{e,\parallel}$ . Therefore, it is difficult to radiate at low temperatures. Applying this estimate to ITER ( $T_{e,b} \cong 260\text{eV}$ ) with coronal equilibrium rates and using the fatal fractions  $f_Z$  as discussed for the radiation loss estimate for the main chamber (Be (0.14), C (0.07), Ne(0.025), Ar(0.0054)) and again using 1/3 of this fatal fraction, because only a part of the losses will be due to one element, one get maximum radiation losses (expressed now in  $q_{\parallel}$  values in  $\text{GW}/\text{m}^2$ ) of Be (0.14), C (0.23), Ne(0.48), Ar(0.68). For 300 MW alpha-power one has about  $1.5 \text{ GW}/\text{m}^2$  parallel power flow for ITER. Therefore, it is clear that coronal equilibrium impurities are not adequate for power removal. One needs enhancements of the radiation loss function  $L_Z$ .

### 13.3. Non-coronal effects

There are two possible candidates for these non-equilibrium effects.

#### 13.3.1. Effect of transport

The first (and most important) is the effect of transport, which produces a lag of the actual ionization degree behind its equilibrium value. This is especially important for the limited residence time of impurities close to the plate, where fast recycling shifts the ionization balance toward lower charge states (Fig. 13.2).

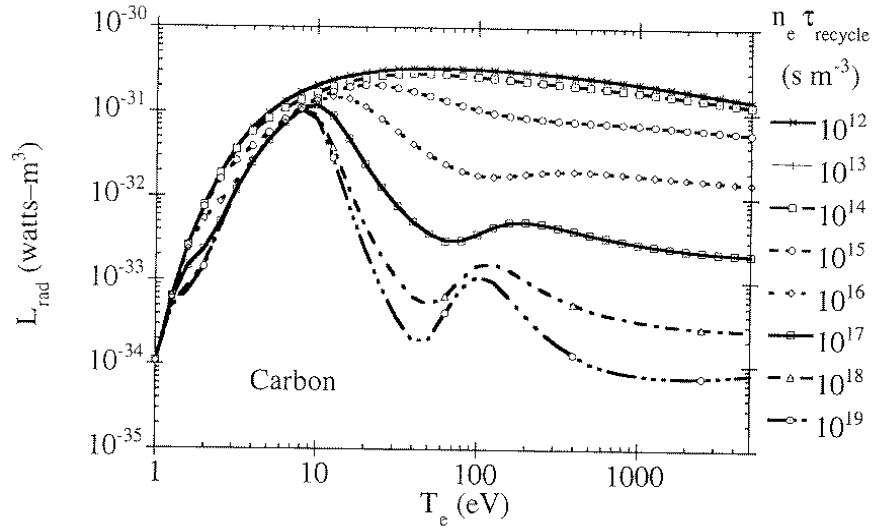


Figure 13.2.: Radiation loss function for carbon as a function of electron temperature for different values of  $n_e \tau_{\text{recycle}}$  (D. Post). For reduced residence times one gets considerably larger values of the radiation loss function.



### 13.3.2. Charge exchange recombination

The second effect is CX recombination in the presence of neutral hydrogen ( $H^0 + A^{i+} \Rightarrow H^+ + (A^{i-1})^*$ ), which also shifts the ionization balance toward lower charge states (Fig. 13.3).

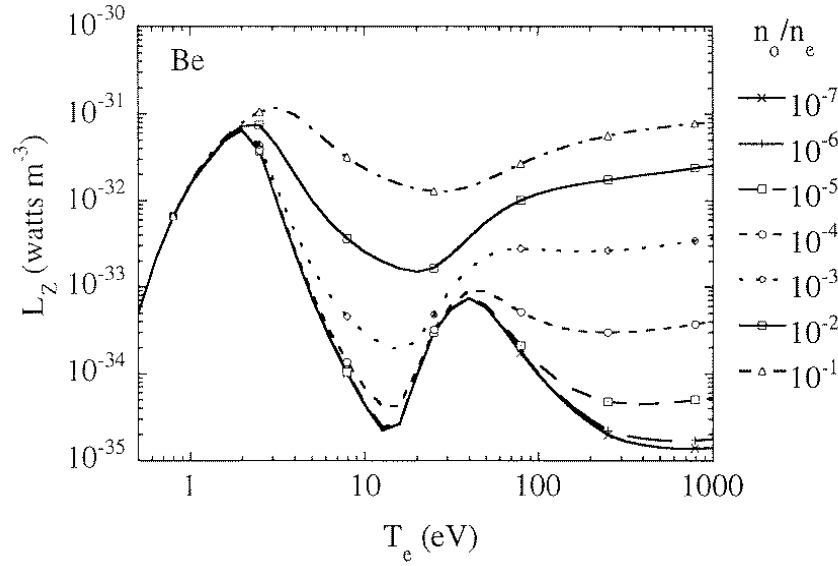


Figure 13.3.: Radiation loss function for beryllium as a function of electron temperature for different values of neutral hydrogen to electron density  $n_0/n_e$  (D. Post). For larger neutral hydrogen densities one gets considerably larger values of the radiation loss function.

Using multifluid SOL transport codes like B2-Eirene to account for these effects, it is demonstrated that these non-equilibrium effects are strong enough that one gets enough radiation losses for sufficient power exhaust for ITER [68]. It is necessary to use the losses in series concept, because relying on only one impurity and one loss channel (main chamber mantle, SOL, divertor) is not robust! Also, the location of the radiation zone has to be taken into account. If it is too close to the target it does not help very much for reduction of the power load, because half of the energy is redeposited on the target by radiation. Nevertheless it was demonstrated for ITER that it is possible to get a reasonable solution with radiation losses, from the 300 MW alpha heating plus 100 MW additional heating power, of approximately 100 to 200 MW in the main chamber (100 MW bremsstrahlung, 100 MW mantle radiation), allowing for about 50 MW to reach the target plates with tolerable heat loads (including power load from radiation). The remaining losses (150 MW) are achieved in the divertor and SOL regions.

## 13.4. Influence of perpendicular transport

As a result of these calculations, one gets aware of one problem for the equilibrium estimate. The main radiation (even for low-Z impurities) comes from SOL mantle region due to small  $\kappa_{||} \approx T^{5/2}$  at low temperatures. This is compensated by non-equilibrium effects

plus an additional effect due to perpendicular transport, which can enlarge strongly the radiation region [69].

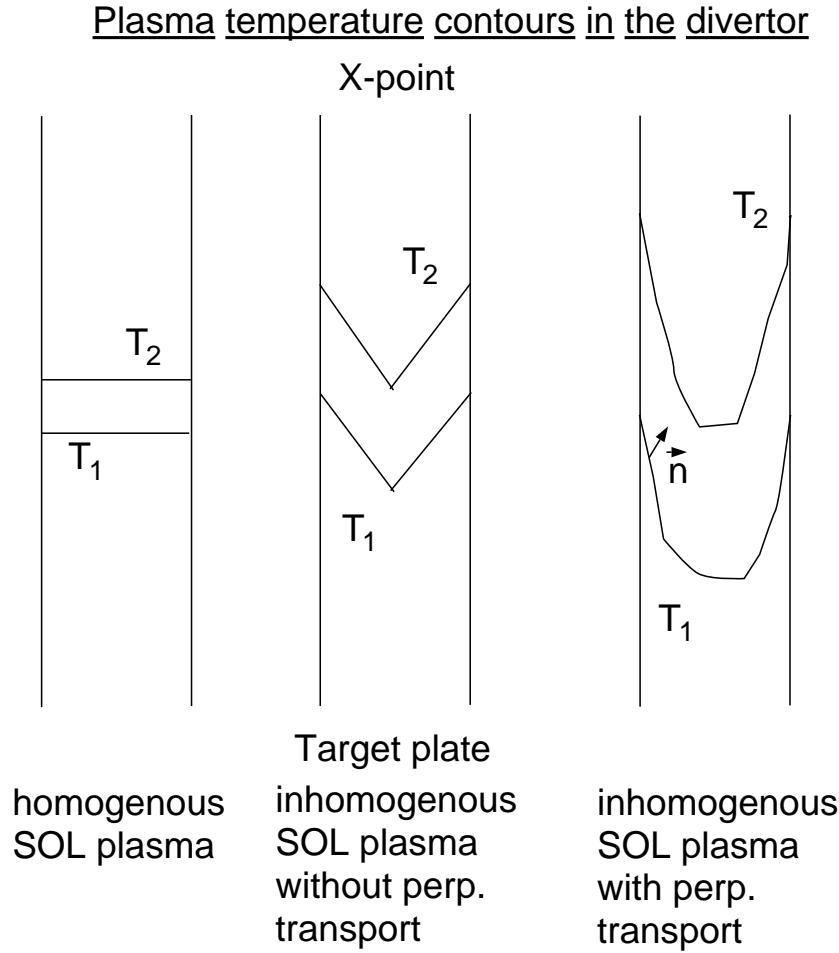


Figure 13.4.: Plasma temperature contours in the divertor for a homogenous SOL plasma (left), an inhomogenous SOL plasma without perpendicular transport (middle) and an inhomogenous SOL plasma with perpendicular transport (right). The surface of the radiating front increases strongly from the left to the right and by this one gets much larger radiation losses (S. Krasheninikov).

To analyse this effect, one formulates the energy balance for normal coordinate  $l_n$  (along  $\vec{n}$ , see Fig. 13.4)

$$\frac{\partial}{\partial l_n} (\kappa_{\perp} + ((\vec{n} \cdot \vec{y})^2 (B_{pol}/B_{tot})^2 \kappa_{\parallel})) \frac{\partial T_e}{\partial l_n} = -n_e^2 f_Z L_Z T_e R_{imp}. \quad (13.12)$$

Parallel heat conduction terms produce upstream losses (mantle). They can be neglected for the divertor radiation.

Integration gives impurity radiation loss from divertor  $Q_{rad,div}$  (see radiation loss estimate for main chamber):

$$q_{\perp} = S_{rad,flame} \cdot 2 \int_0^{T_C} n_e^2 f_Z L_Z (T_e) \kappa_{\perp} dT_e, \quad (13.13)$$

but now the surface of the radiating front enters ( $S_{rad,flame}$ ), which is, because of perpendicular transport, much larger than for the case without (Fig. 13.4).

### 13.5. Advanced 2-point model including radiation losses

As already used in the discussion of the clean plasma, the 2-point model can be generalized to an advanced 2-point model including radiation losses [27]. For this, one starts with the standard 2-point model equations with

$$q_{||} = q_{\perp} L / \Delta_E \quad (13.14)$$

(divergence of  $q_{||}$  equals divergence of  $q_{\perp}$ ) with perpendicular heat flux

$$q_{\perp} = P_{heat} \cdot (1 - f_{rad,core}) / (4\pi^2 a R \sqrt{\kappa}) \quad (13.15)$$

and SOL energy width  $\Delta_E$  ( $\kappa$  is the elongation of the plasma).

Momentum balance between the flow stagnation point on a field line (usually taken in outer mid-plane) and the target plate gives (Bernoulli equation):

$$n_d T_d (1 + \gamma M_d^2) = (1 - f_{mom}) n_b T_b, \quad (13.16)$$

where index b indicates the midplane quantities at the separatrix and index d the divertor plate quantities at the separatrix,  $\gamma$  the adiabatic coefficient,  $M$  the mach number and  $f_{mom}$  the momentum loss factor.

Energy balance obtained by the solution of the parallel heat conduction equation along fieldlines results in:

$$T_b^{7/2} - T_d^{7/2} = 4.6 \cdot 10^{-14} q_{||} L \quad (13.17)$$

for a parallel heat flux  $q_{||}$  and a field line length from separatrix midplane to the target plate  $L$ .

Additionally, the relation between target particle and energy fluxes completes the set of equations:

$$\underbrace{\delta_e T_D \Gamma_D}_{(targetload)} + \underbrace{\epsilon_{ion} \frac{\Gamma_D}{1 - f_{rec}}}_{(hydrogen)} = \underbrace{(1 - f_{rad,div})}_{(impurities)} q_{||}, \quad (13.18)$$

where the sheath transmission factor  $\delta_e$  consists of a kinetic factor  $\tilde{\delta}_e$  plus  $(5/2) + (\gamma M_d^2/2)$  due to convective factor and acceleration due to the Bohm condition.

The first term represent the targetload, the second the hydrogenic recycling losses by ionisation (with effective ionisation loss  $\epsilon_{ion}$  and possible recombination  $f_{rec}$ ). In addition, radiation losses on open field lines by impurities have to be taken into account by the radiation loss factor  $f_{rad,div}$ .

For the cold divertor regime ( $T_b^{7/2} \gg T_d^{7/2}$ ) one has

$$T_b = 1.55 \cdot 10^{-4} (q_{||} L)^{2/7}. \quad (13.19)$$

This gives:

$$n_b = 2.1 \cdot 10^{-2} \frac{(1 - f_{rad,total})}{(1 - f_{rad,core})^{2/7} (1 - f_{mom})} \cdot \left( \frac{P_{heat}}{\Delta_E} \right)^{5/7} \cdot \left( \frac{1}{4\pi^2 a R \sqrt{\kappa}} \right)^{5/7} \cdot L^{3/7} \cdot F(M_d, T_d), \quad (13.20)$$

with

$$(1 - f_{rad,total}) = (1 - f_{rad,core})(1 - f_{rad,div}) \quad (13.21)$$

and

$$F(M_d, T_d) = \frac{(1 + \gamma M_d^2)}{M_d \sqrt{\gamma/\mu}} \cdot \frac{\sqrt{T_d}}{\delta_e k T_d + \epsilon_{ion,eff}/(1 - f_{rec})}. \quad (13.22)$$

The resulting equation shows the coupled effect of momentum loss ( $f_{mom}$ ) and radiation loss ( $f_{rad}$ ). Also, the dominant dependence for the upstream conditions is the total radiation loss, whereas there exists only a weak dependence on the splitting of radiation losses [70].



# 14. SOL density limit

## 14.1. Basic idea

From the 2-point models, for given (machine) parameters and boundary conditions, one can, in principle, obtain arbitrarily high separatrix density values by increasing, for instance, the particle content in the system. An upper bound must result from an additional constraint that limits the accessible part of the solution space (threshold condition) [71]. Possible threshold conditions might be the onset condition of a thermal instability. A special situation is given if the threshold condition can be formulated in terms of edge quantities alone.

## 14.2. Scaling considerations

A central element of such a edge threshold condition and a resulting SOL based density limit is the observation that maximum separatrix densities are reached at complete detachment [70, 72] (see also Fig. 14.1). A reduction of this density limit due to other limiting mechanisms like earlier onset of radiation instabilities in dirty plasmas is naturally possible. Complete detachment is characterized by a large drop of the integral of the ion saturation current (at least by one order of magnitude), an increase of the  $D_\alpha$  signal in the divertor and an increase of the divertor neutral fluxes. In the modelling this is explained by the onset of volume recombination [39], which was also spectroscopically observed in ASDEX-Upgrade L-mode high density discharges [72, 40]. Under these conditions, this results at the gas target entrance, which is formed at complete detachment, in a sufficiently strong variation of the Mach number with transverse neutral collisionality, limiting the maximum separatrix density [70] and giving a very weakly power dependent scaling for this maximum density. For other transverse neutral collisionalities (different SOL width), one gets a scaling which is depending on the square root of power. Following the arguments given in the previous chapter, it is evident that the net input power, which is the power into the gas target, is the adequate parameter to characterize a SOL with a well developed gas target. As was shown before, the actual splitting of radiation losses into main chamber core and SOL/divertor radiation has virtually negligible effect on the upstream separatrix density. Also, the splitting of radiation is usually difficult to determine experimentally. In L-mode density limit studies in ASDEX-Upgrade, a power-dependency of the maximum separatrix density with net input power is found ( $P^{0.6}$  for D and  $P^{0.6}$  for H, where P is the net input power defined as the difference of heating power and total radiation losses). B2-Eirene reproduces the experimental findings for ASDEX Upgrade (Fig. 14.2). In contrast, B2-Eirene studies for JET gave a power-independent,

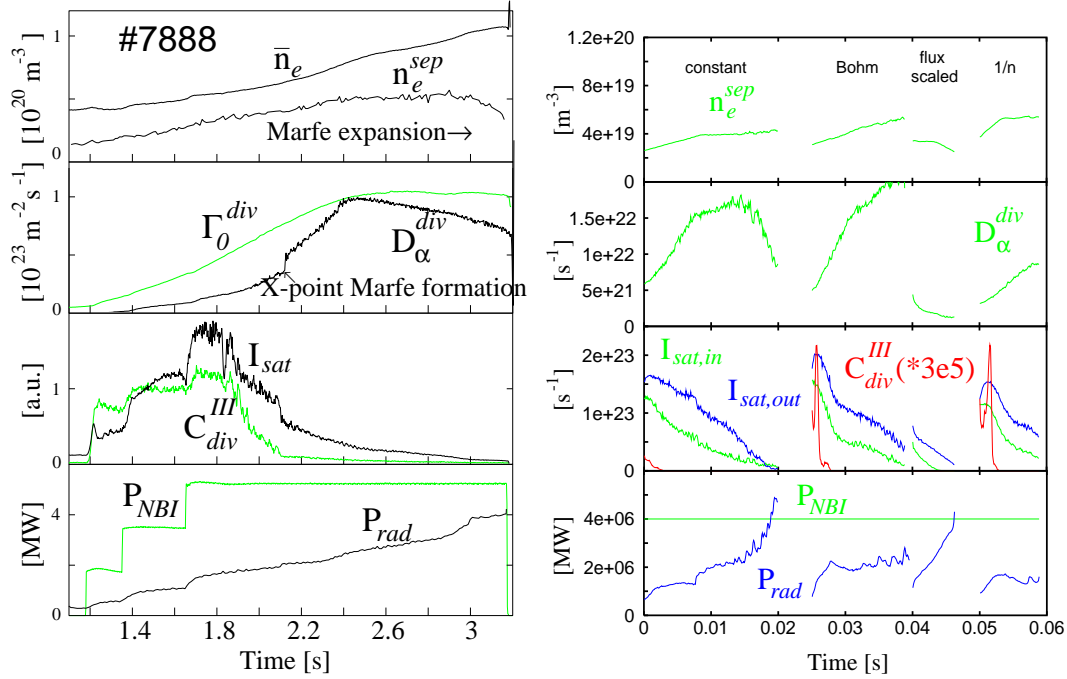


Figure 14.1.: Experimental (left) and modelled (right) time traces for ASDEX-Upgrade shot # 7888. Line-averaged and separatrix density (top) rise up to complete detachment, where the particle flux in the divertor  $\Gamma_0$  and  $D_\alpha^{div}$  saturate or even slightly drop, ion saturation current  $I_{sat}$  drops by at least one order of magnitude and carbon line emission of  $C^{2+}$  just above the plate ( $C_{div}^{III}$ ) have already dropped (because temperature gets below 3 eV). The total radiated power  $P_{rad}$  reaches a maximum of about 1 MW below the injected neutral beam power  $P_{NBI}$ . In the modelling results, different type of anomalous transport laws are compared: radially constant, locally Bohm-like, flux-scaled and globally  $1/n$  scaled transport. All different transport laws give similar values for the upstream density, whereas they behave slightly differently in the different signals, where, with the exception of the flux-scaled transport law, all descriptions are in acceptable agreement with experiment.

$1/q$ -type scaling (Hugill-Greenwald type scaling,  $P^{0.1}$ ) [70]. The modelling results for ASDEX-Upgrade indicate also a transition into this kind of intermediate transverse neutral collisionality for net input powers above 2.5 MW, where up to now no experimental points were accessible.

### 14.3. Detailed analysis of density limit scenarios

A detailed comparison of modelling and experimental results was done for shot 7888 (4.0 MW power into the SOL for hydrogen, see also Fig. 14.1), focussing especially on the comparison of the  $H_\alpha$  in the divertor (Fig. 14.3). From low recycling to detachment the  $H_\alpha$  profile at the target plate (viewed from the top) changes in intensity and shape. In the phase from low recycling to high recycling the intensity gets larger. As soon as

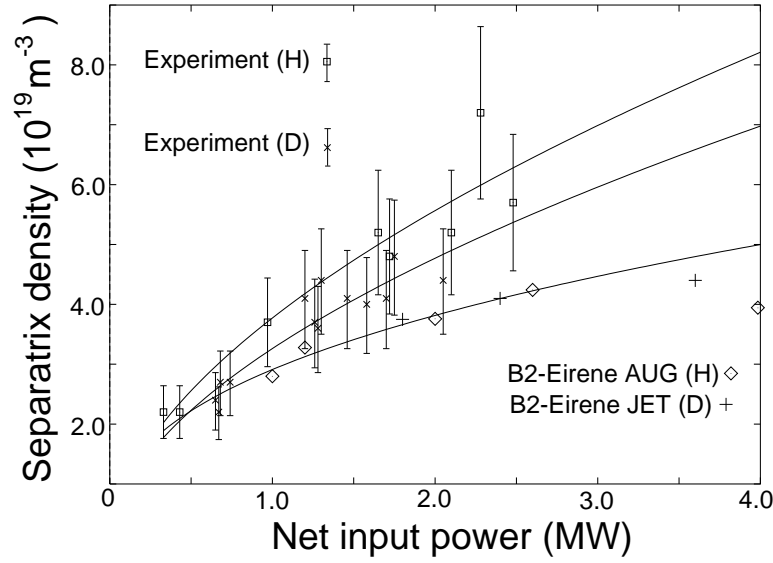


Figure 14.2.: Maximum separatrix density vs. net input power for ASDEX-Upgrade. Included are also B2-Eirene modelling results for ASDEX-Upgrade and JET [58].

a MARFE (a radiation instability originating from a region close to the X-point which will be discussed later) appears, an additional shoulder develops. This behaviour is well reproduced by the code. The shoulder is related to  $H_\alpha$  radiation from the high density MARFE region.

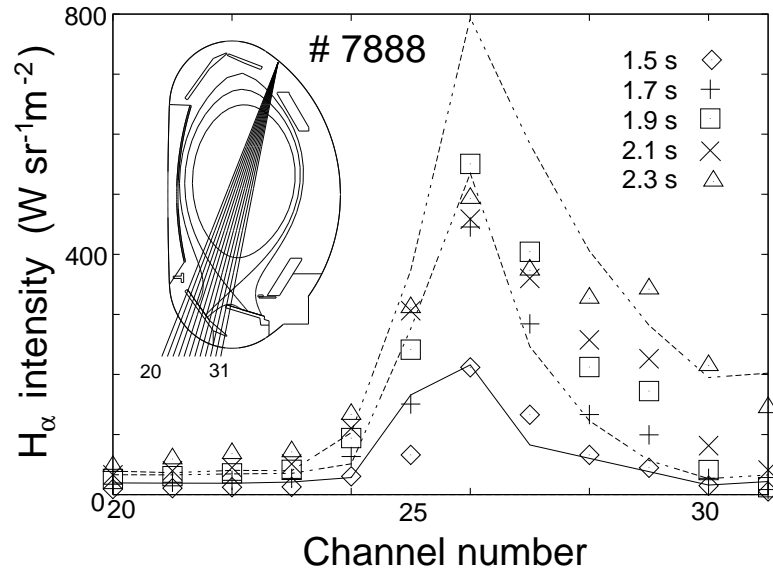


Figure 14.3.: Measured (symbols) and modelled (lines)  $H_\alpha$  intensity profile in the inner divertor for density limit shot 7888 [58].

This is also a consequence of the location of radiation zone: close to detachment it moves up to the X-point (Fig. 14.4). This process is not strictly an instability, but a fast process



with regard to upstream density.

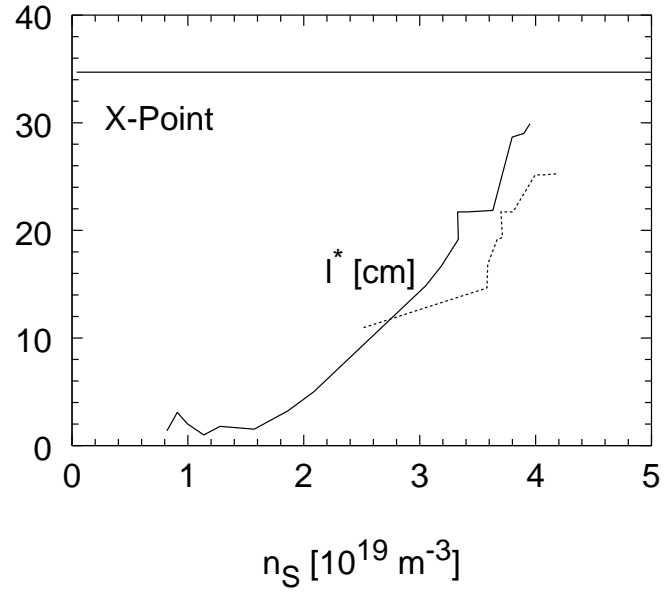


Figure 14.4.: Location of the radiation zone (distance above plate) as a function of separatrix density for a JET Mark I B2-Eirene run [39].

# 15. Impurity flow pattern, flow reversal

## 15.1. Parallel force balance

As for the pure plasma, the flow pattern of the impurities has to be discussed. This flow pattern is determined by the parallel force balance, where different contributions are determining the impurity flow. The parallel momentum balance of species  $a$  ( $1 \leq a \leq N$ ) can be written in a somewhat symbolic form (because in e.g. B2 a more exact and complete formulation based on 21-moment ansatz is used [73]):

$$\frac{\partial}{\partial t}(m_a n_a u_{||a}) + \dots = -\frac{\partial p_a}{\partial s} - Z \frac{n_a}{n_e} \frac{\partial p_e}{\partial s} + 0.71(Z^2 - Z)n_a \frac{\partial T_e}{\partial s} + c_i^*(Z^2 - Z) \frac{\partial T_i}{\partial s} + \sum_{b=1}^N F_{ab} \quad (15.1)$$

One can identify the different terms: the self pressure force  $-\frac{\partial p_a}{\partial s}$  ( $\propto Z^0$ ), the electric field force  $-Z \frac{n_a}{n_e} \frac{\partial p_e}{\partial s} - Z 0.71 n_a \frac{\partial T_e}{\partial s} - Z c_i^* \frac{\partial T_i}{\partial s}$  ( $\propto Z^1$ ), the electron thermal force  $\propto \frac{\partial T_e}{\partial s}$  ( $\propto Z^2$ ), the ion thermal force  $\propto \frac{\partial T_i}{\partial s}$  ( $\propto Z^2$ ) and the friction  $\sum_{b=1}^N F_{ab}$  ( $\propto Z^2$ ).

The frictional force is proportional to the velocity difference between background plasma and impurity ions

$$\frac{m_Z n_Z (V - V_Z)}{\tau_Z} \quad (15.2)$$

with

$$\tau_Z = \frac{3(kT_i)^{3/2} m_Z^2}{4(2\pi m)^{1/2} e^4 Z^2 n_i \ln \Lambda (m + m_Z)} \quad (15.3)$$

[18].

This is valid for trace impurities, e.g.  $n_Z Z^2 \ll n_e$ . Otherwise more complicated expressions are derived from the 21-moment description. In a simple picture, it is a velocity shift in the direction of the background flow for the impurities (Fig. 15.1).

The ion thermal force is a consequence of the scaling of the Coulomb cross-section ( $\sigma_{Coulomb} \sim 1/v^4$ ). Therefore, an impurity in a temperature gradient (determined by the background plasma) gets an asymmetric distribution function  $f(v_i)$ . Mapped into a fluid description this results in a force proportional to  $C_i n_Z \frac{\partial T_i}{\partial s}$  with

$$C_i = -3 \frac{1 - \mu - 5\sqrt{2}Z^2(1.1\mu^{5/2} - 0.35\mu^{3/2})}{2.6 - 2\mu + 5.4\mu^2} \approx 2.21Z^2 \quad (15.4)$$

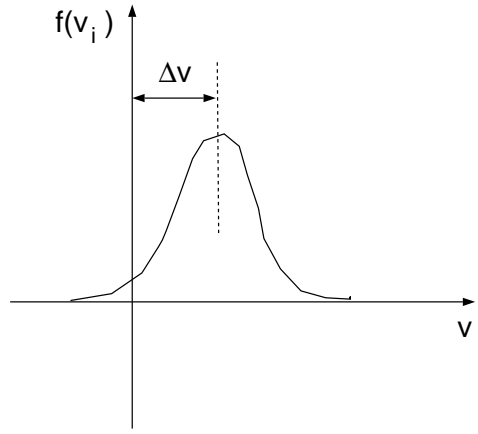


Figure 15.1.: Sketch of the impurity ion velocity distribution function for a trace impurity situation, where the impurity is strongly coupled to the plasma background

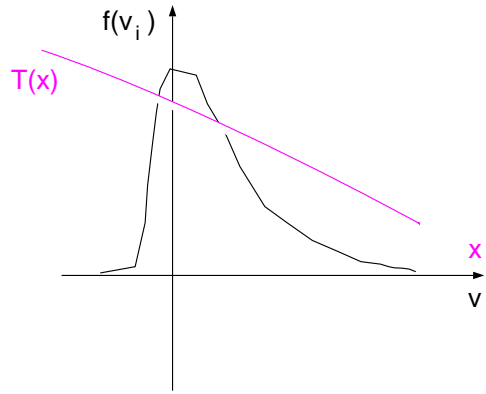


Figure 15.2.: Sketch of the impurity ion velocity distribution function for a trace impurity situation, where the impurity experience a gradient of the background temperature.

[74]. This force tries to move the impurities up the gradient of the ion temperature (lower temperature - and thus lower velocity - means more collisions, Fig. 15.2).

Using B2-Eirene results, one can analyse, for a medium and a high density case, the parallel force balance for e.g.  $Ne^{3+}$  in a particular flux tube close to the separatrix in the divertor (Fig. 15.3).

In the region close to the target plate, the friction force is quite strong because of the acceleration of ions towards the sheath (Bohm condition) and impurities are swept onto target plates together with the background hydrogen. The backward thermal force wins, if the local Mach number becomes smaller than the ratio of the ion mean free path to the temperature gradient length [75]:

$$M_{\parallel} < \lambda_{ii}/\lambda_{T,\parallel} \quad (15.5)$$

(only applicable for small  $M_{\parallel}$ ).

As a consequence of the physics discussed before, the behaviour of impurities produced

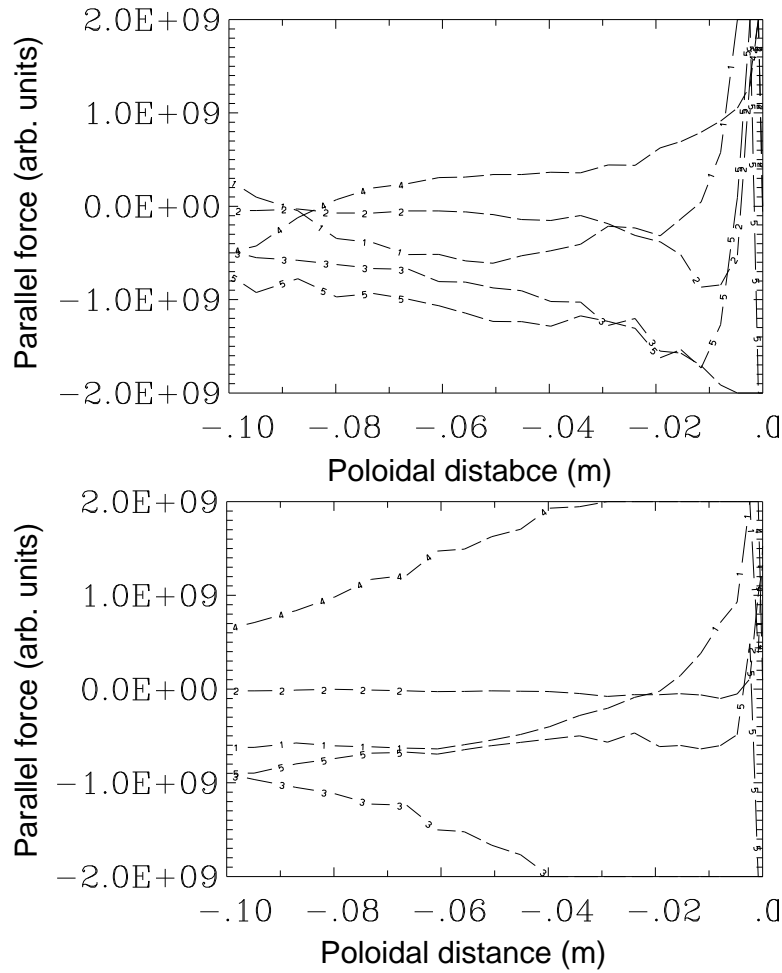


Figure 15.3.: Parallel force balance for  $Ne^{3+}$  versus poloidal distance in a flux tube close to the separatrix (outer divertor) for a medium (top) and high (bottom) density case. The poloidal distance is counted starting from 0 at the plate. Plotted are the different contributions to the force balance: (1) is the self-pressure force, (2) the parallel electric field force, (3) the thermal forces, (4) the friction force and (5) the sum of all contributions.

at the plate and those at other places is quite different. Target produced impurities are well retained due to the strong friction force. This is significantly worse, if impurities are introduced upstream (recycling gases, throat sputtering) due to the thermal force usually dominating there.

This results in the following density distributions of the different neon charge states in this particular flux tube, which are (see later discussion) also influenced by the 2-D structure of the impurity transport (Fig. 15.4). They show up as a kind of shell-like structure, where the impurity densities are not only determined by the temperature (which would be the case for coronal equilibrium conditions) but also by the strong transport effects (with reduced residence times of the impurities in the plasma, especially close to the plate).

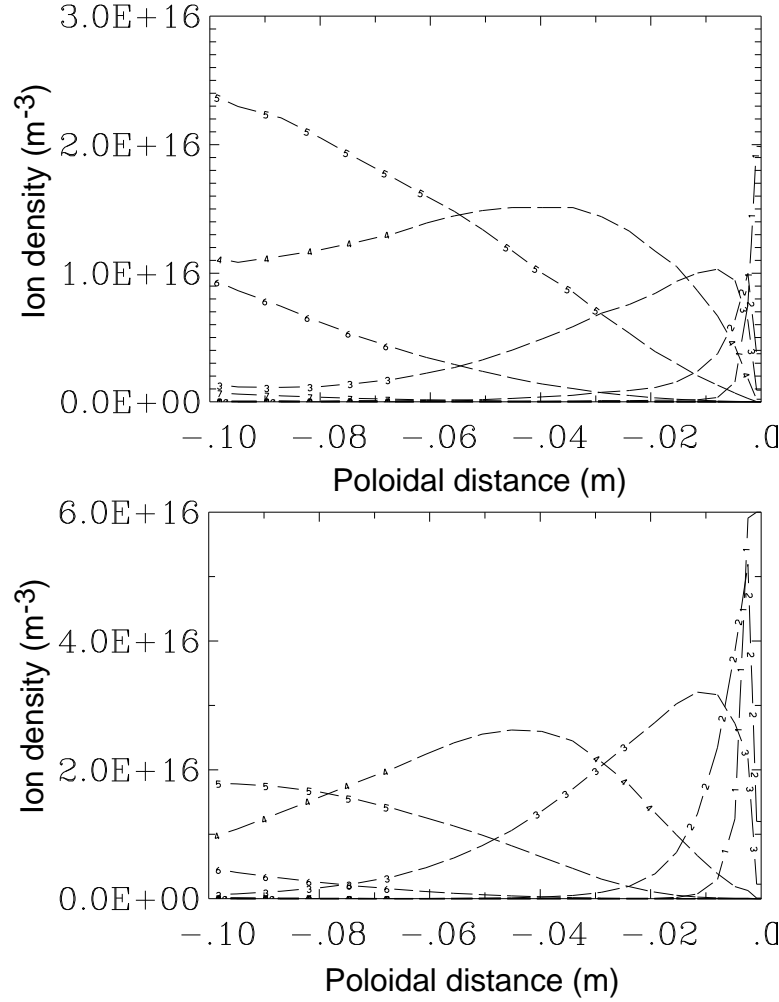


Figure 15.4.: Ion density distribution for neon in a flux tube close to the separatrix (outer divertor) for a medium (top) and high (bottom) density case. The poloidal distance is counted starting from 0 at the plate. The numbers in the plot corresponds to the different charge states of neon, e.g. (2) is  $Ne^{2+}$ .

## 15.2. Impurity regimes and corrections to the fluid model

Up to now, most of the arguments were given for trace impurity situations. In this case, one has an almost pure plasma ( $Z_{eff} \cong 1, n_e \cong n_i \gg \sum_j n_j Z_j^2$ ), where only the energy balance is affected due to the radiation losses, but not the profiles of the plasma background. For dirtier cases, one has an intermediate situation ( $Z_{eff} \geq 1 + \sqrt{\frac{2}{1+m_Z/m_i}}$ ), where the impurity behaviour is determined mainly by mutual collisions of impurity ions, e.g. plasmas where  $Z_{eff}(C) \geq 1.6, Z_{eff}(Fe) \geq 1.3, Z_{eff}(W) \geq 1.2$ . In very dirty plasmas ( $Z_{eff} \geq 2$ ), impurities start to determine also the background plasma parameters. Experimentally, one is often in the intermediate case, sometimes even in the dirty situation. Therefore, description of impurity transport cannot be done with trace impurity limits,

but needs more correct expressions like the 21-moment description.

The effect of kinetic corrections on impurity transport have also to be checked. In B2 a limit of thermal forces is applied, using as the maximum allowed temperature gradient along the field lines [76]:

$$\lambda_{T_e} = \lambda \cdot (1 + Z)^{1/2} / 5.1 \quad (15.6)$$

with a mean free path of the tail electrons [5]

$$\lambda(m) = 7.5 \cdot 10^{16} \cdot T_e^2(\text{eV}) / (n_e(m^{-3}) * (B_p/B)). \quad (15.7)$$

A fudge factor of  $1/0.3$  for this maximum temperature decay length seems to work quite well, suppressing impurity accumulation especially in regions of cold plasma at the outside of the plates, which otherwise produce severe numerical problems without affecting the global solution. The same procedure is done for the ions.

### 15.3. Impurity flow pattern

Up to now the discussion focussed on the parallel forces. However, impurities (like He and Ne) are even earlier in a 2-D situation, where they have longer mean-free paths than typical SOL widths compared to D (Fig. 15.5).

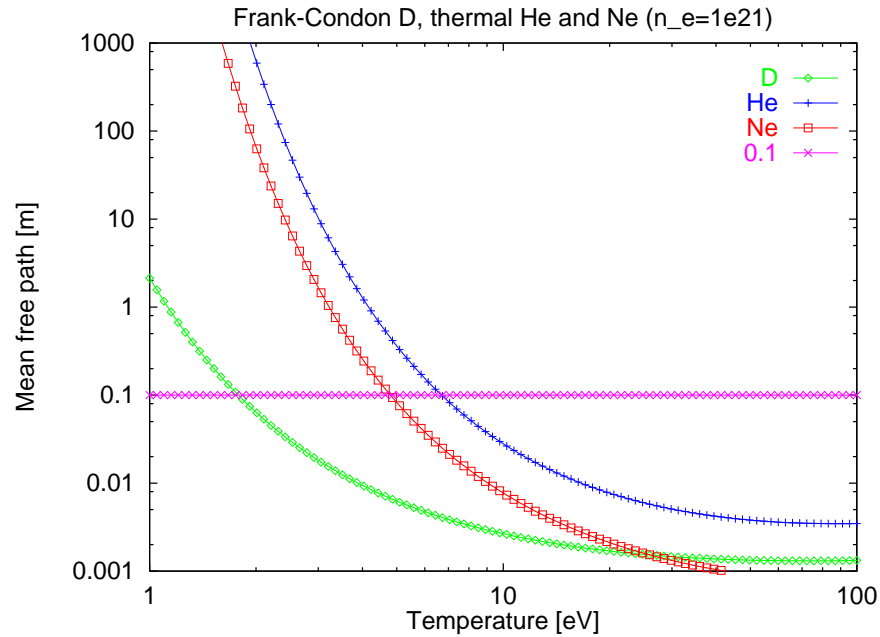


Figure 15.5.: Mean free path of Franck-Condon deuterium, thermal helium and thermal neon atoms as a function of temperature for an electron density of  $1 \cdot 10^{21} m^{-3}$ , representing high recycling divertor conditions. Ne and He have larger mean free paths than a typical SOL length scale of 0.1 m much earlier than D, indicating the transition from a 1-D to a 2-D dominated regime.

Therefore, it is evident that, for analysis of impurity compression or divertor retention, 2-D models are necessary, whereas one gets for 1-D cases unrealistic results (either complete retention or zero retention).

Analysing the flow pattern of the hydrogen background together with the impurities, e.g. neon, from multifluid B2-Eirene runs (where all charge states of ions are followed) for a medium and a high density case, one sees that the flow reversal of the impurities is independent of the hydrogen background (Fig. 15.6). The flow reversal creates kind of convective cells where particles are flowing backwards from the divertor into the main chamber close to the separatrix and are then transported radially by the anomalous transport and flow towards the target plate in the outer SOL, where practically low-recycling conditions exist, with relatively strong Mach numbers (up to 0.3) even at the divertor entrance and very weak temperature gradients along fieldlines. The D flow reversal (at the outer divertor) sets in only at high densities, whereas the neon flow reversal is independent of the background plasma. The reason for this is that the flow reversal zones for impurities are created due to the influence of the thermal force (especially that of the ions). The existence or non-existence of flow reversal of the hydrogenic background is unimportant, because the Mach numbers in these regions are very small (below about 0.1) and therefore the friction force is negligible. Influence of impurity flows by changes of the hydrogenic background (e.g. by strong gas puffing and pumping) are therefore very unlikely.

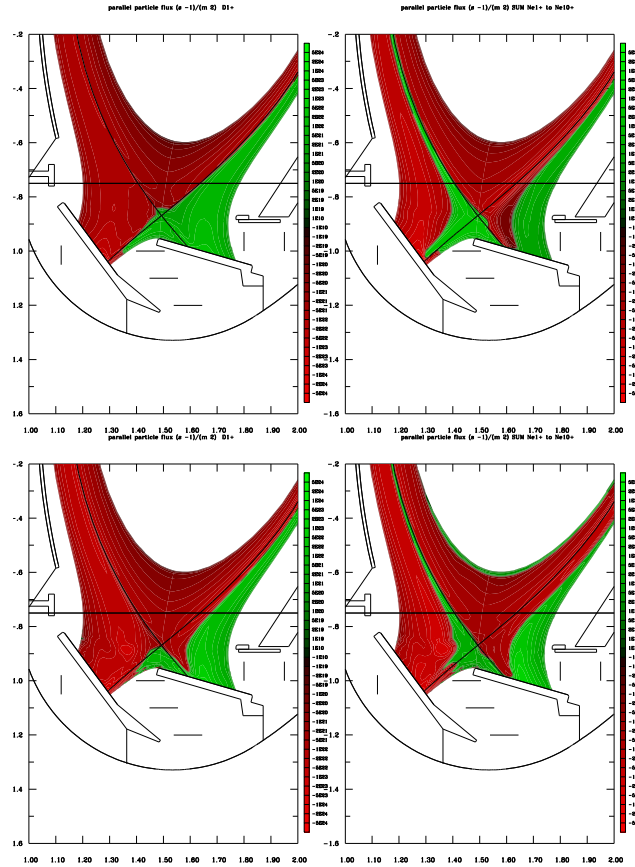


Figure 15.6.: Contours of parallel particle flux for deuterium (left) and neon (right) for medium (top) and high (bottom) density B2-Eirene results. Flows in the direction towards the outer target plate are in green, flows in the direction towards the inner target plate are red.

Generally, there is an ongoing discussion, if puff and pump scenarios are able to give strong impurity entrainment and thus improve considerably impurity divertor compression. This seems to be very unlikely following the above argumentation. Additionally, the externally applied fluxes (gas puffs) have then to compete with intrinsic recycling fluxes, which are usually several orders of magnitude larger.

Consistent with this picture, it was proven experimentally [77] at ASDEX-Upgrade that the internal recycling fluxes are responsible for the divertor retention of impurities, not the external flux. This was demonstrated by doing shots with identical divertor neutral densities, but different pumping speed (switching off turbopumps) and therefore different external flux. One gets identical results for practically all quantities (with the exception of the gas puff rate due to the different pumping rates), especially for neon compression. One has to note, however, that experiments in DIII-D gave a variation of the compression by a factor of 2 with different gas puff rates [78]. However, a full analysis of these scenarios with 2-D modelling is still missing.

## 15.4. Impurity ion flow in the divertor

Measurement of ion flows in the divertor is also experimentally quite difficult. At ASDEX-Upgrade, a high resolution spectroscopy system is used with two toroidally counterviewing sets of line-of-sights. Analysing the Doppler shift of the two opposite toroidal lines of sight one gets the velocities of the impurity ions. This was applied to measure the velocities of *CIII* ( $C^{2+}$ ) in the outer divertor: these ions move towards the outer target plate with a velocity of 11 km/s [79] (Fig. 15.7).

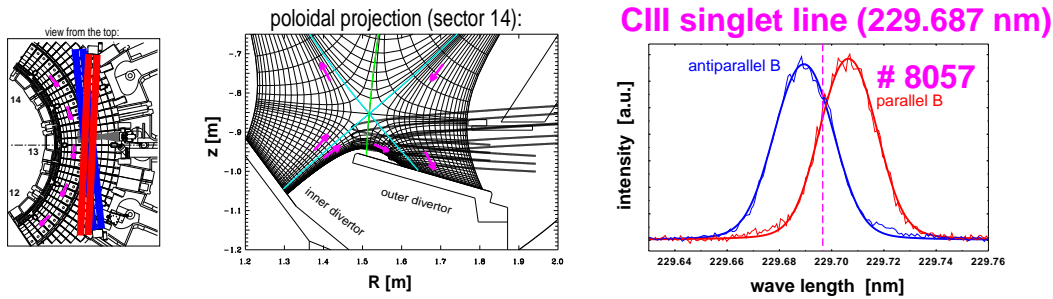


Figure 15.7.: Toroidal geometry of the high-resolution spectroscopy system at ASDEX-Upgrade (left) and the projection of these toroidal line-of-sights onto the poloidal plane (middle). From the measured Doppler shift of *CIII* (right) a velocity of 11 km/s (in the direction of the outer divertor) was derived (J. Gafert).

Comparison with similar B2-Eirene runs gave a very good agreement (within a factor of 2) between modelling and experiment (Fig. 15.8).

From the contours of emissivity of *CIII*, it is also obvious that this charge state is not very well suited to diagnose flow reversal zones in the divertor, because the maximum emission comes from the outer parts of the SOL (or at the private flux), where the dominant contribution to the parallel force balance is the friction force, whereas thermal forces are small, because the temperature gradients along the fieldlines are small, too. For a



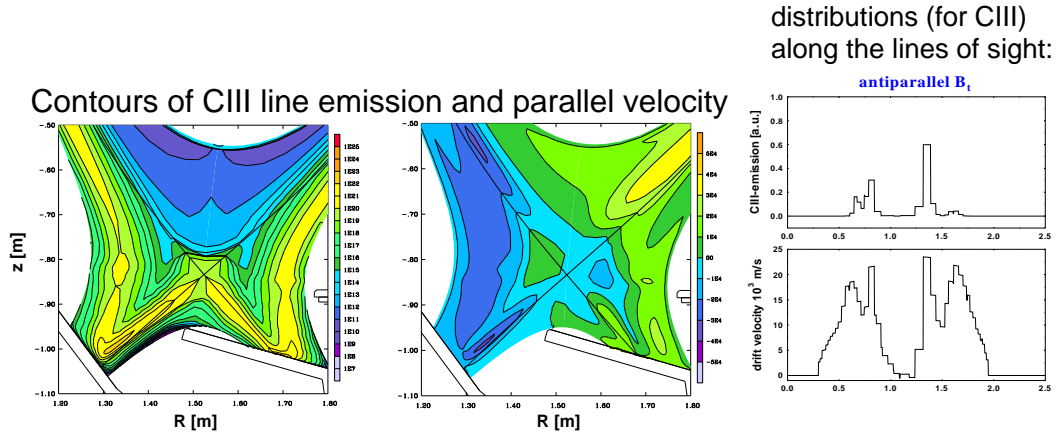


Figure 15.8.: Contours of emissivity (left) and density (middle) of  $CIII$  from a B2-Eirene run. For one particular line of sight of the toroidal spectroscopic system the emissivities and velocities along this line of sight are plotted (right). Only where the emissivity is large does one get the major contributions for the measurement, resulting in this case in velocities of about 15 km/s.

measurement of flow reversal one has to move to higher charge states, which is difficult because their lines requires measurement in the vacuum-UV, or to use a different geometry with an optimised spectroscopic line of sight setup according to modelling results.

# 16. Compression, helium pumping

## 16.1. Experimental characterization of compression

With the physics discussed before, one now has the necessary ingredients for a detailed analysis of impurity effects in the SOL, where two quantities will be used. The first one is compression, which is the ratio between the neutral density in the pump duct and the average ion midplane density close to the separatrix (Fig. 16.1). The ratio of impurity compression to hydrogen compression defines the second quantity, which is the enrichment factor. The compression is of particular interest because it determines the pumping efficiency for impurities necessary for feedback control. Experimentally, one obtains the compression from impurity pump experiments (with small gas puffs of impurities applied upstream). From the spectroscopically measured decay time of the impurities, one gets the compression from a simple 2-chamber model [80].

## 16.2. Importance of helium compression for a reactor

The compression of helium and the helium pumping is important to know, because one has to avoid too much helium ash which would extinguish the burning plasma in a reactor. A global 0-d model for burning D-T plasma is used, addressing the effect of impurities on ignition condition [81, 82]. It uses several simplifying assumptions:

- 1) uniform plasma with same temperature for all species:  $T = T_e = T_i = T_{He} = T_Z$
- 2) single impurity contamination
- 3)  $\alpha$  particles transfer their whole initial energy  $E_\alpha = 3.52 \text{ MeV}$  to the plasma
- 4) pressure of energetic, non-thermalized  $\alpha$  particles is neglected
- 5) concentration of impurities:  $f_Z = n_Z/n_e$ ,  $f_{He} = n_{He}/n_e$  (fully stripped impurities due to high temperatures of 10 keV and higher)
- 6) equal deuterium and tritium densities:  $n_D = n_T$
- 7) ion density:  $n_i = n_D + n_T$

Quasi-neutrality gives for the dilution parameter

$$f_i = \frac{n_i}{n_e} = 1 - Zf_Z - 2f_{He} \quad (16.1)$$

and for total particle density

$$n_{tot} = n_e + n_i + n_Z + n_{He} = n_e(2 - (Z - 1)f_Z - f_{He}) = n_e f_{tot}. \quad (16.2)$$

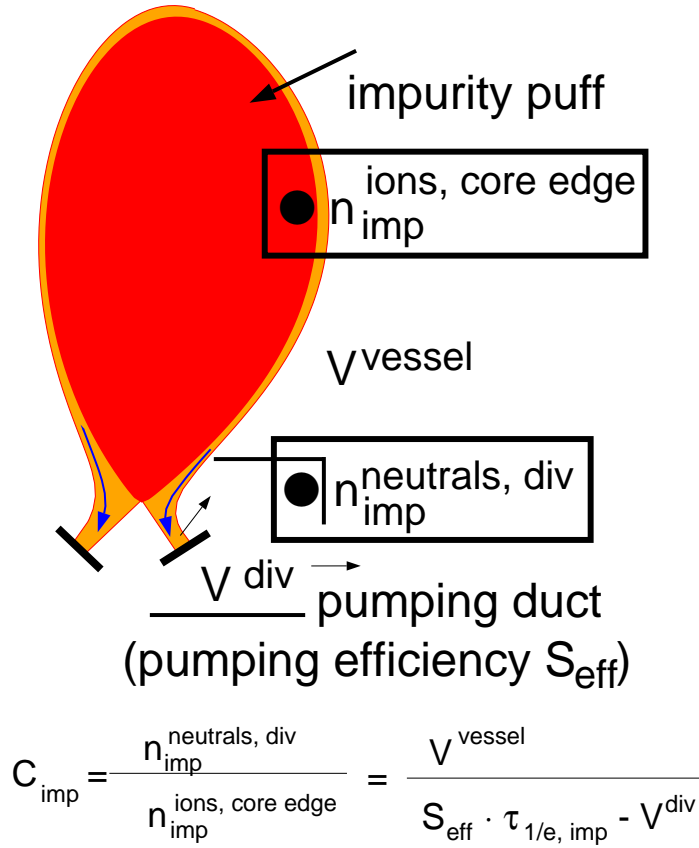


Figure 16.1.: Definition of compression for impurity species  $imp$ . From the spectroscopically measured decay rates  $\tau_{1/e, imp}$ , one gets from a 2-chamber model (with the volumes of vessel  $V^{vessel}$  and divertor  $V^{div}$  and the pumping efficiency  $S_{eff}$ ) the impurity compression.

For the ignition condition, one has the balance between  $\alpha$  particle power production and losses due to conduction and convection and due to volume radiation losses

$$\frac{1}{4} n_e^2 f_i^2 E_\alpha < \sigma v > = \frac{3}{2} \frac{1}{\tau_E} n_e f_{tot} T + R_{rad} n_e^2, \quad (16.3)$$

with the energy confinement time  $\tau_E$ .

This can be rewritten as

$$n_e \tau_E = \frac{\frac{3}{2} f_{tot} T}{\frac{<\sigma v>}{4} f_i^2 E_\alpha - R_{rad}}. \quad (16.4)$$

The  $\alpha$  particle balance is

$$\frac{1}{4} n_e^2 f_i^2 < \sigma v > = \frac{n_{He}}{\tau_\alpha^*} = \frac{n_{He} f_{He}}{\rho \tau_E}, \quad (16.5)$$

where

$$\rho = \tau_\alpha^* / \tau_E \quad (16.6)$$

is the ratio of the global  $\alpha$  particle confinement time and the energy confinement time. The global  $\alpha$  particle confinement time is the ratio of the number of  $\alpha$  particles in the burning region with volume  $V$  and the exhaust flux leaving this region

$$\tau_{\alpha}^* = N_{\alpha} / \Phi_{exhaust}, \quad (16.7)$$

where the exhaust flux is the difference between outward and return flux

$$\Phi_{exhaust} = \Phi_{\alpha,out} - \Phi_{\alpha,ret}. \quad (16.8)$$

It can be shown that  $\tau_{\alpha}^*$  is the sum of a contribution from the internal (core)  $\alpha$  particle confinement time and the contribution from recycling

$$\tau_{\alpha}^* = \tau_{\alpha_1}^* + \frac{R_{eff}}{(1 - R_{eff})} \tau_{\alpha_2}^*, \quad (16.9)$$

where the factor  $\frac{R_{eff}}{(1 - R_{eff})}$  is the mean number of recycling events back into the burning region experienced by the  $\alpha$  particles before being finally pumped away. Combining the above equations gives a cubic equation for  $f_{He}$ . Solving it, one gets the solution for  $n_e \tau_E$  (Fig. 16.2).

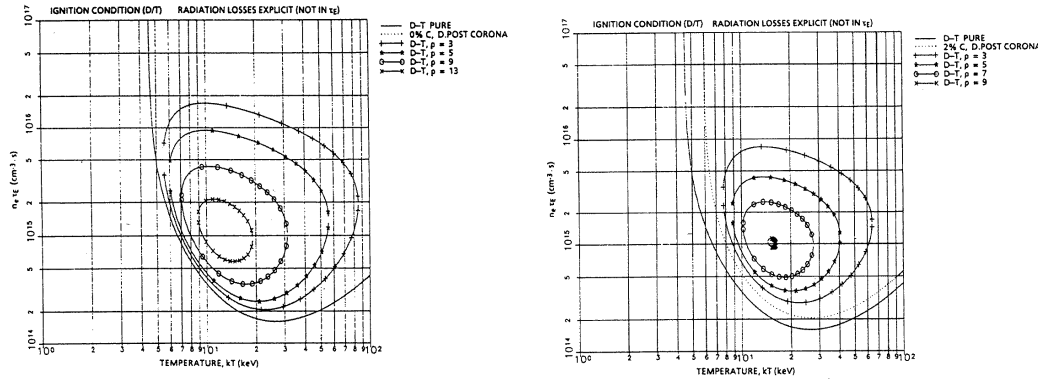


Figure 16.2.: Ignition parameter (radiation losses not accounted for in  $\tau_E$ ) versus temperature for various constant confinement time ratios  $\rho$  in a pure burning D-T plasma (no impurities except  ${}^4\text{He}$ , left) and in a D-T plasma with additionally assumed 2% C (right) [81].

Depending on the assumed concentration of additional impurities, one only gets solutions, if the ratio of the global  $\alpha$  particle confinement time and the energy confinement time  $\rho = \tau_{\alpha}^* / \tau_E$  is less than 10 to 15 (see Fig. 16.2). Otherwise, the helium ash just extinguishes the burning plasma. The demonstration of sufficient low  $\rho$  values for reactor relevant scenarios was done by DIII-D, JET, ASDEX-Upgrade and JT-60U. For ITER one needs a scenario with sufficient helium pumping ability by the pump system. To be able to do this extrapolation properly, the 2-D codes for the ITER design have to be validated at existing machines. Doing this for impurity compression is therefore of particular interest.

### 16.3. Impurity compression at ASDEX-Upgrade

For a scan of the neutral gas flux density in the divertor, done by changing the midplane density (without changing any of the validated transport parameters in the code) one gets the compression of neon and helium at the position of the pump duct relative to the midplane density.

Comparing with the experimental results, the model calculations are obviously able to describe qualitatively as well as quantitatively the observed experimental behaviour: compression of neon and helium (neon is better compressed than helium) increases with higher neutral gas flux density in the divertor (Fig. 16.3).

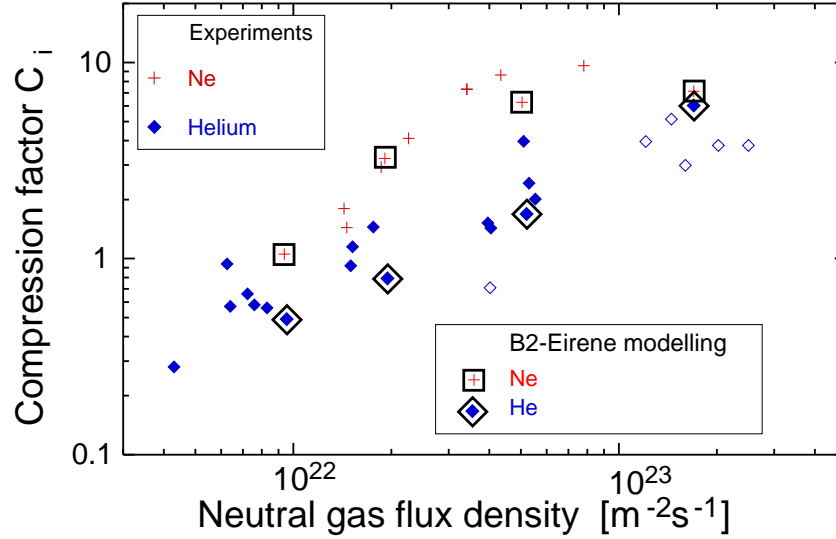


Figure 16.3.: Experimental and modelling results for the compression of neon and helium as a function of divertor neutral gas flux density.

The basic mechanism for the compression is the recycling cycle in the outer SOL. For ASDEX-Upgrade DivI, the existence of a pumping baffle in the outer divertor is quite important for the observed compression. Integrating the modelling result over the SOL, this baffle affects the parallel particle flux of the deuterium background due to the effect of recirculation of neutrals in the pumping duct (limited leakage by the baffle) back to the SOL (Fig. 16.4). The difference between neon and helium can be seen from the different distributions of the radially integrated ionisation sources, where neon neutrals are kept more efficiently in the divertor compared to helium due to their smaller mean free paths.

The physics of the compression can be reduced to a rather simple model, characterised by a layer of the width of the mean free path of the impurity neutrals from where they are able to feed the pump duct below the baffle, establishing a second particle flux maximum in the outer SOL at the plate. Doing a simple flux balance at the entrance of the box [83] then shows that the compression is determined by the instreaming flow velocity of the impurity. In this outer SOL region, there are no strong temperature gradients and the deuterium background has a relatively strong forward flow. Therefore, the impurity flow velocity is due to the dominant friction force of the deuterium background and is practically identical (at least for higher densities) to this background velocity. Enhancing the

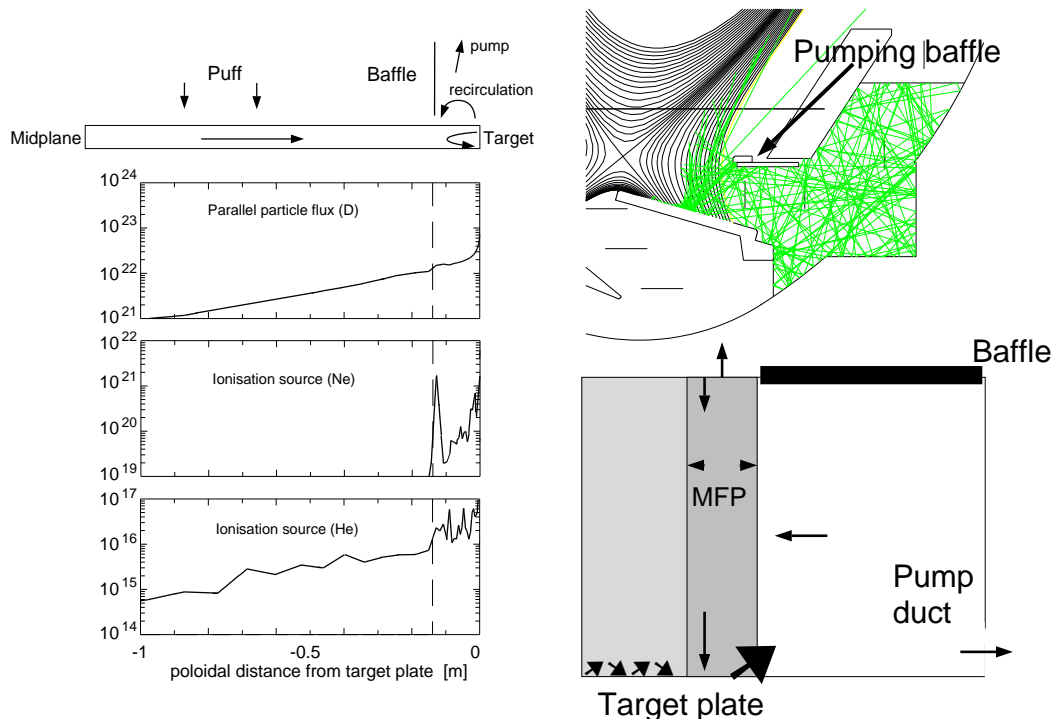


Figure 16.4.: Radially integrated parallel particle flux (D) and ionisation sources (Ne and He) for the outer divertor (left side). Trajectories of 100 neon neutrals from the outer target plate (right side top) and schematic model (right side bottom).

midplane separatrix density and therefore the neutral gas flux density in the divertor results in larger deuterium flows in this outer part due to stronger friction with CX neutrals. This outer layer then acts as a quasi diffusion pump for the impurities. As a consequence, larger deuterium neutral gas flux density in the divertor gives larger compression. The difference between neon and helium is just a consequence of the mass difference (which is the dominant factor in the difference of the mean free paths of neutrals). From these considerations, the difference between deuterium and the other impurities is also clear: deuterium neutral transport is dominated by charge-exchange, in contrast to the impurity neutrals. The deuterium recycling is well confined in this baffle region under conditions where the impurity neutrals are leaking out, because charge exchange in this outer part of the SOL with low densities and low temperatures very effectively traps the deuterium neutrals. Therefore, the effect of the baffle is less pronounced for deuterium than for impurities. The compression of deuterium therefore varies by only a factor of 2 to 3, in agreement with experiment.

This kind of concept offers a very attractive potential for separation of power and particle exhaust: particle exhaust can be done just in the outer part of the SOL (allowing geometry optimization), whereas power exhaust is related to the region close to the separatrix.

Doing multifluid calculations based on these model validation results of the existing Divertor I configuration [53], one gets for the final Lyra configuration (as well as for the open Lyra and the inner orthogonal Divertor I) a much better compression of helium

(an enrichment of helium of typically 2 is now observed at the pumping duct location) than for Divertor I (enrichment factors for helium between 0.1 and 0.4). The very good compression of neon in the outside tilted Divertor I (enrichment of 1 to 6) is reduced to practically the same as the hydrogen compression (enrichment 1 to 1.5), but is still large enough for effective feedback control.

In the Lyra the pumping duct recycling cycle is now in the dome region close to the separatrix (Fig. 16.5).

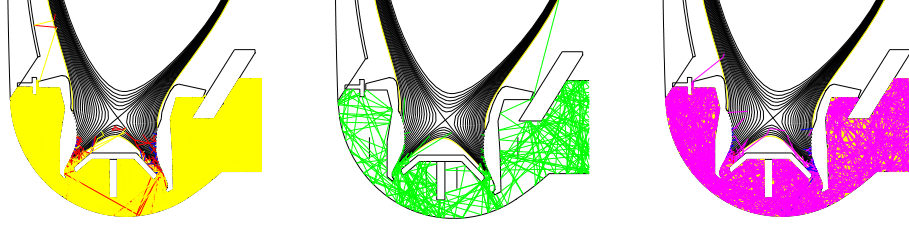


Figure 16.5.: Neutral trajectories for D, Ne and He in DivII.

Due to the higher electron densities there, creation of impurity neutrals at the plate and reionization of colder neutrals from the dome occur at practically the same position. The better compression of helium in the Lyra is then due to the fact that the helium neutral atoms have a longer mean free path than neon and are therefore more easily escaping from the target plate into this dome and from there into the pump.

## 16.4. Consequences for ITER

In the following consequences of the impurity transport results for the ITER design will be discussed. Due to the thermal load limitations, ITER will probably have to move at least into the layer detachment regime. In this case, to define the operational point for ITER the dominating SOL physics can be summarised for a strictly 1-D parallel case, where the radial transport is small compared to the parallel.

Starting with an equation for the residual charged particle energy flux to the target plate (assuming also a regime without volume recombination),

$$q_{||,targetplate} = M_d n_{ed} \sqrt{\frac{(\gamma + 1) k T_{ed}}{\mu m_{prot}}} (\delta_e k T_{ed} + \epsilon_{ion}) \sim p_{ed} \sqrt{T_{ed}} (\delta_e k + \frac{\epsilon_{ion}}{T_{ed}}), \quad (16.10)$$

where  $M_d$ ,  $n_{ed}$  and  $T_{ed}$  are Mach number, electron density and temperature at the plate,  $\gamma$  is the adiabatic constant,  $\mu m_{prot}$  is the ion mass,  $\delta_e$  is the electron energy transfer coefficient and  $\epsilon_{ion}$  is the effective ionization energy (including radiation losses from hydrogen as an enhancement).

Using momentum balance (if there is no momentum loss out of the fan and with the assumption  $T_i = T_e$ ),

$$p_b = 2p_{ed} + p_0, \quad (16.11)$$

the midplane pressure  $p_b$  is balanced by the sum of twice the divertor electron pressure and the neutral pressure at the plate.

Particle balance determines the ratio of plasma to neutral pressure, (particle flow to the target = total ionization in a plasma column perpendicular to the plate)

$$M_d n_{ed} \sqrt{\frac{(\gamma+1)kT_{ed}}{\mu m_{prot}}} \sin \alpha = \int_0^\infty n_e \langle \sigma_{ion} v_{th,e} \rangle n_0 dx. \quad (16.12)$$

Using the simple neutral diffusion model (already discussed before) in the perpendicular direction away from the plate (CX gives rise to diffusion and ionisation to the loss of neutrals)

$$\frac{d}{dx} \lambda_{CX} v_{th,0} \frac{dn_0}{dx} = n_e \langle \sigma_{ion} v_{th,e} \rangle n_0 \quad (16.13)$$

reproduces the well known result for the spatial distribution of neutrals

$$n_0(x) = n_{0,d} e^{-\xi / \sqrt{\lambda_{ion,0} * \lambda_{CX,0}}} \quad (16.14)$$

in terms of CX and ionisation mean-free paths at reference electron density  $n_e d$  in the coordinate

$$\xi = \int_0^x n_e / n_{ed} dx. \quad (16.15)$$

The total ionisation rate (per unit area and for an optically thick SOL) becomes

$$\int_0^\infty n_e \langle \sigma_{ion} v_{th,e} \rangle n_0 dx = n_{0,d} v_{th,0} \sqrt{\frac{\lambda_{CX,0}}{\lambda_{ion,0}}} \quad (16.16)$$

or

$$\int_0^\infty n_e \langle \sigma_{ion} v_{th,e} \rangle n_0 dx = \frac{p_0}{\sqrt{T_0}} \sqrt{\frac{\gamma k}{\mu m_{prot}}} \sqrt{\frac{\lambda_{CX,0}}{\lambda_{ion,0}}}. \quad (16.17)$$

This gives a relation between neutral and plasma pressure, resulting in

$$q_{||,targetplate} = 10^4 \sqrt{\frac{\gamma}{\mu}} p_b \frac{\Theta M}{2\Theta \sqrt{\frac{\gamma}{\gamma+1}} + M \sin \alpha} \sqrt{T_{ed}} (\delta_e + \frac{\epsilon_{ion}}{T_{ed}}) \quad (16.18)$$

where

$$\Theta = \sqrt{\frac{T_{ed}}{T_0}} \sqrt{\frac{\lambda_{CX,0}}{\lambda_{ion,0}}} \quad (16.19)$$

Plotting  $\frac{q_{||,targetplate}}{p_b}$  (where temperatures and  $\epsilon_{ion}$  are in eV, all other quantities in SI) one gets, for typical ITER conditions ( $n_{e,b} = 0.5 - 1.0 \cdot 10^{20} m^{-3}$ ,  $T_e = 100 - 500 eV$ ), the operational point for a desired heat flux value of  $5 MW/m^2$  in a temperature range between 1 and 3 eV (Fig. 16.6), consistent with the assumption of an semi-detached state made at the beginning.



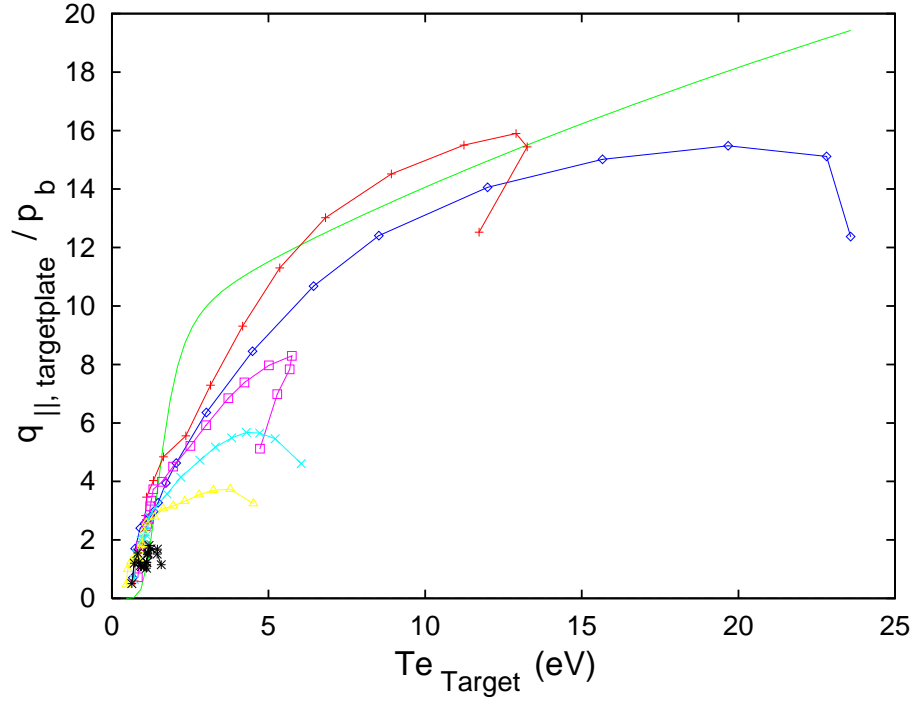


Figure 16.6.: Parallel power flux to the plate normalised to the upstream pressure  $q_{||, targetplate} / p_b$  as a function of the plasma electron temperature at the target plate (see text).

For comparison with the simple model, data from several B2-Eirene runs are also shown (Fig. 16.6). Calculating for each run locally at the (outer) target plate, this function gives the additional lines (for different input powers) in the plot, showing an overall good agreement between the simple estimate and more complex modelling. Deviations originate from the fact that the assumption of strictly 1-D transport is not valid.

In ITER, there is a strong limitation of the maximum  $Z_{eff}$ , compatible with ignition (max. 1.6; 0.3 already from He, Be [68]). Impurities (like He and Ne) are even earlier in a situation, where they have longer mean free paths than typical SOL widths compared to D. Therefore, there is the need for strong impurity entrainment: ideally, a strong flow of D into the divertor produce a dominating friction force able to overcome the thermal force pushing the impurities back to the main chamber. As a consequence, flame detachment characterised by complete energy and momentum detachment and a large reduction of particle fluxes to the plate will be probably unacceptable (also problems with stability: formation of X-point radiation instabilities - MARFES - [84, 85]). Layer detachment (similar to high recycling conditions, but in contrast to these already energy detached) offer the best perspective. Operating in this layer detachment is quite delicate and needs advanced feedback control (probably of divertor neutral gas deuterium and low-Z seed impurity densities to control divertor losses and pumping as well as medium or high-Z seed impurity densities in the main chamber to control the main chamber radiation), because the transition to flame detachment has to be avoided, but is possible as demonstrated experimentally (CDH mode in ASDEX Upgrade [86]) and in simulations. In the simulation for ITER a scenario was found where it is possible to radiate enough

power at a proper position in the divertor in a stable state, compatible with helium particle exhaust and core confinement [87].



# 17. Time-dependent phenomena: Type III ELMs, MARFEs

To complete the discussion of the impurity effects time-dependent scenarios have to be included as well.

## 17.1. Type III ELMs

### 17.1.1. Edge operational diagram

To structure the operational scenarios it is helpful to look at the so-called edge operational diagram [88, 89, 90]. Here, the electron temperatures and densities 2 cm inside the separatrix are plotted (Fig. 17.1). Several regimes can be seen, where most of them are characterized by time-dependent effects. Type I ELMs are consistent with an ideal ballooning limit scaling (as already discussed before). Going to lower boundary tempera-

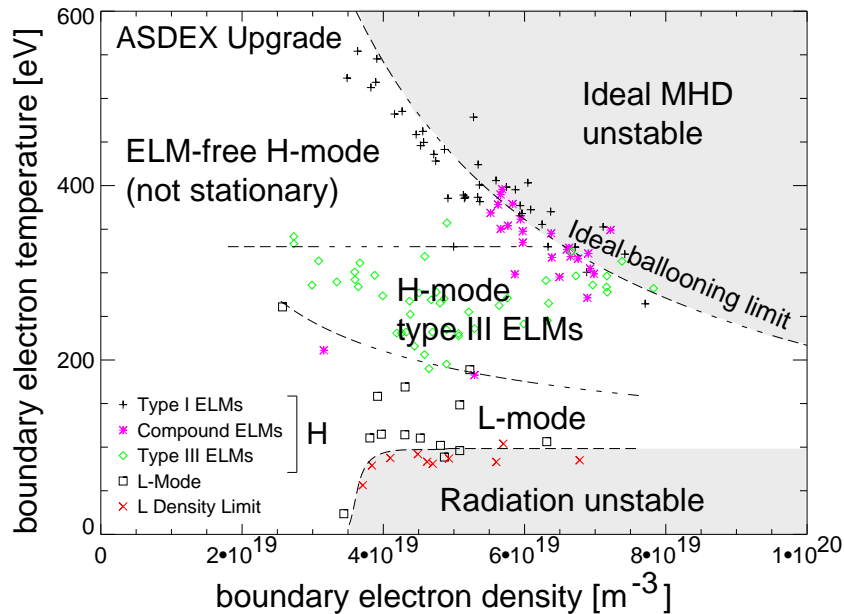


Figure 17.1.: Electron temperatures and densities 2 cm inside the separatrix for various ASDEX-Upgrade scenarios [88].

tures one gets smaller type III ELMs, which are possibly related to resistive instabilities

and their frequency decreases with power [50]. Falling back to L-mode, which is the only scenario without time-dependent effects and is therefore already covered by the discussion done before (e.g. SOL density limit), one ends in the radiation unstable part (MARFEs). Therefore, the characterization of the type III ELM regime and the radiation unstable part (MARFEs) require both a time-dependent analysis and a full set of physics including impurities. After the discussion of the basic physics ingredients including impurities, this part will be used to demonstrate the interaction of very different mechanisms and aspects of the SOL physics, from the impurity production mechanism up to time-dependent impurity radiation effects. This most complex combination of all SOL physics ingredients presented up to here will be the topic of this chapter.

### 17.1.2. Completely detached H-mode at ASDEX Upgrade

The analysis of type III ELMs in the CDH (completely detached H) mode [86] for ASDEX-Upgrade has to account also for the effect of impurities, because extrinsic impurities are used to experimentally control the detachment. Due to the combination of high neutral gas pressure in the divertor and additional (feedback controlled) impurity radiation losses by neon, stable operation close to the H-L back-transition threshold is established. The plasma shows H-mode confinement, but no longer burns through the divertor during strong type I ELMs, instead remaining detached in the sense of layer detachment with much smaller type III ELMs (Fig. 17.2).

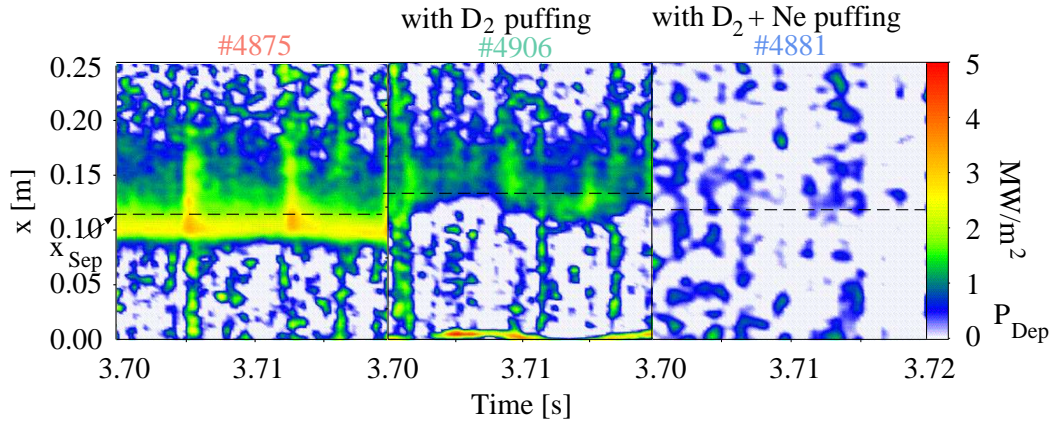


Figure 17.2.: Thermography profiles along the outer target plate (separatrix is marked by a broken line) for three different scenarios: type I ELMs burning through to the divertor at every ELM (left), strongly gas puffed scenario (middle) where the ELM effect is already smaller and combined  $D_2$  and Ne gas puffing CDH mode (right).

Carbon is produced at the target plates and side walls by physical and chemical sputtering (although physical sputtering is unimportant due to the low plasma temperatures). A chemical sputtering coefficient of 0.02 is used in B2-Eirene with the exception of the target plates. There, the value has to be reduced by a factor of 10 as otherwise the high carbon influx results in a radiation collapse. This reflects the experimentally ob-

served flux dependence of chemical sputtering. Neon is introduced by a gas puff in the modelling and is feedback-controlled to a separatrix neon density of  $3.0 \cdot 10^{17} m^{-3}$ . Typically, the CDH scenarios are run with all 4 NBI sources, e.g. an input power of about 7 MW. Adding neon into the simulation reproduces the experimental observation that the thermography profiles from the outer target plate show no longer any ELM effects and are below  $0.5 MW/m^2$  [85] (Fig. 17.3). One gets a reasonable overall agreement for

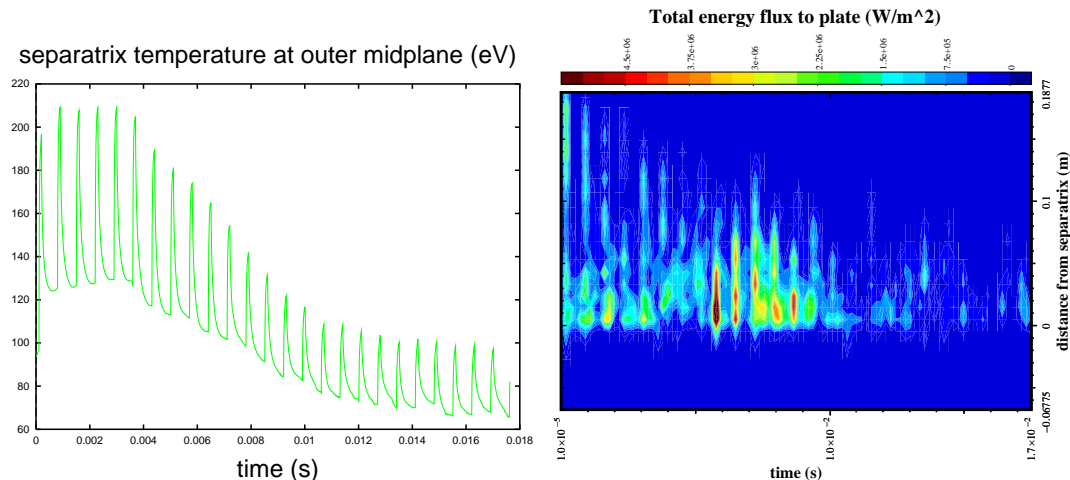


Figure 17.3.: Separatrix temperature in the outer midplane as a function of time (left) for a B2-Eirene run where neon is added at  $t=0$  s. Due to neon radiation losses the temperature drops and the excursion of temperature due to ELMs gets smaller. Modelled total energy flux to the outer target plate for adding neon in the B2-Eirene run (right). As in the experiment, one passes from a strong burn-through type I ELM-like phase to a completely detached quasi-stationary phase at the end.

the CDH scenario with midplane density and temperature profiles, target plate thermography, pressure gauges, bolometer and spectroscopy measurements for a hydrogen core density of  $8 \cdot 10^{19} m^{-3}$  (at the separatrix  $5 \cdot 10^{19} m^{-3}$ ) and the following anomalous transport coefficients: a particle diffusion coefficient of  $0.2 m^2/s$  was used for all species (no pinch velocity), electron and ion heat diffusivities of  $1.0 m^2/s$  in the core up to about 2 cm inside the separatrix and from there up to the SOL  $0.5 m^2/s$  (see Fig. 17.3).

As an example, the comparison of the modelling results with the experimental bolometer signals are shown in Fig. 17.4. To be able to obtain a reasonable fit of the bolometer signals for the radiation distribution, it is necessary to include a model for the type III ELMs (following the results of type I modelling [55]) by increasing the radial transport for a period of 0.1 ms to  $5 m^2/s$  in the whole domain, repeated every 0.7 ms (these times are chosen according to experimental CII, CIII measurements). The missing background is due to radiation in the core not covered by the B2 grid.

The type III ELMs stabilize the system, because they push (due to the enhanced power flow into the divertor during the ELM) the detachment zone closer to the plate, moving to the X-point again after the ELM. One sees a kind of dynamic jittering of the CII, CIII and  $H_{\alpha}$ - signals. This push-back effect allows then a larger radiation loss than without ELMs, where the radiation loss zone would have the tendency to form an X-point MARFE and

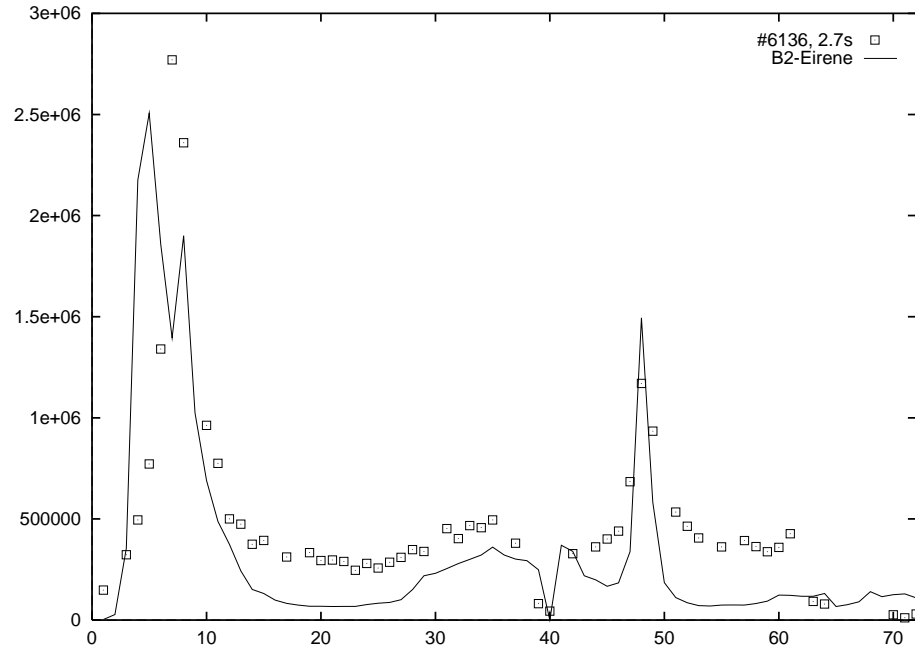


Figure 17.4.: Experimental (open symbols) and B2-Eirene (full line) bolometer signals.

move into closed flux surfaces.

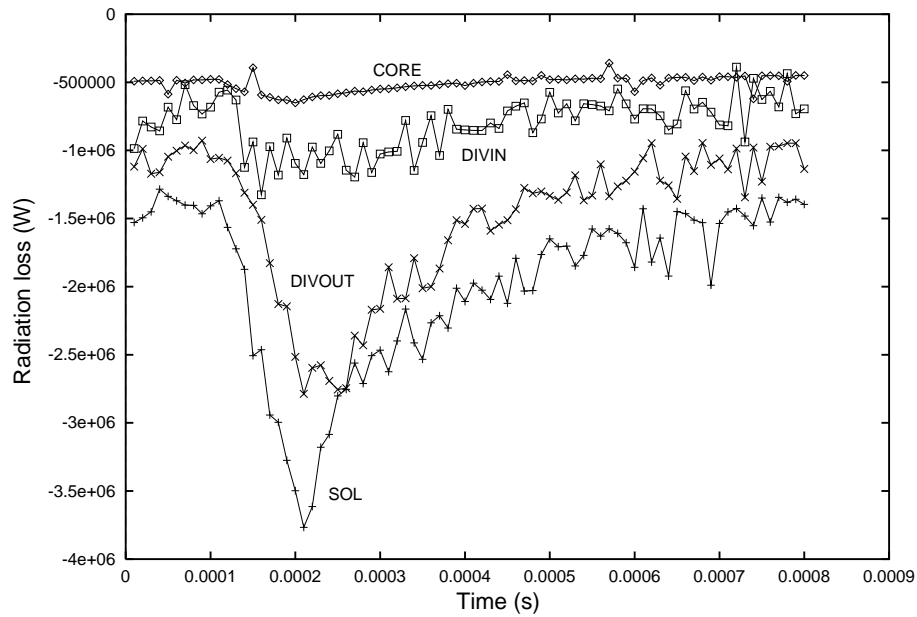


Figure 17.5.: Integral radiation loss in core, SOL above the X-point, inner and outer divertor during one type III ELM from B2-Eirene.

During the ELM due to the increased temperature at the midplane (a rise of about 10 eV) and the widened density profile energy losses from impurities increase strongly, partially buffering the ELM effect (Fig. 17.5).

### FLUX BALANCE (CDH)

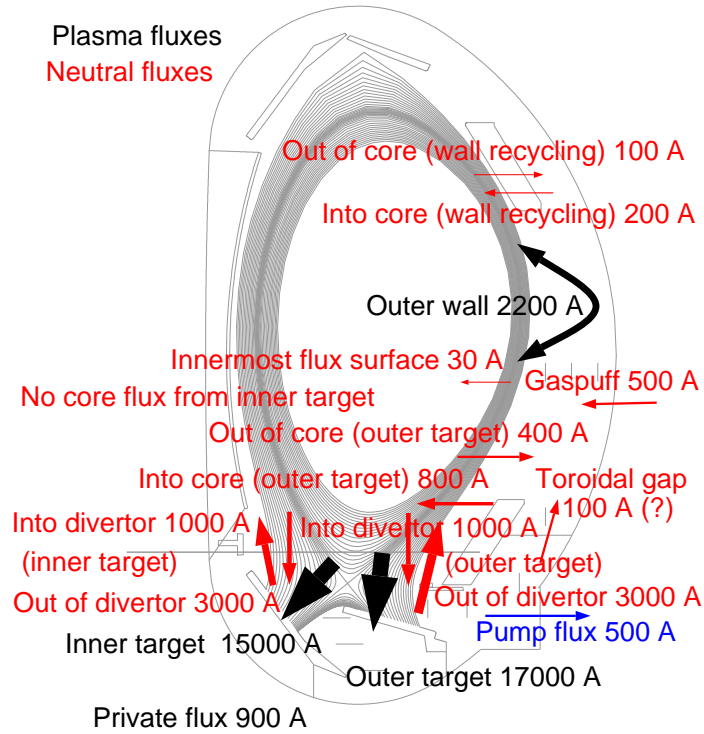


Figure 17.6.: Total particle flux balance for CDH

In the case of the CDH scenario it was possible to derive a total flux particle balance (Fig. 17.6). The intrinsic recycling fluxes are the dominant contributions, whereas the pumping fluxes are minor corrections to this. The contributions from main chamber recycling and divertor leakage fluxes to the neutral fluxes into the core over the separatrix are comparable to each other.

## 17.2. MARFEs

Another important time-dependent phenomena is the occurrence of a radiation instability, a so-called MARFE (multifaceted asymmetric radiation from the edge).

This radiation instability build up if one gets higher radiation losses at lower temperature. For the instability, the temperature dependence of the total sum of radiation losses (minus heating power) is important [91] (see Fig. 17.7).

Such a kind of condensation instability exists also in astrophysics. In solar prominences (a cloud of solar gas held above the surface of the sun by the sun's magnetic field) one has a condensation of the solar corona (see Fig. 17.8,  $T \sim 100\text{eV}$ ,  $n \sim 10^{14}\text{m}^{-3}$ ) with about 100 times larger density and lower temperature with a length-scale of  $10^4 - 10^5$  km and a lifetime of several weeks.

For tokamaks, this instability appears as a toroidally symmetric radiation belt close to the X-point (see Fig. 17.7). The MARFE is then characterized by a low temperature, usually



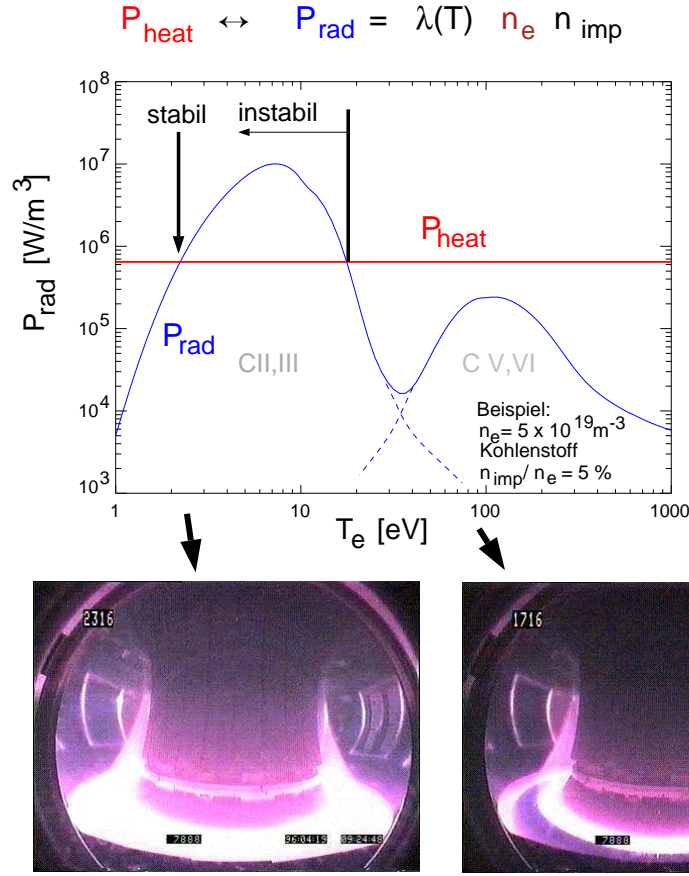


Figure 17.7.: The radiation function of carbon exhibits (depending on the local heating power), for electron temperatures below about 50 eV, an unstable branch, leading to the formation of a condensation instability at low temperatures. This results in a transition from low radiation level (concentrated in the divertor; see TV camera picture in the optical wavelength in the bottom right) to rather large radiation levels (concentrated close to the X-point; see TV camera picture in the optical wavelength in the bottom left).

starting from the X-point. Due to the fact that this region lies on closed field lines and neutral densities are rather small, the assumption of pressure constancy along fieldlines is very well fulfilled, resulting in quite large densities and therefore quite large radiation losses. Due to the relatively low temperatures (below about 50 eV), the counteracting parallel heat conduction, which would try to keep the temperature up at the X-point, decreases strongly with temperature and thus facilitates MARFE formation. From this, the simplest MARFE criteria is that a parallel temperature gradient from the midplane to the X-point can be established, e.g. the mean free path of the heat conduction (high energy) tail electrons has to be smaller than the connection length from midplane to the MARFE region at the X-point:

$$\lambda_{hc} < L_{||, \text{MARFE}}. \quad (17.1)$$

The MARFE will tend to occur at poloidal positions most separated in terms of connection



Figure 17.8.: The view of a solar prominence (27.1.1997, Big Bear Observatory, Caltech, USA).

length with respect to the cross-field heat source. The cross-field heat source is minimal close to the X-point for a single null case due to the large expansion of flux surfaces in its vicinity, and at the inner midplane for a double-null case (symmetry argument). The X-point in a single null is also characterized by a very small effective heat conduction coefficient due to the shallow pitch angle there, creating strong temperature gradients poloidally. In other terms, due to the long connection length in this region the radiation has a tendency to focus here.

Comparing the radiation functions of the different elements it is obvious that one has the possibility to custom-tailor the total radiation function by combining different impurities, like C plus Ne, and by this reduce the tendency for instability. In contrast to the low-Z elements, medium or high-Z do not have this pronounced instability branch in the radiation loss function (Fig. 17.9). Therefore, using e.g. neon as a radiator can reduce the instability formation and allow higher radiation losses before a MARFE is formed.

This radiation instability cools the plasma edge (Fig. 17.10), which can lead to growth of magnetic islands and finally to a disruption, if the current profile becomes unstable.

Tomographical reconstruction of bolometer measurements show the sequence which leads to a MARFE formation. One starts with radiation predominantly in the divertor with the radiation zone of the outer zone moving up to the X-point. As soon as the radiation is appearing on closed fieldlines the MARFE instability starts (Fig. 17.11).

The same sequence is well reproduced by B2-Eirene modelling [92].

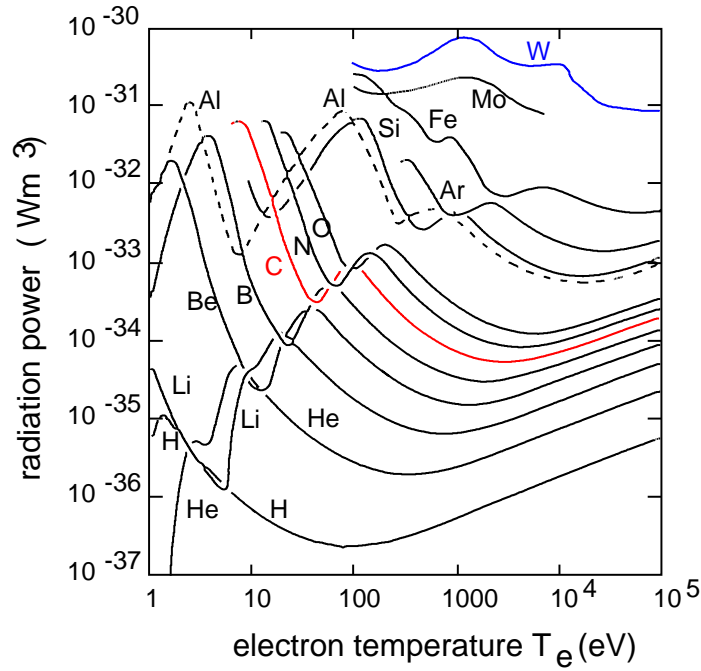


Figure 17.9.: Radiation power  $\frac{P_{rad}}{Vol \cdot n_e \cdot n_{imp}}$  as a function of electron temperature as a function of electron temperature (D. Post et al.)

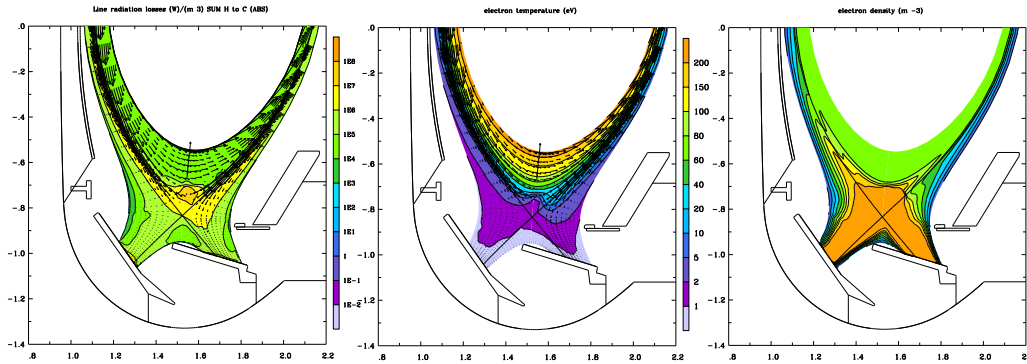


Figure 17.10.: Contours of radiation losses (left), electron temperature (middle) and electron density (right), for a MARFE in B2-Eirene. The MARFE is not characterized by 100% radiation loss, but there is still power flowing around the MARFE as can be seen from the arrows representing the total power flux. The MARFE is characterized by a high-density low-temperature region close to the X-point on closed fieldlines (maximum of radiation losses).

### 17.3. Characterisation of a stable MARFE

Using B2-Eirene a stability analysis of MARFE scenarios were done [93, 94]. If all discharge parameters (boundary conditions) are kept constant, it was found that MARFE plasma states are essentially unstable for multi-fluid calculations. Following the experimental procedure and including a feed-back loop on the impurity line radiation into the

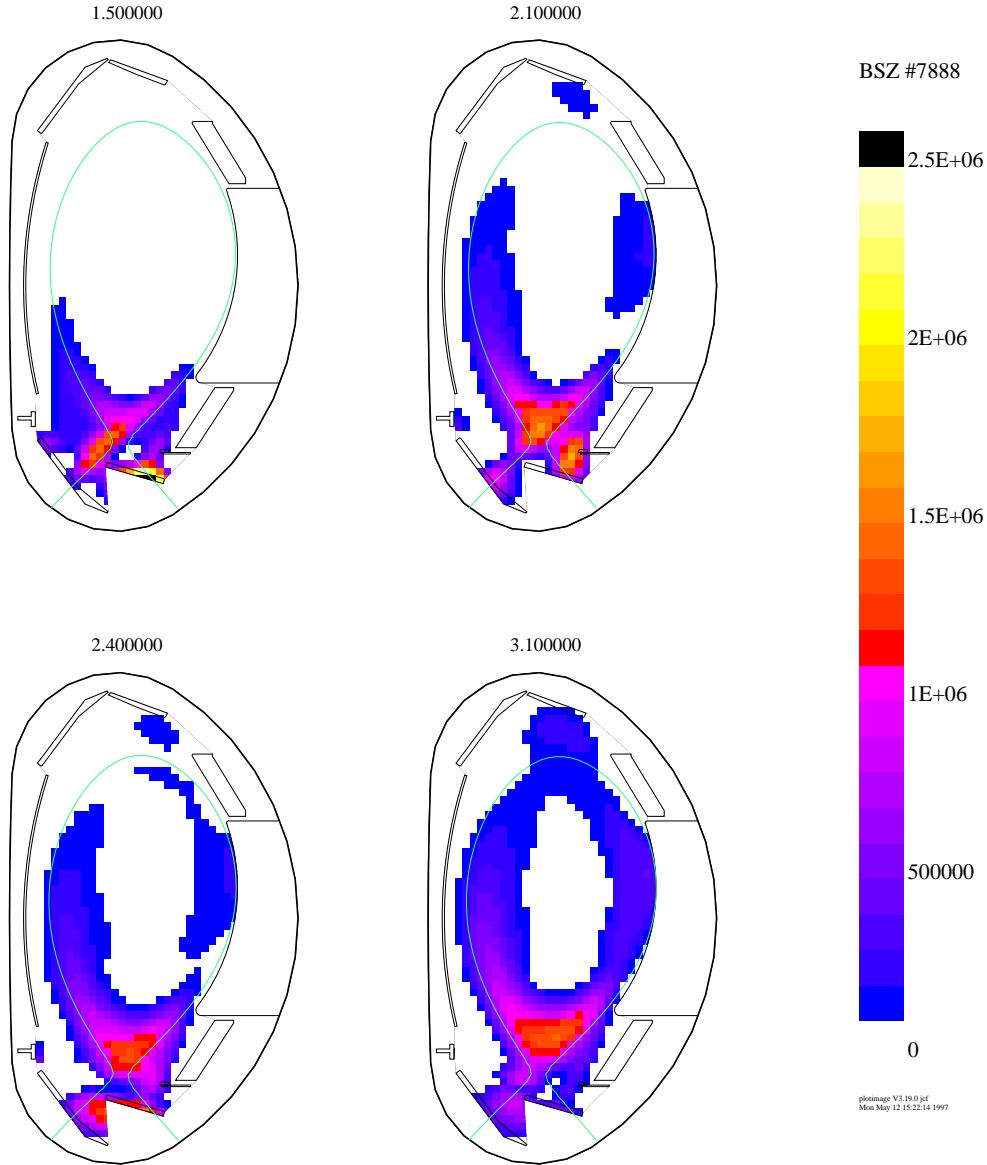


Figure 17.11.: Tomographical reconstructions of bolometer measurements of ASDEX-Upgrade shot # 7888 (C. Fuchs).

plasma equations controlling the external gas puff of deuterium to obtain radiation losses between 0 and nearly 100 percent, beyond a critical puff rate steady MARFE solutions, well separated from the B2 boundary, are obtained. Transient unstable MARFEs can be stabilized in this way.

The complete set of stationary solutions of this generalized system can be represented in a puff rate versus radiation losses diagram of steady states with a double-valued function, the two branches of which describing MARFE-free and MARFE plasma states, respectively. The internal mechanism of stationary MARFEs is as follows. The density maximum is sustained by a complex 2-D pattern of parallel and radial particle and energy fluxes (Fig. 17.12).

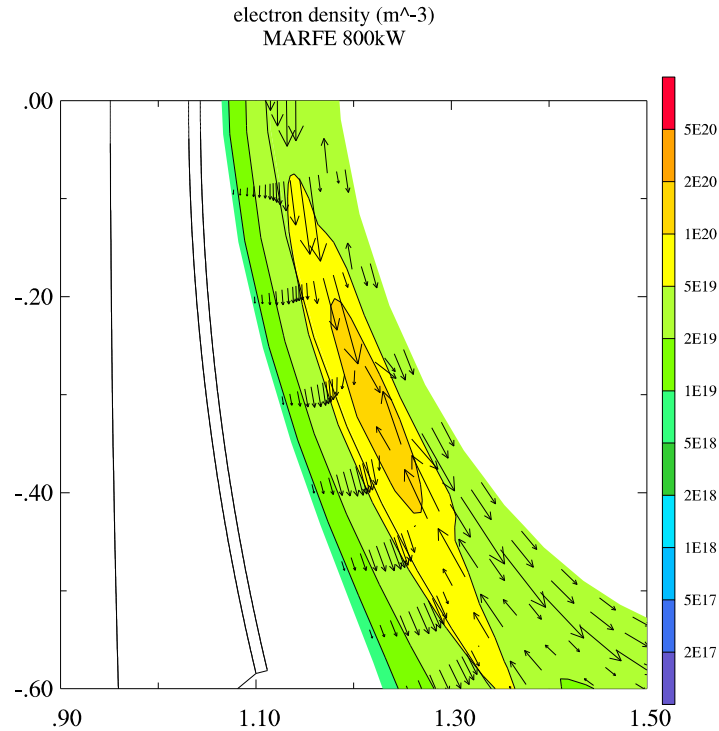


Figure 17.12.: Electron density contours for a feedback-stabilized main chamber MARFE. Arrows show the particle flux pattern for hydrogen.

The ions are transported to the density maximum in parallel direction and removed from there radially by anomalous diffusion. The dominant forces driving the deuterium and the lower charged carbon ions in the parallel direction to the density maximum are thermal forces, and, in the near vicinity of the density maximum, pressure gradient forces. They are essentially compensated by frictional forces. Even for higher charge states, where the thermal forces reverse their sign (driving the ions away from the temperature minimum), the ions are dragged to the density maximum, mainly due to strong frictional coupling with the background plasma.

Due to the existence of the large parallel flow into the MARFE, the MARFE acts as a strong pump inside the separatrix attracting the particle in this condensation instability. This leads, after the formation of an MARFE, to a drop of the outer separatrix density, because now this internal pump is switched on.

# 18. ASDEX-Upgrade DivII results

## 18.1. Divertor configurations

This chapter tries to analyze in detail one particular machine, including all the different aspects discussed before.

One of the critical questions to be solved for ITER (or any other reactor) is the exhaust problem for power and particles consistent with good core confinement. The operational point for ITER even slightly above the Greenwald limit motivates the analysis of high density operation, especially for detached divertor conditions [95].

Optimised divertors have to be tested in existing machines based mainly on the idea of closing them very efficiently to the main chamber and, by the choice of the plate and baffle geometry, positively influencing the detachment properties and reducing the target power load especially close to the separatrix. Additionally, ASDEX Upgrade needed an improved divertor to be able to operate at increased heating power, especially with doubled NBI power of up to 20 MW for deuterium, without target power load problems leading e.g. to carbon blooms.

Results with the original, relatively open (Div-I) divertor configuration are compared with those obtained with the new, fairly closed LYRA divertor (Div-II), being more similar to the present ITER reference design (Fig. 18.1). Detached operation is favourable as an op-

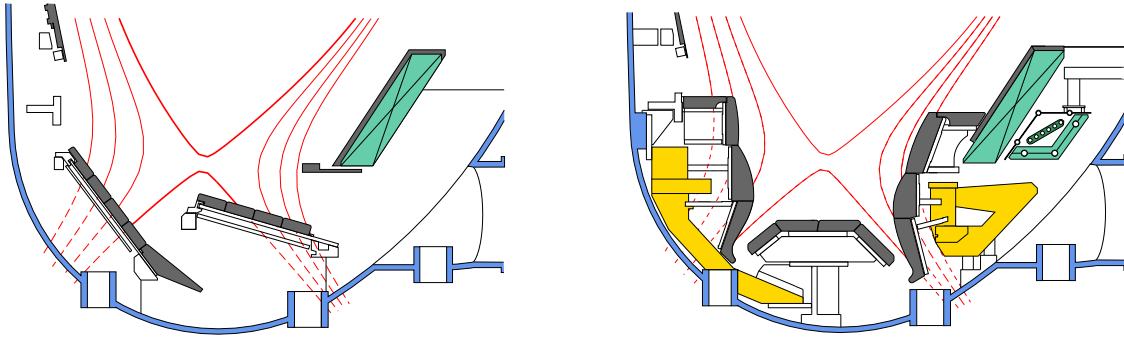


Figure 18.1.: Poloidal cross-section of ASDEX-Upgrade with Div-I (left) and Div-II in the Lyra configuration (right).

erational scenario to solve the peak power load problem by reducing the target power loads to values below  $5 \text{ MW/m}^2$ . In detached divertor operation one can identify essentially three loss mechanisms for reducing the target power load. The first one, if one starts from the target plate, is the loss through hydrogen, predominantly through radiation, which occurs at about 5-7 eV. The relatively low temperature also means that this loss channel

gets important only if already others have reduced the temperature and parallel power flow considerably compared to the midplane. The hydrogenic losses are determining the detachment physics and - through the pressure balance profile along fieldlines - midplane scrape-off layer profiles and by this even core performance, e.g. through a scrape-off layer density limit. The charge exchange energy losses by hydrogen atoms are getting important only for the gas target cushion, removing the remaining small part of the parallel heat flux in front of the target and allowing onset of strong volume recombination [39]. The second loss mechanism is the loss through impurity radiation, which in the case of carbon as the dominant intrinsic impurity is occurring between 10-15 eV. These losses are very beneficial for the power load problem, because they do the necessary reduction of power flux and temperature to make the hydrogen losses important. A last mechanism can be the spreading of the power flow by radial transport. As we will see, it is also important in the analysis of the behaviour of the two divertor configurations in ASDEX-Upgrade, especially for reduction of peak power loads even in attached operation.

The Div-I configuration (Fig. 18.1) was characterised by flat horizontal divertor plates, where the outer target plate was put close to the X-point to benefit from the large flux expansion in that region. The material was fine grain graphite. It had a relatively open divertor chamber with a small pumping baffle in the outer divertor, which nevertheless was quite important for good particle exhaust. For pumping, 14 turbomolecular pumps adjacent to the outer divertor plate provide  $12\text{ m}^3/\text{s}$  total pumping efficiency.

The new, fairly closed Div-II (Fig. 18.1) has curved vertical plates, is relatively deep and well baffled towards the main chamber. To maximize power exhaust capability even for attached conditions, CFC is used at the strike points. The pumping is done through the private flux region, where a dome baffle is used to enhance pumping. In addition to the turbomolecular pumps, a cryopump has been installed with a pumping efficiency of  $100\text{ m}^3/\text{s}$ .

## 18.2. Detachment properties

The old Div-I had an practically orthogonal inner plate and an outward tilted outer plate, reflecting the neutrals away from the hot zone close to the separatrix into the outer scrape-off layer.

In contrast, the rationale for the construction of the Div-II configuration was the optimization of neutral losses in the region close to the separatrix by strongly tilting the plate to reflect the neutrals preferentially into this hot region (Fig. 18.2). This causes quite different detachment properties.

In Div-I, detachment as defined by a drop of the total ion saturation current by at least one order of magnitude, developed rather uniformly and rather close to the density limit. In Div-II one observes an earlier detachment at the separatrix associated with an earlier onset of strong volume recombination (Figs. 18.3 and 18.4).

This is accompanied by an earlier drop of the separatrix ion saturation current compared with Div-I as predicted by B2-Eirene modelling (Fig 18.5).

This reduction of detachment threshold with geometry was already seen on Alcator C-Mod [96] and in the new JET MK-II divertor [97].

## B2-Eirene modelling:

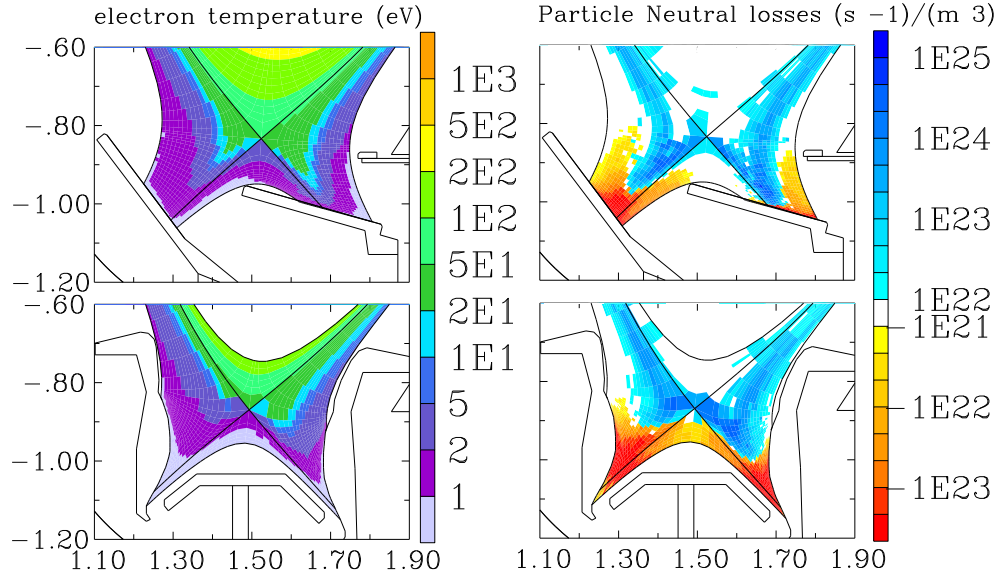


Figure 18.2.: B2-Eirene modelling results for the same upstream conditions for Div-I and Div-II. The electron temperature contours (left) show for the Div-II already quite low temperature close to the separatrix, where also the neutral losses (right) are maximum due to the preferential reflection of neutrals from the target plate into this direction.

## Langmuir divertor probes (density ramp-up)

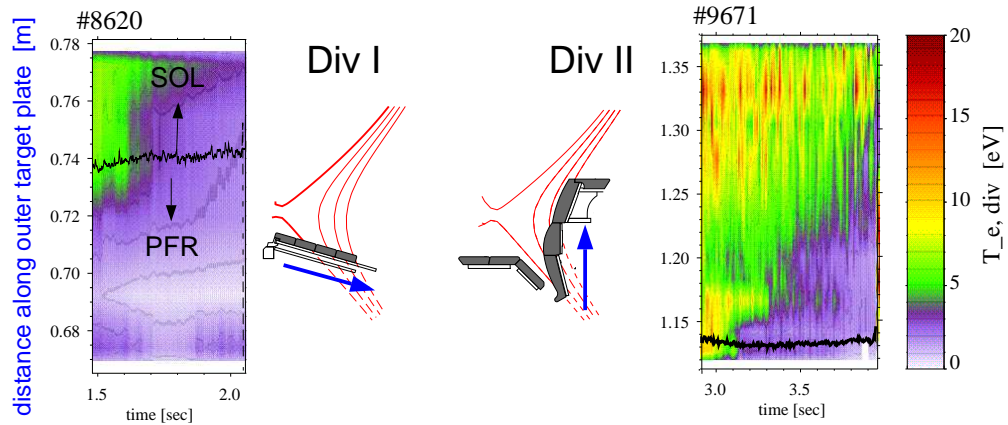


Figure 18.3.: Time-dependence of measured Langmuir saturation currents for similar conditions along the target plates of Div-I (left) and Div-II (right). In Div-I there is an abrupt change of the ion saturation current close to the density limit, but in a rather uniform way. In Div-II one observes an earlier detachment at the separatrix extending then further out into the SOL. The far outer SOL stays attached up to the density limit.



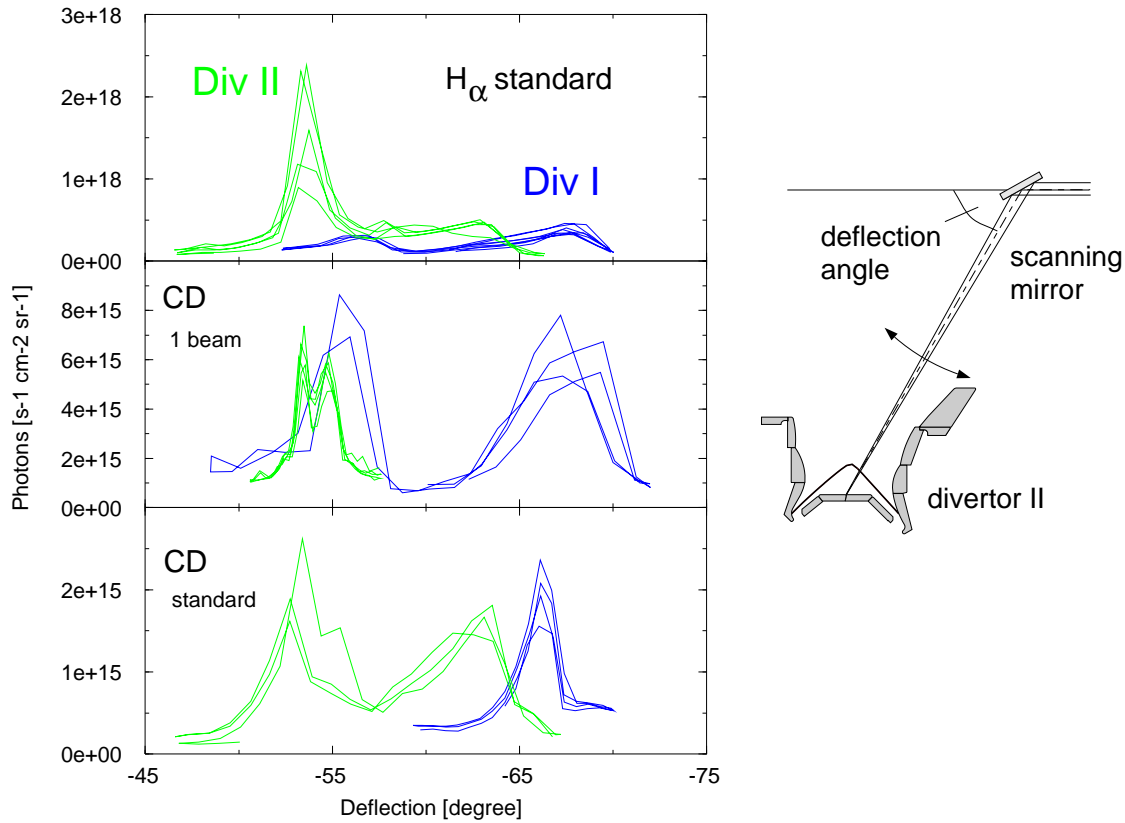


Figure 18.4.: Spectroscopic measurements (left) of  $H_\alpha$  (top) as a function of deflection angle. The results are shown for both Div-I and Div-II for standard ohmic shot conditions and same line integral density range. Different curves represent different scans in time, respectively for different line integral densities. The location of the inner and the outer divertor are indicated in the top part of the figure. For Div-II the deepest part of the outer divertor is hidden by the divertor modules (see right part of the figure). For line integral densities, where one observes for Div-II a strong  $H_\alpha$  emission in the inner divertor a much lower and more uniform  $H_\alpha$  distribution is seen for Div-I. The strong  $H_\alpha$  emission is a kind of fingerprint for the onset of strong volume recombination, existing at this range of line integral densities already in the inner divertor of Div-II, but not for Div-I. The spectroscopic measurements of CD band emission for same standard ohmic shot (bottom) and NBI heated shot conditions (middle) show no large difference for both divertor configurations. For some measurements the scan was not done for the whole divertor. On the right side the schematic setup of the spectroscopic lines-of-sight is shown.

Detachment in Div-II progresses from the separatrix to the outer scrape-off layer, which stays attached up to the global density limit. This effect also shows up in the B2-Eirene simulations. From these calculations, one also understands the observation that the earlier drop of the separatrix ion saturation current in Div-II is not seen in the total integrated particle flux, because in Div-II the outer scrape-off layer stays attached due to inverted temperature profiles up to a global detachment of the target plates. This defines for Div-

## B2-Eirene:

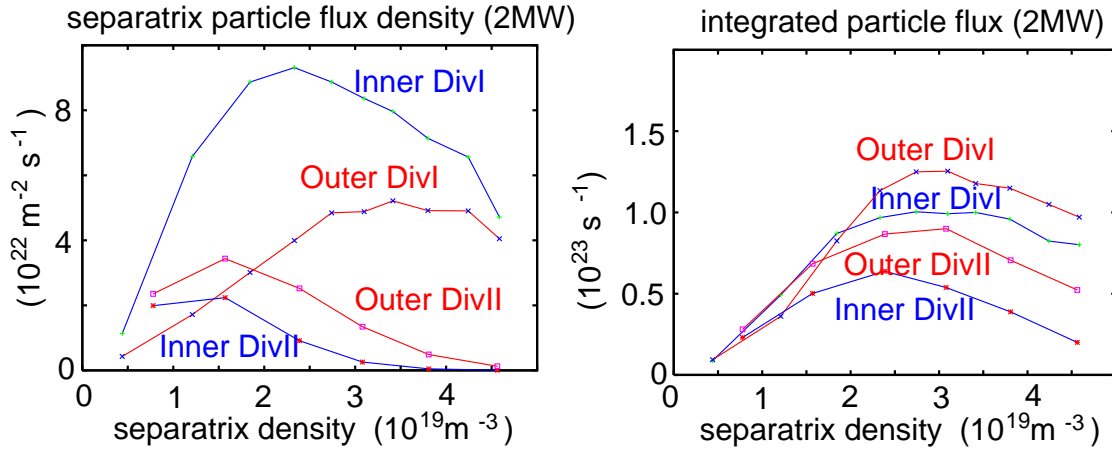


Figure 18.5.: B2-Eirene density-scan for pure hydrogen plasmas with 2 MW input power. On the left side, the dependence of the separatrix particle flux density is shown as a function of midplane separatrix density for inner and outer target in Div-I and Div-II. On the right side, the same dependence is plotted for the integrated particle flux.

II an optimum operational window with a factor of 2 difference for upstream separatrix densities between start of detachment at the separatrix and complete global detachment, associated with the appearance of a MARFE on closed field lines and with the global L-mode density limit. This makes plausible that the global density limits for Div-I and Div-II are the same both in L and H-mode.

Specific detachment studies are possible in Div-II due to the new diagnostics installed there. A detailed study of the recombining state was possible. This recombining phase is determined by the formation of a recombination-ionization double layer, where, in the net recombining zone close to the target plates, the plasma gets neutralized forming a kind of virtual target below a temperature of about 1 eV as measured by spectroscopy [98]. The neutrals then travel upstream in a 2-D way by leaving the zone sideways and getting through multiple reflections at the side walls and the plasma into hotter upstream regions where they are ionized (5-7 eV) [39]. In this ionization front zone one drives quite large Mach flows even up to or above Mach 1, as measured with a fast moveable Langmuir divertor probe [99], due to the large neutral sources there (Fig. 18.6).

In contrast, the net recombination zone is characterized by quite small flow velocities, as measured with a sophisticated toroidally viewing spectroscopy system [100], giving the plasma enough time to recombine (Fig. 18.7). For a combined NBI heating ramp with increasing the line-averaged and by this the divertor neutral density (top) one gets several phases where the divertor starts to detach (reduction of CIII-signal as a signal for temperature below about 3 eV; middle part) and reattach with increasing heating power. For the detached phases one gets a considerable slowing-down of the hydrogenic flow close

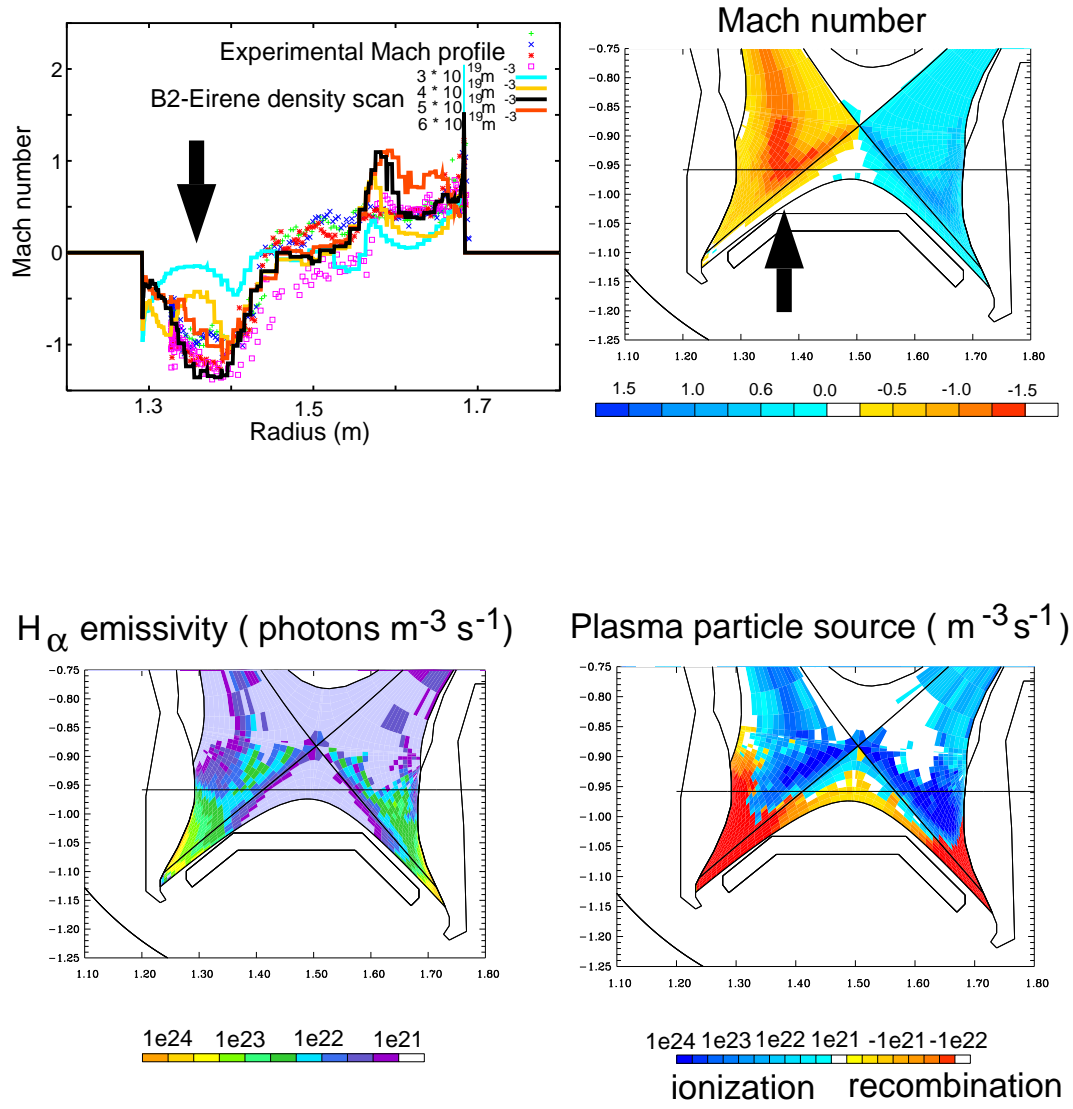


Figure 18.6.: Experimental (top left) and modelled (top right) Mach profiles. The experimental values are taken for several midplane densities along the line indicated in the contour plot of the modelling result. The arrows indicate the region where one gets both in experiment and modelling rather large Mach numbers in between X-point and target plate. The modelling result is shown for a density where the detachment front is just passing through the experimental line-of-sight. This can be seen from the calculated  $H_\alpha$  (bottom left) and particle source (bottom right), showing the typical double layer structure with strong recombination (and enhanced  $H_\alpha$ ) close to the plate and ionization zone upstream.

to the separatrix in agreement with the modelling prediction.

## Density Ramp in L-Mode:

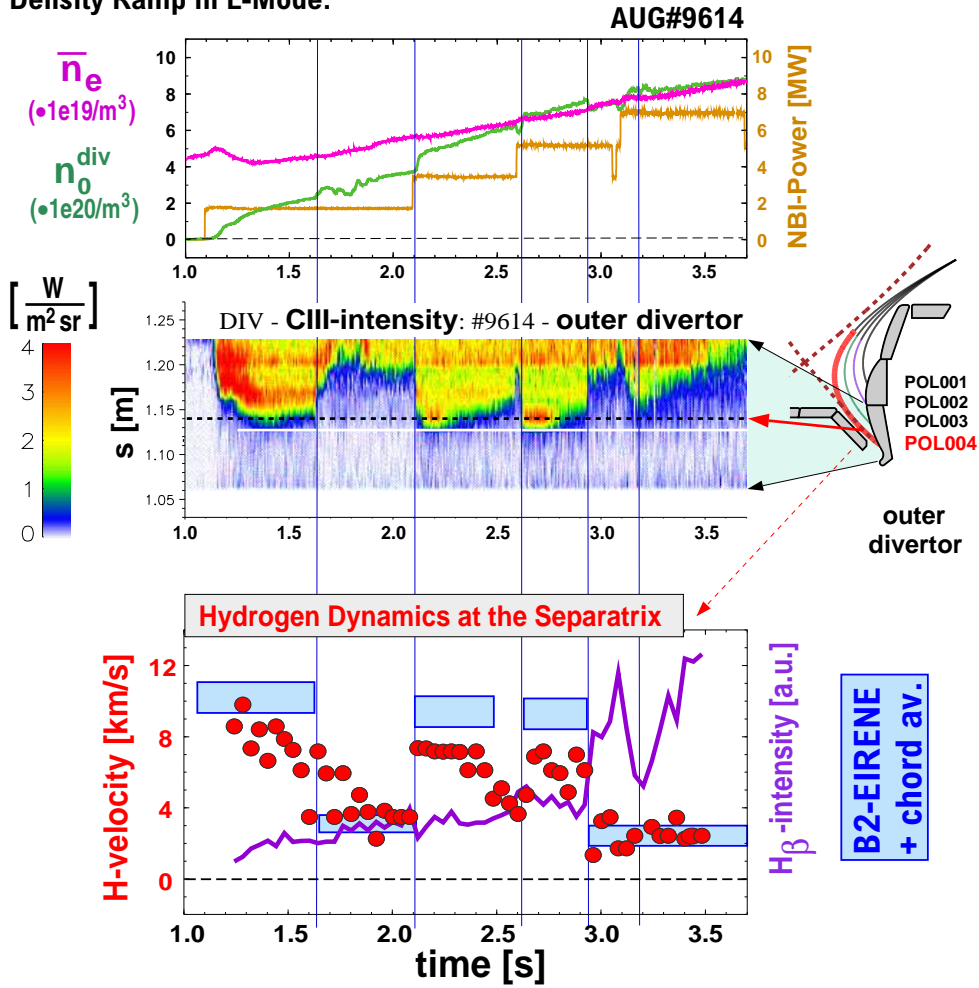


Figure 18.7.: Experimental measurements of the velocity of hydrogen ions close to the separatrix compared with modelling results (bottom). As an indicator for the onset of volume recombination also the experimental signal for  $H_{\beta}$  is shown. For a combined NBI heating ramp with increasing the line-averaged and by this the divertor neutral density (top) one gets several phases where the divertor starts to detach (reduction of CIII-signal as a signal for temperature below about 3 eV; middle part) and reattach with increasing heating power. For the detached phases one gets a considerable slowing-down of the hydrogenic flow close to the separatrix in agreement with the modelling prediction.

### 18.3. Divertor power load

The power distribution on the divertor in Div-II is much broader than in Div-I, resulting in a large reduction of peak power loads both in L and H-mode (factor of 2-4) and allowing now safe operation with less than  $4 \text{ MW}/\text{m}^2$  in the full operational range without problems for the target plates even with 20 MW input power in H-mode [101]. This very positive effect is more than expected from simple geometry, because the outer target plate of Div-I

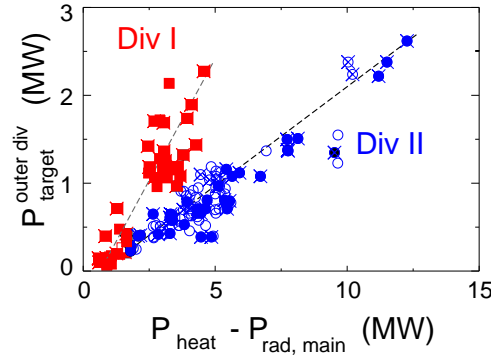


Figure 18.8.: The total power reaching the outer target plate  $P_{target}^{outerdiv}$  as measured with thermography is shown as a function of the power going into the divertor, which is the difference of heating power  $P_{heat}$  and main chamber radiation  $P_{rad,main}$  as determined from bolometry. Open symbols are hydrogen, full symbols deuterium shots. Crosses indicate H-mode conditions.

had the same geometrical reduction due to field line inclination as the outer target plate of Div-II. The first did benefit from the large flux expansion close to the X-point, whereas the Div-II achieves the same by tilting the plate. Comparing the total power reaching the outer target as a function of the total heating power minus the radiation loss in the main chamber above the X-point (Fig. 18.8), it is obvious that the radiation losses in the divertor of Div-II are much larger than in the Div-I (by the factor of 2-4). Comparing the bolometer deconvolution of radiation for two similar shots, the radiation pattern in Div-II is much more concentrated in the divertor with a pronounced maximum in the divertor tip and an emission zone of carbon close to the separatrix, resulting in a larger divertor radiation for Div-II (Fig. 18.9).

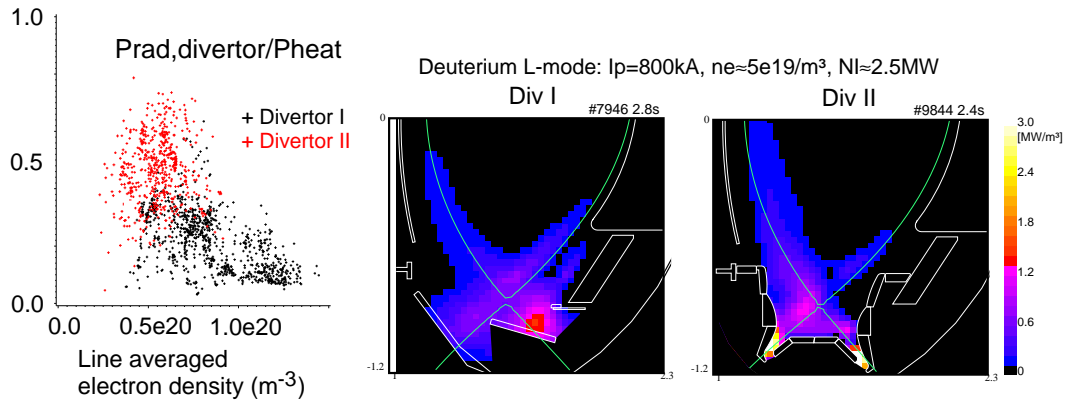


Figure 18.9.: Left: normalised divertor radiation as a function of line-averaged electron density  
Right: radiation pattern from bolometer lines-of-sight deconvolution for similar upstream conditions for Div-I (left) and Div-II (right).

Doing vertical-shift experiments the resolution of the bolometer system can be improved considerably allowing to identify the predicted radiation pattern along the separatrix (Figs. 18.10 and 18.11).

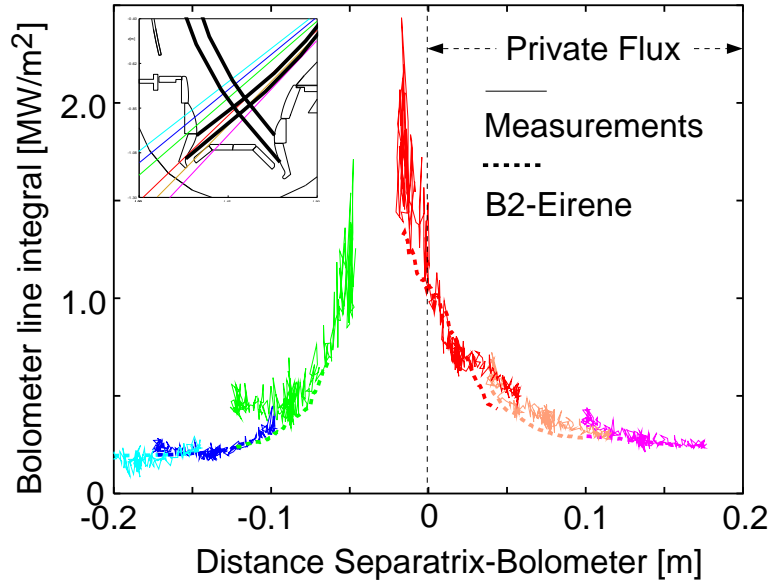


Figure 18.10.: Measured and predicted bolometer line integrals for z-shift experiments creating additional bolometer lines-of-sight for improved resolution of the separatrix-near region of the inner divertor. Both experimentally and in modelling it was checked that the z-shift can be interpreted like just moving the divertor up and down without changing the conditions.

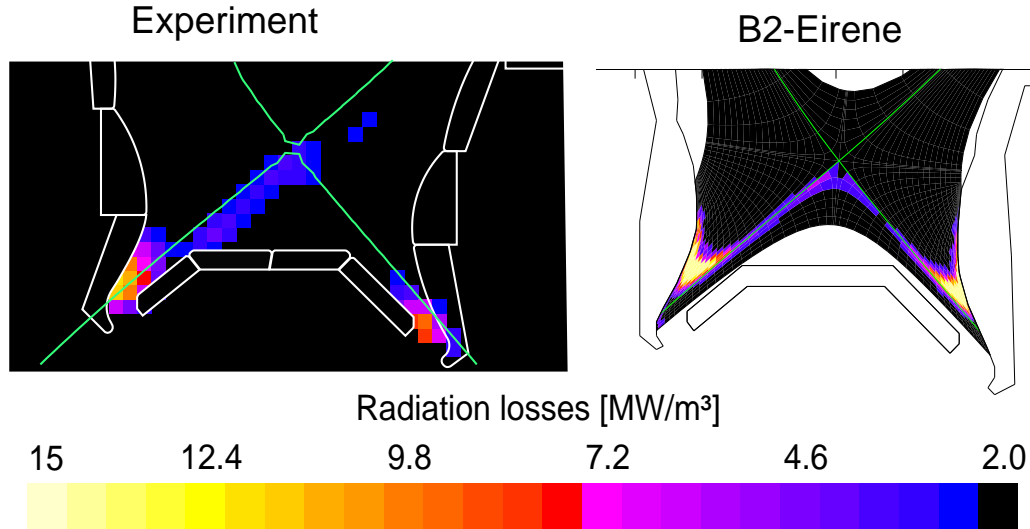


Figure 18.11.: Radiation losses as derived from the deconvolution of the experimental bolometer signals and from B2-Eirene calculations. A radiation band close to the separatrix can be identified.

For the reduced power load, the different possible loss mechanisms have to be discussed. For relatively low power cases (total input power below about 2 MW), the effect of the preferential reflection of neutrals towards the separatrix with maximized losses there can already explain, for pure plasma conditions, a factor of 2 reduction at high densities (Fig.

18.12).

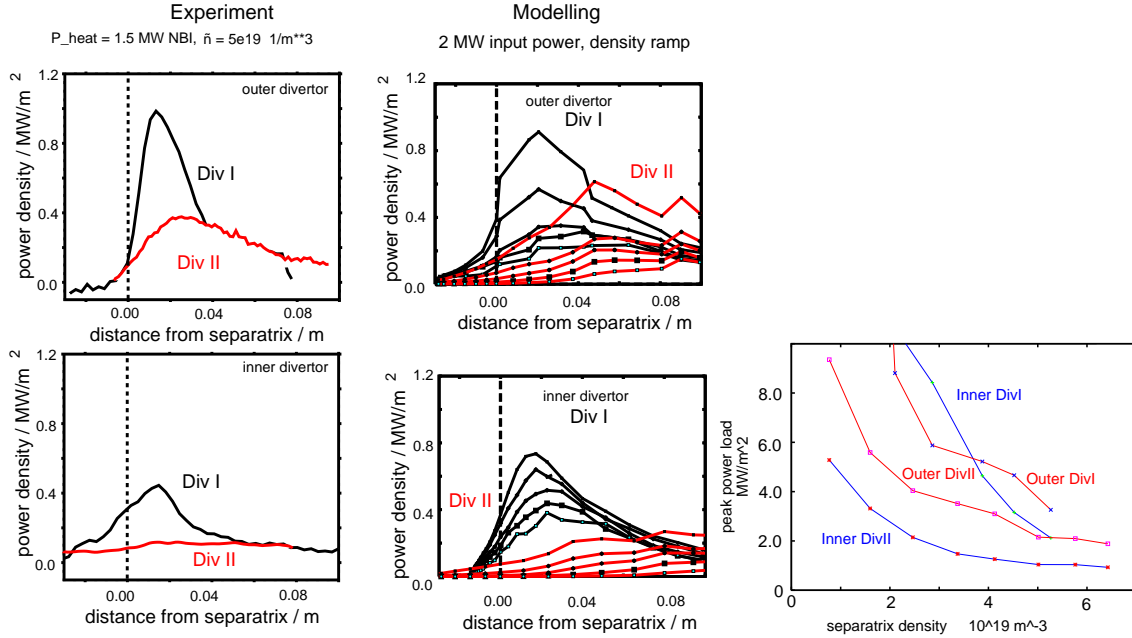


Figure 18.12.: Power density profiles for similar experimental conditions for Div-I and Div-II (left). Modelling predicts the same trend for density ramp-up due to preferential reflection of neutrals towards the separatrix (middle). This leads to a reduction of the peak power load at the target in the modelling results (right).

However, the experimental results of thermography, calorimetry and Langmuir probes show this power load reduction also for attached conditions. That this effect has to be related to changes of the radial transport (or changes of the radial flow pattern) in the divertor region and not to changes of the upstream transport is experimentally indicated by no significant change of the midplane energy fall-off length from Div-I to Div-II [102].

In the code predictions, the larger compression of the flux surfaces in the deeper Divertor II results in larger anomalous radial fluxes when they are assumed to be described as a diffusion process determined by the local gradient in real space (Fig. 18.13).

This produces already for attached conditions a considerable broadening of the profile and by this a reduction of the power load maximum. If the diffusion process is assumed to be constant in flux-coordinates, this effect disappears.

Comparing the spectroscopically measured impurity production, e.g. by measurements of the CD bands (Fig. 18.4), for Div-I and Div-II, the larger divertor radiation in Div-II cannot be understood by larger impurity production. The large values for the radiation losses of up to  $10 - 20 \text{ MW/m}^3$  in Div-II can be explained by both the radial transport, allowing to enhance the radiation volume [69], and the transport of energy into the radiation zone not only by conduction but predominantly by convection in the cold divertor region as already discussed by DIII-D [103].

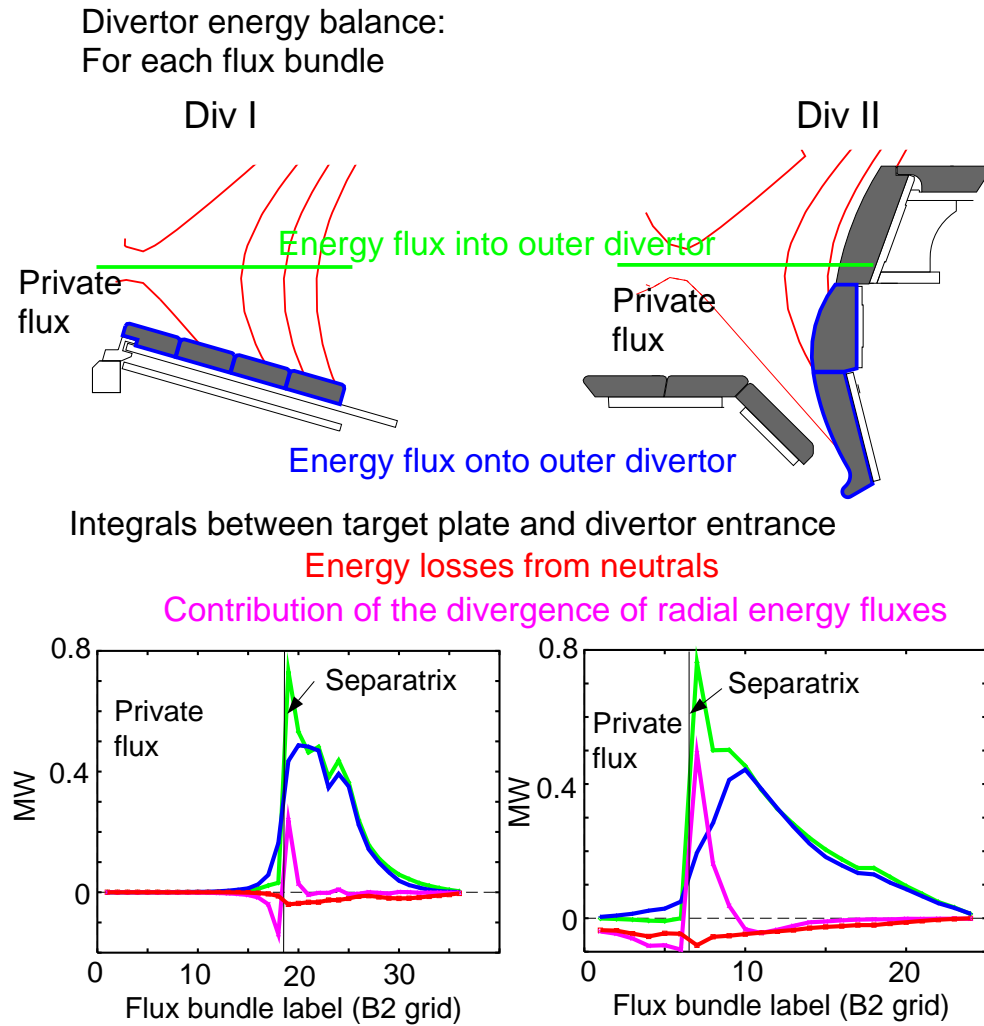


Figure 18.13.: Calculation of the divertor energy balance (top). For each flux bundle the integrals between target plate and divertor entrance of energy losses from neutrals and the contribution from the radial diffusion if assumed to be determined by the local gradient in real space are compared (bottom). Also shown are the energy fluxes into the outer divertor (which are the same for both configurations) and the energy fluxes onto the plate.

The earlier onset of volume recombination in Div-II close to the separatrix also enhances the carbon losses there, since due to the slowing down of the parallel flow in this region, one gets a higher density of deuterium or hydrogen there. Also, the carbon residence time in the separatrix-near region is large, because the carbon ion mass flow pattern (Fig. 18.14) shows a flow reversal zone due to the ion thermal force with small flow velocities close to the separatrix and a forward flow in the outer scrape-off layer with relatively fast flow [100].

Spectroscopically determined radiation potentials for the dominant divertor radiator CIII, defined as the ratio of the radiation power emitted from the CIII charge state along a



Large losses obtained in Div II:  
radial transport (radiation zone inclined to fieldlines)

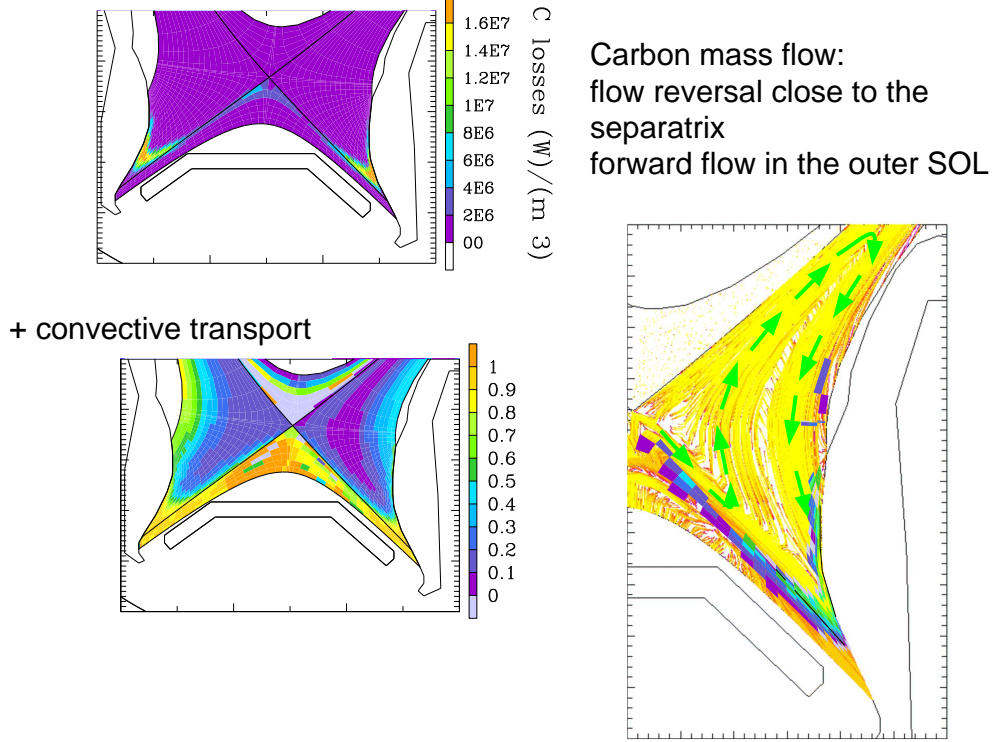


Figure 18.14.: Location of the carbon losses from B2-Eirene (left top) and ratio of convective to conductive transport (left bottom) from B2-Eirene for Div-II. The large values for the radiation losses of up to  $10 - 20 \text{ MW/m}^3$  in Div-II can be explained by both the radial transport, allowing to enhance the radiation volume and the transport of energy into the radiation zone not only by conduction but predominantly by convection in the cold divertor region. The ion mass flow pattern (right) for a B2-Eirene simulation with hydrogen and physically and chemically sputtered carbon for 4 MW input power and a midplane separatrix density of  $2.6 \cdot 10^{19} \text{ m}^{-3}$ . Trace particles are started according to the distribution of the total carbon density in the outer divertor and followed according to the radial and parallel velocities until they reach either a B2 side-wall or the target plate. The total carbon velocities and densities are obtained from the sum of the individual transported carbon charge states. The flow pattern is characterized by a flow reversal zone close to the separatrix and a forward flow zone in the outer scrape-off layer. For guiding the eye, the green arrows show one possible carbon trajectory. Also shown is the location of the ionization of the neutral carbon close to the separatrix and close to the plate.

line-of-sight and the influx of CIII along this line-of-sight getting ionized, are strongly temperature-dependent, as shown in Fig. 18.15 using the ADAS database [104].

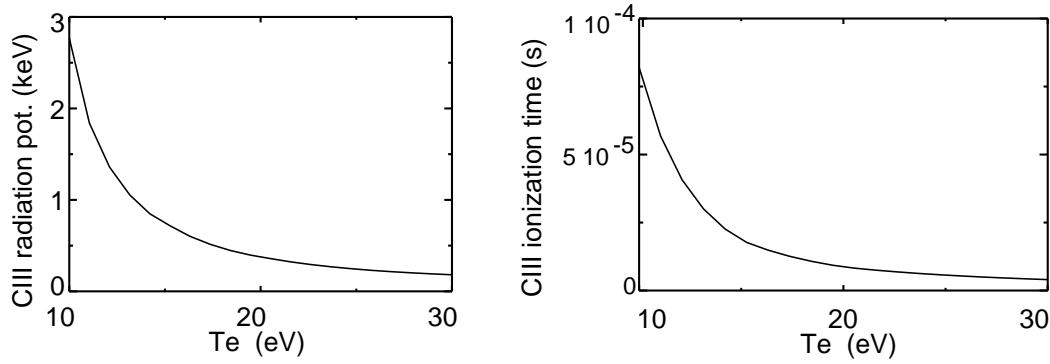


Figure 18.15.: CIII radiation potential as a function of temperature (left) from ADAS for an electron density of  $1.0 \cdot 10^{20} \text{ m}^{-3}$ . CIII ionization times as a function of temperature (right) from ADAS for an electron density of  $1.0 \cdot 10^{20} \text{ m}^{-3}$ .

They reach values up to 2-3 keV for temperatures close to 10 eV, rather independent of electron density. This method is only applicable if the CIII has enough time to ionize, which means that one really measures spectroscopically a particle flux. Therefore, for lower temperatures the transport time has to get large in order to allow for this ionization process. This is possible due to the reduced carbon ion flow in the radiation zone close to the separatrix. However, in regions close to the target plate with strong forward flow, the basic assumption for a flux measurement fails.

All effects discussed before increase the losses in Div-II also in ELMy H-mode (Fig. 18.8) and broaden the deposition profile in the divertor like in L-mode. Therefore, one obtains in Div-II much lower peak power loads also during ELMs [101]. For type III ELMs one can get in Div-II detachment during ELMs like in the CDH mode in Div-I now even without adding extrinsic impurities. The same power and particle fluxes should enter Div-II as Div-I during ELMs, because the limiting structure for the ELMs is still the contour of the 4 ICRH antennas, which typically follow the 3 cm midplane magnetic flux contour. Therefore, the narrower divertor entrance in Div-II does not affect the overall ELM characteristics. One difference exists due to the strongly inclined geometry in Div-II: the variation of the separatrix position during ELMs (several mm in the midplane) translate in Div-II into large shifts of the separatrix at the target plate (several cm distance along the target plate), whereas in Div-I for the more orthogonal plates no strong shift was observed.

## 18.4. Pumping and helium exhaust

The particle exhaust is as important as the power exhaust for any reactor, because removal of the helium ash is necessary to avoid extinguishing the burning plasma and good pumping is necessary to achieve burn control and feedback operation.

The design of Div-II was done for optimizing the pumping capability by reducing the plasma pumping in the private flux region with a dome baffle [47] (see also section 10.2).

As predicted by B2-Eirene, one gets larger neutral gas flux densities in the divertor for the same midplane separatrix and line averaged densities [102, 105]. In contrast, the main chamber neutral fluxes do not change [102, 105] for medium and high densities, also consistent with B2-Eirene predictions. Therefore, the main chamber neutral flux is apparently not determined by the divertor leakage in Div-I or Div-II, but through main chamber recycling at baffles or limiters. The closest surfaces in the main chamber are 4 ICRH antennas, which follow typically the 3 cm midplane magnetic flux contour. Additionally, due to the existence of shoulders in density and temperature profiles (possibly caused by strongly enhanced turbulence by e.g. flute-like modes in the outer scrape-off layer [106]) extending even into the shadow of limiters, one expects a contribution from direct main chamber recycling which is nearly independent of the distance of the closest limiting structure from the main plasma. Therefore, the closing of the divertor seems not to be too important for good core performance as long as the plasma plugging itself is doing enough, which works very efficiently in the inclined target setup of Div-II with the attached outer scrape-off layer. From this argument, it is plausible that the core plasma performance, e.g. L- and H-mode density limits, confinement times and L-H threshold scaling, be practically unchanged from Div-I to Div-II. For low densities, which are usually not the standard ASDEX-Upgrade operation, the main chamber neutral fluxes are reduced considerably [105], because for these conditions the divertor leakage is large and any improvement of the divertor baffling appear in the main chamber neutral fluxes.

The impurity (and also hydrogenic) compression in Div-I was determined by recycling in the outer scrape-off layer, where the existence of a small pumping baffle was quite important [53, 58]. In contrast, in Div-II the feeding of the pump duct is now done through the private flux region. Experimentally, one observes in Div-II very good helium exhaust with  $\tau_{He}^*/\tau_E \approx 4$  for H-mode conditions and, in contrast to Div-I, a much better compression of helium compared to neon [107, 105]. Both measurements agree with B2-Eirene predictions, which allow an analysis of the different mechanisms. Due to the flow pattern of helium and neon which is rather similar to that of carbon one gets a second particle flux maximum away from the separatrix for impurities in both divertor configurations in the region of the outer scrape-off layer with strong forward flow. In Div-II, neon and helium have to enter the pumping plenum by direct reflection of neutrals (neon and helium have no dominant charge-exchange process in contrast to hydrogen). Therefore, the longer mean free path of helium gives better compression for helium compared to neon [58].

Another check of this hypothesis is possible, because experiments where one vertically shifts the plasma and thus moves the intersection of the separatrix on the target plates show a strong sensitivity of helium and neon compression, whereas hydrogen compression and pumping are much less affected [105]. This is expected from the picture given above, because hydrogen compression and pumping is not determined by direct reflection of neutrals into the pumping plenum but through multiple CX collisions, whereas neon and helium compression are dominated by this ballistic effect.

In ASDEX-Upgrade no strong effect on impurity compression and overall divertor performance was seen by puff and pump experiments, neither in Div-I nor in Div-II [105, 77], in agreement with B2-Eirene predictions and in contradiction to results of DIII-D [78].

Overall, the Div-II results for ASDEX-Upgrade demonstrate the possibility to optimize the geometry to obtain minimum power load together with optimum particle exhaust and large operational window without affecting negatively the core confinement. However, one loses experimental flexibility concerning MHD equilibria fitting into the divertor. Therefore, the design of a flexible divertor especially for high triangularity might need to relax some of the optimization criteria.

## 18.5. Target power load reduction

Experimentally, ASDEX-Upgrade has observed a regime where the power radiated in the divertor and the peak power flux to the target increase linearly with input power at the same separatrix density (Fig. 18.16)[108, 109]. In an attempt to understand this regime an extensive set of B2-Eirene [110, 111, 112] runs have been performed.

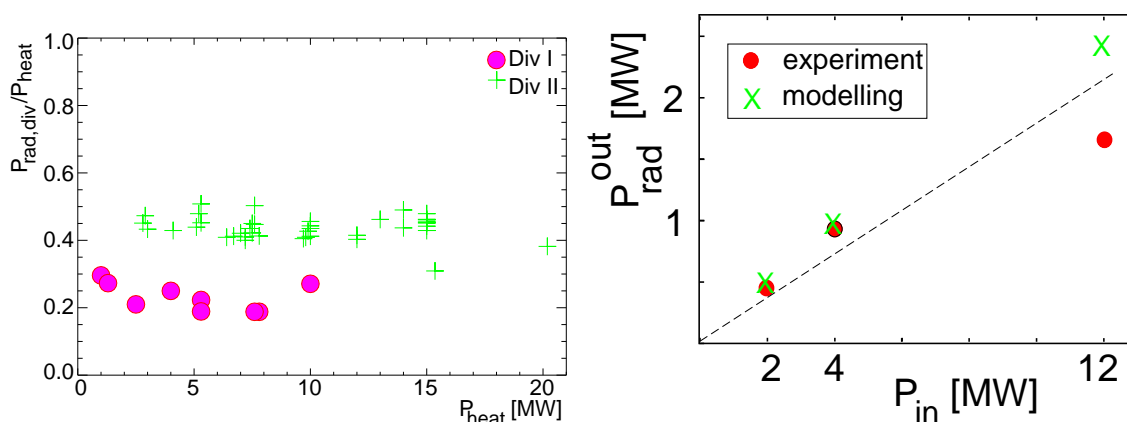


Figure 18.16.: Divertor radiation normalised to heating power as a function of input power (left) and outboard divertor radiation from the experiment and B2-Eirene simulations.

In order to understand how the the power loading on the target plate varies with plasma conditions, the physical processes that determine this have to be identified. The first ingredient is the power flux across the separatrix. There is then a competition between radial transport and parallel transport of this power which determines the radial power decay length. Considering a flux tube linking the main chamber to the divertor, energy can be lost from the flux tube by radial transport (moving the energy to a neighbouring flux tube), by radiation (either from impurities or from hydrogen) and by charge exchange; each of these processes might also deposit energy into the flux tube (though the coupling between flux tubes by radiation is usually unimportant). The remaining energy will reach the target plate. Both the radial and parallel transport of energy can be by convection or by conduction. Under low density conditions most of the energy crossing the separatrix reaches one of the divertor plates (radiation is then usually unimportant though exchange can account for some losses), and the peak power flux is largely determined by the radial power decay length at the midplane and geometry. As the density is increased, losses

along the flux tube increase. Extrinsic (e.g. neon or argon) and intrinsic (e.g. carbon or boron) impurities will radiate as will the working gas (hydrogen or deuterium). At high enough densities the temperature in front of the plate will fall to the 1 eV range and volume recombination can occur — further increasing the losses by radiation. Under these high density conditions it is the difference between the input power to the flux tube and the losses from the flux tube, both of which are large, that determines the power reaching the target plate (often small). Thus, the understanding of the power flux to the target is predicated on the understanding of these two large numbers: the power into the flux tube, and the subsequent losses from the flux tube before the target.

The power flux into the flux tube is determined by the upstream power decay length, or relatedly, the upstream temperature and density decay lengths. For H-mode type conditions with type I ELMs, there seems to be a pressure ( $P$ ) gradient limit (probably determined by some sort of ballooning criterium) in the pedestal region. If, as it seems likely, there is a radial correlation of the transport of a centimeter or so, this will also influence the transport just outside the separatrix. Under the assumption that  $\nabla P$  is a constant (determined by plasma current and geometry), one gets

$$\nabla P = n\nabla T + T\nabla n = n\nabla T\left(1 + \frac{1}{\eta}\right) = \text{constant} \quad (18.1)$$

where  $\eta$  is the ratio of density ( $n$ ) to temperature ( $T$ ) scale lengths. In ASDEX-Upgrade  $\eta$  seems to be a weakly varying number of order two. Thus when the input power is increased, the transport coefficient describing the radial energy flux also increases in this regime. This only weakly affects the amount of impurity radiation but strongly affects the peak power flux to the target (Fig. 18.17).

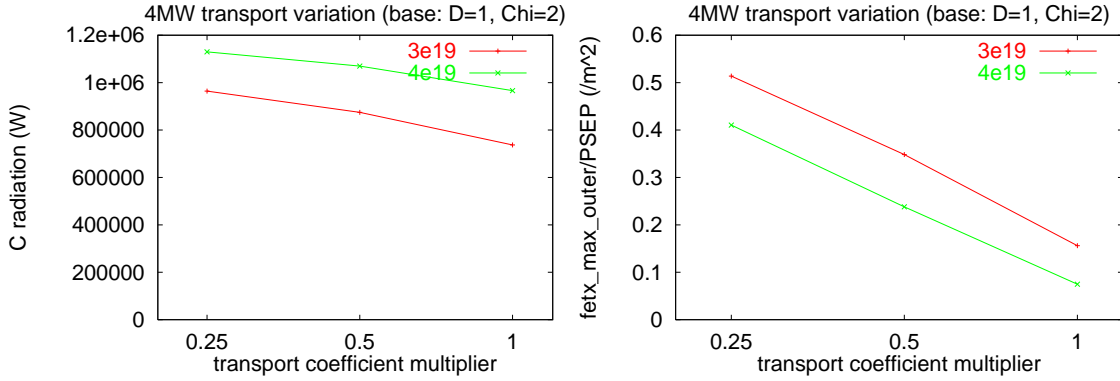


Figure 18.17.: Dependence of impurity radiation and peak target power flux on transport coefficients.

The amount of impurity radiation is proportional to the density of the impurity, and for C this density is partially determined by the chemical sputtering yield. How strongly this affects the peak power flux density depends on the radiated power fraction (figure 18.18). For the nearly detached regime a relationship exists between the amount of radiation and the input power.

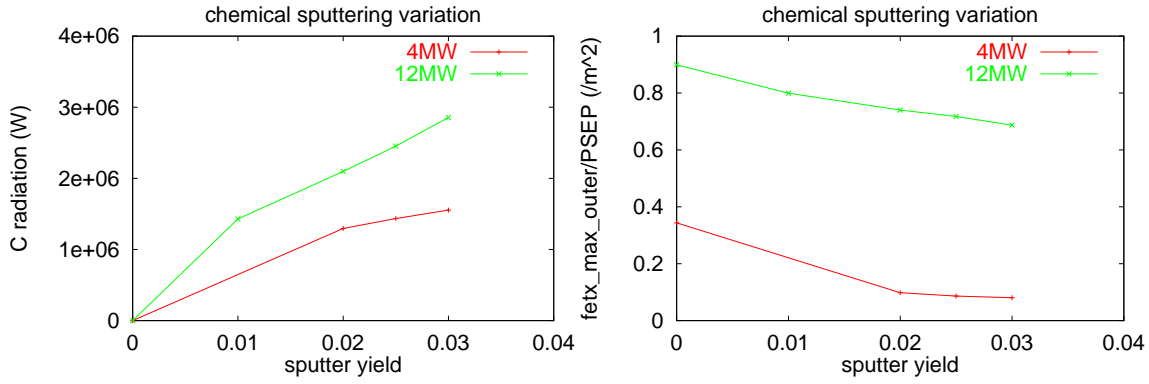


Figure 18.18.: Dependence of impurity radiation and peak target power flux on chemical sputter yield.

## 18.6. A simple model of the detached or nearly detached regime

The energy to the target plate,  $\Gamma_{e,t}$ , is given by

$$\Gamma_{e,t} = \Gamma_{e,0} - \Gamma_{e,rad} \quad (18.2)$$

where  $\Gamma_{e,0}$  is the input energy (energy crossing the separatrix) and  $\Gamma_{e,rad}$  is the energy radiated outside the main plasma. Now

$$\Gamma_{e,t} = \Gamma_t(13.6 + \alpha T) \quad (18.3)$$

where  $\Gamma_t$  is the target particle flux, and  $\alpha T$  the thermal energy per particle at the target plate. Arising from the plasma particle flux to the target a flux of neutrals away from the plate for hydrogen and carbon is created, respectively,

$$\Gamma_H = \Gamma_t \quad (18.4)$$

and

$$\Gamma_C = \gamma \Gamma_t \quad (18.5)$$

where  $\gamma$  is the chemical sputtering coefficient (physical sputtering is ignored because of the low temperatures in the nearly detached regime). Now

$$\Gamma_{e,rad} = 1000\Gamma_C + 20\Gamma_H = \Gamma_{e,t} \frac{1000\gamma + 20}{13.6 + \alpha T} \quad (18.6)$$

where a radiation potential of 1000 eV for C and 20 eV for H was assumed. Therefore,

$$\Gamma_{e,t} = \Gamma_{e,0} - \Gamma_{e,t} \frac{1000\gamma + 20}{13.6 + \alpha T} = \Gamma_{e,0} \frac{1}{1 + \frac{1000\gamma + 20}{13.6 + \alpha T}} \approx \Gamma_{e,0} \frac{1}{5} \quad (18.7)$$

where, for the approximation, a chemical sputtering yield of 3% and  $T \ll 13.6/\alpha$  is assumed. The carbon radiation as a fraction of the total radiation is

$$f_C = \frac{1000\gamma}{1000\gamma + 20} \approx \frac{30}{30 + 20} \approx 0.6 \quad (18.8)$$

with hydrogen accounting for the remaining 40%.

Some simplifying assumptions were used for here and they have to be discussed. The fraction of power reaching the target is a function of the target plasma temperature as well as of the chemical sputter yield (Fig. 18.19).

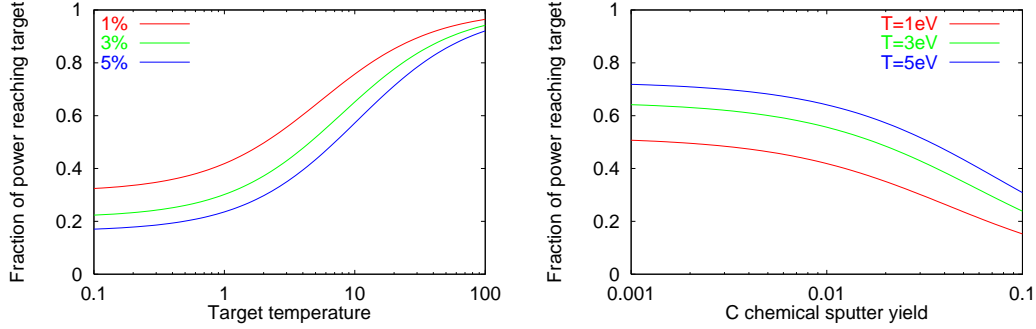


Figure 18.19.: Fraction of the power reaching the target as a function of target plasma temperature (left) and sputter yield assumptions (middle).

The actual chemical sputter yield is not a constant, but varies with plasma temperature and flux[113] (Fig. 18.20). This dependence would stabilize the operation in the experiment in this lower temperature regime as the effective yield increases with temperature thus increasing the losses.

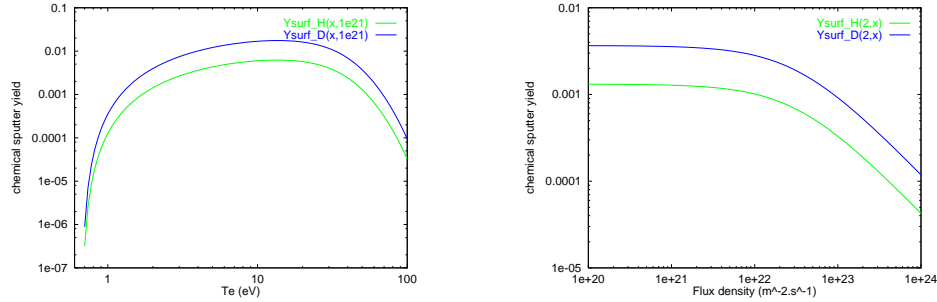


Figure 18.20.: Dependence of the chemical sputter yield on target plasma temperature (left) and flux (middle).

The additional assumption of constant radiation potentials is not quite correct in that the B2-Eirene runs show a slight increase in radiation potential with density.

In summary, the power reaching the target is critically dependent on losses between the upstream region and the target. The peak power flux density is also dependent on these losses, but, in addition, depends on the upstream power decay lengths. The loss due to divertor radiation depends strongly on the amount of impurities and only weakly on the cross field transport. The peak power flux depends strongly on the cross field transport but the strength of its dependence on the impurity concentration depends on the divertor conditions: close to detachment the dependence is strong; in the strongly attached regime the dependence is weak. In the detached or nearly detached regime there exists an approximately linear dependence of radiation from chemically sputtered carbon and hydrogen to the input power.

## 18.7. Role of divertor inclination

In Fig. 18.21 the results of B2-Eirene simulations for the pure hydrogen case are presented. The inclined targets of Divertor II lowers the required upstream density so that the target temperature equals 1 eV. This is true for both the inner and outer targets, and for the 2 MW and 8 MW cases.

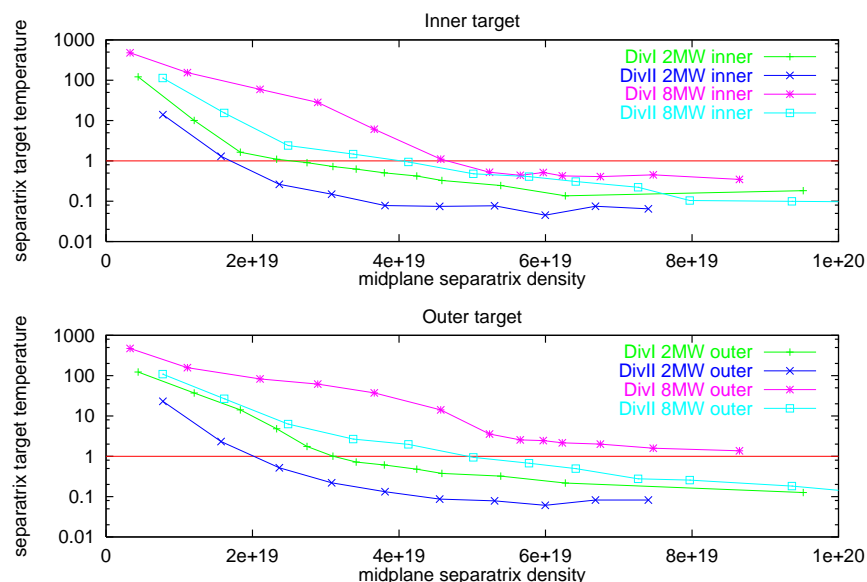


Figure 18.21.: Separatrix target plasma temperature for inner and outer target as a function of midplane separatrix density for 2 and 8 MW input power.

## 18.8. Replacement of carbon

Comparing the radiation potential of argon, neon and carbon (Fig. 18.22) one sees that it will be very problematic to replace the carbon in a machine by high-Z materials and then



adding additional recycling impurities (like Ne or Ar). As discussed before, the success and good performance of the existing divertor machines benefit a lot from the carbon radiation losses in the divertor. On the other hand the problem of chemical erosion might force one not to use carbon in a possible reactor design. However, the recycling noble gas impurities are obviously much less effective, so that higher impurity concentration is necessarily getting into conflict with the strict  $Z_{eff}$  limits ( $\leq 1.4$ , already corrected for helium contributions) of the core plasma for reactors.

Therefore, further test experiments with machines without carbon are needed to clarify this problem. Also, there is an urgent need for a predictive model of the chemical sputtering effect of carbon, because a possible flux-dependence (reduction of chemical sputtering yield) might relax the carbon problem.

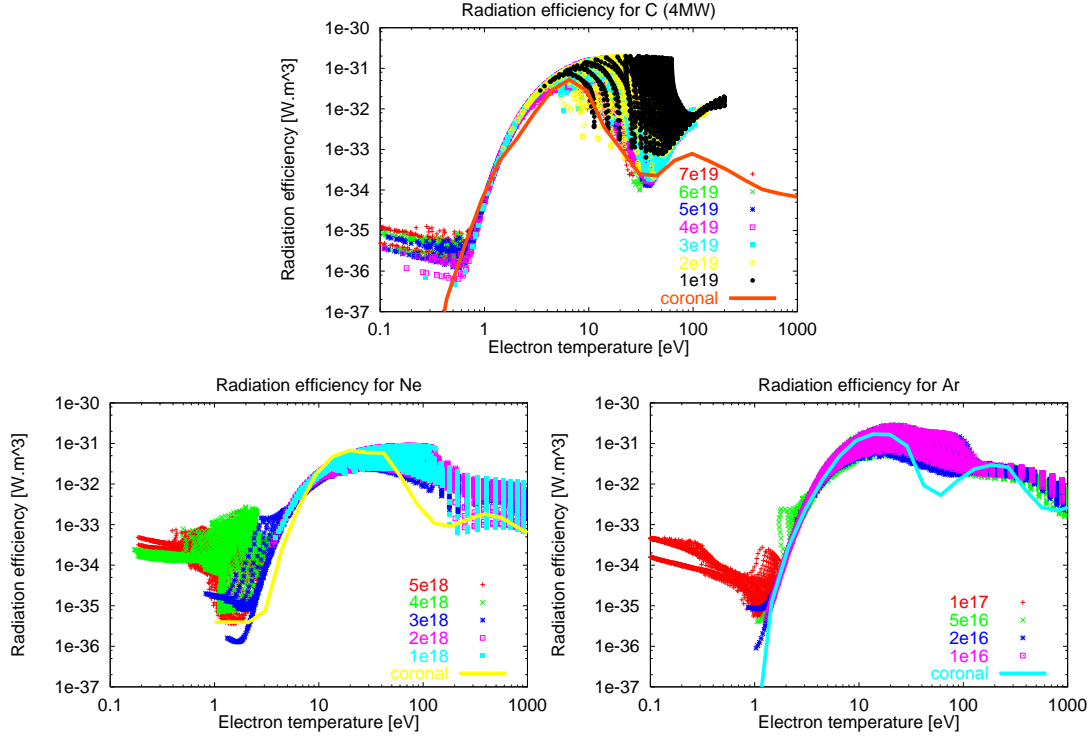


Figure 18.22.: Radiation potentials for carbon (top), neon (bottom left) and argon (bottom right) as derived from B2-Eirene runs. Especially carbon shows a large enhancement compared with the coronal value for temperatures above 10 eV. This enhancement is due to transport effects as discussed before, e.g. flow pattern effects. Neon and argon show some enhancements for low temperatures due to their recycling properties enhancing their radiation efficiency. However, this low temperature region usually does not contribute as much as the higher temperature range to the integral losses.

# 19. Drifts and currents

Experimental results show the importance of drifts and currents, e.g B-reversal can exchange the temperature and density conditions from the inner to the outer divertor (changing from hot outer to hot inner divertor) [114, 115]. Also, drift effects are very important for the core region close to the separatrix, where steep gradients of the order of the poloidal ion gyro-radius produce large drifts. Related to this is the question of what is defining the radial electric field and determines the transport barrier and pedestal physics. To be able to study these effects a new version of B2 was developed (B2-SOLPS5.0[116, 117, 118]), which will be presented in the following.

## 19.1. General treatment

For the implementation of these effects in edge transport codes a critical point is that large divergence free parts can produce numerical problems. The physics behind this is that diamagnetic drifts do not contribute to fluxes, because the flux of a superposition of particle rotations about their guiding centers is automatically divergence free. To overcome this, one should separate the divergent parts and put only these into the codes [115, 119]. This philosophy is used also in the B2-solps5.0, which is a version of B2 with drifts and currents including a fluid model for neutrals to speed up the convergence compared to using Eirene by large factors: instead of running days and weeks, one needs now typical tens of minutes.

In recent years it has been recognised that the impact of electric fields and drifts is important for redistribution of plasma and impurities between the divertor legs [120, 121, 122, 123]. The radial electric fields in the vicinity of a separatrix are responsible for the transition into improved confinement regime (L-H transition). Therefore, effects associated with the electric field should be included into the transport codes. However, the 2D problem of calculation of self-consistent electric fields is quite complicated, since it is necessary to perform calculations both on open and closed field lines, while the electric field is determined by various mechanisms of perpendicular conductivity. Rather subtle effects such as diamagnetic currents, different components of the viscosity tensor, inertia and collisions with neutrals determine the effective transverse conductivity, and, therefore, the current distribution and electric fields in the edge plasma. Up to now only some of these effects were taken into account in the codes. The full set of transport equations based on the Braginskii formalism is derived. To avoid numerical problems divergence-free terms are cancelled analytically in particle and current balance equations. As similar cancellation are made in the parallel momentum balance and energy balance equations, where inertia terms are combined with gyroviscosity terms, and is taking into account the fact that the diamagnetic heat fluxes are almost divergence-free. This approach is similar

to [124, 125, 126, 127] , however, several important terms which were previously absent are kept. This approach differs from that based on the moments of kinetic equation in the guiding centre approximation [128], still having much in common in results. Anomalous effects are introduced by replacing the classical perpendicular particle and heat fluxes with anomalous fluxes and perpendicular viscosity coefficient with its anomalous value. Results of the edge plasma simulation of ASDEX-Upgrade tokamak by means of B2.5 in the single fluid case (deuterium) are presented below. Plasma parameters of ASDEX-Upgrade in the vicinity of the separatrix and in the SOL correspond to the Pfirsch-Schlüter regime, thus justifying by this the applicability of fluid equations.

## 19.2. Numerics

The code is completely written in Fortran 90 using dynamic allocation of memory. A fully indirect addressing scheme using neighbourhood arrays is used avoiding any problems with topological cuts and preparing for grid refinement or coarsening. For this, the momentum equation is now also solved on non-staggered grids. The method of Rhie and Chow [129] was implemented, requiring a fundamental modification: all velocities, momentum source terms, momentum residuals were moved from cell faces to cell centers. The test conditions at the beginning of all subroutines involving these variables were modified. The viscosities and momentum fluxes are defined on cell faces now. The main subroutine for the method of Rhie and Chow is the one calculating the mass fluxes. Here the correction for the influence of the pressure gradient on the velocities is introduced. The routines calculating momentum boundary conditions as well as all the routines involving transformed variables were modified. The convergence of the new non-staggered code has been tested on pure hydrogen plasmas as well as on plasmas with deuterium and carbon. Run-times are as fast as with the non-staggered version and results are very similar.

Due to the fact that complex non-linear reactions due to e.g. recycling or sputtering, influence the system, full effects need to be implemented. Analysing drift effects just for the pure plasma usually gives small effects, whereas effects due to impurities (change of radiation losses from inboard to outboard divertor) with B-reversal are very strong.

## 19.3. Model equations

As discussed before, the equations are written on a curvilinear orthogonal coordinate system. The  $x$ -coordinate varies along flux surfaces and the  $y$ -coordinate varies perpendicular to flux surfaces (see Fig. 19.1),  $z$  is the toroidal direction.

The metric coefficients are  $h_x = 1/\|\nabla x\|$ ,  $h_y = 1/\|\nabla y\|$  and  $\sqrt{g} = h_x h_y h_z$ . One can replace  $h_z$  by  $2\pi R$ , where  $R$  is the local major radius. Components of a vector are the projections on unit basis vectors ; they are not the contravariant or covariant components ( $b_x = B_x/B$ ,  $b_z = B_z/B$ ). Ion velocities  $V_\perp$  (velocity perpendicular both to magnetic field  $B$  and the  $y$ -axis) and  $V_y$  are determined from the two components of the momentum balance equation for ions perpendicular to a magnetic field. Using the Braginskii expression for the friction force, one obtains:

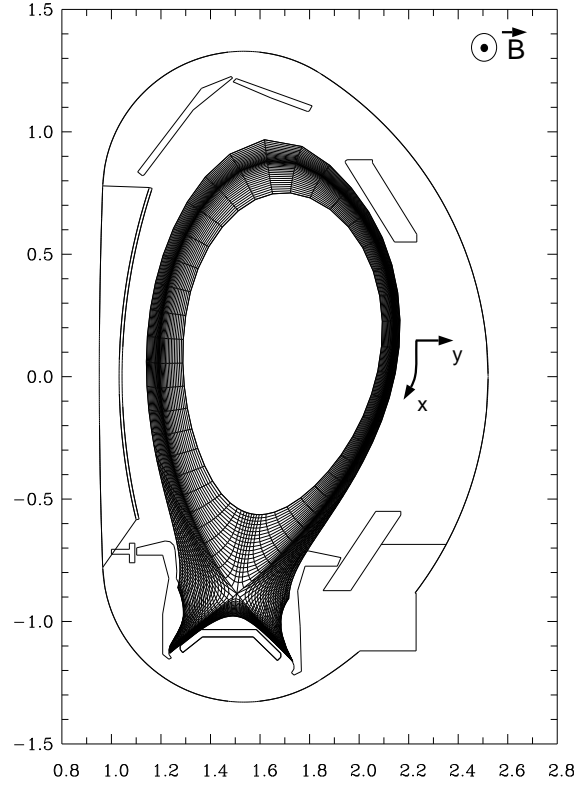


Figure 19.1.: Coordinate system:  $x$  is the poloidal coordinate,  $y$  is the radial coordinate orthogonal to the flux surfaces. The coordinate  $\perp$  corresponds to the direction perpendicular both to the magnetic field and to the  $y$ -axis. The directions of magnetic field and plasma current correspond to normal operation conditions of ASDEX-Upgrade (ion  $\nabla B$  drift directed towards the X-point).

$$V_{\perp} = V_{\perp}^{(a)} - \frac{1}{enB} \frac{1}{h_y} \frac{\partial n T_i}{\partial y} + V_{\perp}^{(in)} + V_{\perp}^{(vis)} + V_{\perp}^{(s)} \quad (19.1)$$

$$V_y = V_y^{(a)} + \frac{B_z}{enB^2} \frac{1}{h_x} \frac{\partial n T_i}{\partial x} + V_y^{(in)} + V_y^{(vis)} + V_y^{(s)} \quad (19.2)$$

Velocities  $V_{\perp,y}^{(a)}$  are the sum of the  $\vec{E} \times \vec{B}$  drifts and diffusive and thermodiffusive velocities. This part corresponds to the ambipolar flux. It is the same both for ions and electrons. The second term in the r.h.s. of Eqs. 19.1, 19.2) corresponds to diamagnetic flow of ions, while the other terms are caused by inertial, viscous and ion-neutral friction forces. These non-ambipolar terms are connected with currents:  $\vec{V}^{(in)} = \vec{j}^{(in)}/en$ ,  $\vec{V}^{(vis)} = \vec{j}^{(vis)}/en$ ,  $\vec{V}^{(s)} = \vec{j}^{(s)}/en$ .

In the presence of anomalous transport ( $D$  is the classical diffusion coefficient,  $D = \frac{T_e + T_i}{eb} \frac{\nu_{ei}}{\omega_{ce}}$ , with electron cyclotron frequency  $\omega_{ce}$  and electron-ion collision frequency  $\nu_{ei}$ )

$$V_{\perp}^{(a)} = -\frac{1}{B} \frac{1}{h_y} \frac{\partial \Phi}{\partial y} - \frac{D}{T_e + T_i} \frac{b_z}{h_x} \left( \frac{\partial p}{n \partial x} - \frac{3}{2} \frac{\partial T_e}{\partial x} \right) - D_{AN}^n \frac{1}{h_x n} \frac{\partial n}{\partial x} - D_{AN}^p \frac{1}{h_x n} \frac{\partial p_i}{\partial x} \quad (19.3)$$

$$V_y^{(a)} = -\frac{B_z}{B^2} \frac{1}{h_x} \frac{\partial \Phi}{\partial x} - \frac{D}{T_e + T_i} \frac{1}{h_y} \left( \frac{\partial p}{n \partial y} - \frac{3}{2} \frac{\partial T_e}{\partial y} \right) - D_{AN}^n \frac{1}{h_y n} \frac{\partial n}{\partial y} - D_{AN}^p \frac{1}{h_y n} \frac{\partial p_i}{\partial y} \quad (19.4)$$

The poloidal velocity is a sum  $V_x = b_z V_\perp + b_x V_\parallel$ .

In the particle balance the fact is that the diamagnetic velocity is almost divergence free is taken into account. Therefore, instead of the diamagnetic velocity it is possible to introduce an effective velocity  $\tilde{V}^{(dia)}$ , which gives the same contribution to the divergence of the particle flux:

$$\frac{\partial n}{\partial t} + \frac{1}{\sqrt{g}} \frac{\partial}{\partial x} \left( \frac{\sqrt{g}}{h_x} n (b_x V_\parallel + b_z V_\perp^{(0)}) \right) + \frac{1}{\sqrt{g}} \frac{\partial}{\partial y} \left( \frac{\sqrt{g}}{h_y} n V_y^{(0)} \right) = S^m \quad (19.5)$$

$$V_\perp^{(0)} = V_\perp^{(a)} + V_\perp^{(in)} + V_\perp^{(vis)} + V_\perp^{(s)} + \tilde{V}_\perp^{(dia)} \quad (19.6)$$

$$V_y^{(0)} = V_y^{(a)} + V_y^{(in)} + V_y^{(vis)} + V_y^{(s)} + \tilde{V}_y^{(dia)} \quad (19.7)$$

$$\tilde{V}_\perp^{(dia)} = \frac{T_i B_z}{e b_z} \frac{\partial}{h_y \partial y} \left( \frac{1}{B^2} \right) \quad (19.8)$$

$$\tilde{V}_y^{(dia)} = -\frac{T_i B_z}{e} \frac{\partial}{h_x \partial x} \left( \frac{1}{B^2} \right) \quad (19.9)$$

The velocity  $\tilde{V}^{(dia)}$  is an effective velocity. It represents vertical guiding centre drift of ions caused by  $\nabla B$ .

Combining the inertia and gyroviscosity terms in the Braginskii equations, one finds

$$\begin{aligned} m_i \left[ \frac{\partial n V_\parallel}{\partial t} + \frac{1}{\sqrt{g}} \frac{\partial}{\partial x} \left( \frac{\sqrt{g}}{h_x} n (V_\perp^{(0)} b_z + V_\parallel b_x) V_\parallel \right) + \frac{1}{\sqrt{g}} \frac{\partial}{\partial y} \left( \frac{\sqrt{g}}{h_y} n V_y^{(0)} V_\parallel \right) \right] = \\ - \frac{b_x}{h_x} \frac{\partial n T_i}{\partial x} - b_x \frac{e n}{h_x} \frac{\partial \Phi}{\partial x} + F_k + \frac{4}{3} b_x B^{3/2} \frac{\partial}{h_x \partial x} \left( \frac{\eta_0 b_x}{B^2} \frac{\partial (\sqrt{B} V_\parallel)}{h_x \partial x} \right) + \\ B^{3/2} b_x \frac{\partial}{h_x \partial x} \left( \frac{b_x}{\nu_{ii} B^2} \frac{\partial (\sqrt{B} q_{i\parallel}^{(0)})}{h_x \partial x} \right) + \frac{1}{\sqrt{g}} \frac{\partial}{\partial y} \left( \frac{\sqrt{g}}{h_y^2} \eta_2 \frac{\partial V_\parallel}{\partial y} \right) + \frac{1}{\sqrt{g}} \frac{\partial}{\partial x} \left( \frac{\sqrt{g}}{h_x^2} \eta_2 \frac{\partial V_\parallel}{\partial x} \right) S_{i\parallel}^m + R_{ie\parallel} \end{aligned} \quad (19.10)$$

The diamagnetic terms in the l.h.s. of (19.10) are almost cancelled [124, 125, 126, 127], so that velocities normal to the flux surface in the second and third term, as in the particle balance equation, are determined by 19.1 and 19.2. In [127] the divergent part of diamagnetic velocity has been neglected. Here, it is kept, because the corresponding flux is still relatively large and can be comparable with the diffusive flux even for anomalous

diffusion coefficients. The authors of [124, 125, 126] also kept this flux. In contrast to [124, 125, 126] there is an additional term of the same kind in the r.h.s. of Eq. 19.10:

$$F_k = -m_i \left( \frac{1}{\sqrt{g}} \frac{\partial}{\partial x} \left( \frac{\sqrt{g}}{h_x} n V_{\parallel} \tilde{V}_{\perp}^{(dia)} b_z \right) + \frac{1}{\sqrt{g}} \frac{\partial}{\partial y} \left( \frac{\sqrt{g}}{h_y} n V_{\parallel} \tilde{V}_y^{(dia)} \right) \right) \quad (19.11)$$

This parallel force is the Coriolis force, connected with the diamagnetic drift velocity and toroidal (parallel) rotation. This force can be obtained in a different way by averaging the drift kinetic equation [128] and is of the same order as the inertia terms.

Parallel viscosity is represented by the fourth and fifth terms in the r.h.s. The former is the Braginskii parallel viscosity with coefficient  $\eta_0 = 0.96 n T_i / \nu_{ii}$ . The latter corresponds to the parallel viscosity driven by parallel ion heat flux  $q_{i\parallel}^{(0)} = -\kappa_{i\parallel} b_x \frac{1}{h_x} \frac{\partial T_i}{\partial x}$ . This viscosity is absent in the Braginskii equations, however, in a tokamak, where parallel particle flux multiplied by temperature is of the order of the ion heat flux, these two viscosities are of the same order. On closed flux surfaces far from the separatrix, the flux-surface-averaged parallel viscosity coincides with the well-known neoclassical expression for the Pfirsch-Schlüter regime [130]. Thus, parallel viscosity in Eq. 19.10 provides smooth transition to neoclassical theory. The classical perpendicular viscosity coefficient can be replaced by an anomalous value as in [124, 125, 126]:  $\eta_2 = n m_i D_{AN}^n$ . Perpendicular viscosity and inertia terms with the anomalous particle flux are responsible for the transport of the parallel momentum in radial and poloidal directions. The radial transport can be rather important despite the fact that  $\eta_2 \ll \eta_0$ , since the scale in the radial direction is rather small.

The term  $S_{i\parallel}^m$  represents the momentum loss due to ion-neutral friction and momentum input from neutral beam injection.  $R_{ie\parallel}$  is the ion-electron friction.

The parallel momentum balance for electrons has the standard form:

$$j_{\parallel} = \sigma_{\parallel} \left( \frac{b_x}{e} \frac{1}{h_x} \left( \frac{\partial n T_e}{\partial x} + 0.71 \frac{\partial T_e}{\partial x} \right) - \frac{b_x}{h_x} \frac{\partial \Phi}{\partial x} \right). \quad (19.12)$$

Expressions for  $j_{\perp}$  and  $j_y$  are obtained from radial and poloidal projections of the total momentum balance equation (the sum of electron and ion momentum balance equations). The resulting current is a sum of contributions from pressure gradient (diamagnetic current)  $\vec{j}^{(dia)}$ , inertia and gyroviscosity  $\vec{j}^{(in)}$ , viscosity  $\vec{j}^{(vis)}$  and ion-neutral friction  $\vec{j}^{(s)}$ . Similar to the particle continuity equation, the effective current  $\vec{j}$  is introduced, which gives the same contribution to  $\nabla \cdot \vec{j}$ , as the ordinary current. This gives the current continuity equation

$$\frac{1}{\sqrt{g}} \frac{\partial}{\partial x} \left( \frac{\sqrt{g}}{h_x} \tilde{j}_x \right) + \frac{1}{\sqrt{g}} \frac{\partial}{\partial y} \left( \frac{\sqrt{g}}{h_y} \tilde{j}_y \right) = 0. \quad (19.13)$$

$$\tilde{j}_x = b_z \tilde{j}_{\perp} + b_x \tilde{j}_{\parallel}. \quad (19.14)$$

$$\vec{j} = \vec{j}^{(dia)} + \vec{j}^{(in)} + \vec{j}^{(vis)} + \vec{j}^{(s)} + \vec{j}_{\parallel}. \quad (19.15)$$

The effective diamagnetic current can be chosen in a form

$$\tilde{j}_{\perp}^{(dia)} = \frac{1}{b_z} \frac{n (T_e + T_i) B_z}{h_y} \frac{\partial}{\partial y} \left( \frac{1}{B^2} \right), \quad (19.16)$$

$$\tilde{j}_y^{(dia)} = -\frac{n(T_e + T_i)B_z}{h_x} \frac{\partial}{\partial x} \left( \frac{1}{B^2} \right). \quad (19.17)$$

Current driven by parallel viscosity should be taken into account in Eqs. 19.13, 19.14 and 19.15. This current is a small correction to the diamagnetic current Eqs. 19.16 and 19.17. However, on closed flux surfaces, where the pressure is almost constant, the diamagnetic current averaged over the flux surfaces tends to zero. The resulting remaining part can become comparable to the parallel viscosity-driven current, which is necessary to satisfy the condition that the averaged net radial current should be zero. The terms, which contain viscosity coefficient, produce almost divergence-free currents. Similar to the case of diamagnetic currents, it can be reduced to

$$\tilde{j}_\perp^{(vis||)} = -\frac{B_x \eta_0}{3\sqrt{B}} \frac{\partial (V_\parallel \sqrt{B})}{h_x \partial x} \frac{\partial}{h_y \partial y} \left( \frac{1}{B^2} \right) \quad (19.18)$$

$$\tilde{j}_y^{(vis||)} = b_z \frac{B_x \eta_0}{3\sqrt{B}} \frac{\partial (V_\parallel \sqrt{B})}{h_x \partial x} \frac{\partial}{h_x \partial x} \left( \frac{1}{B^2} \right) \quad (19.19)$$

The current produced by components of viscosity tensor connected with heat fluxes is:

$$\tilde{j}_\perp^{(visq)} = -\frac{0.24 B_x}{\sqrt{B} \nu_{ii}} \frac{\partial (q_{i||}^{(0)} \sqrt{B})}{h_x \partial x} \frac{\partial}{h_y \partial y} \left( \frac{1}{B^2} \right) \quad (19.20)$$

$$\tilde{j}_y^{(visq)} = b_z \frac{0.24 B_x}{\sqrt{B} \nu_{ii}} \frac{\partial (q_{i||}^{(0)} \sqrt{B})}{h_x \partial x} \frac{\partial}{h_x \partial x} \left( \frac{1}{B^2} \right) \quad (19.21)$$

The second part of the current contains contributions from both inertia and gyroviscosity forces. In contrast to the parallel momentum balance, the cancellation is not complete (as has been noticed in [127]). Expressions for this part of the current are

$$\begin{aligned} j_\perp^{(in)} = & -\frac{m_i}{B} \left[ \frac{\partial n V_y}{\partial t} + \frac{1}{\sqrt{g}} \frac{\partial}{\partial x} \left( \frac{\sqrt{g}}{h_x} n (V_\perp^{(0)} b_z + V_\parallel b_x) V_y \right) + \frac{1}{\sqrt{g}} \frac{\partial}{\partial y} \left( \frac{\sqrt{g}}{h_y} n V_y^{(0)} V_y \right) \right] \\ & - \frac{2b_x}{B} \frac{1}{h_x} \frac{\partial}{\partial x} \left( \eta_3 \frac{\partial V_\parallel}{h_x \partial x} \right) + \frac{m_i}{B} n V_\parallel^2 \frac{\partial \ln h_z}{h_y \partial y} \end{aligned} \quad (19.22)$$

$$\begin{aligned} j_y^{(in)} = & \frac{m_i}{B} \left[ \frac{\partial n V_\perp}{\partial t} + \frac{1}{\sqrt{g}} \frac{\partial}{\partial x} \left( \frac{\sqrt{g}}{h_x} n (V_\perp^{(0)} b_z + V_\parallel b_x) V_\perp \right) + \frac{1}{\sqrt{g}} \frac{\partial}{\partial y} \left( \frac{\sqrt{g}}{h_y} n V_y^{(0)} V_\perp \right) \right] \\ & - \frac{2b_x}{B} \frac{1}{h_x} \frac{\partial}{\partial x} \left( \eta_3 \frac{\partial V_\parallel}{h_y \partial y} \right) - \frac{m_i}{B} n V_\parallel^2 \frac{\partial \ln h_z}{h_x \partial x} \end{aligned} \quad (19.23)$$

where  $\eta_3 = \frac{n T_i}{2\omega_{ci}}$ ,  $\eta_1 = \frac{\eta_2}{4}$ .

The last terms proportional to the gradient of B correspond to the vertical guiding centre drift of ions caused by the centrifugal force. This current can be simply added to the diamagnetic current. Other terms seem to be less important.

The contribution from perpendicular viscosity is

$$j_{\perp}^{(vis\perp)} = \frac{1}{B} \left[ \frac{1}{h_x} \frac{\partial}{\partial x} \left( \eta_1 \frac{\partial V_y}{h_x \partial x} \right) + \frac{1}{h_y} \frac{\partial}{\partial y} \left( \eta_1 \frac{\partial V_y}{h_y \partial y} \right) + \frac{1}{h_x h_y} \frac{\partial \eta_1}{\partial x} \frac{\partial V_{\perp}}{\partial y} - \frac{1}{h_x h_y} \frac{\partial \eta_1}{\partial y} \frac{\partial V_{\perp}}{\partial x} \right] \\ + \frac{4b_x}{B} \frac{1}{h_x h_y} \left( \frac{\partial \eta_1}{\partial x} \frac{\partial V_{\parallel}}{\partial y} - \frac{\partial \eta_1}{\partial y} \frac{\partial V_{\parallel}}{\partial x} \right) \quad (19.24)$$

$$j_y^{(vis\perp)} = -\frac{1}{B} \left[ \frac{1}{h_y} \frac{\partial}{\partial y} \left( \eta_1 \frac{\partial V_{\perp}}{h_y \partial y} \right) + \frac{1}{h_x} \frac{\partial}{\partial x} \left( \eta_1 \frac{\partial V_{\perp}}{h_x \partial x} \right) - \frac{1}{h_x h_y} \frac{\partial \eta_1}{\partial x} \frac{\partial V_y}{\partial y} + \frac{1}{h_x h_y} \frac{\partial \eta_1}{\partial y} \frac{\partial V_y}{\partial x} \right]. \quad (19.25)$$

Here, the largest term is the first one in the r.h.s. of the expression for the radial current, since the radial derivatives are the largest. This current corresponds to a pure cylindrical approximation. It is responsible, for example, for closing currents near flush-mounted probes [131]. It was taken into account in [126, 119]. However, in the problem of global current structure in the edge plasma, the currents driven by parallel viscosity seem to be more important.

The total current caused by viscosity is

$$\vec{j}^{(vis)} = \vec{j}^{(vis\parallel)} + \vec{j}^{(vis\perp)} + \vec{j}^{(visq)}. \quad (19.26)$$

The contribution from ion neutral friction is

$$j_{\perp}^{(s)} = \frac{S_{iy}^m}{B}. \quad (19.27)$$

$$j_y^{(s)} = -\frac{S_{i\perp}^m}{B}, \quad (19.28)$$

where  $S_{iy}^m, S_{i\perp}^m$  are the momentum sinks due to ion-neutral friction.

$$S_{i\perp}^m = -n\mu_{iN}\nu_{iN} (V_{\perp} - V_{\perp N}), \quad (19.29)$$

$$S_{iy}^m = -n\mu_{iN}\nu_{iN} (V_y - V_{yN}), \quad (19.30)$$

where  $\mu_{iN} = m_i/2$  is the effective mass,  $\nu_{iN} = n_N < V_i N \sigma_{cx} >$  is the ion-neutral collision frequency,  $n_N$  is the neutral density and  $\vec{V}_N$  is the neutral mean velocity. For the ion velocity used above, only electric and diamagnetic drifts are left, neglecting smaller terms, to obtain

$$\tilde{j}_x^{(s)} = \tilde{j}_{\perp}^{(s)} b_z = -\sigma_{iN} b_z^2 \frac{\partial \Phi}{h_x \partial x} - \sigma_{iN} b_z^2 \frac{1}{en} \frac{\partial n T_i}{h_x \partial x} + \sigma_{iN} B_z V_{yN}, \quad (19.31)$$

$$\tilde{j}_y^{(s)} = -\sigma_{iN} \frac{\partial \Phi}{h_y \partial y} - \sigma_{iN} \frac{1}{en} \frac{\partial n T_i}{h_y \partial y} - \sigma_{iN} B V_{\perp N}, \quad (19.32)$$



where  $\sigma_{iN}$  is the ion-neutral perpendicular conductivity

$$\sigma_{iN} = \frac{nm_i \langle V_{in}\sigma_{cx} \rangle n_N}{2B^2} . \quad (19.33)$$

The rate of charge-exchange  $\langle V_{in}\sigma_{cx} \rangle$  can be expressed through the mobility  $K_0$  measured in the absence of a magnetic field for room temperature and atmospheric pressure for deuterium [132]:

$$K_0 = \frac{2e}{m_i \langle V_{in}\sigma_{cx} \rangle n_N^{(0)}} , \quad (19.34)$$

with  $n_N^{(0)} = 2.687 \cdot 10^{25} m^{-3}$  and  $K_0 = 11.2 \cdot 10^{-4} \frac{m^2}{sV}$ . Assuming that the charge-exchange cross-section is approximately constant one gets

$$\langle V_{in}\sigma_{cx} \rangle = 3.2 \cdot 10^{-15} \sqrt{\frac{T_i}{0.026}} \frac{m^3}{s} , \quad (19.35)$$

where  $T_i$  is measured in eV. A similar expression, which gives approximately the same result, is [133]:

$$\langle V_{in}\sigma_{cx} \rangle = \frac{32\sigma_{cx}}{3\sqrt{\pi}} \sqrt{\frac{T_i}{m_i}} \frac{m^3}{s} . \quad (19.36)$$

In the energy balance equations appears a special problem, which is the possible inclusion of an anomalous radial current. The basic guidelines are as follows

- The expression must be as simple as possible, and the most convenient format is an Ohm-like expression
- The system of equations must be informed about this non-classical contribution, but
- The classical core of the equations must not be disturbed

Apparently, the radial current would enter the electron energy equation via the Joule term, but this manipulation is inappropriate since one cannot be sure that this term directly heats the electrons, which is the case in a purely classical setup. The proper thing to do is to keep only the non-radial classical contribution in the Joule term, and construct additional heat exchange terms containing the radial current. In this way, the system decides how to thermodynamically allocate the "alien" heat term, among electrons and ion species.

For this reason, one cannot simply use the standard Ohm's law in the radial direction with anomalous coefficients, or any other prescribed expression whatsoever, as a constructive procedure is necessary for simultaneously producing the radial current as well as the heat exchange terms. At this point it has to be mentioned that this peculiarity arises only in the multifluid case, whereas in the single species case these heat exchange terms can indeed be constructed even using a prescribed expression for the radial current.

The trick for carrying out this program is to correct the electron friction density  $\vec{R}^e$  by

adding the term  $n_e e \tilde{\eta}_\perp \vec{J}_\perp$  similar to the classical one, only using the *ad hoc* parameter  $\tilde{\eta}_\perp$ . Since  $\vec{R}^e = -\sum_a \vec{R}^a$ , one has a modified total ion momentum equation at hand which in conjunction with the pressure equilibrium (not affected by the additional term)  $\vec{J} \times \vec{B} = \nabla P$ , gives the diffusive part of the radial current, namely

$$J_y^{diff} = \frac{\tilde{\eta}_\perp e n_e}{B^2} \frac{\partial P_i}{\partial y} \quad (19.37)$$

where  $P_i$  is the total ion pressure. This dependency is also found in [124]. Moreover, an additional dependence on the radial electric field can potentially be added without interfering with the procedure.

The final step, namely the construction of the heat exchange terms, is performed by claiming that the well known relation [19] (adapted for the multifluid case)

$$Q_e = -\sum_a \left( Q_a + (\vec{u}^a - \vec{u}^e) \cdot \vec{R}^a \right),$$

which stems from the fundamental null space of the collision operator, is still true while carrying the modified friction. Claiming this, after performing the proper manipulations in the energy equations, one reveals the *ad hoc* contribution as the exchange term that one wants, which reads  $\sum_a (\vec{u}^a - \vec{u}^e)_\perp n_a \frac{Z_a^2}{Z_{eff}} e \tilde{\eta}_\perp \vec{J}_\perp$  added in the total ion energy equation and subtracted from the electron equation. Note that in the single species case, this term boils down to  $\tilde{\eta}_\perp J_\perp^2$  removing energy from the electrons, depositing it to the ions, a feature predicted by neoclassical theory [134].

In the final form of the energy balance equations, the convective heat flux and the diamagnetic heat flux are combined as in [124, 125, 126, 127], see also [131].

The energy balance equation for the electrons is

$$\begin{aligned} & \frac{3}{2} \frac{\partial n T_e}{\partial t} + \frac{1}{\sqrt{g}} \frac{\partial}{\partial x} \left( \frac{\sqrt{g}}{h_x} \tilde{q}_{ex} \right) + \frac{1}{\sqrt{g}} \frac{\partial}{\partial y} \left( \frac{\sqrt{g}}{h_y} \tilde{q}_{ey} \right) + \frac{n T_e}{\sqrt{g}} \frac{\partial}{\partial x} \left( \frac{\sqrt{g}}{h_x} (V_\parallel - j_\parallel / en) b_x \right) \\ & = Q_e + n T_e B \frac{1}{h_x h_y} \left( \frac{\partial \Phi}{\partial y} \frac{\partial}{\partial x} \left( \frac{1}{B^2} \right) - \frac{\partial \Phi}{\partial x} \frac{\partial}{\partial y} \left( \frac{1}{B^2} \right) \right), \end{aligned} \quad (19.38)$$

where

$$\begin{aligned} \tilde{q}_{ex} = & \frac{3}{2} n T_e \left( -\frac{b_z}{B h_y} \frac{\partial \Phi}{\partial y} + b_x V_\parallel - b_x j_\parallel / en \right) \\ & + \frac{5}{2} n T_e b_z \left( -\frac{D}{T_e + T_i} \frac{b_z}{h_x} \left( \frac{\partial p}{n \partial x} - \frac{3}{2} \frac{\partial T_e}{\partial x} \right) - D_{AN}^n \frac{1}{h_x n} \frac{\partial n}{\partial x} - D_{AN}^p \frac{1}{h_x n} \frac{\partial p_i}{\partial x} \right) \\ & - 0.71 b_x j_\parallel T_e / e - \kappa_{e\parallel} \frac{b_x^2}{h_x} \frac{\partial T_e}{\partial x} - \kappa_{e\perp} b_z^2 \frac{1}{h_x} \frac{\partial T_e}{\partial x} \\ & + \frac{3}{2} \frac{T_e}{e B} \frac{\nu_{ei}}{\omega_{ce}} \frac{b_z^2}{h_x} \frac{\partial n}{\partial x} (T_e + T_i) - \frac{5}{2} n T_e^2 \frac{B_z}{e} \frac{\partial}{h_y \partial y} \left( \frac{1}{B^2} \right), \end{aligned} \quad (19.39)$$

$$\tilde{q}_{ey} = \frac{3}{2} n T_e \frac{B_z}{B^2} \frac{1}{h_x} \frac{\partial \Phi}{\partial x} \quad (19.40)$$

$$+ \frac{5}{2} n T_e \left( -\frac{D}{T_e + T_i} \frac{1}{h_y} \left( \frac{\partial p}{n \partial y} - \frac{3}{2} \frac{\partial T_e}{\partial y} \right) - D_{AN}^n \frac{1}{h_y n} \frac{\partial n}{\partial y} - D_{AN}^p \frac{1}{h_y n} \frac{\partial p_i}{\partial y} \right) \quad (19.41)$$

$$- \kappa_{e\perp} \frac{1}{h_y} \frac{\partial T_e}{\partial y} + \frac{3}{2} \frac{T_e}{e B} \frac{\nu_{ei}}{\omega_{ce}} \frac{1}{h_y} \frac{\partial n (T_e + T_i)}{\partial y} + \frac{5}{2} n T_e^2 \frac{B_z}{e} \frac{\partial}{h_x \partial x} \left( \frac{1}{B^2} \right), \quad (19.42)$$

$$Q_\Delta = \frac{3m_e}{m_i} n \nu_{ei} (T_e - T_i), \quad (19.43)$$

$$Q_u = R_{ie\parallel} j_{\parallel} / en, \quad (19.44)$$

$$Q_{AN} = \sum_a (\vec{u}^a - \vec{u}^e)_{\perp} n_a \frac{Z_a^2}{Z_{eff}} e \tilde{\eta}_{\perp} \vec{J}_{\perp}, \quad (19.45)$$

$$Q_e = -Q_\Delta - Q_u - Q_{AN}. \quad (19.46)$$

Here  $\kappa_{e\parallel}$  is the Braginskii heat conductivity with a possible heat flux limit [116]. The perpendicular heat conductivity  $\kappa_{e\perp}$  can be either classical or anomalous. In the last term of the energy balance equation, it is taken into account that the  $\vec{E} \times \vec{B}$  drift velocity is almost divergence-free.

The ion energy balance equation is

$$\begin{aligned} & \frac{3}{2} \frac{\partial n T_i}{\partial t} + \frac{1}{\sqrt{g}} \frac{\partial}{\partial x} \left( \frac{\sqrt{g}}{h_x} \tilde{q}_{ix} \right) + \frac{1}{\sqrt{g}} \frac{\partial}{\partial y} \left( \frac{\sqrt{g}}{h_y} \tilde{q}_{iy} \right) + \frac{n T_i}{\sqrt{g}} \frac{\partial}{\partial x} \left( \frac{\sqrt{g}}{h_x} V_{\parallel} b_x \right) \\ & = Q_\Delta + Q_{AN} + \frac{\eta_0}{3} \left( 2 b_x \frac{\partial V_{\parallel}}{h_x \partial x} \right)^2 + n T_i B \frac{1}{h_x h_y} \left( \frac{\partial \Phi}{\partial y} \frac{\partial}{\partial x} \left( \frac{1}{B^2} \right) - \frac{\partial \Phi}{\partial x} \frac{\partial}{\partial y} \left( \frac{1}{B^2} \right) \right), \end{aligned} \quad (19.47)$$

where

$$\begin{aligned} \tilde{q}_{ix} &= \frac{3}{2} n T_i \left( -\frac{b_z}{B h_y} \frac{\partial \Phi}{\partial y} + b_x V_{\parallel} \right) \\ &+ \frac{5}{2} n T_i b_z \left( -\frac{D}{T_e + T_i} \frac{b_z}{h_x} \left( \frac{\partial p}{n \partial x} - \frac{3}{2} \frac{\partial T_e}{\partial x} \right) - D_{AN}^n \frac{1}{h_x n} \frac{\partial n}{\partial x} - D_{AN}^p \frac{1}{h_x n} \frac{\partial p_i}{\partial x} \right) \\ &+ \frac{5}{2} n T_i b_z \tilde{V}_{\perp}^{(dia)} - \kappa_{i\parallel} \frac{b_x^2}{h_x} \frac{\partial T_i}{\partial x} - \kappa_{i\perp} b_z^2 \frac{1}{h_x} \frac{\partial T_i}{\partial x}, \end{aligned} \quad (19.48)$$

$$\begin{aligned} \tilde{q}_{iy} &= \frac{3}{2} n T_i \frac{B_z}{B^2} \frac{1}{h_x} \frac{\partial \Phi}{\partial x} \\ &+ \frac{5}{2} n T_i \left( -\frac{D}{T_e + T_i} \frac{1}{h_y} \left( \frac{\partial p}{n \partial y} - \frac{3}{2} \frac{\partial T_e}{\partial y} \right) - D_{AN}^n \frac{1}{h_y n} \frac{\partial n}{\partial y} - D_{AN}^p \frac{1}{h_y n} \frac{\partial p_i}{\partial y} \right) \\ &- \kappa_{e\perp} \frac{1}{h_y} \frac{\partial T_i}{\partial y} + \frac{5}{2} n T_i \tilde{V}_y^{(dia)} \end{aligned} \quad (19.49)$$

As for the electrons, the parallel heat conductivity is classical with a possible heat flux limit, while the perpendicular contribution can be either classical or anomalous.

There is discussion in the literature on how to take into account anomalous terms in the energy balance equations. One point of view (see e.g. [135]) is to cancel the contribution from anomalous particle fluxes in the terms  $p_i \nabla \cdot \vec{V}_i$  (or  $\vec{V}_i \nabla p_i$  if equations are written in a difference form). In contrast, according to the derivation [127], where a kinetic equation with fluctuating term has been integrated, the anomalous fluxes should be kept in all terms of the energy balance equations. This variant was used in UEDGE [124, 125, 126]. In B2 only the contribution from anomalous radial particle flux to the convective heat flux are left in the expressions for  $\tilde{q}_{e,i}$ . In the term  $p_i \nabla \cdot \vec{V}_i$  the anomalous particle flux is absent.

## 19.4. Boundary conditions with drifts and currents

Whether one deals with the diamagnetic or  $\mathbf{E} \times \mathbf{B}$  perpendicular drift velocity, special care must be taken to avoid unphysical flows at the plates. The standard boundary condition is to require that the flow be at least sonic at the sheath entrance [136], which translates into:

$$V_{\parallel} \geq C_s - \frac{b_z}{b_x} V_{\perp} , \quad (19.50)$$

where  $C_s$  is the local sound speed and  $\frac{b_z}{b_x}$  is the inverse of the field line pitch. However, for very small pitch angles, as in stellarators, the  $V_{\perp}$  term may overpower the sound velocity [137] and then the boundary condition would require a plasma flow exiting the plate. Therefore, the pitch angle at the plates is limited to be no less than 1 degree, motivated by the engineering limits met when attempting to align the divertor tiles with the magnetic field. The solution procedure of the code was also modified so as ensure that no unphysical flows were being created, and solves the parallel momentum equation using the updated electric potential.

Boundary conditions for the current continuity equation at the plates correspond to sheath current-voltage characteristics

$$j_x = en \left( b_x c_s - b_x \frac{1}{\sqrt{2\pi}} \sqrt{\frac{T_e}{m_e}} \exp \left( -\frac{e\Phi}{T_e} \right) (1 - \gamma) \right) , \quad (19.51)$$

where  $\gamma$  is the secondary electron emission coefficient. At the inner (core) flux surface the currents are set either to the divergent part of the diamagnetic current or to zero. Both variants give the same result and both guarantee that the net current integrated over the inner flux surface should be zero. At the walls, the same conditions on the normal current components were imposed as for the inner core.

The electron and ion heat fluxes to the target plates are

$$\tilde{q}_{ex} = b_x \frac{n}{\sqrt{2\pi}} \sqrt{\frac{T_e}{m_e}} \exp \left( -\frac{e\Phi}{T_e} \right) (1 - \gamma) \left( T_e \frac{1 + \gamma}{1 - \gamma} + e\Phi \right) , \quad (19.52)$$

$$\tilde{q}_{ex} = \frac{3}{2} n T_i c_s b_x . \quad (19.53)$$

The question of kinetic boundary conditions including drifts is not yet finally clarified and will need further work from both kinetic and fluid modelling [138, 136].

## 19.5. Structure of the radial electric field close to the edge

Simulations were performed for ASDEX-Upgrade both for Ohmic discharge and discharges with additional heating. To provide convergence of the numerical scheme, an anomalous current was added in the form

$$\vec{j}^{(AN)} = -\sigma^{(AN)} \nabla \Phi, \sigma^{(AN)} = k^{(AN)} en, k^{(AN)} = 3 \cdot 10^{-6} - 10^{-3} \quad (19.54)$$

Such low values of  $\sigma^{(AN)}$  on the one hand provide the convergence of the numerical scheme, and on the other hand do not influence the final result. It should be noted that anomalous conductivity does not exist in the presence of turbulence, in contrast to diffusion or heat conductivity, due to the ambipolar nature of Coulomb collisions (see, e.g. [128]). The indirect influence of anomalous transport is connected with transport of momentum due to inertia and viscosity terms.

To test sensitivity of the potential profile to different types of transverse currents, all currents, except diamagnetic and anomalous currents, were switched off in some runs. In other words, anomalous conductivity in this case represents the effective transverse conductivity in the edge plasma with  $3 \cdot 10^{-6} \leq k^{(AN)} \leq 10^{-3}$ . The  $\mathbf{E} \times \mathbf{B}$  and diamagnetic drifts were also switched off in these test runs. The potential profile and the electric field on the closed flux surfaces and in SOL in the vicinity of the separatrix is very sensitive to the value of  $\sigma^{(AN)}$ . The electric potential in the core is negative and is (roughly speaking) inversely proportional to  $\sigma^{(AN)}$  (Fig. 19.2).

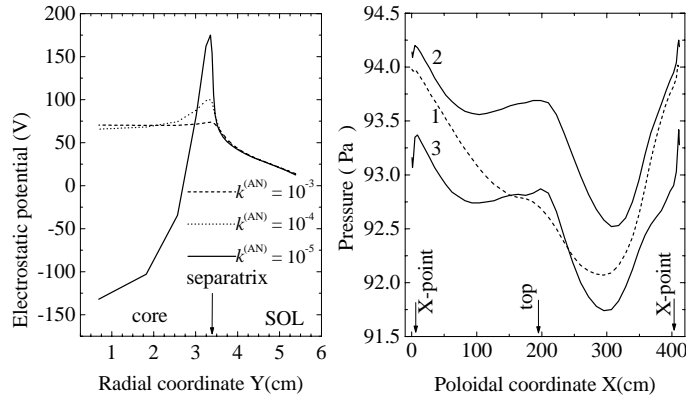


Figure 19.2.: Left: potential profile at outer midplane. Anomalous perpendicular current balances diamagnetic drift current. All other transverse current are switched off.  $\mathbf{E} \times \mathbf{B}$  drifts and diamagnetic drifts are also switched off. Right: pressure profiles on a closed flux surface. 1. All drifts switched off. 2.  $\mathbf{E} \times \mathbf{B}$  drifts switched on. 3. Both  $\mathbf{E} \times \mathbf{B}$  and diamagnetic drifts switched on.

This can be understood since averaged over flux surfaces the diamagnetic current is balanced by the radial anomalous current. Surface averaged diamagnetic current in the absence of  $\mathbf{E} \times \mathbf{B}$  drifts is a given value determined by quite subtle details of pressure distribution over the flux surface (Fig. 19.2). Therefore, to balance it for smaller anomalous conductivity the larger radial electric field is necessary. In contrast, in the SOL not very close to the separatrix the potential distribution is quite insensitive to the value of the transverse conductivity.

Switching on  $\mathbf{E} \times \mathbf{B}$  (Fig. 19.4) and diamagnetic drifts causes a redistribution of the density, temperature and pressure over the flux surfaces (Fig. 19.2). Thus  $\mathbf{E} \times \mathbf{B}$  drifts have a strong influence on the diamagnetic current averaged over the closed flux surfaces, and, finally, on the radial potential profile. For simulation of normal discharges, the anomalous conductivity was reduced to quite low values ( $k^{(AN)} = 3 \cdot 10^{-6}$ ), and all important perpendicular currents and all drifts were switched on. The anomalous conductivity in this case was more than two orders of magnitude smaller than the anomalous conductivity using Einstein relation,  $\sigma^{(AN)} = \frac{ne^2}{T_e} D_{AN}^n$ . To check the relative influence of various types of perpendicular currents these currents were switched on and off.

First, a ohmic discharge for the normal direction of B (ion  $\nabla B$  drift is directed towards the X-point) was studied (Fig. 19.3).

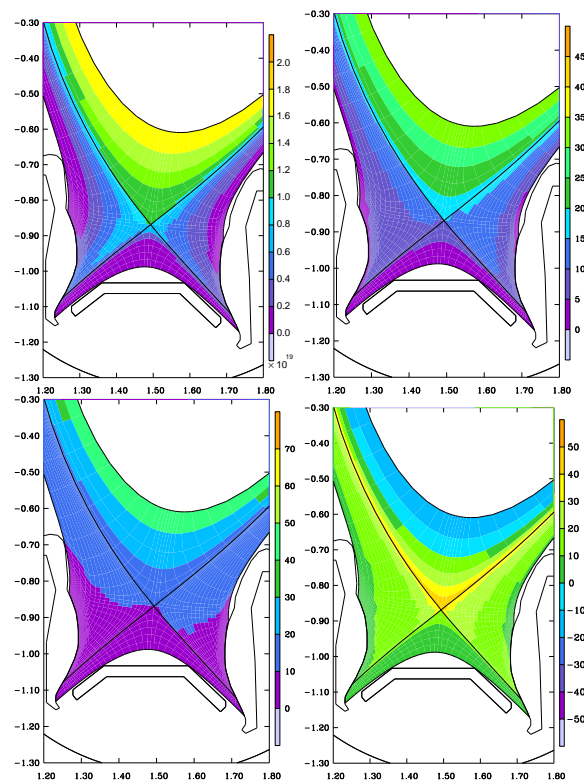


Figure 19.3.: Main plasma parameters for ohmic discharge with all drifts switched on: electron density (left top, in  $m^{-3}$ ), electron temperature (right top, in eV), ion temperature (left bottom, in eV) and potential (right bottom, in V).

The potential reaches its maximum somewhere near the separatrix, is negative in the core and it is positive in the SOL (Fig. 19.5). The radial electric field is negative in the core

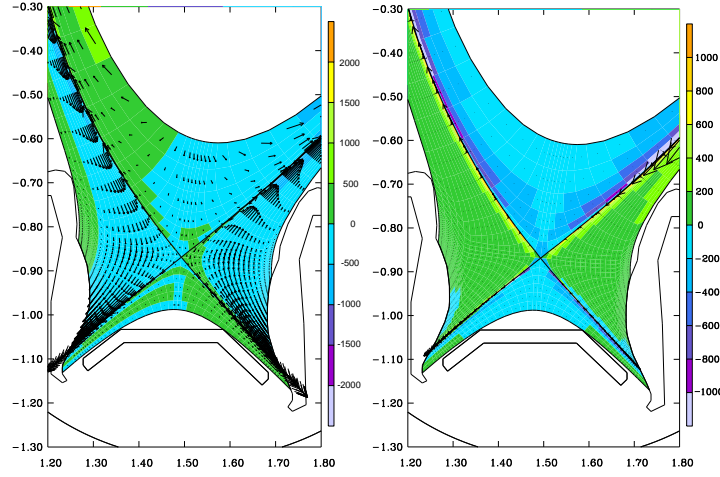


Figure 19.4.: Poloidal current(left) and poloidal  $\mathbf{E} \times \mathbf{B}$  drift velocity (right) for the ohmic discharge. Arrows represent the total current (left) or the full drifts (right). Colours represent the values of the poloidal current (left) or the values of the poloidal drift (right).

and positive in SOL. The  $\mathbf{E} \times \mathbf{B}$  drifts are directed from the inner to the outer plate in the SOL and from the outer to the inner plate in the private flux region (Fig. 19.4). The core plasma rotates in the direction opposite to that in the SOL, thus creating a strong shear near the separatrix. This is consistent with the results of other simulations and experiments [126, 119, 127].

The divergent part of the diamagnetic current corresponds to the particle guiding centre vertical current. Its radial component is the largest in the system. On the closed flux surfaces far from the separatrix this current is closed by the parallel Pfirsch-Schlüter current

$$j_{\parallel} = j_{\parallel}^{P.S.} = \frac{\partial p}{\sqrt{h_y} \partial y} \frac{B_z}{B_x B} \left(1 - \frac{B^2}{B_0^2}\right) \quad (19.55)$$

This expression is in good agreement with simulation results (Fig. 19.5).

This fact can be considered as a good test for the code itself. On the open field lines parallel current is a combination of a Pfirsch-Schlüter current and thermal current which flows from outer to inner plate due to the temperature differences in the divertor legs.

Since the anomalous conductivity is reduced to quite low values, diamagnetic current averaged over the closed flux surfaces is balanced by other currents. The radial potential profile in the equatorial midplane is not changed significantly by switching on current driven by ion-neutral collisions and inertial current (centrifugal effect, Fig. 19.5).

The radial potential profile strongly depends on the plasma temperature and density in the vicinity of the separatrix and in the core. For larger power inputs into the electron and ion components the radial electric field in the core is larger (Fig. 19.6). Far from the separatrix it is of the order of neoclassical electric field (Fig. 19.6). The neoclassical field has been calculated according to

$$E^{(NEO)} = \frac{T_i}{e} \left( \frac{1}{h_y} \frac{d \ln n}{dy} + 2.7 \frac{1}{h_y} \frac{d \ln T_i}{dy} \right). \quad (19.56)$$

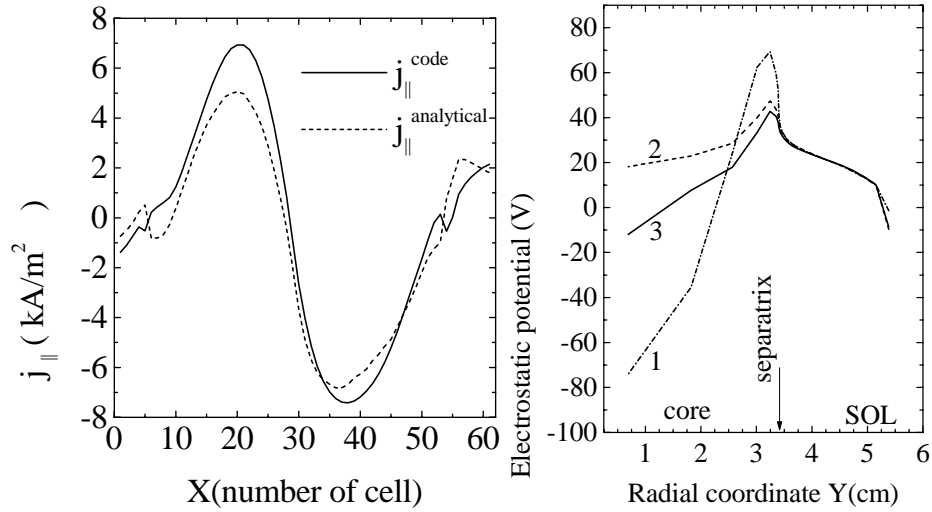


Figure 19.5.: Left: parallel current on the closed flux surface as a function of poloidal coordinate.

Right: radial potential profiles at outer midplane. 1.  $\mathbf{E} \times \mathbf{B}$  drifts and diamagnetic particle fluxes switched off. 2.  $\mathbf{E} \times \mathbf{B}$  drifts switched on. 3. All drifts and fluxes switched on.

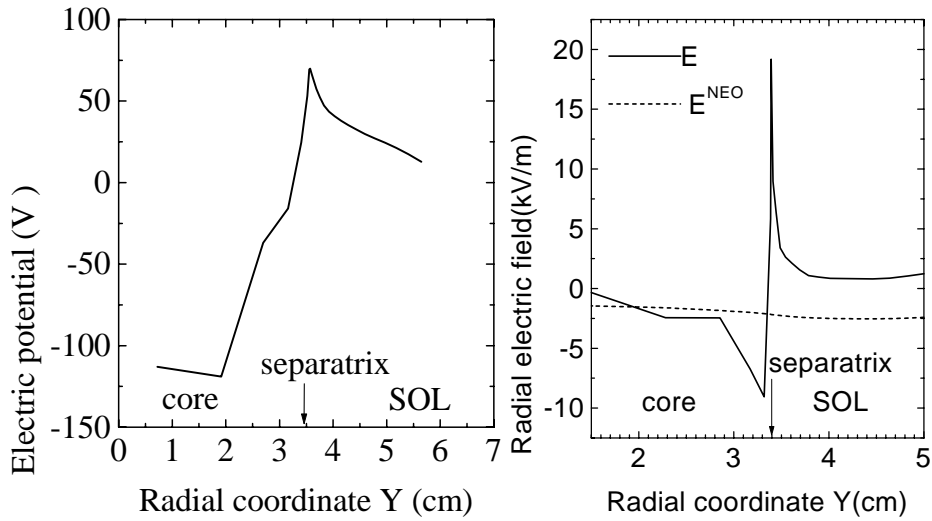


Figure 19.6.: Left: radial potential profile at outer midplane for increased power input (additional heating).

Right: comparison of radial electric field at outer midplane with neoclassical electric field.

To test the role of electrostatic drifts, several runs were made without drifts and without either poloidal or radial components of  $\mathbf{E} \times \mathbf{B}$  drifts. In the ohmic regime the influence of the drifts is relatively modest. Switching on the poloidal drifts results in density decrease near the inner divertor and an increase near the outer divertor leg of the order of 10%



in accordance with the direction of the poloidal drifts. Temperature rise in the inner divertor leg is about 10%. An asymmetry of parallel particle flow in the upper part of SOL was observed (Fig. 19.7). Parallel flow here is directed towards the inner leg even if

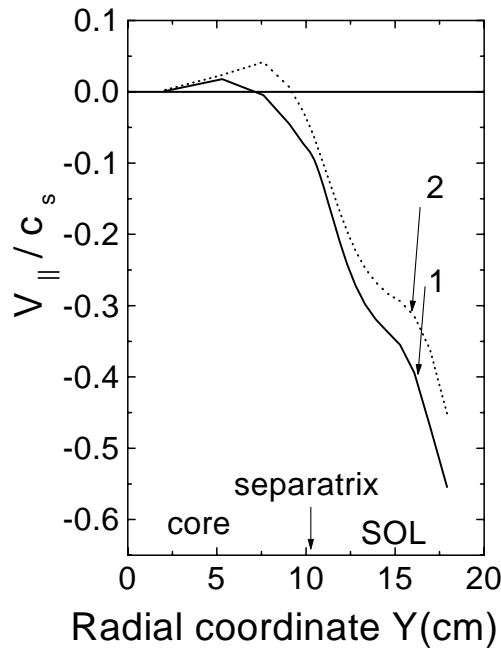


Figure 19.7.: Radial profile of the parallel velocity in the upper part of the SOL 1. in the presence of poloidal  $\mathbf{E} \times \mathbf{B}$  drift and 2. in the absence of drift.

the poloidal  $\mathbf{E} \times \mathbf{B}$  drifts are switched off. Switching on the poloidal drifts leads to further increase of the parallel velocity, because the poloidal projection of the parallel velocity compensates poloidal  $\mathbf{E} \times \mathbf{B}$  drifts, so that poloidal rotation roughly remains the same (as was predicted in [122]). The exception is the region very close to separatrix where contribution from  $\mathbf{E} \times \mathbf{B}$  to the poloidal rotation is the largest. Switching on radial drifts results in smaller variation of plasma parameters (less than 10%): density increases near the inner plate and decreases near the outer plate, while the temperatures change in the opposite direction.

## 19.6. Drift effects in the SOL

Here, the discussion will concentrate on the analysis of open fieldlines, where the potential profile is dominated by the contact to the target plates. Of special interest is the experimental observation of strong magnetic field reversal effects even reversing the divertor in-out asymmetry. This was studied by simulating an ASDEX-Upgrade ohmic scenario. First, the analysis was done for 300 kW input power accounting for impurity losses by a reduction of the nominal input power of 800 kW. Comparison of the simulation results with experimental measurements using a fast-moving Langmuir probe in the divertor region of ASDEX-Upgrade (see Fig. 19.8) was possible.

The simulation gets comparable inboard and outboard temperatures quite unlike experiment (Fig. 19.8). The effect of  $\mathbf{E} \times \mathbf{B}$  drifts (which are the dominant terms in this case)

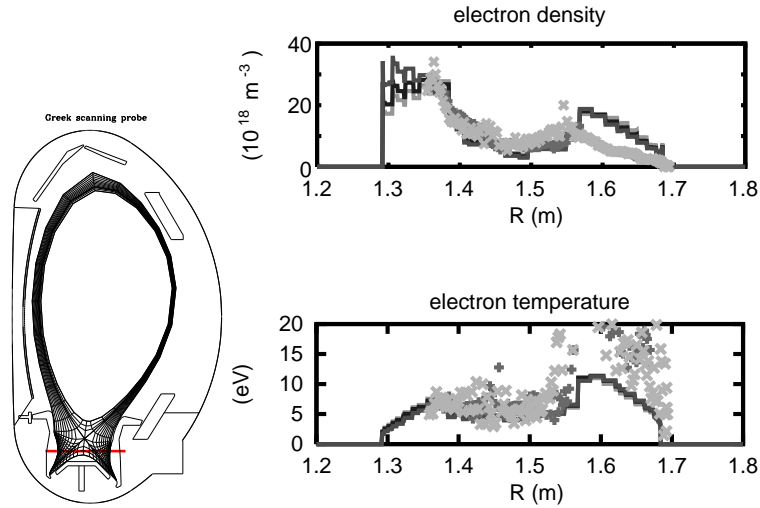


Figure 19.8.: Left: poloidal cross-section of ASDEX-Upgrade with mesh used for the B2-solps5.0 runs. The red line indicates the line where the fast Langmuir probes moves in and out during the discharge.

Right: electron density and electron temperature along the movement path of the fast reciprocating Langmuir probe as measured (X and +) and calculated from B2-solps5.0 (lines).

are weak and do not lead to a better match of experiment. As soon as a multifluid model (D+C, 500 kW input power) including 1% chemical sputtering is used, the asymmetry as seen in the experiment is well reproduced for the direction of the magnetic field used in the experiment (Fig. 19.9).

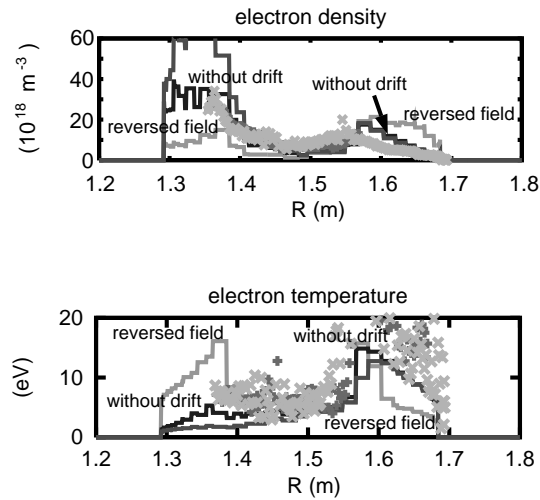


Figure 19.9.: Electron density and electron temperature along the movement path of the fast reciprocating Langmuir probe as measured (X and +) and calculated from B2-solps5.0 (lines) with the inclusion of carbon (right).

In this case, the reversal of magnetic field in the simulation now also causes a strong

change in the divertor properties leading to a colder outer and a hotter inner divertor (also seen in other experiments [139], Fig. 19.10).

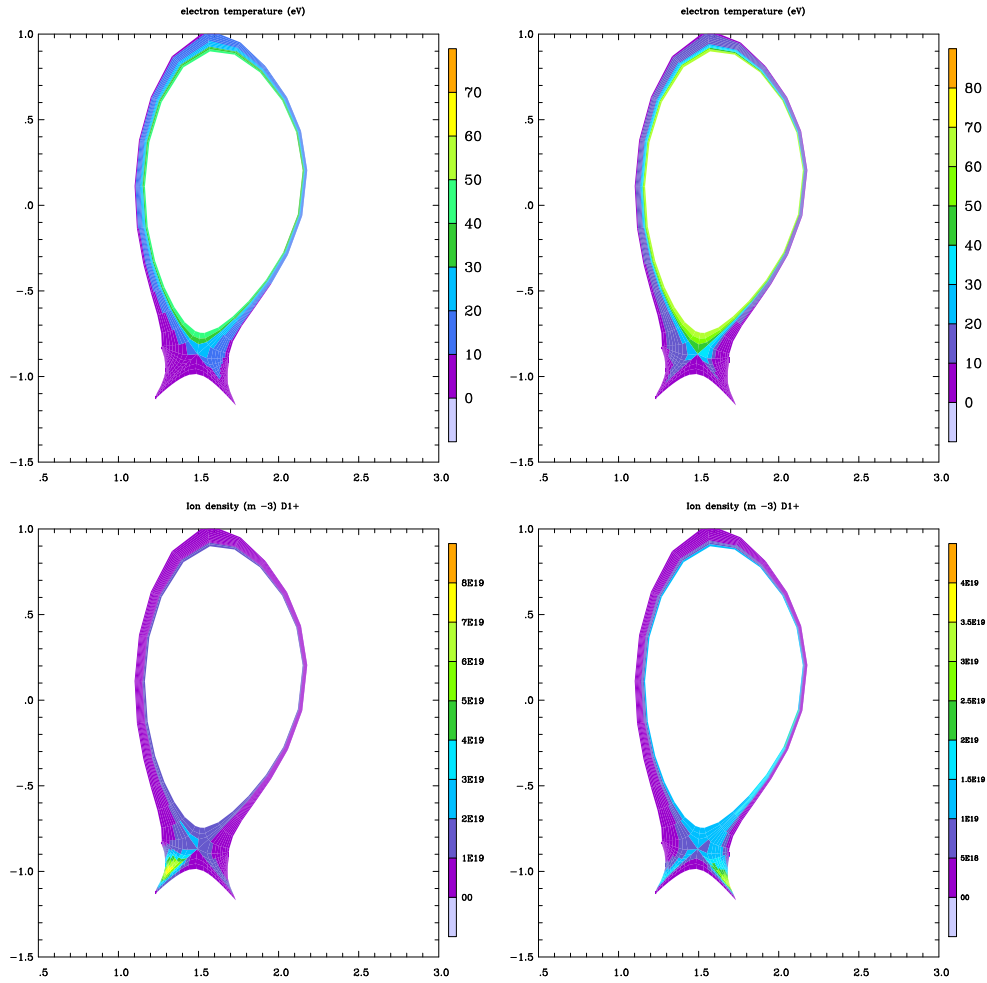


Figure 19.10.: Electron temperature (top) and density (bottom) contours for 600 kW input power, chemical and physical sputtering and  $\mathbf{E} \times \mathbf{B}$  drifts. For the positive field direction (left, as used for shot # 9199), the inner divertor is colder than the outer, whereas for the reversed field (right) the outer divertor gets colder than the inner.

This strong field-reversal effect is consistent with experimental results reporting that B-reversal can exchange the temperature and density conditions from the inner to the outer divertor (changing from hot outer to hot inner divertor) [114, 115].

## 19.7. Effect of neutral beam injection

In this section the effect of unbalanced neutral beam injection (NBI) for the edge plasma in ASDEX-Upgrade is discussed. The toroidal momentum transport over the separatrix and down to the plates is calculated and compared with a simple analytical solution.

Toroidal rotation changes also the radial electric field in the core and SOL. In the SOL transport of toroidal momentum causes asymmetry of pressure and of particle and heat fluxes to the plates.

For a regime without momentum input a zero radial momentum flux of parallel momentum was used as a boundary condition at the inner core boundary, while NBI scenarios are simulated with a constant radial flux of parallel momentum or a constant parallel velocity. The parameters were chosen such that typical ASDEX-Upgrade NBI scenarios were analysed (up to 30 km/s parallel velocities as measured with spectroscopy). Depending on the core boundary condition for the parallel velocity one gets different parallel velocities at the outer midplane averaged over the flux surface (Fig. 19.11).

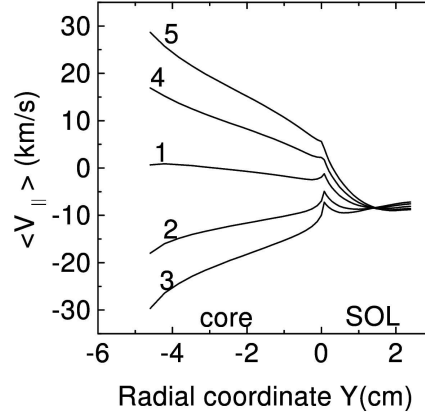


Figure 19.11.: Radial profile of surface averaged parallel velocity at the outer midplane. In the SOL the average is done over the region above the X-point. 1. No NBI ( $V_{\parallel}(\text{inner core}) = 0$  km/s), 2.  $V_{\parallel}(\text{inner core}) = -18$  km/s, 3.  $V_{\parallel}(\text{inner core}) = -30$  km/s, 4.  $V_{\parallel}(\text{inner core}) = +18$  km/s, 5.  $V_{\parallel}(\text{inner core}) = +30$  km/s. Typically, parallel velocities at the inner boundary are negative for co-injection, positive for counter-injection.

The average velocity gradually decreases towards the separatrix, while the radial flux of toroidal momentum remains almost constant since it is generated by the boundary condition and then transported to the separatrix (no other sink or source terms in the core). Positive (in the counter direction) averaged toroidal velocity was observed even in the absence of unbalanced NBI. Therefore, a part of the momentum is generated by averaged parallel viscosity and pressure gradient.

This can be understood from the toroidal component of the momentum balance equation

$$d\Gamma^{(m)}/dt = -j_y B_x, \quad (19.57)$$

where the l.h.s. represents radial transport of toroidal momentum. Since the net current through the flux surface in the core should be zero, the following condition should be fulfilled:

$$\int \frac{\sqrt{g}}{h_y B_x} \frac{d\Gamma^{(m)}}{dt} dx = 0. \quad (19.58)$$

This condition requires a finite flux-surface-averaged parallel velocity in the core, because of the complicated character of the parallel velocity over the flux surface. The latter is to

a large extent determined by the coupling with the SOL, where the poloidal distribution of the parallel velocity is connected with geometrical effects (different particle fluxes to the plates due to different plasma densities, temperatures, angle of incidence and plate surfaces). The poloidal dependence of the particle flux from the core is also important.

The transport of the toroidal momentum over the separatrix and further down to the plates can also be understood from a simplified slab model of a SOL with the x-axis directed from inner to outer plate. Neglecting the parallel and anomalous viscosity in the SOL and integrating the parallel momentum balance equation over the SOL volume, one gets

$$\int_{x_-}^{x_+} \Gamma^{(m)} dx = m_i \langle V_{\parallel} \rangle_s \int_{x_-}^{x_+} \Gamma_s dx \quad (19.59)$$

$$m_i \langle V_{\parallel} \rangle_s \int_{x_-}^{x_+} \Gamma_s dx = m_i \int dy (\Gamma_{x_+} V_{\parallel,+} - \Gamma_{x_-} V_{\parallel,-}) + \int dy (B_x/B) (p_+ - p_-). \quad (19.60)$$

Here, the subscript  $s$  denotes the separatrix,  $+$  and  $-$  correspond to inner and outer plate. This equation means that radial flux of parallel momentum through the separatrix (l.h.s) is transported by poloidal particle flux to the plates and also causes pressure asymmetry. Pressure asymmetry produces differences in particle and energy fluxes to the plates. This effect was observed in ASDEX [140]. Substituting simplified boundary conditions (neglecting  $\mathbf{E} \times \mathbf{B}$  drifts; setting parallel velocity to sound speed), one gets (since  $\Gamma_x = (B_x/B)V_{\parallel}$  without  $\mathbf{E} \times \mathbf{B}$  drift) that the two r.h.s terms are equal to each other

$$\frac{1}{2} m_i \langle V_{\parallel} \rangle_s \int_{x_-}^{x_+} \Gamma_s dx = \int dy (B_x/B) (p_+ - p_-). \quad (19.61)$$

In other words, in this simplified model half of the radial flux of toroidal momentum, which is generated in the core and then flows over the separatrix, is responsible for the pressure asymmetry at the plates. For the case of co-injection one has  $p_- > p_+$ , and vice versa for counter-injection.

Small pressure asymmetry and asymmetries of poloidal and parallel fluxes in the SOL exist even in the absence of unbalanced NBI, due to geometrical effects (Fig. 19.12).

The quantity  $\int \int \sqrt{g}/h_x (B_x/B) (\partial p / \partial x) dy dx$  calculated in the code for the SOL (which corresponds to the r.h.s. of the simple model) minus the value for the balanced NBI equals  $k \int_{x_-}^{x_+} \Gamma^{(m)} \sqrt{g}/h_y dx$ , where  $k=0.31, 0.44$  for co- and counter-injection respectively and  $\langle V_{\parallel} \rangle (innercore) = -$  or  $+30 km/s$ . Therefore, the simple model gives a reasonable estimate. The effect is modest, since it should be of the order of  $\langle V_{\parallel} \rangle_s / c_{s-or+}$ , where  $\langle V_{\parallel} \rangle_s$  is the average parallel velocity at the separatrix and  $c_{s-or+}$  is the sound velocity at the plates.

The potential profile and the electric field are such that the electric field in the core region far from the separatrix is positive during co-injection and negative during counter-injection (Figs. 19.13 and 19.14).

The electric field structure in the core is as expected from prediction of neoclassical theory, where the combination of  $\langle BV_{\parallel} \rangle - \frac{B \partial \Phi}{B_x h_y \partial y}$  should remain a function of density and temperature gradients. However, close to the separatrix the electric field is negative

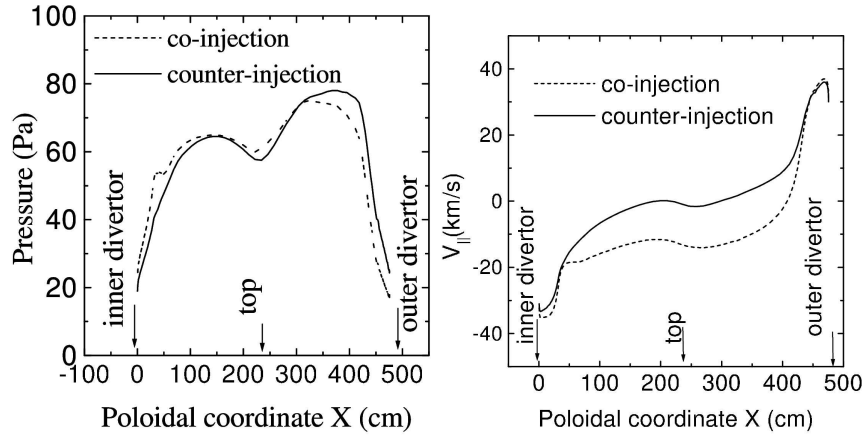


Figure 19.12.: Left: pressure profiles on the open field lines near the separatrix for co- ( $V_{||}(\text{inner core}) = -30$  km/s) and counter-injection ( $V_{||}(\text{inner core}) = +30$  km/s).

Right: parallel velocity profiles on the open field lines near the separatrix for co- ( $V_{||}(\text{inner core}) = -30$  km/s) and counter-injection ( $V_{||}(\text{inner core}) = +30$  km/s).

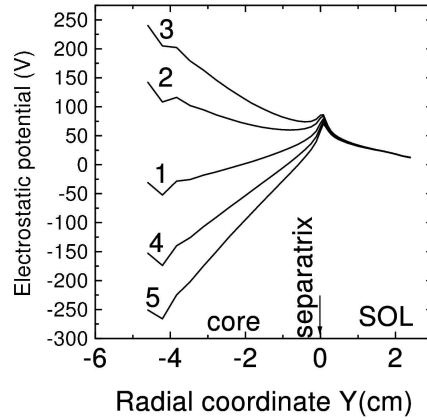


Figure 19.13.: Potential profiles at the outer midplane for 1. No NBI ( $V_{||}(\text{inner core}) = 0$  km/s), 2.  $V_{||}(\text{inner core}) = -18$  km/s, 3.  $V_{||}(\text{inner core}) = -30$  km/s, 4.  $V_{||}(\text{inner core}) = +18$  km/s, 5.  $V_{||}(\text{inner core}) = +30$  km/s. Typically, parallel velocities at the inner boundary are negative for co-injection, positive for counter-injection.

as in ohmic regime. For counter NBI the shear of the poloidal  $\mathbf{E} \times \mathbf{B}$  rotation near the separatrix is larger, so that the threshold for L-H transition should be lower (a larger shear weakens the turbulent eddies by tearing them apart). Both for co- and counter-injection at the separatrix vicinity from the core side there exists a region of strong electric field (a 'dip'). Its spatial scale is of the order of few mm, and electric field differs here significantly from the neoclassical value. This scale is to a large extent determined by the closing of the divergence of anomalous radial particle flux by the divergence of poloidal  $\mathbf{E} \times \mathbf{B}$  drift. Further inside, the electric field is smoother and closer to the neoclassical value, however

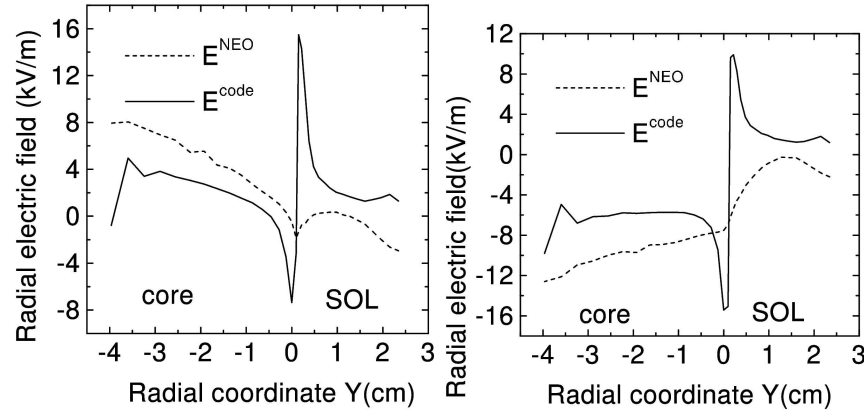


Figure 19.14.: Radial electric field at the outer midplane for co-injection ( $V_{\parallel}(\text{inner core}) = -23 \text{ km/s}$ )(left) and for counter-injection ( $V_{\parallel}(\text{inner core}) = +23 \text{ km/s}$ )(right).

one can notice considerable differences. The electric field profiles agree qualitatively with experimental results on DIII-D [141].

During NBI, additional radial electric fields are also generated in the SOL in the separatrix vicinity (Fig. 19.14). Indeed, due to momentum transport the average velocity in the SOL becomes more negative in the case of co-injection and more positive for counter-injection. In the first case, the point where parallel velocity changes its sign is shifted towards the outer plate. For counter-injection this point is shifted towards the inner plate. Assuming that the particle flux from the core is carried poloidally only by the parallel flux, most of the particle flux from the core would flow to the inner divertor in the first case, and to the outer divertor in the second case. This, however, is inconsistent with parallel momentum balance and the result that only modest changes in the pressure profiles appear. Therefore, additional radial electric fields arise to generate additional  $\mathbf{E} \times \mathbf{B}$  drift, which keeps almost the same poloidal flux as in the absence of NBI. Indeed, in contrast to the parallel flux, the poloidal flux is less sensitive to the direction of the NBI torque. The observed effect is inverse of that typical for biasing experiments, which was predicted in [142] and observed in TdeV [143]. There, the radial electric field is generated by biasing, and medium toroidal velocity was observed to keep the poloidal flux more or less independent of the biasing voltage.

## 19.8. Topology effects: Stellarator island divertor

Current (CHS, W7-AS) and future (W7-X) stellarators are being built with so-called “island divertors” [144, 3], where the divertor plates intersect magnetic islands situated at the edge of the plasma. This leads to unique geometrical features: as one moves away from the center of the island, one first encounters closed field lines, then open lines ending at the divertor plates, and finally closed lines again in the plasma core region. The presence of these two spatially separated closed field lines regions makes the physics characteristics of island divertors quite different from more conventional plasma-wall interaction regions. The island divertor concept, as envisioned in W7-AS and W7-X, is studied using the

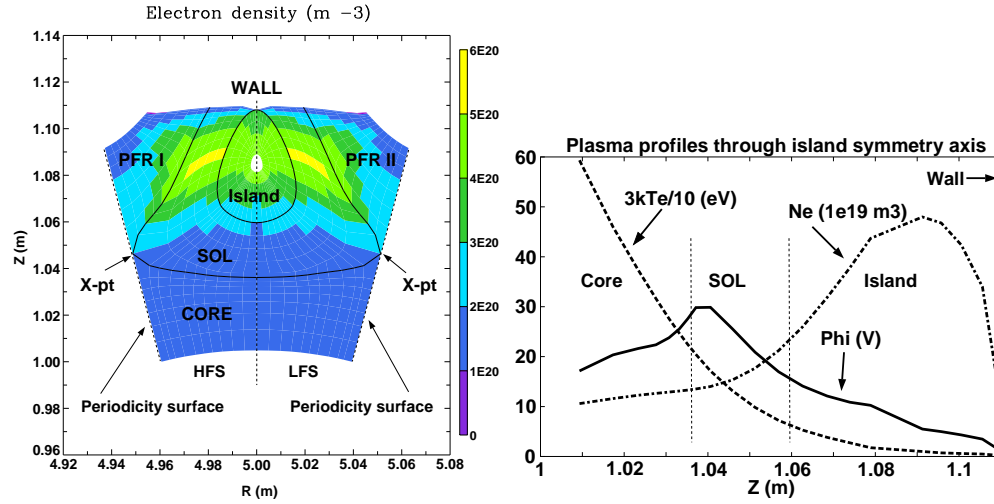


Figure 19.15.: Left: typical density distribution obtained for a no-drifts high-recycling case. The island, core, SOL and private flux regions (PFR I and II), their boundaries, X-points and periodicity surfaces are also shown. The dashed line shows the cut used for the 1-D profiles. HFS: High-field side; LFS: Low-field side.

Right: temperature (dashed line), density (dot-dashed line) and electric potential (solid line) profiles. The profiles are taken along the symmetry line at  $R = 5.00$  m (dashed line). Note the clear potential maximum just outside the separatrix, the density accumulation inside the island and the scale difference between  $3kT_e$  and  $\phi$ .

B2-solps5.0 Scrape-Off Layer Plasma Simulation code. Since the code is two-dimensional, the magnetic geometry is represented by a toroidally averaged grid [145]. This 2-D ansatz forces us to restrict the analysis mostly to the structure of the electric potential and electric field, concentrating on the impact of the topological features of the island divertor, without attempting a detailed engineering study. In itself, the island divertor already constitutes an interesting system for investigating terms driving radial transport and the establishment of potential gradients.

Although full 3-D models of stellarator plasma edge transport are becoming available [137, 146], they do not yet treat self-consistently the electric potential, or contain drifts and currents [147]. It is thus useful to obtain knowledge about the electric field structure of island divertors using the current 2-D tokamak simulation tools. First, results of simulations involving no drift terms are presented, so as to establish a reference case. Diamagnetic and parallel viscosity terms are then added, and their influence described. Finally, the further impact of the  $\mathbf{E} \times \mathbf{B}$  terms are discussed.

First, the geometry of the island divertor is specified (cf. Fig. 19.15).

For the purposes of the simulations, a toroidally-averaged grid is used computed from a W7-AS equilibrium [145] with a  $m/n = 5/9$  diverted island chain [3, 148]. Since one restricts to a general study of drift effects in island divertors, specific details of the individual W7-AS or W7-X islands can be neglected. In the Figure, the wall is the top edge of the simulation domain, and the interface with the core is the bottom boundary. In



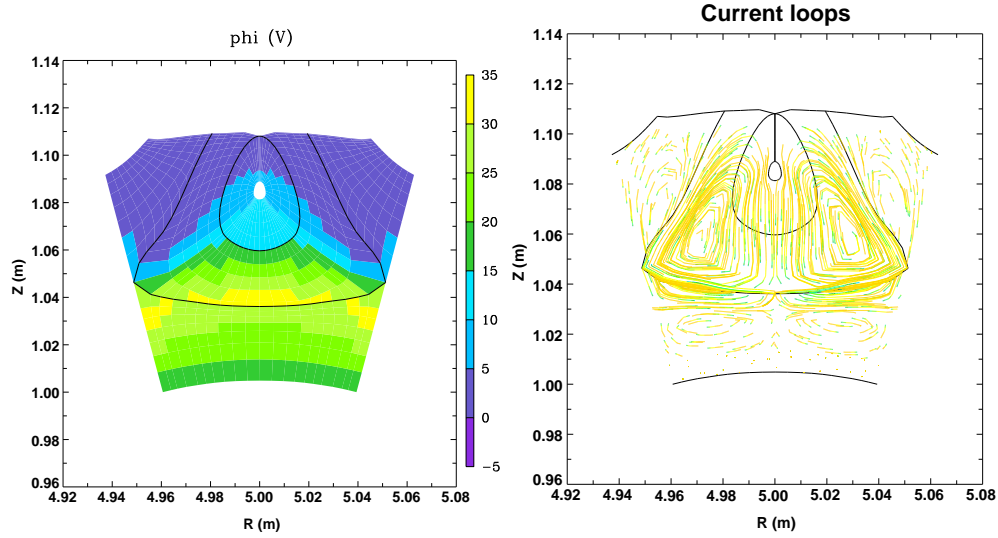


Figure 19.16.: Left: electric potential distribution for the case shown in Fig. 19.15.

Right: test charge trajectories illustrating the current flow loops present in the plasma for the case shown in Fig. 19.15.

the poloidal direction, periodic boundary conditions are used, where computational cells on the left edge of the domain are assumed to be neighbouring those on the right edge of the domain.

The dominating feature of these plasma configurations is particle accumulation inside the island [3]. In that sense, the island divertor behaves very differently from a standard tokamak divertor. The density distribution for a typical high-recycling case is shown in Fig. 19.15. A density “pillow” across the island and SOL regions is readily apparent. For this run,  $n_e^{core} = 10^{20} m^{-3}$  and a heat flux through the core boundary of 220 kW were chosen as boundary conditions (corresponding to 1.1 MW of SOL power influx for the complete 5-island system in W7-X). Out of these 220 kW, only about 20 kW reach the plates, and the remaining 200 kW are lost to radiation and ionization of the recycled neutrals, of which 50 kW are dissipated inside the island region. Analysis of the particle flows shows that many recycled neutrals penetrate into the island and are ionized there, thus creating a density increase in and about the island region.

As can be seen in Figs. 19.15 and 19.16, the potential profile favors this density distribution by adopting a maximum near the separatrix and in general being very different from the values given by the simple  $\phi = 3kT$  ansatz. Concurrently (cf. Fig. 19.16), current loops get established which interconnect the SOL and the island region, but do not cross into the core plasma.

Mirroring current flow loops also exist in both the core and the side private flux regions. As explained in [3], the “pillow” density depends strongly on the recycling conditions (in Figs. 19.15–19.16 a 99% recycling coefficient is used). Since the true geometry of the island is 3-dimensional and the plates are not toroidally continuous, the 2-dimensional simulations (with toroidally continuous plates) will overestimate the density accumulation. When correcting for this over-estimation by lowering the recycling coefficient, the island density accumulation rapidly disappears, while the current loops in the SOL become narrower,

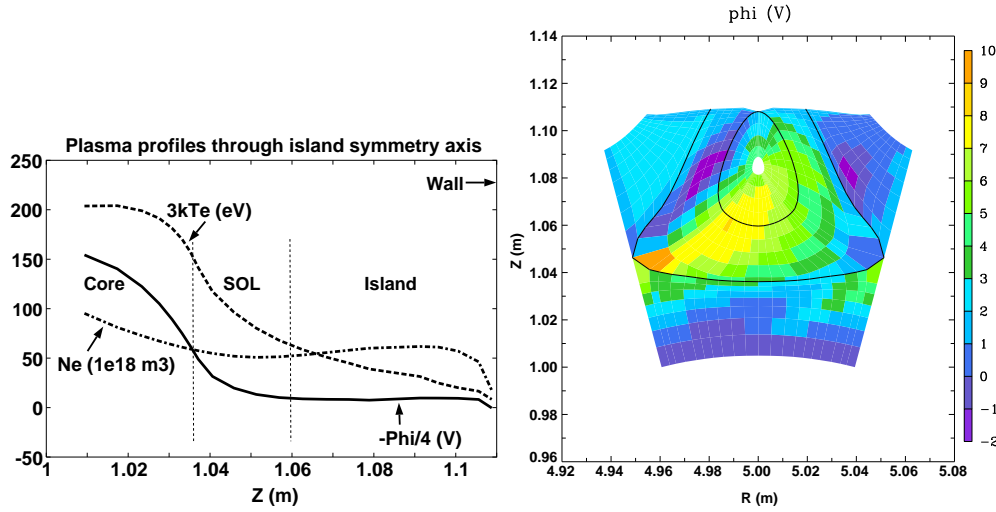


Figure 19.17.: Left: same as Fig. 19.15, but with diamagnetic and parallel viscosity effects included. Note the shallow density build-up inside the island and the change of scales for all three quantities. The electric potential had its sign changed for clarity of presentation. Right: same as Fig. 19.16, but with  $\mathbf{E} \times \mathbf{B}$  drift included.

eventually failing to cross over into the island region.

For the island case the formalism used for the core boundary conditions, which assumes closed field lines and balances diamagnetic and parallel viscosity currents [118, 117], has been generalized to handle the island center boundary as well. Lastly, the toroidal averaging algorithm [145] gives divergent values for the magnetic field strength (but not for the pitch angle) along the island symmetry axis. Hence, the values of  $B_z$  and  $B_x$  were modified ( $B_y = 0$  by construction) so that (1) the magnitude of  $B$  match that expected in the divertor region of W7-X and (2) the field line pitch  $\frac{B_x}{B_z}$  remain the same as in the toroidally averaged grid (thus keeping connection lengths unchanged). Since  $B$  is then no longer toroidally averaged in an absolute sense, it loses its strict periodicity. Thus avoiding computing the derivatives of  $1/B^2$  across the periodicity boundary by using face-centered values for the field components in cells next to that boundary.

The main consequence of the inclusion of the diamagnetic terms is the establishment of very strong radial potential gradients in the core region, fundamentally altering the electric field structure (see Fig. 19.17).

These gradients destroy the current loops that were previously connecting the SOL and diverted island regions and thus wash away most of the density inversion seen in the no-drifts case, with only the centre of the island still maintaining a slight density enhancement, as ionization of recycled neutrals still takes place in this region. Most of the current now flows in a semi-vertical pattern (in this geometry): from the plates, around the island, radially drifting towards the separatrix and once inside the core plasma almost purely radially. This behaviour is similar to what has been seen for tokamak cases [117]. The diamagnetic and parallel viscosity currents replace the anomalous perpendicular current (used for numerical stability reasons) of the no-drifts runs. As that numerical ansatz is relaxed, the potential gradient increases, roughly as the inverse of the anomalous

perpendicular conductivity.

Adding the  $\mathbf{E} \times \mathbf{B}$  terms is rather difficult for this geometry. In particular, the potential and momentum equations are coupled non-linearly by the  $\mathbf{E} \times \mathbf{B}$  velocity terms. This effect is most serious at the divertor plates, as discussed in the previous sections. Applying only the  $\mathbf{E} \times \mathbf{B}$  terms, without their diamagnetic counterparts, one sees, as expected, a large imbalance between the two sides of the SOL region. For this geometry, it is the high-field side of the SOL that experiences a density enhancement and where the potential minimum resides, although the actual values of the potential remain small.

As seen in Fig. 19.17, the region of maximum potential forms an asymmetrical ridge going from the high-field side X-point to the island center, falling off rapidly towards the inner divertor plate, and much more slowly in the opposite poloidal direction. The current loops have been strongly deformed, the high-field side loops elongating and swallowing most of the low-field side structures, while the core current becomes mostly poloidal.

The most challenging step is of course to turn on both the diamagnetic and the  $\mathbf{E} \times \mathbf{B}$  terms together. Numerical difficulties have been encountered, mostly at or near the X-points and at the core boundary. For example, the current flow patterns in the core, in the pure diamagnetic and pure  $\mathbf{E} \times \mathbf{B}$  cases, are essentially perpendicular to each other, and thus reaching a proper numerical steady-state equilibrium requires special care in the way the solution is approached and the new physics terms turned on. Particular attention must also be paid to the boundary condition at the core as well as to the rows of cells where the periodic boundary conditions are being applied.

Summarizing the results, due to the topological peculiarities of the problem, the potential profile is non-trivial ( $\phi \neq 3kT$ ), and can favor large density accumulation in the island and SOL regions for high-recycling conditions. Current loops are also established in the SOL which may connect to the diverted island region. These current loops grow lopsided under the influence of the  $\mathbf{E} \times \mathbf{B}$  drift, but are practically destroyed by diamagnetic effects. Concurrently, the island density accumulation is significantly reduced with the inclusion of drift effects.

## 20. Anomalous transport

Despite the fact that SOL modelling is very successfully able to identify basic physics mechanisms and represent even quantitatively the experimental results, the largest uncertainty in the SOL description is the question of anomalous transport.

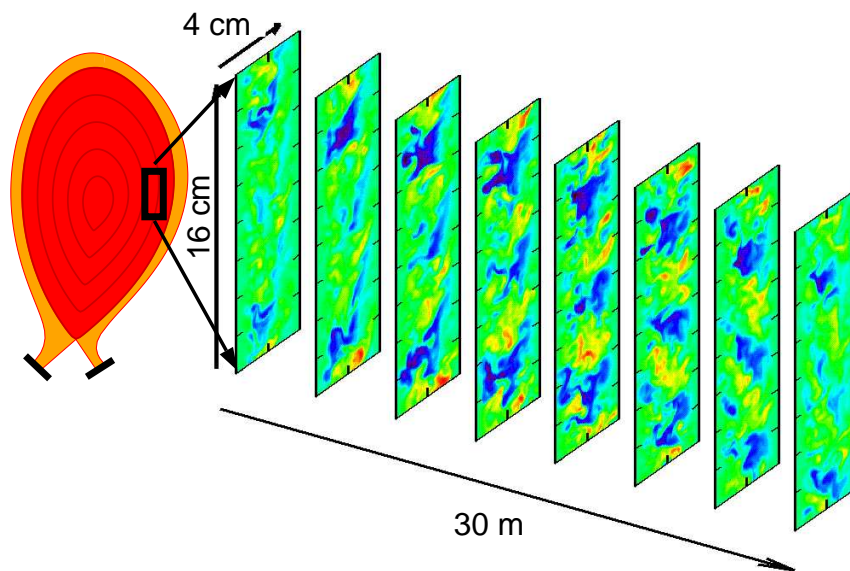


Figure 20.1.: Drift-wave turbulence calculations(B. Scott).

The turbulence in tokamaks is determined by small scale, low frequency drift turbulence involving eddies, waves or vortices of the  $\mathbf{ExB}$  velocity. The  $\mathbf{ExB}$  eddies advect the background thermal gradient to produce disturbances in all the thermodynamic state variables. The disturbances are then carried with the flow for as long as the eddies last. Then, they are picked up by new eddies and carried further. This does have the nature of a diffusive process if the size of the eddies and their lifetime are small and short compared to the scales of the background, and the net time-averaged transport does indeed scale with the background gradients if the turbulence is local. As a consequence of this underlying mechanism for the turbulence an anomalous resistivity cannot lead to anomalous transport of  $\mathbf{ExB}$  flows (or generating of radial electric field), because resistivity is a momentum conserving friction between electrons and ions [149].

Drift-wave turbulence in full geometry offers eventually a full predictive capability for the edge transport. It was already possible to demonstrate the effect of reducing the turbulent flow strongly by going from L-mode to H-mode conditions due to the break-up of large eddies by flow shear in H-mode [150].

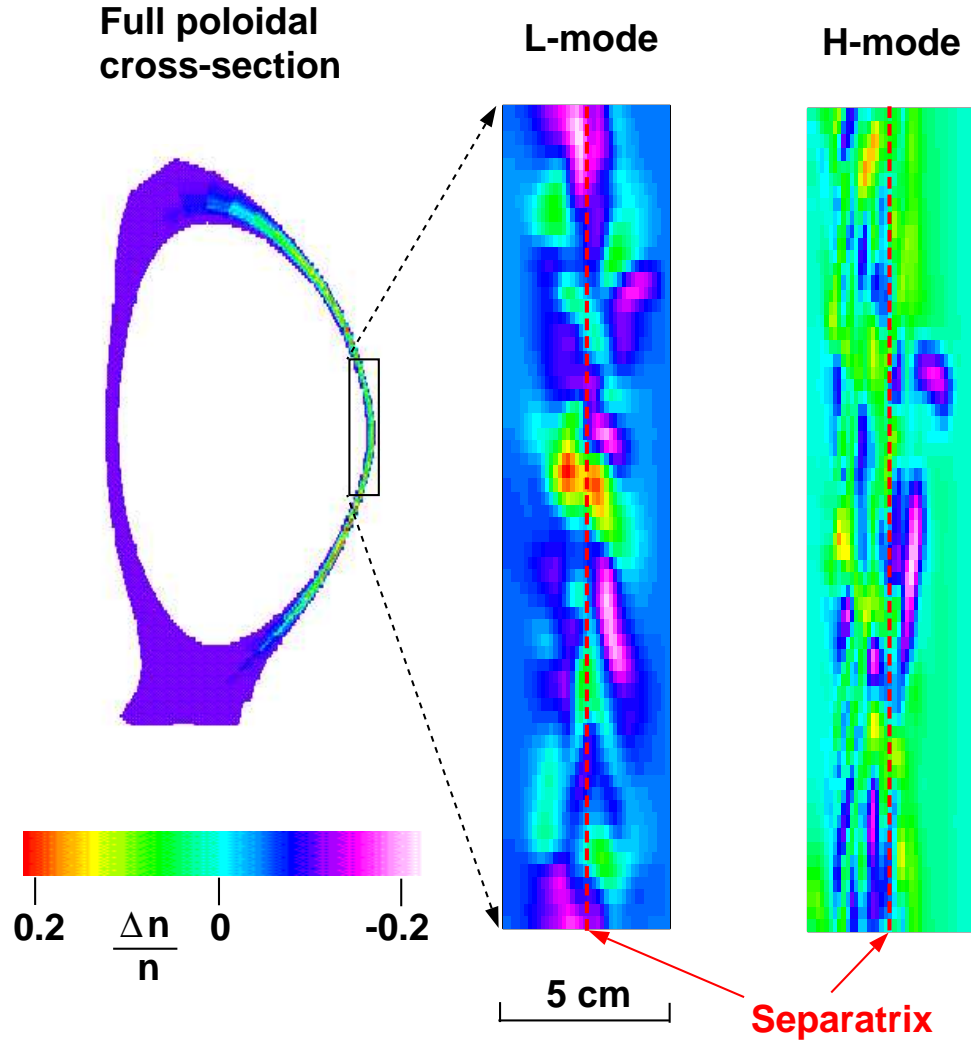


Figure 20.2.: 3D turbulence simulations show large density fluctuations on outboard side, large eddies in L-mode are broken up by flow shear in H-mode [150].

For ASDEX-Upgrade at high power, high density operation it looks like one has three regions of transport close to the edge. On closed fieldlines in H-mode one is determined operating at a critical pressure gradient (see previous discussion of edge-operational diagram). Then, one approaches the transition region close to the separatrix, where both critical MHD pressure gradients as well as detachment limits are getting important. Finally, the far outer SOL seems to be dominated by rather large radial plasma transport creating rather flat plasma profiles extending to the main chamber walls. This might be created by flute-like turbulence in nearly unmagnetized plasmas (here, the  $\nabla B$  drift becomes rather strong due to the sheath resistivity with a rather small plasma resistivity). Plasma filaments (probably created close to the separatrix) propagate outwards to the outer wall due to  $\nabla B$  and  $E \times B$  drift [151].

For a large variety of effects discussed before and as long as one is interested in a more qualitative comparison between experiment and modelling (trends) the SOL physics is not

so much dominated by the absolute value or dependence of the anomalous transport on SOL conditions. This is reflected in the fact that it is usually not possible to discriminate between e.g. a radially constant and a Bohm-like transport law [92] by comparing SOL modelling and experiment, because within the other uncertainties in the SOL model (e.g. wall pumping) and accounting also for experimental error bars different laws represent the measurements with an acceptable accuracy. Therefore, trying to derive from the SOL modelling some evidence for even more complex effects like poloidally varying transport in ballooning-like regimes or anomalous inward pinch velocities is difficult.

The most promising ansatz for this is to use automatic fit routines to derive databases of transport coefficients for regression analysis [152, 153, 154]. The major difficulty in predicting divertor conditions for future tokamaks is the uncertainty in the magnitude of the anomalous radial transport of energy and particles.

One approach is to take experimentally measured gradient lengths of power, temperature and/or density from existing machines, and then to extrapolate these quantities to future machines. These numbers have then been compared to code predictions for these future machines and, if necessary, to adjust the transport coefficients in the codes to produce a better match[155].

Another approach is to try and find scalings of the transport coefficients directly. For this, the 2-dimensional edge plasma fluid code, B2-SOLPS5.0[116, 117, 118], is used to determine the appropriate transport coefficients for various experimental discharges, and then scalings of these transport coefficients are sought.

This particular approach started on ASDEX-Upgrade (AUG) with the fitting of analytic or semi-analytic heat transport models to data gathered from the edge laser system[152]. In order to allow for convective effects, as well as to determine the particle diffusivity, development started on an interpretive version of the code[153].

Other, similar work includes the fitting of multi-1D models such as the onion-skin model of Stangeby[156].

## 20.1. Fit procedure

The basic procedure is outlined in Figure 20.3. A non-linear, multi-variable fit procedure is used to minimise the differences between the experimental and code results by varying the input to the plasma code. Every “function” evaluation of the fit is a full run of the plasma code. The residual that is minimised is the weighted sum of the squares of the differences between the code results and the experimental measurements, and the quantities that are varied to find this minimum would include transport coefficients and boundary conditions.

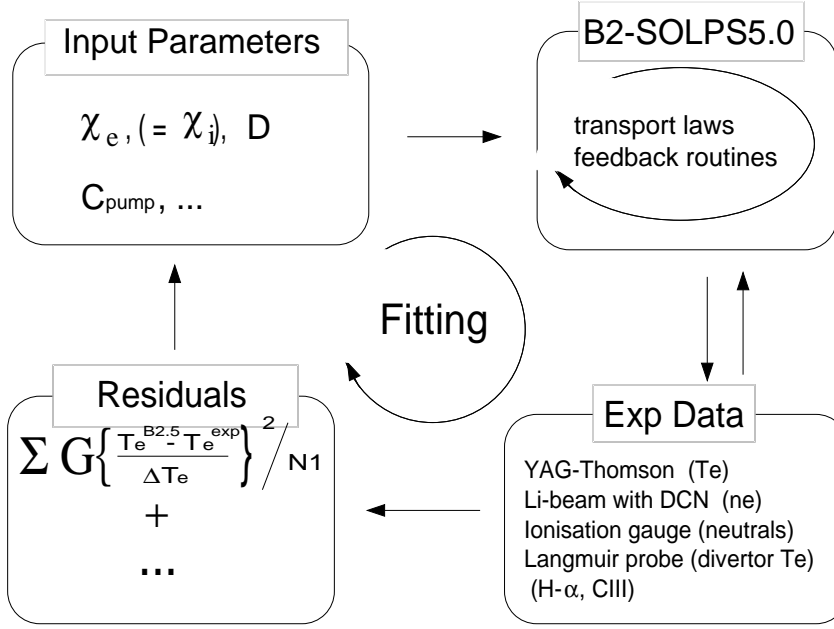


Figure 20.3.: The fit procedure used by the interpretive code.

The residual,  $R$ , is given by

$$\begin{aligned}
 R = & \alpha_1 \frac{1}{M} \sum_M G_{T_e} \left( \frac{T_e^{exp} - T_e^{code}}{\Delta T_e^{exp}} \right)^2 \\
 & + \alpha_2 \frac{1}{N} \sum_N G_{n_e} \left( \frac{n_e^{exp} - n_e^{code}}{\Delta n_e^{exp}} \right)^2 \\
 & + \alpha_3 \frac{1}{N} \sum_N G_{\nabla n_e} \left( \frac{\nabla n_e^{exp} - \nabla n_e^{code}}{\Delta \nabla n_e^{exp}} \right)^2 \\
 & + \alpha_4 \left( \frac{\Gamma_{pump}^{exp} - \Gamma_{pump}^{code}}{\Delta \Gamma_{pump}^{exp}} \right)^2 \\
 & + \alpha_5 \left( \frac{\Gamma_{wall}^{exp} - \Gamma_{wall}^{code}}{\Delta \Gamma_{wall}^{exp}} \right)^2
 \end{aligned} \tag{20.1}$$

and the fitted quantities are a radially and poloidally constant particle ( $D$ ) and thermal ( $\chi$ ) diffusivity, the electron density on the inner boundary ( $n_{e,core}$ ) and a quantity determining the amount of pumping from the private flux region ( $c_{pump}$ ).

The plasma code includes the ion-neutral recycling shown in Figure 20.4 (see[153]) and the bypass neutral recycling[157] as an additional gas puff.

As the core edge boundary condition, a fixed density( $n_{e,core}$ ) which is varied as a fit quantity is given to the plasma code. A fixed flux boundary condition was found to lead to bifurcations.

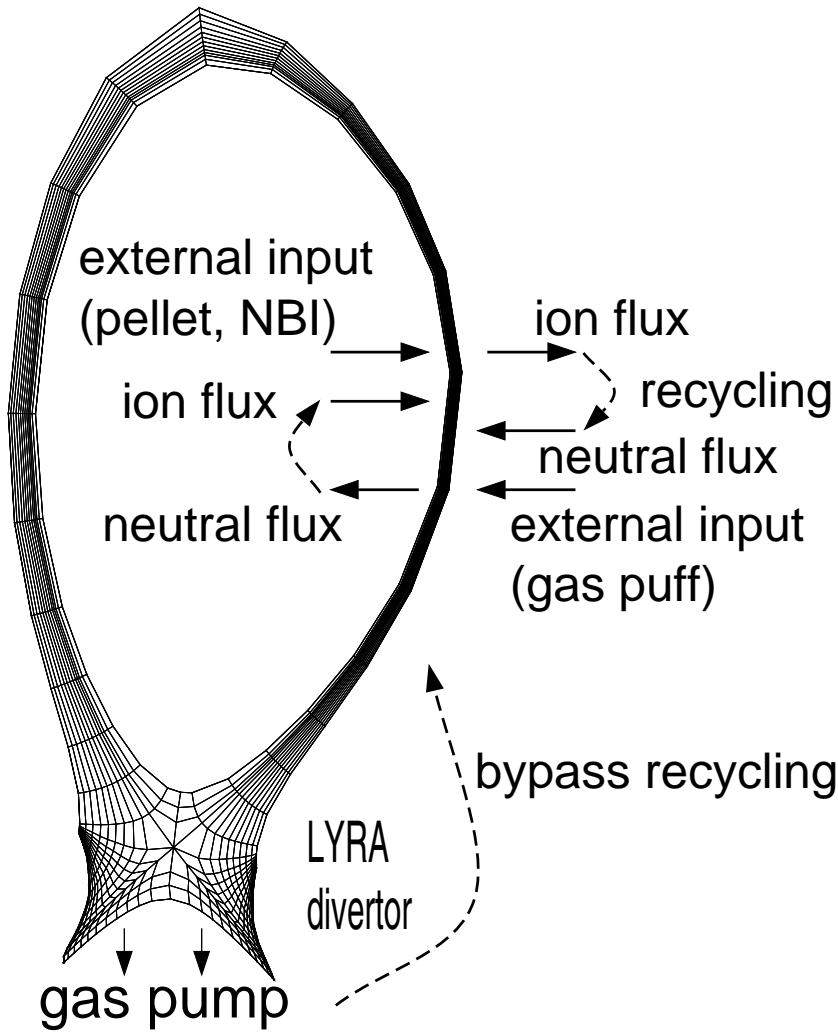


Figure 20.4.: The calculation region of the plasma code and boundary conditions

## 20.2. First database on ASDEX-Upgrade

The construction of a database of the radial transport coefficients has started on ASDEX-Upgrade (AUG). Only the limited number of discharges for which the YAG Thomson laser was at the edge and a slow radial scan of the plasma was performed[152] have been analyzed resulting in 44 shots with a range of plasma parameters as shown in Table 20.1. The results of a fit are shown in Figure 20.8a.

The range of fitted transport coefficients,  $\chi$  and  $D$ , are shown in Figure 20.5. Obviously the transport coefficients and their ratio vary substantially over this data set, which contains shots with rather different parameters and confinement regimes. In order to identify first scaling trends, the transport coefficients are plotted against various parameters of interest. For instance, Figure 20.6 shows a clear tendency of  $\chi$  with respect to  $\frac{\bar{n}_e}{n_{GW}}$ . It seems that the  $\chi$  of hydrogen plasmas depends on  $\frac{\bar{n}_e}{n_{GW}}$  more strongly than that of deuterium. (Earlier work[153] showed that  $\chi$  is not as dependent on boundary conditions.)



gas	$D_2, H_2$
type	H-mode (ELM I & III), L-mode
$I_p$	$0.4MA \sim 1.2MA$
$P_{sol}$	$1.7MW \sim 11MW$
$q_{95}$	$3.2 \sim 11$
$B_t$	$1.5T \sim 2.6T$
$\bar{n}_e$	$2.8 \times 10^{19}m^{-3} \sim 9.9 \times 10^{19}m^{-3}$
$\frac{\bar{n}_e}{n_{GW}}$	$0.34 \sim 0.81$

Table 20.1.: Range of experimental conditions in the edge transport database.

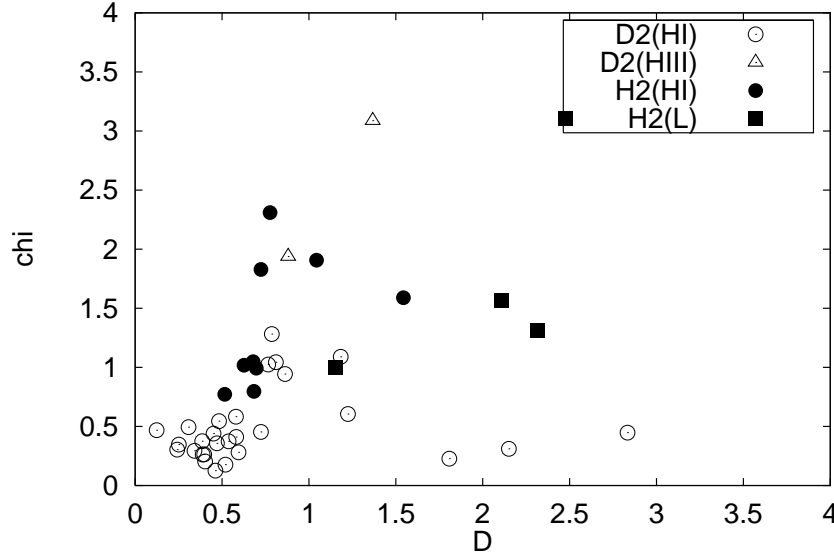


Figure 20.5.: The fitted radial transport coefficients

### 20.3. Preliminary multiple regression fit to $\chi$

A multiple regression fit to the data was performed fitting a power law (using a multiple linear regression to the logarithms of the quantities). Fitting to  $I_p$ ,  $P_{sol}$  and  $\bar{n}_e$  a fit for the deuterium H-mode discharges was obtained,

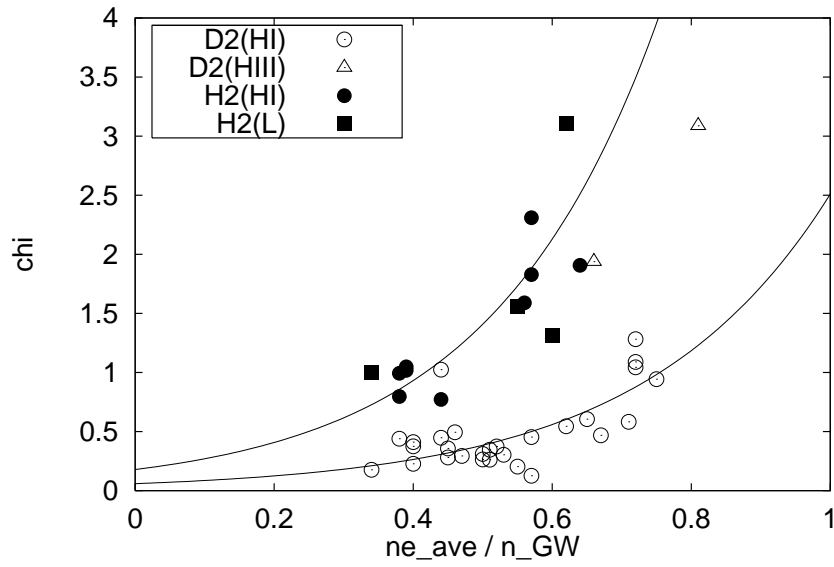
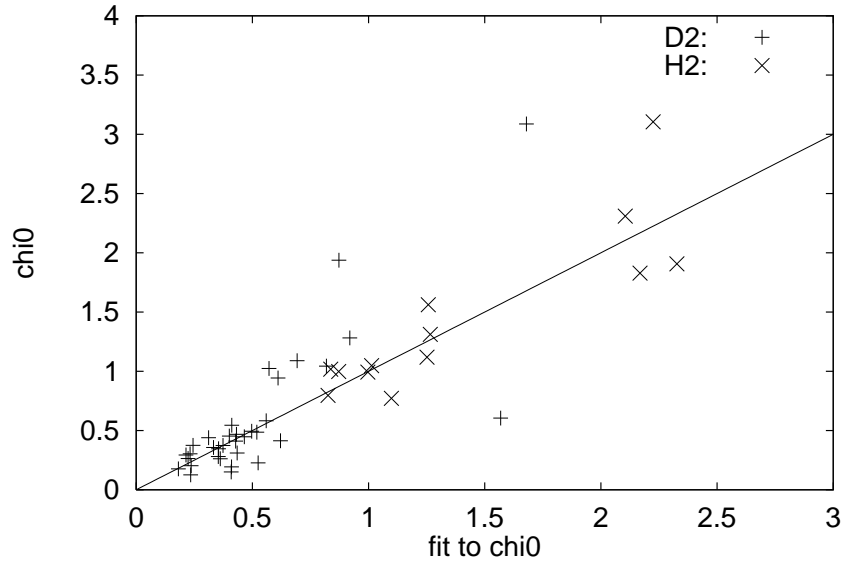
$$\chi \propto I_p^{-2.11 \pm 0.46} P_{sol}^{0.64 \pm 0.19} \bar{n}_e^{0.65 \pm 0.44} \quad (20.2)$$

and

$$\chi \propto I_p^{-1.69 \pm 0.45} P_{sol}^{0.00 \pm 0.52} \bar{n}_e^{0.68 \pm 0.68} \quad (20.3)$$

for the hydrogen h-mode discharges. This fit is shown in Figure 20.7

A strong decrease of transport with increasing plasma current is observed (as might be expected by assuming some sort of ballooning *ansatz*), an increase of transport with increasing separatrix density, and for the deuterium, an increase of transport with increasing power across the separatrix.

Figure 20.6.: The dependency of  $\chi$  on  $\frac{\bar{n}_e}{n_{GW}}$ Figure 20.7.: A multiple regression fit to  $\chi$ 

The fit is improved somewhat if the ELM frequency is included as a fit parameter, though this then obscures the dependence on the remaining parameters because of the dependence of the ELM frequency on these parameters.

## 20.4. Including an inward pinch

In some case it was not possible to get a good fit to the entire density profile. By extending the fitted quantities to include an inward pinch ( $v_{in}$ ) and a main chamber gas puff ( $\Gamma_{puff}$ ),

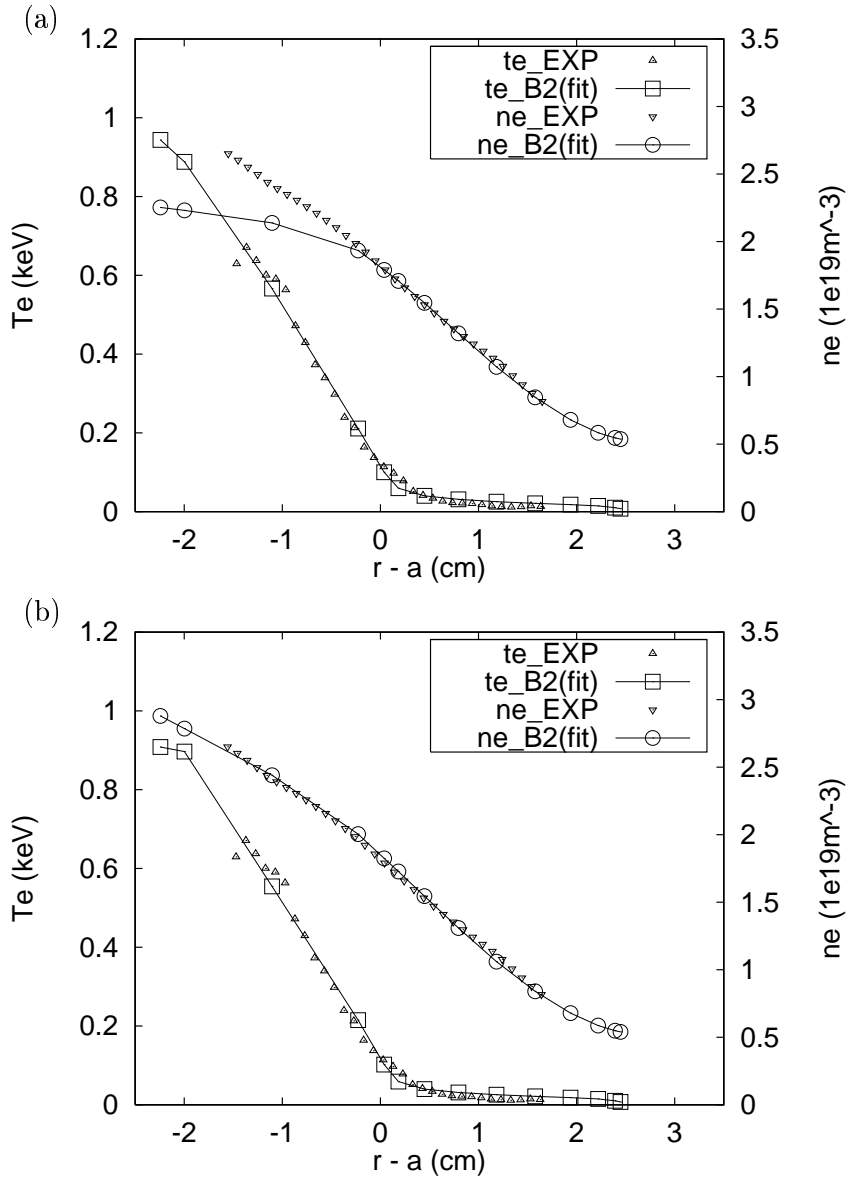


Figure 20.8.: The fitted  $T_e$  and  $n_e$  profiles of the shot #10814 (a) without and (b) with inward pinch

and augmenting the residuals of equation 20.1 by

$$\begin{aligned}
 R = & R_{eq20.1} \\
 & + \alpha_6 \left( \frac{T_{e,divin}^{exp} - T_{e,divin}^{code}}{\Delta T_{e,divin}^{exp}} \right)^2 \\
 & + \alpha_7 \left( \frac{T_{e,divout}^{exp} - T_{e,divout}^{code}}{\Delta T_{e,divout}^{exp}} \right)^2 \\
 & + \alpha_8 \left( \frac{\Gamma_{core}^{exp} - \Gamma_{core}^{code}}{\Delta \Gamma_{core}^{exp}} \right)^2
 \end{aligned} \tag{20.4}$$

a better fit was possible, as can be seen in Figure 20.4. Expanding the fitted quantities comes at the expense of added CPU time for the fit procedure, increasing it by about a factor of three.

## 20.5. Self-consistent coupling of turbulence and transport models

Trying to introduce into the SOL transport models an *ab-initio*, self-consistent description of the anomalous transport is a very challenging task.

To overcome the misbalance in the SOL modelling between very sophisticated models for neutral transport and plasma transport parallel to fieldlines (21-moment ansatz, kinetic limits, ...), including drifts and currents and to achieve for the SOL modelling a predictive quality comparable with engineering codes e.g. for airplanes it is nevertheless absolutely necessary to try to reach this goal.

Combining the knowledge of the SOL transport studies and those of the rapidly (with increasing computer power) improving turbulence simulations as e.g. studied by drift-wave turbulence calculations (even accounting for magnetic effects) [158, 159, 160, 161, 162] gives some hope that perhaps in an iterative scheme the turbulent transport could be self-consistently determined for the SOL. The iterative scheme is probably necessary, because the transport times in the SOL requires for an equilibrium calculation times of up to about 10 ms (related with ion and neutral transport along fieldlines) or even higher (including e.g. wall processes for saturation and pumping or equilibration times for the core). On the other side, resolving the turbulence requires very small timesteps (of the order of the plasma frequency, e.g. about  $10^{-11} - 10^{-10}$  s). Therefore, studying effects indirectly driven (maybe even in a rather non-linear way) by global neutral or ion transport in a turbulence code is practically impossible, because this kind of code is limited to rather small explicit time steps whereas the other processes need an implicit code (allowing to overcome the explicit limit set by the strong parallel heat conduction in the SOL). Coupling the two codes is therefore the only promising ansatz to represent well all these different timescales.



## 21. Summary

The aim of this work was to give insight into the physics in the scrape-off layer (SOL), which is defined as the region of open fieldlines intersecting walls. It is characterised by the competition of parallel and perpendicular transport. The description of the plasma-wall interaction due to the existence of walls and atomic processes are necessary ingredients for an understanding of the scrape-off layer. This introduction mainly focussed on divertor tokamaks, but most of the arguments and principles can be easily adapted also to other concepts like island divertors in stellarators or limiter devices. Results from the 2D SOL transport code B2-Eirene as well as simplified models were used as tools to identify the basic physics mechanisms and apply this knowledge for design optimisation of the ASDEX-Upgrade divertor.

The first part introduced, after a short motivation, the basic concepts for power and particle exhaust in the SOL. The discussion of the different length scales involved in the SOL physics followed, including sheath physics. The second major part covered the physics of the pure hydrogen plasma based on a fluid description. Starting from simple models, the influence of neutral transport and the characteristics of the different operation regimes was there the main topic. This part finished with time-dependent phenomena for the pure plasma, so-called Edge Localised Modes (ELMs), and their effect on the SOL. The next part discussed the influence of impurities on the SOL plasma. For the understanding of impurity physics in the SOL one needs a rather complex combination of different aspects. The impurity production process has to be understood, then the effects of impurities in terms of radiation losses have to be included and finally the impurity transport is necessary. This was introduced with rising complexity starting with simple estimates, analysing then the detailed parallel force balance and the flow pattern of impurities. Using this, impurity compression and radiation instabilities were discussed. This part ended, combining all the elements introduced before, with specific, detailed results from ASDEX-Upgrade (especially for the optimized new divertor configuration). The predictive capability of the 2D-SOL code B2-Eirene was demonstrated for this new design based on transport calculations.

The effect of drifts and currents was addressed in the next part, including the derivation of the basic equations and some examples. This was necessary to get closer insight into the physics of the formation of large radial electric fields close to the separatrix as well as in-out asymmetry between the divertor legs and influence of the toroidal momentum input on this asymmetry. A specific topology effect appears for the (toroidally averaged) island divertor of a stellarator due to the existence of an additional region of closed fieldlines in the island. The resulting potential and current profile is quite sensitive to the effect of drifts. Finally, some work on deriving scaling laws for the anomalous turbulent transport based on automatic edge transport code fitting procedures was described. Looking forward, the

necessary work to achieve a self-consistent SOL model including the anomalous turbulent transport was discussed.

The necessary ingredients for a model being able to describe the SOL are shown in Fig. 21.1. Elements from quite different physics fields have to be combined. The knowledge

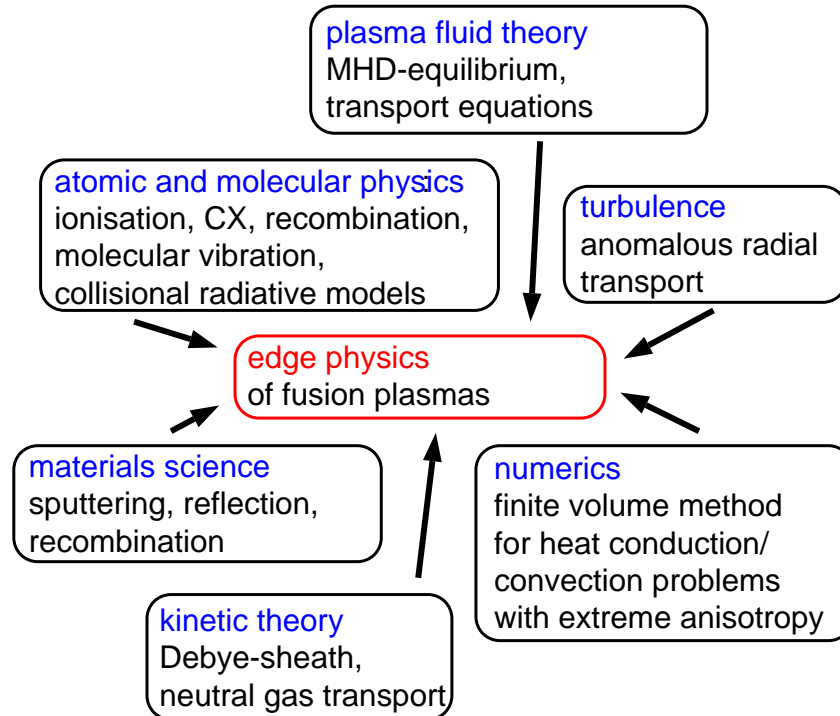


Figure 21.1.:

of the experimental magneto-hydrodynamical equilibrium is a necessary prerequisite for any work in this area. Plasma fluid theory in a general sense is needed to obtain the transport equations governing the transport in the edge of a plasma. Kinetic theory is necessary to deliver the correct description of the sheath forming in front of a wall which is in contact with the plasma. This defines boundary conditions for the fluid models used in the transport codes. The interaction of plasma with walls also introduces the need for detailed understanding of processes creating neutrals or ions at surfaces (sputtering, reflection, recombination, ...). Atomic and molecular processes affect strongly the plasma through ionisation and recombination, thus collisional-radiative models are used (even accounting for vibrationally excited molecules). The classical transport of neutrals strongly determines the operational regime. To be able to optimize existing designs the complete kinetic transport equation has to be solved in full geometry. Due to the existence of the turbulent radial transport in fusion devices, either scaling laws or direct coupling to turbulence codes are necessary for a full predictive quality. Last but not least, the numerical problems of solving the extremely anisotropic transport equations (very strong parallel heat conduction of electrons) and combining all the elements to a usable code for producing results based on a rather complete physics description within reasonable run-time has to be solved. All these elements together defines this working field as a fascinating one with inputs from many areas.

# A. Scrape-off layer diagnostics

The experimental characterization of a system is necessary for any discussion of physics. Therefore, in the following a short description of important SOL diagnostics will be given based on ASDEX-Upgrade systems.

## A.1. Langmuir probes (M. Weinlich, A. Carlson)

### A.1.1. Single probe without magnetic field

Electrons have a much higher mobility than ions, so every wall in contact with a plasma will be charged up negatively. The magnitude of this effect will adjust itself so that no net current is flowing towards the wall. The resulting potential difference with respect to the plasma potential is the so-called *floating potential*. In front of this wall, the quasi neutrality of the plasma must be violated to shield the negative wall. The characteristic length is the Debye length

$$\lambda_{Debye} = \sqrt{\frac{\varepsilon_0 k_B T_e}{n_e e^2}}. \quad (\text{A.1})$$

Every equation is in SI units, the subscript  $_e$  ( $_i$ ) denotes quantities referring to electrons (ions). The ions' motion towards the wall is determined by the *Bohm criterion*, i.e., their velocity exceeds the sound speed at the Debye sheath entrance:

$$v_{ion} \geq c_s = \sqrt{\frac{k_B (Z T_e + \gamma_i T_i)}{m_i}}. \quad (\text{A.2})$$

This equation is valid for ions of charge number  $Z$ , mass  $m_i$  and an adiabatic coefficient  $\gamma_i$ , which can take on values between 1 and 3. We prefer  $\gamma_i = 3$ , which is in good accordance with kinetic simulations. The equivalent coefficient for the electrons does not appear, because we assume isothermal electrons ( $\gamma_e = 1$ ).

At every probe voltage (below the plasma potential) all ions reach the probe surface and we can calculate the ion (saturation) current density:

$$j_{i,sat} = e Z n_i c_s, \quad (\text{A.3})$$

where  $j_{i,sat}$  is defined as a positive number.

The electrons move with a thermal velocity

$$c_{e,th} = \langle |v_e| \rangle = \sqrt{\frac{8 k_B T_e}{\pi m_e}} \quad (\text{A.4})$$



so the net electron flux toward the wall can be expressed as

$$j_{e,th} = \frac{1}{4} e n_e c_{e,th} (1 - \gamma_{see}). \quad (\text{A.5})$$

The factor  $1/4$  accounts for the isotropic spatial dimensions, and  $\gamma_{see}$  for the secondary electron emission at the surface. Typical values of  $\gamma_{see}$  for boundary layer plasma ( $T_e < 100 \text{ eV}$ ) in contact with carbon surfaces lie in the range of 0.4 to 0.6. Most electrons will be reflected in front of the probe, so only a small fraction, described by a Boltzmann factor  $\exp(-E_{pot}/k_B T_e)$ , influences the probe current. The total current to a probe, which is biased negatively with respect to the plasma, can be calculated as the difference between the ion and electron currents:

$$I_{probe} = -A_{probe} j_{i,sat} + A_{probe} j_{e,th} \exp\left(\frac{e(V_{probe} - V_{plasma})}{k_B T_e}\right). \quad (\text{A.6})$$

$A_{probe}$  is that area of the probe which determines the current, usually the total surface. We can now calculate the *floating potential*, i.e., the potential difference between the plasma and the wall at zero net current ( $I_{probe} = 0$ ) using the definitions of  $j_{i,sat}$  and  $j_{e,th}$ :

$$\Delta V_{fl} = V_{fl} - V_{plasma} = \frac{k_B T_e}{e} \ln\left(\frac{c_s}{c_{e,th}} \frac{4}{1 - \gamma_{see}}\right) \quad (\text{A.7})$$

The probe equation (A.6) is also often used taking the floating potential (A.7) as reference:

$$I_{probe} = -A_{probe} j_{i,sat} \left[ 1 - \exp\left(\frac{e(V_{probe} - V_{fl})}{k_B T_e}\right) \right]. \quad (\text{A.8})$$

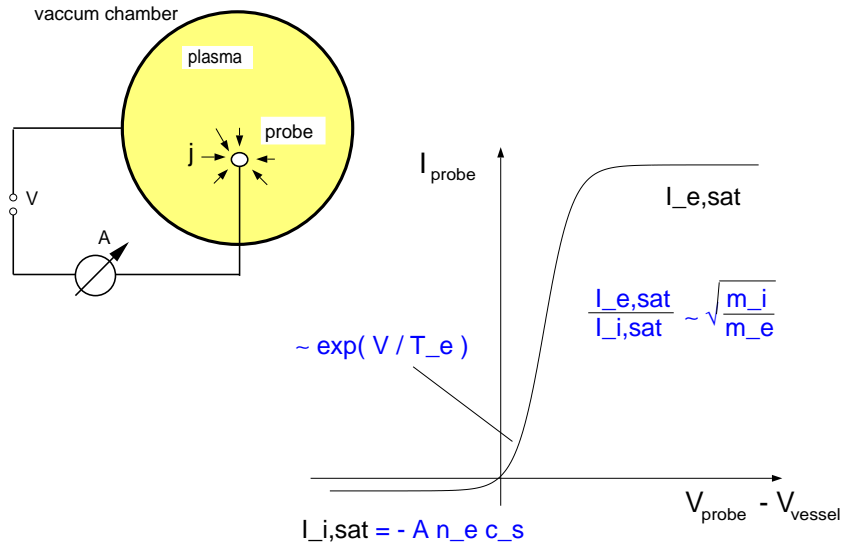


Figure A.1.: Principle of a single probe measurement.

This is the simplest model of a Langmuir probe.

At large negative voltages all electrons are repelled and we measure the ion saturation

current ( $I_{i,sat} = A_{probe} j_{i,sat}$ ). From that we can derive the electron (and ion) density in front of the probe, assuming we know the probe surface and the sound velocity

$$n_e = Z n_i = \frac{I_{i,sat}}{A_{probe} e c_s} \quad (\text{A.9})$$

Reducing the negative probe voltage allows more and more electrons to reach the probe, thereby reducing and finally reversing the current flow. From the slope of the  $I$ - $V$  characteristic in a logarithmic plot we can calculate the electron temperature, assuming a Maxwellian distribution function for the electron population (i.e., we use the Boltzmann relation):

$$T_e = \frac{e (V_{probe} - V_{fl})}{k_B} \left[ \ln \left( 1 + \frac{I_{probe}}{I_{i,sat}} \right) \right]^{-1}. \quad (\text{A.10})$$

If we further increase the probe voltage, we will reach electron saturation close to the plasma potential. Since electron saturation current is a factor  $m_i/m_e$  higher than ion saturation current, it is avoided by most experimentalists.

To obtain the electron density (A.9) we must calculate the sound velocity (A.2), which requires the ion temperature. For a pure hydrogen plasma, this is the only unknown quantity which cannot be measured by simple probe techniques. Usually  $T_i = T_e$  is used to close the evaluation of probe data. This assumption need not always be fulfilled and can therefore lead to serious errors.

### A.1.2. Double probe without magnetic field

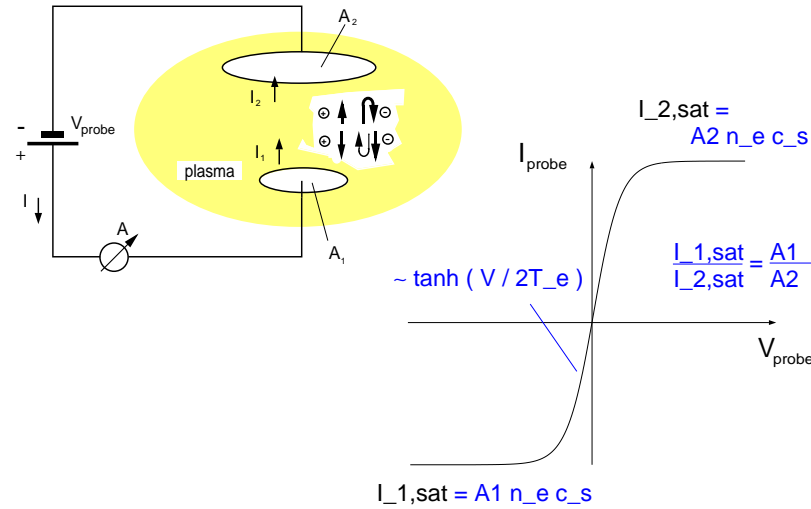


Figure A.2.: Principle of a double probe measurement.

A double probe is a system of two electrodes in a plasma where the probe voltage is applied between these two electrodes (in contrast to a single probe, where the probe voltage is applied between the probe and the vacuum vessel). In the limit of one very large electrode ( $A_{probe,1}/A_{probe,2} \rightarrow 0$ ), this system reduces to that of a single probe, in the contrary limit

of two electrodes of equal area, the  $I$ - $V$  characteristic changes to a symmetric hyperbolic tangent.

At each electrode the probe equation (A.6) is still valid, but we have the additional constraint that the current going into one electrode comes out of the other.

$$I = I_1 = I_2, \quad (\text{A.11})$$

$$I_1 = -A_1 j_{i,sat} + A_1 j_{e,th} \exp\left(\frac{e(V_1 - V_{plasma})}{k_B T_e}\right), \quad (\text{A.12})$$

$$I_2 = +A_2 j_{i,sat} - A_2 j_{e,th} \exp\left(\frac{e(V_2 - V_{plasma})}{k_B T_e}\right). \quad (\text{A.13})$$

The signs of the currents are chosen according to the technical current direction. The applied probe voltage  $V_{probe} = V_1 - V_2$  is given as the potential difference between the electrodes and can be used to eliminate  $V_2$  in Eq. (A.13). Inserting (A.12) and (A.13) into (A.11) leads to an expression for the current in the probe circuit:

$$\begin{aligned} I(V_{probe}) &= A_1 j_{i,sat} \frac{1 - \exp\left(-\frac{eV_{probe}}{k_B T_e}\right)}{A_1/A_2 + \exp\left(-\frac{eV_{probe}}{k_B T_e}\right)} \\ &= \frac{A_1 + A_2}{2} j_{i,sat} \left\{ \tanh\left[\frac{eV_{probe}}{2k_B T_e} - 0.5 \ln\left(\frac{A_2}{A_1}\right)\right] - \frac{A_1 - A_2}{A_1 + A_2} \right\}. \end{aligned} \quad (\text{A.14})$$

The double probe characteristic shows two specific effects: the maximum current in the circuit is always limited by the ion saturation current at one of the electrodes:

$$\begin{aligned} I(V_{probe} \rightarrow -\infty) &= -A_1 j_{i,sat}, \\ I(V_{probe} \rightarrow +\infty) &= +A_2 j_{i,sat}, \end{aligned}$$

and at zero applied voltage no net current flows. The later condition can only be modified if the double probe is inserted into an inhomogeneous plasma.

### A.1.3. Triple probe without magnetic field

A single probe  $I$ - $V$  characteristic consist of many ( $\geq 30$ ) data points. Often we are not interested in the whole characteristic but only in the derived quantities  $n_e$  and  $T_e$ . To reduce the amount of data to be sampled in that case triple probes are widely used.

A triple probe consists of three electrodes, traditonally of equal area, inserted into a uniform plasma and spaced far enough apart to avoid disturbing each other. Every probe element is biased to a different potential and all three  $(I, V)$ -pairs measured at one time point are interpreted as three distinct points on one single  $I$ - $V$  characteristic. If this probe characteristic can be expressed as a function of three parameters (in this case  $n_e$ ,  $T_e$ ,  $V_{fl}$ ), these three quantities can be derived uniquely from the measurement.

To further reduce the amount of data and the experimental equipment, a special setup is often used: two probes are operated as a double probe with a constant bias and the third probe element measures the floating potential. The measured quantities are the current in the double probe, which equals the ion saturation current (assuming the bias voltage is

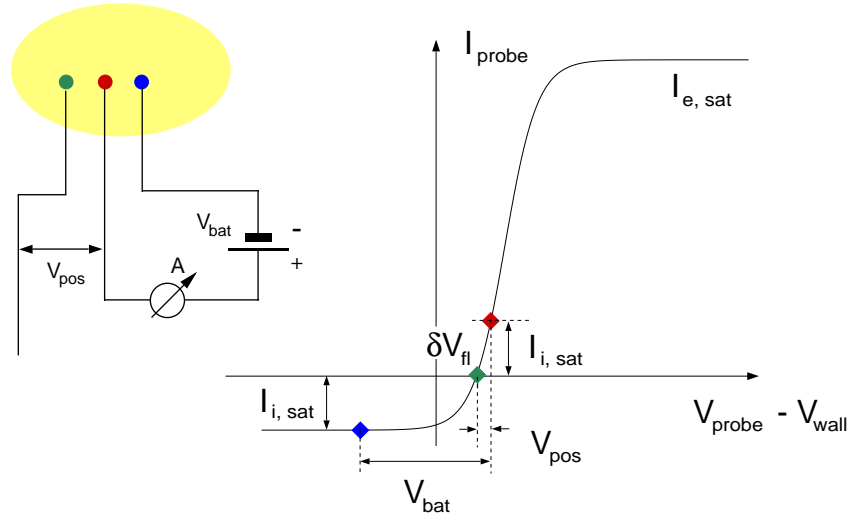


Figure A.3.: Principle of a triple probe measurement.

a few times the electron temperature), and the potential difference between the positive and the floating tip. The probe equation (A.8) can then be reduced to yield:

$$T_e \simeq \frac{e V_{pos}}{k_B \ln 2}, \quad (\text{A.15})$$

$$n_e = \frac{I_{i,sat}}{A_{probe} e c_S}. \quad (\text{A.16})$$

#### A.1.4. Single probe with magnetic field

The presence of a magnetic field forces all charged particles to gyrate around the field lines. Therefore electrons and ions can stream freely along the field lines, but the motion across the field is strongly suppressed. In the limit of an infinite magnetic field without gradients any current originating from a single probe can only flow along the field until the field line intersects some material part of the vessel where the current path will be closed by currents through the vessel. The resulting characteristic is that of a double probe with equal areas. If there exist some (small) cross-field currents, the measurement can still be described by a double probe (Eq. (A.14)) with the area of the counter electrode as an additional free parameter accounting for the unknown magnitude of the cross-field currents. The current collecting area of the probe ( $A_{probe}$ ) is now the projection of the probe onto a plane perpendicular to the magnetic field ( $A_{probe}^{proj}$ ) instead of the total probe surface.

#### A.1.5. Multitip probes

The same arguments as for the field-free case hold also for measurements in the presence of a magnetic field. Multitip probes allow for the best temporal resolution and they minimize the experimental equipment, but they miss a lot of information gained with a complete characteristic. We have to increase the number of simultaneously measuring

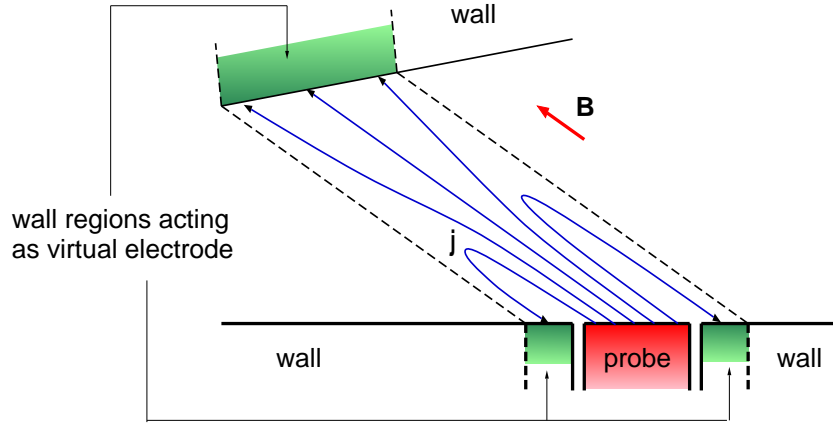


Figure A.4.: A strong magnetic field reduces the cross-field current and leads to the formation of a virtual double probe.

probe elements from three to at least four to gather information on the area of the return current. And we have to take extreme care, that all of them are located on the same flux surface, which can cause serious problems in a non toroidally symmetric machine like a stellarator or on localized structures like limiters.

### A.1.6. Thermal load

In the scrape-off layers of modern fusion devices we have power fluxes parallel to the field of  $q_{\parallel} \geq 50 \text{ MW/m}^2$  whereas the material limits are around  $q_{max} \leq 15 \text{ MW/m}^2$ . This leads to different construction schemes to sustain the thermal load:

- **(fast) moving probe:** the probe body moves in and out with a time constant ( $\approx 20 \text{ ms}$ ) small enough to avoid overheating of the probe tip.
- **heat sink probe:** the (small) probe tip is in good thermal contact with a big (cooled) heat sink. This increases the time the probe can withstand the plasma but it might not work in long pulse machines.
- **flush mounted probe:** probes are only employed in material surfaces which are exposed to the plasma at grazing incidence. The surface of the probe is strictly aligned with the surrounding wall so it can withstand almost every condition the wall can sustain.

The construction of the probe has to be compatible with the experimental demands, there is no “optimal” probe design suitable for every purpose.

### A.1.7. Derived quantities

The ion saturation current is a direct measurement of the charged particle flux to an area comparable to the probe. We have therefore:

$$Z\Gamma_i = \Gamma_e = I_{i,sat}/(eA_{probe}) = n_e c_s. \quad (\text{A.17})$$

The sheath transmission coefficient  $\gamma_s$  states how much energy is brought to the probe (or the target) by one incident electron-ion-pair. The power flux towards the probe can then be calculated by

$$P_{Langmuir} = \Gamma_i \times (\gamma_s k_B T_e + E_{rec}) \quad (A.18)$$

where we take also the recombination energy into account. The literature value for a hydrogen plasma is  $\gamma_s = 8$ .

An additional interesting quantity may be the (dynamic) electron pressure which can be estimated by

$$p_e = 2n_e T_e \quad (A.19)$$

where the factor of two is obtained from sonic particle flow towards the wall. Finally, equation (A.7) allows for a zeroth order estimate of the plasma potential.

$$V_{plasma} - V_{wall} = (V_{fl} - V_{wall})_{\text{measured}} - \frac{k_B T_e}{e} \ln \left( \frac{c_s}{c_{e,th}} \frac{4}{1 - \gamma_{see}} \right) \quad (A.20)$$

If no net current is flowing to/from the wall ( $V_{fl} - V_{wall} = 0$ ), the wall/floating potential for a pure deuterium plasma in contact with a graphite surface ( $\gamma_{see} = 0.4$ ) lies about  $2k_B T_e$  below the plasma potential. Of particular interest is the difference in the plasma potential at different toroidal and poloidal locations which can be obtained if we believe the vessel to be an equipotential surface.

### A.1.8. Sophisticated probes

Mach or Janus probes are widely used to determine the one dimensional flow (or drift) velocity of the plasma. They use the fact that the potential drop in the presheath depends on the flow velocity: inside the presheath the ions are accelerated from their initial velocity up to the sound speed towards the probe surface by a potential drop, which, on the other hand, repels some electrons. The ion density decreases correspondingly to maintain the plasmas quasi-neutrality. If the plasma flows in one direction, the “upstream” side of the probe (where the ions need less acceleration) faces therefore a higher current density ( $qn_{i,up}c_s$ ) then the downstream side ( $qn_{i,down}c_s$ ). For Mach probes, the upstream and the downstream part of the probe are separated by an insulator, both currents are measured and the flow velocity is derived from the current ratio:

$$v_{drift} = \kappa c_s \ln \left( \frac{\dot{J}_{i,sat,up}}{\dot{J}_{i,sat,down}} \right), \quad (A.21)$$

where  $\kappa$  is a numerical constant in the order of 0.5, depending on ion temperature, adiabatic coefficients, etc.

There exists much more complicated electrical devices to measure properties of the boundary layer plasmas than discussed here. We can use retarding field analyzers to obtain information on the electron distribution function. We can use different analyzers to sort the ions by mass and/or charge and we can use ionization gauges to learn something about the neutrals. For special conditions, probes have also been used which measure the ion temperature directly. All of them may also be called “probes”, but they are not Langmuir probes in the strict sense of the word.

### A.1.9. Modifications of the simplest models

In front of each surface a Debye sheath forms and, also in the case of nonperpendicular incidence of a magnetic field, a magnetic sheath forms. These sheaths influence the effective current collecting probe area and the local plasma parameters.

The real plasma is not at all as homogeneous as we have treated it. There are temperature gradients along the field lines and different temperatures in front of different parts of the machine which may drive thermoelectric currents. The plasma potential itself may also not be uniform and drive extra currents. There exists perpendicular gradients in density and temperature which affect the cross-field currents. These gradients must be established and sustained by transport phenomena which have been ignored.

The plasma resistivity along and across the magnetic field may play an important role in the interpretation of probe data. The whole probe measurement can be understood as a lot of resistors in series ( $R_{sheath}$ ,  $R_{||}$ ,  $R_{\perp}$ ) and maybe also in parallel.

The measurements with probes and the understanding of the results obtained involves the complete scrape-off layer physics. This certainly makes probe measurements difficult but it is also a reason for the common interest in this diagnostic tool.

### A.1.10. Langmuir probes at ASDEX-Upgrade

#### Divertor target plate probes (M. Weinlich, A. Carlson)

On ASDEX-Upgrade, flush-mounted Langmuir probes are used to determine the plasma parameters in front of the target plates. The flush-mounted design was chosen because it results in the lowest possible heat flux per surface unit and thus allows for continuous measurements during the whole shot. The data analysis is done taking the effects of grazing incidence of the magnetic field lines into account [163]. The probes (designed as multi-tip probes) cover the whole poloidal cross section of the divertor and are installed at three different toroidal positions.

#### Midplane manipulator (H. Maier)

The manipulator is located in sector 8 and an overall view of the midplane manipulator system and the divertor manipulator system is given in the following figure.

The applications of ASDEX-Upgrade's midplane probe manipulator system can be divided into two categories:

- Langmuir probes for measuring electron density and temperature as well as floating potentials and electron drifts.
- Deposition probes to investigate impurity contents and transport properties.

These diagnostics are not available at the same time; an exchange of the manipulator arm is required.

In the Langmuir probe configuration of the midplane manipulator, a pneumatically reciprocating fast probe enters the plasma from behind an ICRH antenna protection limiter. This can be repeated every 300 ms. Within about 100 ms, it covers a distance of 10 cm from its initial position towards the separatrix. During this motion, a bias voltage is

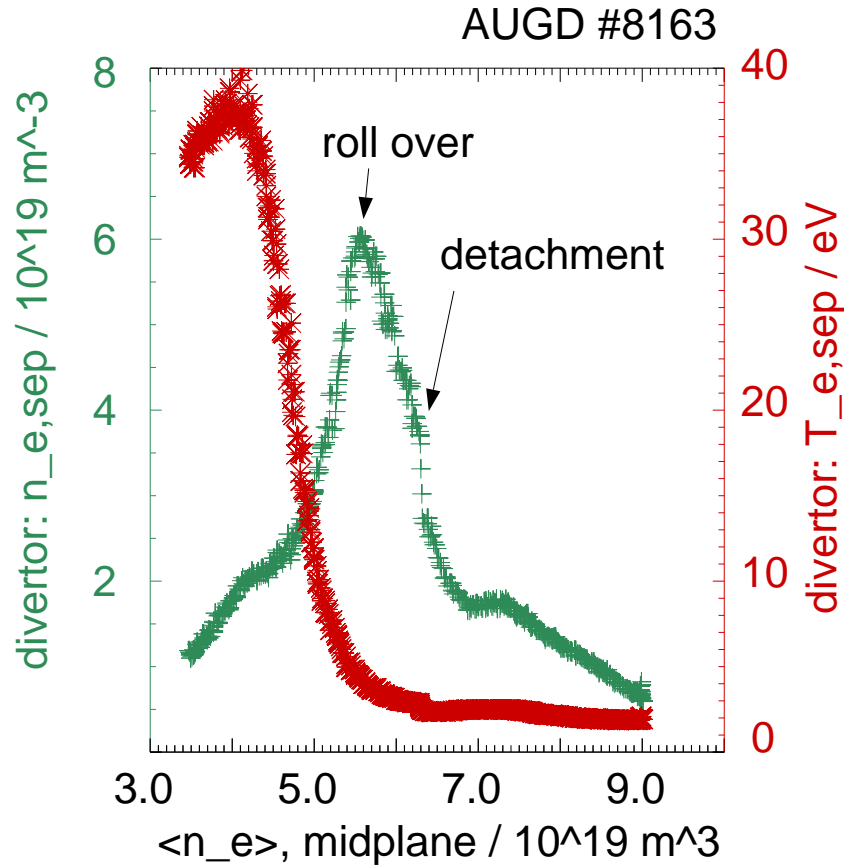


Figure A.5.: During a density ramp the divertor density first follows the gas puff, then saturates and finally rolls over to a detached state. The temperature falls during the major part of the density ramp and must be below 5 eV to allow for the detachment.

swept with a repetition rate of several kHz and the current versus voltage characteristics are measured with a sampling rate of 500 kHz. These Langmuir probe characteristics contain, as discussed before, information about the electron density and temperature at their respective position and time. Depending on the number of characteristics to be averaged, a spatial resolution in the range of 1 mm can be achieved.

Since the probe head contains several measurement pins, floating potentials and ion saturation currents can be measured simultaneously to the sweeping probe characteristics described above.

Even under otherwise constant plasma conditions, the electron density changes by several orders of magnitude between a starting position deep within the limiter shadow and the separatrix position. To acquire data over such a large range, the system correspondingly has to cover several orders of magnitude of current measurement sensitivity.

To investigate the scrape-off layer impurity contents the manipulator system can also be used to expose impurity collector probes into the ICRH limiter shadow. Usually, these probes are made of graphite and the impurities are deposited onto the surface. After



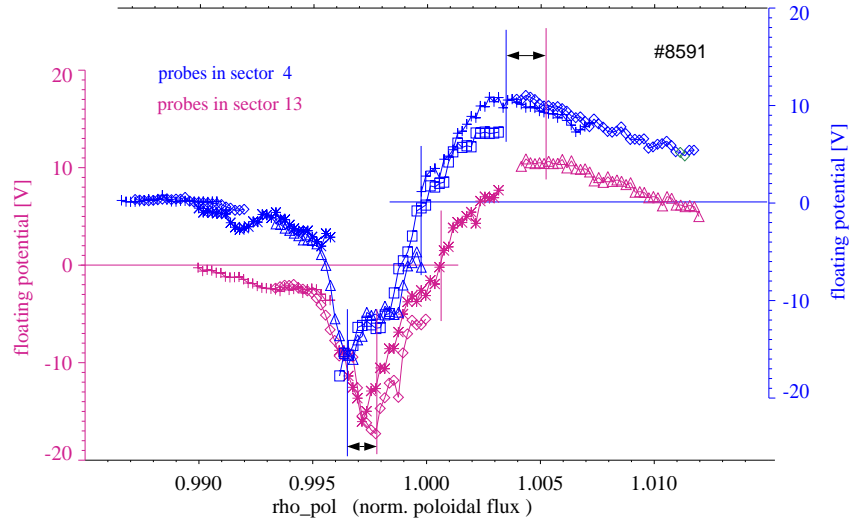


Figure A.6.: Profiles of the floating potential on the outer divertor at two different toroidal positions exhibit a poloidal shift of the profiles of about 1 cm, i.e., a toroidal asymmetry.

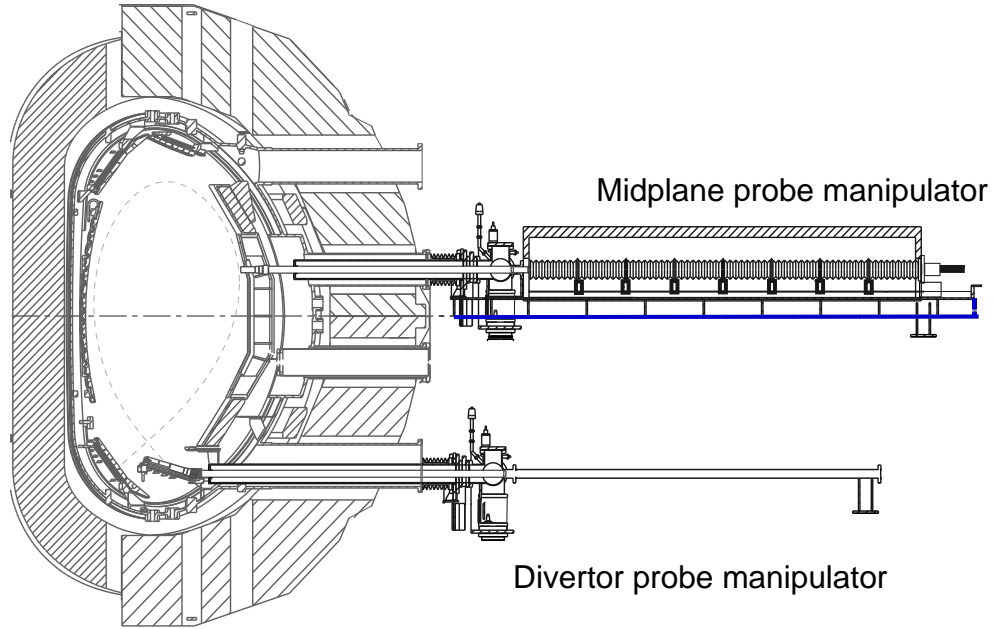


Figure A.7.: General overview of the manipulator systems in the midplane and in the divertor and their positions within the ASDEX-Upgrade vessel.

removing the probe, the amount of deposited material can subsequently be determined by ion beam techniques (Rutherford Backscattering, Particle Induced X-ray Emission, Nuclear Reaction Analysis).

The cylindrical graphite probes are covered by a graphite shield with an exposure slit in the radial direction. To achieve time resolution, the probe can be rotated within this shield at a variable angular speed. This principle of operation together with some non-

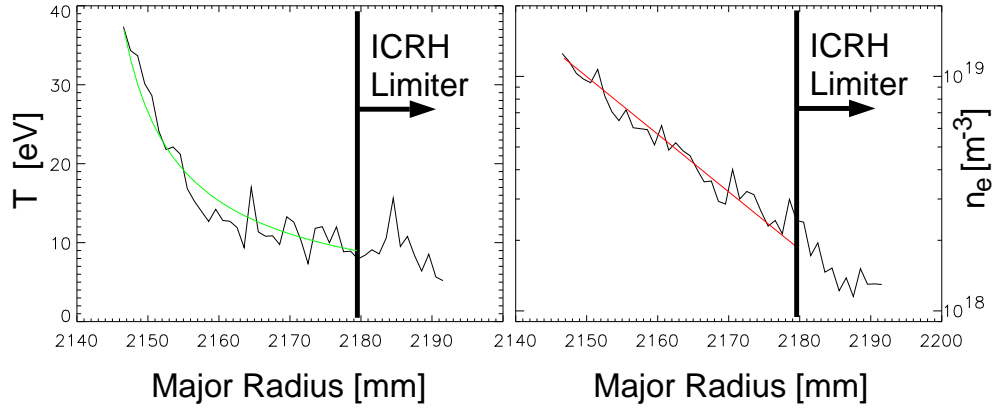


Figure A.8.: Examples of electron temperature (left) and electron density (right) from an ASDEX-Upgrade discharge together with theoretical fits corresponding to  $T: 1/(\lambda_T + x)^{4/5}$ ,  $n: \exp(-x/\lambda_n)$  ( $x = 0$  corresponds to the separatrix position). The vertical solid lines correspond to the position of the limiter. The separatrix is located at the left edge of the plots.

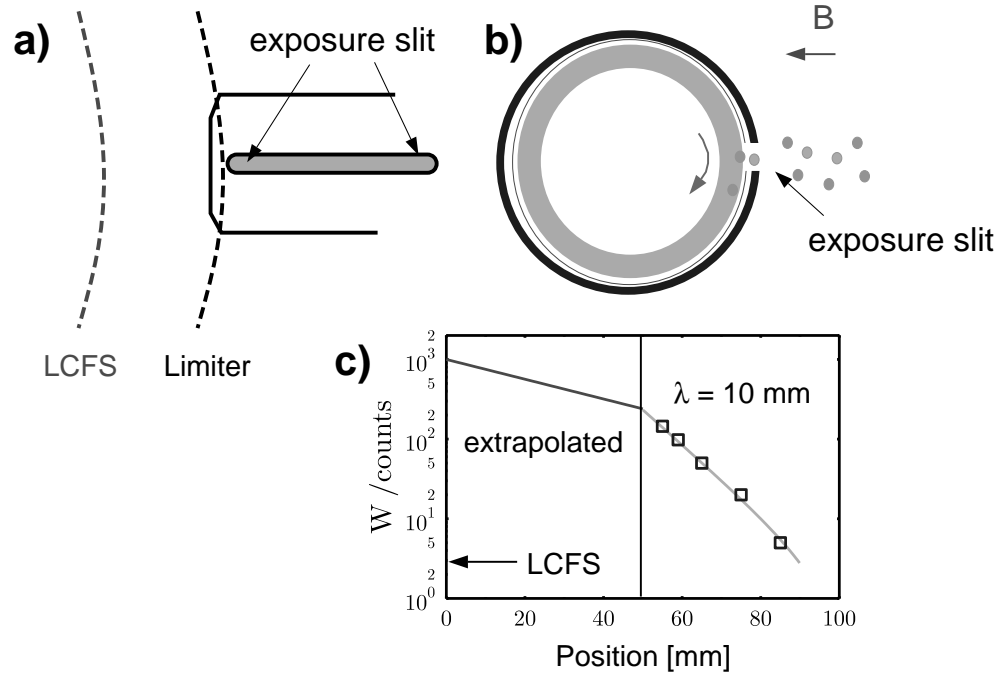


Figure A.9.: a) Configuration of LCFS, limiter shadow and exposure slit. b) Scheme of time-resolved operation. c) Experimental results: tungsten deposition on collector probe.

time-resolved results on tungsten transport is displayed in figure A.9. The data show that, within the limiter shadow, the tungsten concentration decreases exponentially with a typical decay length of 10 mm. The time resolution achievable in this configuration depends on the impurity concentration corresponding to the detection limit of the ion beam methods.

## A.2. $H_\alpha$

Optically viewing of the plasma with CCD cameras gives a very good global impression about recycling and radiation losses. Specifically,  $H_\alpha$  lines of sight are used to determine the particle flux of hydrogen or deuterium, because, over a wide range of temperatures (above about 10 eV), the  $H_\alpha$  intensity can be used to directly measure the number of ionization events, e.g. the particle flux. However, in the divertor there exists a strong temperature dependence of the number of  $H_\alpha$  photons per ionization event (Fig. A.10). Therefore, below about 10 eV this interpretation is no longer so simple and requires detailed knowledge about the (2-D) divertor profiles.

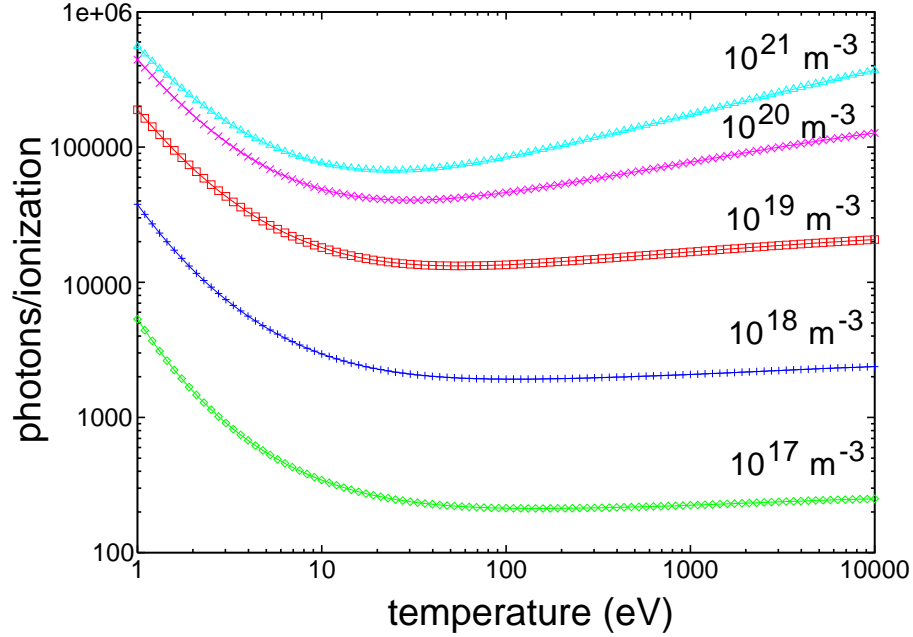


Figure A.10.: Number of  $H_\alpha$  photons per ionization event as a function of temperature for different electron densities.

## A.3. Fast Lithium-beam spectroscopy (J. Schweinzer)

Common plasma diagnostic techniques in particular "passive" photon emission spectroscopy throughout the electromagnetic spectrum, are not ideally suited for investigations in the plasma edge, because of their relatively small spatial extent and inhomogeneity. Better edge plasma diagnostic should therefore comply with the following requirements: Excellent spatial ( $< 1\text{cm}$ ) as well as sufficient temporal ( $\leq \text{ms}$ ) resolution, minimum introduction of plasma disturbances and evaluated plasma parameters which do not strongly depend on modelling procedures or additional assumptions about the plasma condition. All these goals are met by fast Li-beam plasma spectroscopy, i.e. the injection of keV to multi-keV neutral lithium atoms into the plasma, to induce collisional processes which in turn lead to characteristic line radiation delivering the desired diagnostic information. One can distinguish between diagnostic applications which rely on photon emission from

excited Li atoms (Li impact excitation spectroscopy, Li-IXS, e.g. electron density, neutral density, magnetic and electric fields) or which rely on charge exchange processes between fast Li atoms and plasma ions (Li charge exchange spectroscopy, Li-CXS). The latter application is conceptually equivalent to the well-known charge exchange spectroscopy by utilising neutral heating beams. However, such measurements suffer, especially in the plasma edge from insufficient spatial resolution. A further advantage of Li in comparison with a hydrogen beam is the considerable (factor 10 - 50) larger charge exchange cross-sections. First successful applications of Li-CXS on TEXTOR and W7-AS have proven the applicability of this method. On ASDEX-Upgrade, the Li beam diagnostic has been used for measuring the electron density profile in the plasma edge. The Li-Beam will also be used for determining concentrations and temperatures of impurity ions, poloidal plasma rotation as well as to monitor the density of neutral atoms in the main chamber. However, evaluation of raw data provided by the Li-beam for almost all applications requires to model the beam attenuation and excited-state composition carefully. Observation systems and the beam production technique will be described afterwards.

### A.3.1. Li-Beam modeling and related atomic data base

In order to obtain reliable quantitative diagnostic information from Li-beam spectroscopy, the interaction of Li atoms with the plasma constituents such as electrons and protons has to be modelled. These "beam-plasma interactions" lead to excitation, de-excitation and ionization of the injected Li atoms. The attenuation and composition of the injected neutral Li beam along its way into the plasma can be described by a system of coupled differential equations for the occupation numbers  $N_i(z)$  of bound LiI states [ $i=1$  denotes Li(2s),  $i=2$  Li(2p), etc.]. The independent length variable  $z$  is counted along the beam axis ( $z=0$  at the entrance of the Li beam into the plasma).

$$\frac{dN_i(z)}{dz} = \{n_e(z)a_{ij}[T(z)] + b_{ij}\}N_j(z) \quad (1)$$

The term proportional to the electron density  $n_e(z)$  in Equ. 1 (Einstein's sum convention applies) contains all collisional processes of Li atoms with both plasma electrons and protons, whereas spontaneous emission processes are described by coefficients  $b_{ij}$ .

Coefficients  $a_{ij}$  are measured in units of  $cm^2$  and depend on the local plasma temperature  $T(z)$ . In Equ. 2a we define quantities  $R_{ij}^e$  and  $R_{ij}^p$ , which can be interpreted as "reduced" rate coefficients (or "effective" cross-sections) for collisions of monoenergetic Li atoms (beam energy  $E_b$  and corresponding velocity  $v_{Li}$ ) with plasma electrons and protons (temperature  $T$  and Maxwellian velocity distribution  $f(v)$ ). These quantities will be called rate coefficients.

$$R_{ij}^{e,p} := \frac{1}{v_{Li}} \int \int \int_{v^3} d^3v \sigma_{ij}^{e,p}(|\mathbf{v} - \mathbf{v}_{Li}|) \cdot |\mathbf{v} - \mathbf{v}_{Li}| \cdot f(|\mathbf{v}|) \quad (2a)$$

$$a_{ij} = R_{ij}^e + R_{ij}^p \quad (i \neq j) \quad (2b)$$

$$a_{ij} = -\{R_{ii}^e + R_{ii}^p + \sum_{j \neq i} R_{ij}^e + \sum_{j \neq i} R_{ij}^p\} \quad (2c)$$

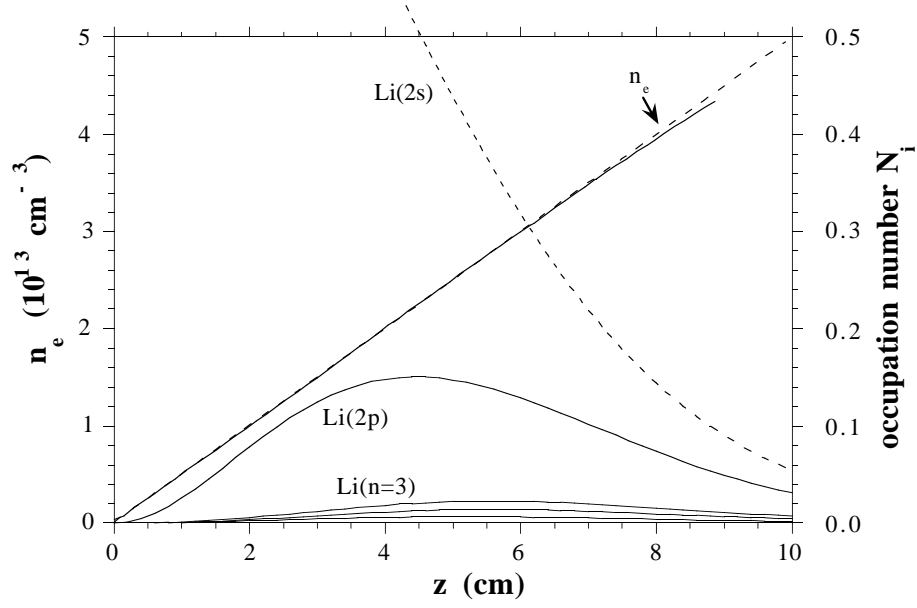


Figure A.11.: Solution of Equ. 1 for occupation numbers  $N_i$  of  $Li(nl, n \leq 3)$  states along the beam axis under the assumption of a density  $n_e(z)$  and temperature profile (not shown) with initial conditions  $N_i(z = 0) = \delta_{1i}$ .

Coefficients  $a_{ij}(j > i)$  refer to excitation of Li atoms in state  $i$  to state  $j$  due to collisions with both electrons and protons (Equ. 2b). In general, cross-sections  $\sigma_{ji}(j > i)$  for de-excitation can be derived from  $\sigma_{ij}(j > i)$  by applying the principle of detailed balancing. Therefore, de-excitation processes are neglected completely. Attenuation of particular Li states  $i$  due to ionization (c.f.  $R_{ii}^e$  in Equ. 2c) in the case of electron impact and due to electron loss processes (ionization + charge transfer, c.f.  $R_{ii}^p$  in Equ. 2c) in the case of proton impact as well as excitation and de-excitation to all other bound states included in Equ. 1 is covered by coefficients  $a_{ii}$ . Rate coefficients  $R_{ij}^{e,p}$  are evaluated for a Maxwellian velocity distribution  $f(v)$  for electrons and protons using absolute cross-sections  $\sigma_{ij}$  for the various processes between plasma constituents and all Li atomic states. Available experimental data on excitation, ionization and charge exchange almost exclusively involve the Li(2s) ground state only. Therefore a critical evaluation of semiempirical and theoretical cross sections including advanced atomic orbital close coupling calculations has been carried out and compiled by the IAEA in "Atomic Collision Database for Li Beam Interaction with Fusion Plasmas".

### A.3.2. Spectroscopical observation systems on ASDEX-Upgrade

#### Electron density measurement

In the former optical system each spatial channel consisted of three 400 micron fibers. These had a poor light collection/transmission efficiency that varied drastically from fiber to fiber. The system could gather only a few percent of the incoming light and was very sensitive to the beam position. To overcome these difficulties a new fiberguide-head was built in which each spatial channel corresponds to a bundle of 34 100/130 micron quartz fibers. The light from each bundle is coupled to a 45m long 600 micron monofiber that

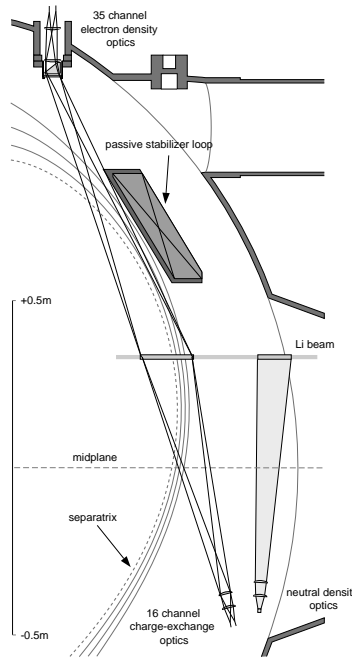


Figure A.12.: Optical observation systems of extended Li-Beam diagnostic on ASDEX Upgrade

carries the light to the detection units. About seven percent of the incoming light can be detected this way. A new BK7 optical system - a wedge and two lenses - was built to gather light in 35 channels from about 16cm along the beam path. The observation region can be radially shifted by a couple of centimeters, so that it can be adapted to different plasma scenarios. Each detection unit is equipped with an interference filter ( $T > 40\%$ ,  $FWHM = 0.7nm$ ) followed by a photomultiplier. We expect 3 - 5 times more signal with the new detection system which will permit to increase the time resolution and to investigate density fluctuations outside the separatrix.

#### CXS measurement

Two quartz lenses ( $\Omega/(4\pi) \approx 1.5 \cdot 10^{-3} sr$ ) focus the light onto an array of 16 400 micron quartz fibers allowing us to measure the radial distribution of the emitted light in a 16cm region around the separatrix with 1cm spatial resolution. The fibers are coupled to the entrance slit of an ACTON mono-chromator (Czerny-Turner,  $f = 1m$ ) and the detector (Proscan CCD - camera,  $512 \times 512$  pixels) is directly flanged to the exit. The spectral resolution is about  $0.02nm/pixel$  with a readout time of about 20ms.

#### Neutral density measurement

Two BK7 lenses ( $\Omega/(4\pi) \approx 1.810^{-3} sr$ ) focus the light onto an array of 21 400 micron quartz fibers that are grouped into three bundles each containing seven consecutive fibers. The light is gathered from a region far from the separatrix where Li excitation by collision with neutrals is the dominant process [5]. Each channel is equipped with an interference filter ( $T > 40\%$ ,  $FWHM = 2nm$ ) to select the Li2p line.

### A.3.3. Neutral lithium beam production

To be acceptable as part of a standard diagnostic, the ion gun must not only produce a high-quality beam, it should do this over a long lifetime with a degree of robustness and reliability such as to virtually eliminate daily servicing and fine-tuning. Employment of the lithium resonance line, as opposed to light originating from higher state transitions, translates into a high beam brightness via collisional excitation, and therefore permits use of a relatively low beam current. The lithium aluminosilicate, -eucryptite ( $Li_2O \cdot Al_2O_3 \cdot 2SiO_2$ ), is the ideal source in terms of simplicity - it need only be heated to near  $1300^\circ\text{C}$  and an electric field applied to extract adequate lithium ion currents. Furthermore, the low temperature yields a low transverse ion temperature, which augments the beam focussing capability.

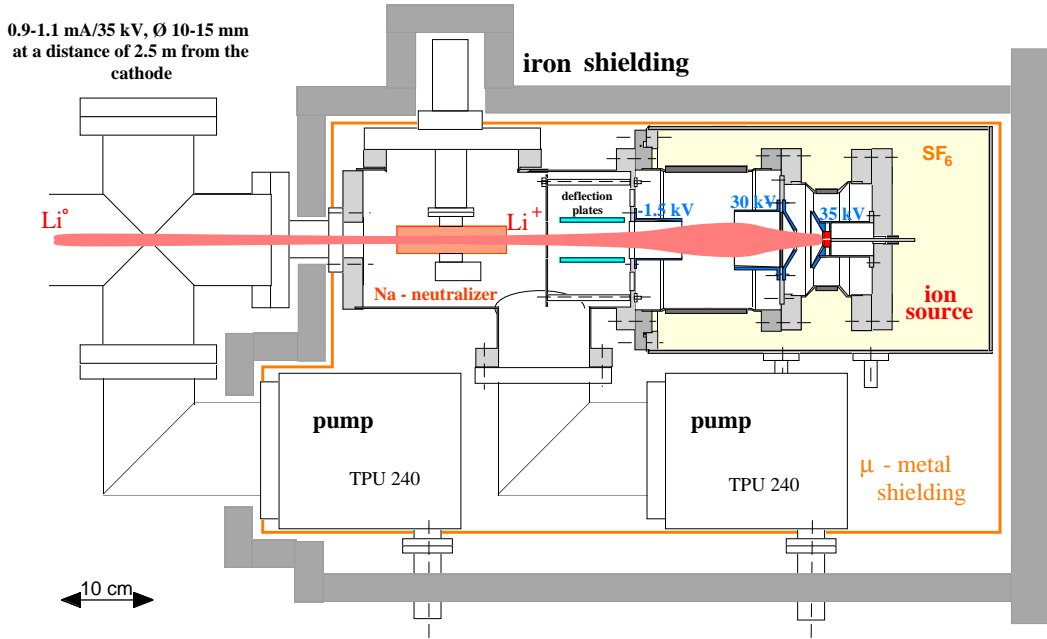


Figure A.13.: Li-beam source.

The emitter (a specially-developed commercial unit from Spectra Mat. in Calif.) consists of a porous tungsten plug base of nominal 15mm diameter which is resistively heated at about 7VAC/32A to attain the temperature needed for copious  $Li^+$  emission from the  $\approx 0.1g$   $\beta$ -eucryptite coating. With a 31.5kV difference between the two-tube immersion lens, application of  $V_{ex} = 3.5kV$  to the extractor (of Pierce design) yields an ion current  $\leq 1.25mA$  which after acceleration to  $V_b = 35kV$  and focussing passes through the sodium vapor neutralizer to form a 1.1mA neutral beam of about 10mm FWHM at  $\approx 2.3m$  from the neutralizer housing. Experimentally it has been established that the neutral beam current may be varied according to the relationship  $I_b$  [mA equivalent] =  $0.0088 V_b^{1.38}$  (over  $V_b = 13 - 70kV$ ), while maintaining the ratio  $V_{ex}/V_b$  in order to preserve good beam quality. The number of lithium neutrals per cm of beam is then  $N_b \approx 3.3 \times 10^6 V_b^{0.88}$  or  $\approx 3 - 14 \times 10^7$  over 13 - 70kV. Experience indicates  $Li^+$  ions stored in the  $\beta$ -eucryptite are not lost by heating alone, but only in combination with an extracting field. At low emission currents ( $< 1mA/cm^2$ ), most ions can be removed from the  $\beta$ -eucryptite lattice,

leading to a mA-sec rating for a 0.1g coating of  $\approx 8.6 \times 10^4$ , or  $\approx 10^4$  2mA pulses of 4 sec. length. The neutralizer, consists of a neutralization tube of 12cm length and 25mm diameter, attached to a reservoir containing sodium. The tube/reservoir are heated independently via coaxial heating cables, typically at 0.8/0.95A for powers of  $\approx 20/65W$ . The reservoir temperature is  $\approx 240^\circ C$ , meaning the tube pressure is in the  $10^{-3}$  mbar range for which sodium loss rates of  $\approx 100\mu g/sec$ , or 1 gram in  $< 3$  hours are expected for the given geometry. To reduce cell losses, operation is on a pulsed basis by means of a valve which seals the reservoir when the beam is not on. Hence, a 1 gram loading of sodium should be lost in about 2000 shots of five seconds length. Sodium is used rather than lithium in order to have the convenience of running at lower temperatures (about  $240^\circ C$  vs.  $500^\circ C$ ), and to avoid having thermal lithium signals interfering with those from the high energy beam. Based on calorimetric measurements, the neutralization efficiencies  $\epsilon$  realized are  $\approx 95 - 68\%$  for 20 - 70kV, and can be approximately summarized in the fit  $\epsilon \approx 107 V_b e^{-0.0065}$ . Taking into account the decrease of  $\epsilon$  with  $V_b$ , and the current  $I_{emitter}$  drawn from the power supply in conjunction with the neutral beam current scaling of above, it emerges that 83 - 90% (20-70kV) of  $I_e$  is utilized, i.e. only about 10 - 17% of the ions leaving the emitter are lost.

## A.4. Thermography (A. Herrmann)

Monitoring the surface temperature of the divertor with optical systems (IR-thermography, CCD-systems) is widely used. From the time evolution of the measured surface temperature, the power load to the divertor can be calculated by solving the heat conduction equation as it is routinely done on ASDEX-Upgrade.

### A.4.1. Principles of measurement and problems

Optical methods open the possibility for remote measurements of surface temperatures and are widely used in industry, medicine and science for different purposes. The physical effect used for such thermographic measurements is the variation of the number of photons emitted per surface unit at the wavelength  $\lambda$  with the temperature of a blackbody,  $T$ , as it is given by Planck's law. In this section the photon formulation is used because the high sensitivity detectors for optical temperature measurement are photon and not power sensitive. The corresponding formulation of Planck's law is:

$$M_p^b(T, \lambda) = \frac{2\pi c}{\lambda^4} \frac{1}{\exp(\frac{hc}{k\lambda T}) - 1}$$

Where  $h$  is Planck's constant,  $c$  the speed of light and  $k$  the Boltzmann constant.

The emittance  $M_p$  of real materials is always less the blackbody emittance,  $M_p^b$ . The emissivity  $\epsilon$  is a measure of how a real source of radiation compares with a blackbody.

$$M_p(T, \lambda) = \epsilon(T, \lambda) M_p^b(T, \lambda)$$

The emissivity can be temperature and wavelength dependent.

The relation between the wavelength of maximum emittance and the blackbody temperature is the Wien displacement law (Wien's law) :

$$\lambda_p^m T = 3622 \mu m K$$

Figure A.14 shows a contour plot of the above equation. Wien's law is indicated.



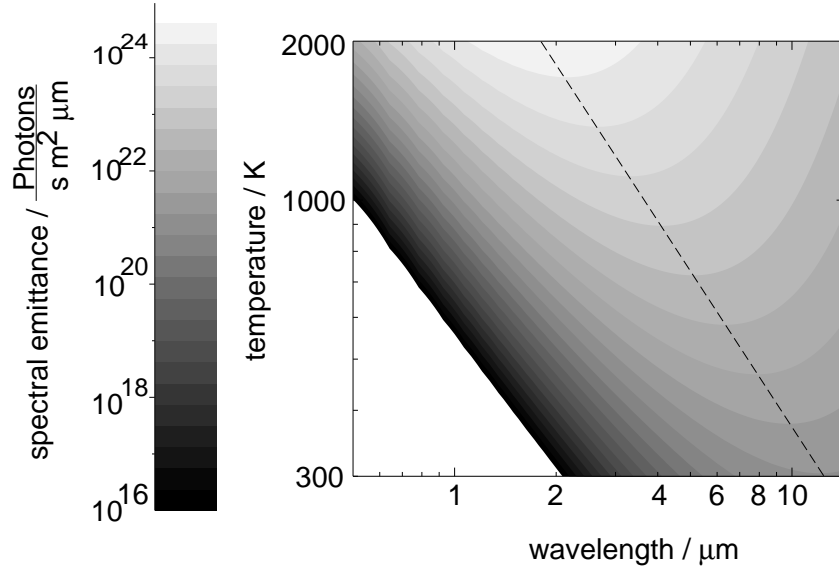


Figure A.14.: Contour plot of the spectral emittance ( $M_p^b(T, \lambda)$ , Planck's law). The dashed line indicates Wien's law.

From Wien's law and Fig. A.14 it follows that the wavelength of maximum emittance of a body at room temperature is at about  $10\mu\text{m}$ . The human eye starts to detect heat radiation if the body is at a temperature of about 900 K corresponding to a maximum wavelength of  $4\mu\text{m}$ . It is also obvious from Fig. A.14, that the flux of photons emitted at a given wavelength varies strongly with temperature. Increasing the temperature from room temperature to 900 K enhance the emittance at a wavelength of  $4.7\mu\text{m}$  by more than a factor of 100.

The strong nonlinear dependence of the emittance on the temperature is a problem for measurements, which require a large dynamic range and a good sensitivity, as is normally necessary in divertor measurements. A measure for the sensitivity is the change of the emittance with temperature as it is shown in Fig. A.15. A linear relation between emittance and temperature would result in a constant sensitivity which is only found at high wavelengths and temperatures above 500 K. Generally, the sensitivity for a given wavelength increases with temperature.

If only a small dynamic range is needed, this effect is negligible, but, in the case of a divertor diagnostic which generally demands a large dynamic range, it is troublesome. To illustrate this, Fig. A.16 shows the change in temperature which is necessary to switch one bit of a 10 bit ADC. The parameter is the maximum of the temperature range. It is assumed that the 10 bit range of the ADC is fitted to the dynamic range.

The detection wavelength selected is  $4.7\mu\text{m}$ , corresponding to the upper end of the spectral response of an InSb detector, which is often used for thermography systems. For example, if a dynamic range of 1500 K is requested, the temperature change per bit is 100 K at room temperature in contrast to 0.7 K at the upper limit.

To maximize the sensitivity at low temperatures a detection wavelength above  $10\mu\text{m}$  is preferred and the dynamic range has to be adapted to the actual temperature by controlling the integration time of the detector.

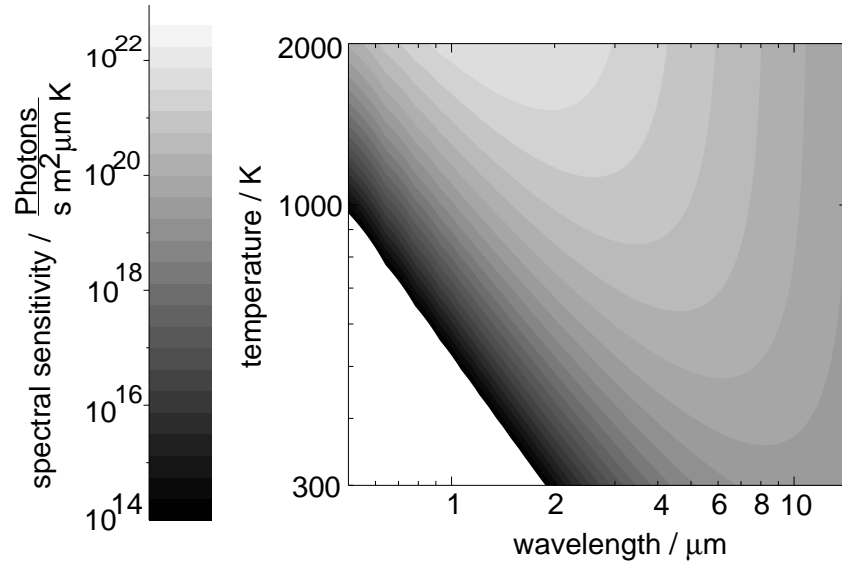


Figure A.15.: Temperature derivative of the spectral emittance ( $\frac{\partial M_p^b(T, \lambda)}{\partial T}$ ).

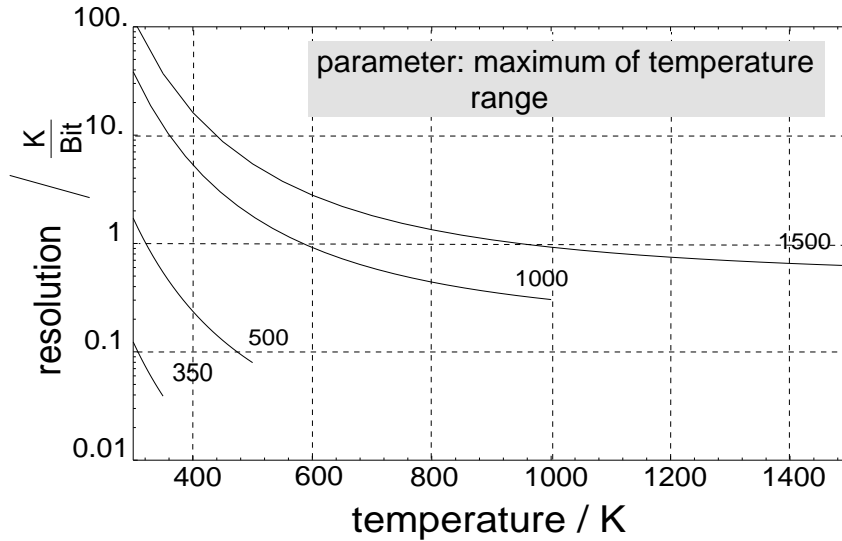


Figure A.16.: Necessary temperature change to set the lowest significant bit of a 10 bit ADC for different dynamic ranges.

### A.4.2. Contribution of bremsstrahlung

Bremsstrahlung is produced inside the plasma column and in dense radiating zones, like MARFEs, in the edge plasma. Its intensity is essentially proportional to the square of the atomic number,  $Z$ , the electron and ion density,  $n_e$ ,  $n_i$ , and inversely proportional to the square of the wavelength,  $\lambda$ :

$$\Phi_{Brems} \sim \frac{Z^2 n_i n_e}{\lambda^2}$$

In the following the contribution of bremsstrahlung to the temperature measurement is estimated. For this, the emittance of a blackbody at a given temperature and wave-

length is calculated and an additional contribution of photons due to bremsstrahlung is added. This sum is assumed to be the measured temperature information which is used to calculate the temperature as it will be done in the thermography measurements.

The order of the flux of photons due to bremsstrahlung is taken from the ASDEX-Upgrade MARFE measurements at 800 nm and then scaled to the detection wavelength using above equation. Fig. A.17 shows the contribution of bremsstrahlung for a thermography diagnostic measuring at  $4.7\mu\text{m}$ .

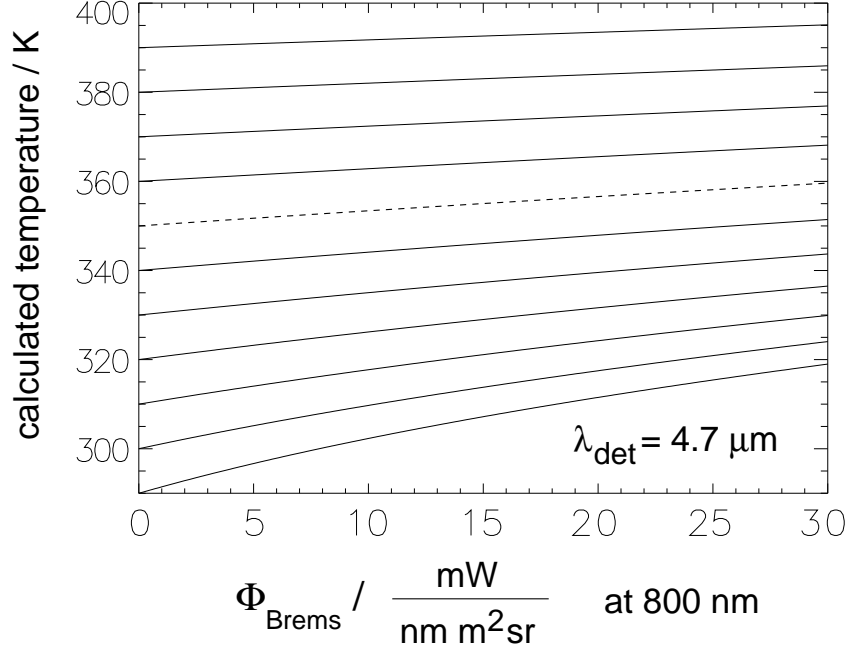


Figure A.17.: Contribution of bremsstrahlung to the calculated temperature. The parameter is the blackbody temperature,  $T(\Phi_{Brems} = 0)$ .

The parameter of the curves is the temperature of the blackbody ( $\Phi_{Brems} = 0$ ). The error in calculating the temperature is only significant at low temperatures. Because of the strong increase of emittance with the blackbody temperature, a temperature rise of a few tens of degrees makes the contribution of bremsstrahlung negligible.

The temperature where the bremsstrahlung may be neglected depends on the detection wavelength. Fig. A.18 shows the blackbody temperature,  $T_{true}$ , where the contribution of bremsstrahlung to the calculated temperature,  $T_{calc}$ , is lower than 10 K as a function of the wavelength.

### A.4.3. Principles of measurement

There are two principles for optical measurement of temperatures: (1) measuring the emittance, (2) measuring the ratio of the emittance for two different wavelengths.

(1) Using equation for the emittance and taking into account the response of the detector and the electronics,  $R$ , the optical geometry of the system,  $F$ , and a contribution of background emittance,  $U_{bck}$ , which is assumed to be constant, then the output signal of the system is:

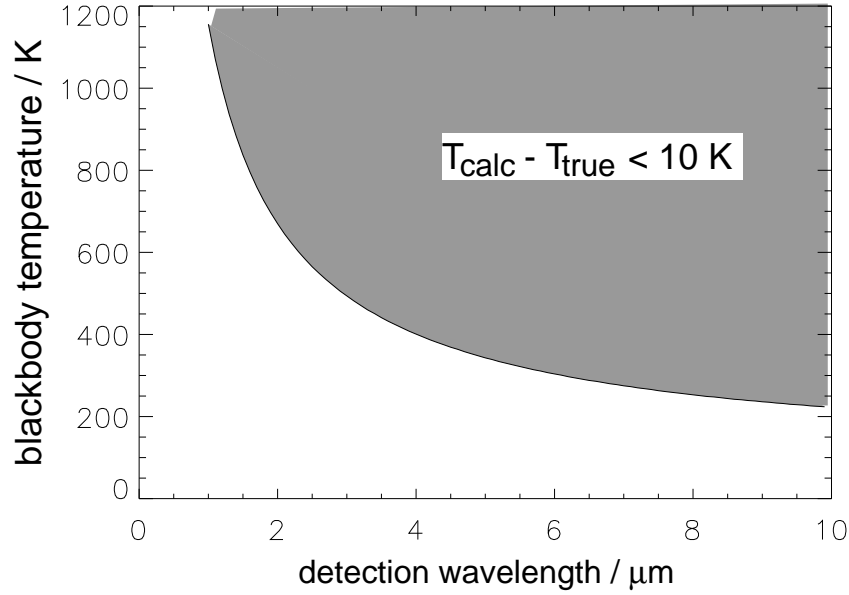


Figure A.18.: Parameter region, where the contribution of bremsstrahlung is lower than 10 K.

$$U_{out} = FR\epsilon M_p^b(T, \lambda) + U_{bck}$$

Calibrating the detection system against the temperature of a blackbody, the contribution of the background and the product of the arrangement dependent parameters, FR, can be determined. If not a blackbody, but a divertor-like arrangement is used, the emissivity,  $\epsilon$ , is also included in the calibration.

(2) Measuring the photon flux at two different wavelengths and taking the ratio of both measurements eliminates the arrangement parameters and the emissivity, provided they are wavelength independent:

$$I(T) = \frac{(U_{out}(T, \lambda_1) - U_{bck})}{(U_{out}(T, \lambda_2) - U_{bck})} = \frac{M_p^b(T, \lambda_1)}{M_p^b(T, \lambda_2)}$$

A typical change of the intensity ratio,  $I(T)$ , with temperature is shown in Fig. A.19. The wavelengths used are conform with the two regions of spectral response for a Silicon/Germanium sandwich diode. In above equation the radiating area is also eliminated and so the two wavelength method may be used in principle to measure the temperature of small hot areas in a large field of view.

#### A.4.4. Accuracy and calibration

Thermography systems used for monitoring the surface temperature of in-vessel components in addition to an IR detector with imaging optics comprise of a vacuum window and a relay optics. Although modern commercially available IR cameras are calibrated, the optical transmission of the additional components has to be taken into account for the overall calibration. If the transmission or reflection of the components is known, the new calibration factor can be calculated. Alternatively the whole IR system used on the experiment has to be calibrated against a black body source either in the laboratory before installation or in situ at the experiment. Once the linearity of the detector has been

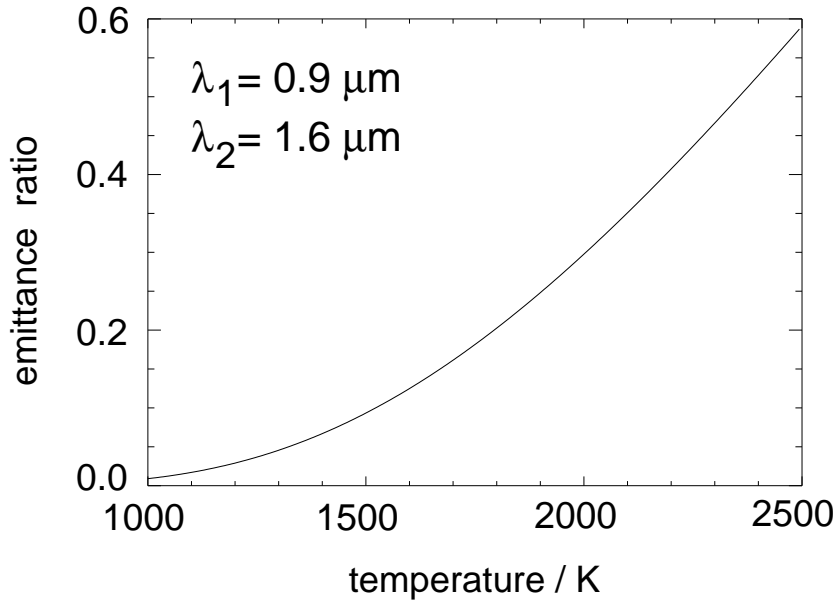


Figure A.19.: Emittance ratio,  $I(T)$ , as a function of the blackbody temperature.

checked the calibration is a two point calibration with FR and  $U_{bck}$  acting as calibration factors.

Calibrating an IR camera or detector against a black body source ( $\epsilon=1$ ), the measuring error at high temperatures is dominated by the error of the black body calibration and is about 1%. At low temperatures, the error due to the background temperature (temperature of the optics) is dominating. In practice, additional uncertainties of temperature measurements are caused by other reasons, such as: (1) uncertainties of the emissivity of the target as function of the temperature and the surface structure which may be changed by particle and neutron impact as well as by deposited layers.

(2) degradation of the optical transmission of the system by coatings or neutron damage.

(3) hot spot radiation from other locations of the inner wall reflected at the target.

(4) bremsstrahlung.

The contributions (1) and (2) reduce the received signal from the target and have to be taken into account when evaluating the signal, whereas (3) and (4) influence the background term.

The error of the temperature calculation is:

$$\frac{\Delta T}{T} = \frac{\lambda T}{c_2} \left( \frac{\Delta \epsilon}{\epsilon} + \frac{\Delta(FR)}{(FR)} \right) \frac{\exp(\frac{c_2}{\lambda T}) - 1}{\exp(\frac{c_2}{\lambda T})}$$

To meet a requirement of 10% temperature error (250 K at 2800 K), the sum of the uncertainties of emissivity, transmission, and the calibration accuracy should be about 50% for a system measuring at  $1\mu m$  and 10% at  $4.5\mu m$ , respectively (Fig. A.20).

A typical change of the emissivity of graphite with temperature at a fixed wavelength is about 8%, and the variation of the emissivity for different graphites, which may be an indication for the influence of graphite layers building up, is of the order of 10%. Thus, a requirement of 10% accuracy is met easily for a system measuring at  $1\mu m$ . However, the spectral range of  $3.2\mu m$  to  $4.8\mu m$  is needed to meet the requirement of measuring

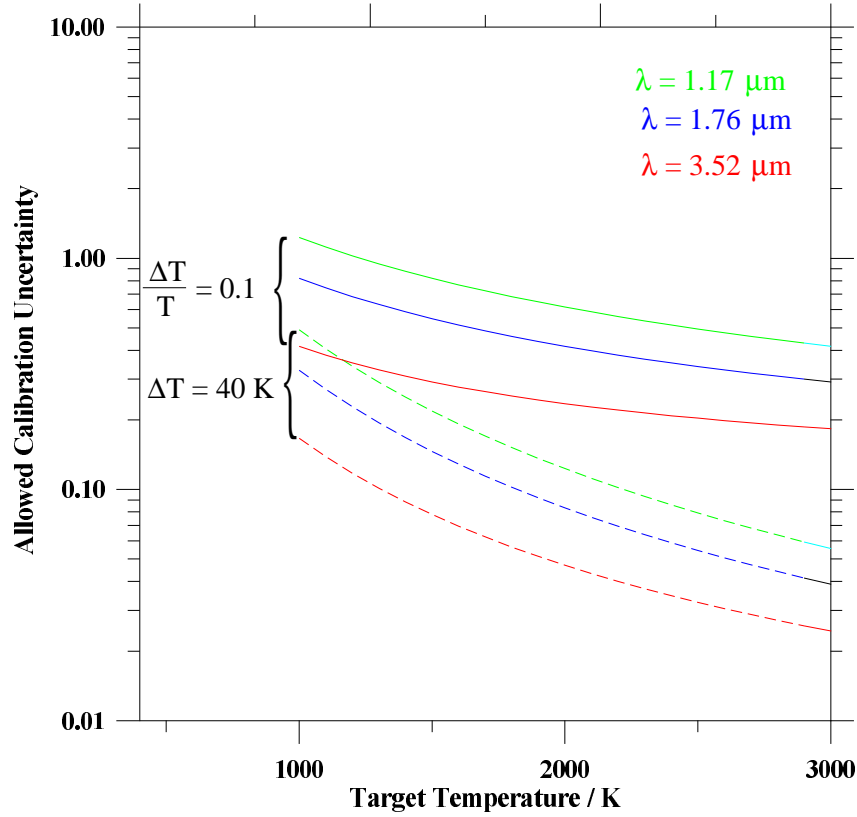


Figure A.20.: Tolerable calibration error for a required accuracy of 10% and 40 K, respectively.

down to room temperature. This requires a higher accuracy and in situ calibration. This can be done by monitoring in between discharges the temperature of the target plates. To avoid a deterioration of the calibration by background radiation it is necessary in this case to keep the temperature of the target well above the temperature of the optics. If this is not possible, an additional measurement must be performed using a heated target of known emissivity placed at the position of the entrance stop.

#### A.4.5. Heat flux calculation

The heat load to the divertor has to be derived by searching the inverse solution of the heat conduction equation. To do this, the boundary and initial conditions have to be known. The boundary condition at the backside - the heat transport into the cooling structure - may be determined in the laboratory. The boundary condition at the front side - the time evolution of the surface temperature - is measured by the thermography diagnostic. At ASDEX-Upgrade the 2D-Code THEODOR (THERmal Energy Onto DivertOR) was developed for solving the 2D heat conduction problem:

$$\rho C \frac{\partial T}{\partial t} = \nabla(\kappa \nabla T)$$

with geometry and edge conditions shown in Fig. A.21.

Because the heat conduction coefficient  $\kappa(T)$  and the heat capacity  $C(T)$  of the graphite

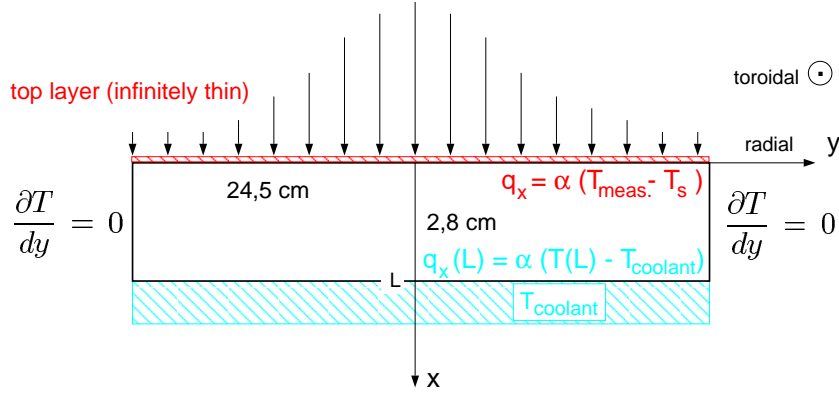


Figure A.21.: Geometry and edge condition used by THEODOR.  $\alpha$ : heat transfer coefficient.  $L$ : tile thickness.

used in ASDEX-Upgrade are strongly dependent on temperature, an effort was made to avoid the Green's function method which is restricted to rather simple geometries and a linear heat conduction equation. To calculate the heat flux to the surface ( $q_s$ ), a procedure was developed which is based on a direct numerical solution of the heat conduction equation for the whole body of a tile. The measured top surface temperature simply becomes a boundary condition, while the other surfaces can easily be taken into account by means of flexibly designed boundary conditions, e.g. an actively cooled back side with non ideal heat transmission. The introduction of a 'heat potential'  $U$  defined by

$$U(T) = \int_0^T dT' \kappa(T')$$

used in place of the temperature  $T$  simplifies above equation to:

$$q_s = -\frac{\partial U}{\partial x} \frac{\partial U}{\partial t} = D \Delta U \quad D(T(U)) = \frac{\kappa}{\rho C}$$

where  $D$  is the temperature-dependent heat diffusion coefficient. The above transformation is of computational advantage if the pertinent  $\kappa$  experimental data are fitted such that  $U(T)$  becomes a simple analytical function.

Toroidal symmetry is assumed for calculating energy flux (power) and deposited energy from thermographic measurements by integrating over the divertor plates and time. These assumptions can be verified by cooling water calorimetry.

#### A.4.6. Design considerations

The photon emittance and the spectral sensitivity depends on the detection wavelength and the temperature. At wavelengths above  $10\mu m$  the sensitivity tends to become constant in contrast to detection wavelengths lower than  $5\mu m$  where it is highly nonlinear. The emittance at  $10\mu m$  is high enough to be detected with today's cameras. Unfortunately, IR-cameras working at  $10\mu m$  are normally based on mechanically scanned systems and can not be used in magnetic fields. IR-cameras with focal plane arrays are available for the  $5\mu m$  region. Focal plane arrays are usable in magnetic fields. A second advantage of the  $10\mu m$  region is the vanishing contribution of bremsstrahlung. But bremsstrahlung

is no problem at  $5\mu\text{m}$  if the divertor temperature is above 400 K as it is found in discharges with low radiation.

## A.5. Calorimetry (P. Franzen)

### A.5.1. Experiment

The cooling water calorimetry system at ASDEX-Upgrade measures the heat load on the inner wall tiles (and the vacuum vessel) poloidally and toroidally resolved. For this, the inlet and return water temperatures as well as the water flow rates of all major cooling water circuits are monitored. Additionally, also the temperatures of some selected inner wall graphite tiles are recorded for the ASDEX-Upgrade safety system.

The hardware consists of

- 127 Platinum resistor thermometers PT100 in the cooling water system outside the vacuum vessel
- 20 PT100 thermometers inside the vacuum vessel between the Divertor II modules
- 27 Annubar flow meters in the cooling water system
- 62 NiCr-Ni thermocouples immediately in the graphite tiles

With this arrangement, the heat load on 98 total single components can be measured, covering more than 90% of the ASDEX-Upgrade inner wall.

### Data evaluation

Due to the short discharge time (a few seconds) in comparison to the heat diffusion time in graphite (some tens of seconds), the inner wall tiles are primarily cooled after the discharge. The typical cooling down time constant of the ASDEX Upgrade divertor tiles is about 500 s. Hence, the system can only measure the total heat load on a component for the whole discharge. The heat load  $E$  can be calculated by

$$E = \int c \dot{M} [T_r(t) - T_i(t - \Delta t)] dt, \quad (\text{A.22})$$

where  $c$  is the specific heat of water,  $\dot{M}$  the water flow rate,  $T_r$  the water return temperature,  $T_i$  the water inlet temperature, and  $\Delta t$  the time delay of the cooling water between the inlet and return temperature measuring devices.

For additionally heated discharges, the fraction of the energy measured to the total input energy — which should be unity — amounts to  $(85 \pm 25)\%$ . The large scatter is due to radiation and charge exchange losses through ports which are not covered by the cooling water circuits.



## Poloidal distribution of heat load

In the case of discharges with normal operation conditions, i.e. single null neutral beam heated ELMy H-mode discharges without disruptions and radiated energy fractions below 68%, the lower outer divertor plates receive between 30% and 40% of the total input power, resulting in heat loads of up to 1 MJ per sector for discharges with 10 MW additional heating power. For normal conditions, the inner divertor tiles receive about 15% of the input energy. Between 5% and 10% of the input energy is deposited on the inner heat shield, the vacuum vessel, lower PSL and the ICRH antennas, whereas the heat load on the upper divertor and PSL is negligible.

The heat load on the outer divertor tiles can be reduced by radiation in the plasma mantle by a factor of about 3, whereas the reduction of the heat load on the inner divertor tiles is only minor. Due to the increased radiation, the heat loads on the other inner wall components also increase, but this increase cannot account for the decrease of the divertor heat load due to loss channels not covered (see above). The heat load on the outer divertor tiles is also reduced for L-mode discharges, disruptive discharges, and discharges with the ion  $\nabla B$  drift towards the upper divertor plates.

## Toroidal distribution of heat load

The toroidal distribution of heat load at the outer divertor plates is asymmetric, both in Divertor I and II. In Divertor I, the maximum values exceed the mean value by more than 15%, and, furthermore, the position of the maxima depends on the discharge conditions, especially on the direction of the ion  $\nabla B$  drift. For the case of normal operation, i.e.  $I_p > 0$  and  $B_T < 0$ , the direction of the ion  $\nabla B$  drift is towards the lower divertor plates, and the maximum heat loads are on the tiles in sectors 10 to 13, whereas in the case of the ion  $\nabla B$  drift towards the upper divertor plates, i.e.  $I_p > 0$  and  $B_T > 0$ , the maximum heat loads are on the tiles in sectors 2 to 4. Apparently, the distribution exhibits a dominant  $n = 1$  structure with a smaller  $n = 2$  distribution. The dependence of the heat load distribution on the ion  $\nabla B$  drift, and not on the sign of the magnetic field, is confirmed by discharges with counter NI injection (i.e.  $I_p < 0$ ), where in the case of  $B_T > 0$  the same distribution as in the case of  $I_p > 0$  and  $B_T < 0$  shows up.

The measured asymmetry in the heat load distribution on the lower outer divertor plates of Divertor I is consistent with other toroidal asymmetries observed in ASDEX-Upgrade. After the start of neutral injection, where the separatrix position was essentially unchanged, a coloured ring was observed at the outer divertor plates. However, the center of this ring was shifted against the geometrical axis in direction of sector 13. Similar observations were made by Langmuir probes in sectors 4 and 13: the separatrix positions differ by about 10 mm, also indicating a shift towards sector 13. Furthermore, all locked modes also lock in sector 13, as observed by the Mirnov coils.

Due to the lack of corresponding discharges, no influence of the ion  $\nabla B$  drift on the heat load distribution in Divertor II can be seen. However, first results indicate a reduction of the asymmetry by a factor of 2 (with regard to the standard deviation). Furthermore, the distribution now shows a dominant  $N = 2$  structure. These differences to Divertor I are not a consequence of the Divertor II configuration, however, at the start of the plasma operations with Divertor II also the magnet of the second neutral injection box

was already installed.

All these observations indicate that the toroidal asymmetries of the heat load distribution at the lower divertor plates of ASDEX-Upgrade are caused by the distortion of the magnetic field line configuration by the neutral beam injection magnets and, with minor influence, the misalignment of the magnetic axis of the magnetic field coils to the geometrical axis of the vacuum vessel.

## A.6. Spectroscopy

### A.6.1. Spectroscopy with the VUV survey spectrometer SPRED (R. Dux)

The SPRED spectrometer (Survey Poor Resolution Extended Domain) is a survey instrument for the vacuum ultraviolet (VUV) spectral range ( $\lambda \approx 10\text{--}150\text{ nm}$ ). It is situated at the midplane in sector 1 and observes the plasma on an horizontal line-of-sight which cuts through the center of the plasma. The temporal resolution is 10 ms. Due to the large instrumental line width ( $\Delta\lambda \approx 0.3\text{ nm}$ ) only the line integrated intensities are used for analysis. Fig. A.22 shows an example for a SPRED spectrum.

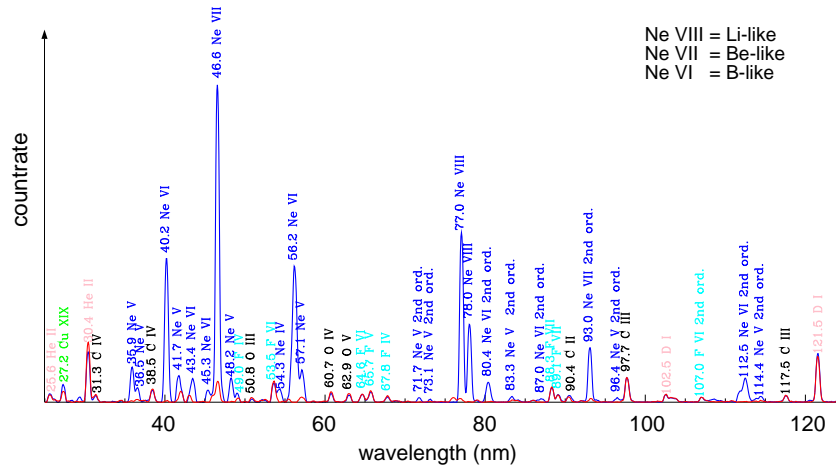


Figure A.22.: SPRED spectra in the wavelength range from 25 to 125 nm prior (red line) and after the addition of neon (blue line) during a H-mode discharge in ASDEX-Upgrade. For every line, wavelength and emitting ion are denoted. After the start of the neon puff, the spectrum is dominated by neon line radiation. The lines of the intrinsic impurities nearly remain unchanged.

The main goal of passive spectroscopy is the determination of impurity densities. Line radiation in tokamak plasmas is emitted in a very wide temperature range, and, for the main impurities (He, B, C, N, O, F, Ne, Cl, Ar, Fe), it comprises radiation from all ionization stages. The radiation of low ionization stages is in the visible and VUV spectral range while H- and He-like ions emit in the X-ray range of the spectrum. The main emitters in the VUV-range are the B-, Be-, and Li-like stages. Spatially, these stages exist around and outside the separatrix for light elements while heavy elements reach these

ionization stages in the confined region of the plasma. Due to the large transport parallel to the magnetic field, the density of ion stages in the confined plasma is (in most cases) constant on magnetic surfaces and the impurity density is a global quantity of the plasma. However, this is not true for the B- to Li-like stages of light elements (e.g. carbon). Here, the line radiation is a local quantity and is a measure of the influx of impurities from the observed surface, which is the inner heat shield in the case of the SPRED spectrometer.

The quantitative calculation of line radiation needs the local population density of the emitting quantum state. To this end, local electron densities and electron temperatures are needed and are taken from measurements. For the low electron densities in a tokamak plasma, the calculation is very much simplified since only two-body collisions between electrons and ions (linear in  $n_e$ ) have to be taken into account while three-body collisions between an ion and two electrons can be neglected because their collision rates are very small. The equilibration time for the population distribution of states of a single ion stage is dominated by the time constants of radiative decay being much shorter than the time constants of collisional excitation and transport times. Thus, the population of ground level and excited states is in equilibrium and just depends on  $n_e$  and  $T_e$ . For resonance lines, it is often sufficient to consider only collisional excitation from the ground state and radiative decay when calculating the equilibrium distribution. This approximation is the so-called coronal equilibrium. For other levels, however, excitation and de-excitation from other excited levels have to be considered and a complex collisional-radiative model has to be solved to find the equilibrium distribution.

The time to reach equilibrium between different ionization stages of an element might be long compared with the residence time of the element in a certain temperature range. Thus, the calculation of the population of ion stages has to include the transport of the impurity. The radial profile of the ion stage density depends on  $n_e$  and  $T_e$ , which determine the collisional rates of ionization and recombination, and on the transport parameters, which govern the mean residence time of the impurity in the relevant temperature range. The effect of transport might be summarized in the following way: an ion in a low ionization stage which quickly moves up the temperature gradient is ionized later compared to an ion which reaches the high temperature zones more slowly (the same argument applies to ions moving from hot to cold regions showing a delayed recombination). Finally, those excited states which cannot decay via dipole radiation should be mentioned. These so-called metastable states (e.g.  $1s2s\ ^3S$  of helium) have a longer time constant for equilibration and the actual population of metastable states might be influenced by transport effects.

The ion stage densities and the resulting line radiation is calculated numerically using the STRAHL code (Fig. A.23). The code solves the system of coupled continuity equations for every ion stage in cylindrical geometry (the radial coordinate is the magnetic flux surface index). From the profiles of the single ionization stages, the emissivity profile of the observed spectral line follows and the photon flux into the direction of the spectrometer is calculated by integration along the line-of-sight of the spectrometer. The atomic data for the relevant collisional processes and the radiative transition probabilities come from the ADAS system [104], a set of codes, which was developed in an international cooperation of astrophysical and plasma physics institutes. In addition, ADAS solves the collisional-radiative model mentioned above. The analysis of the line radiation of many ion stages of one impurity (including the X-ray lines) finally gives a picture of the density profile of

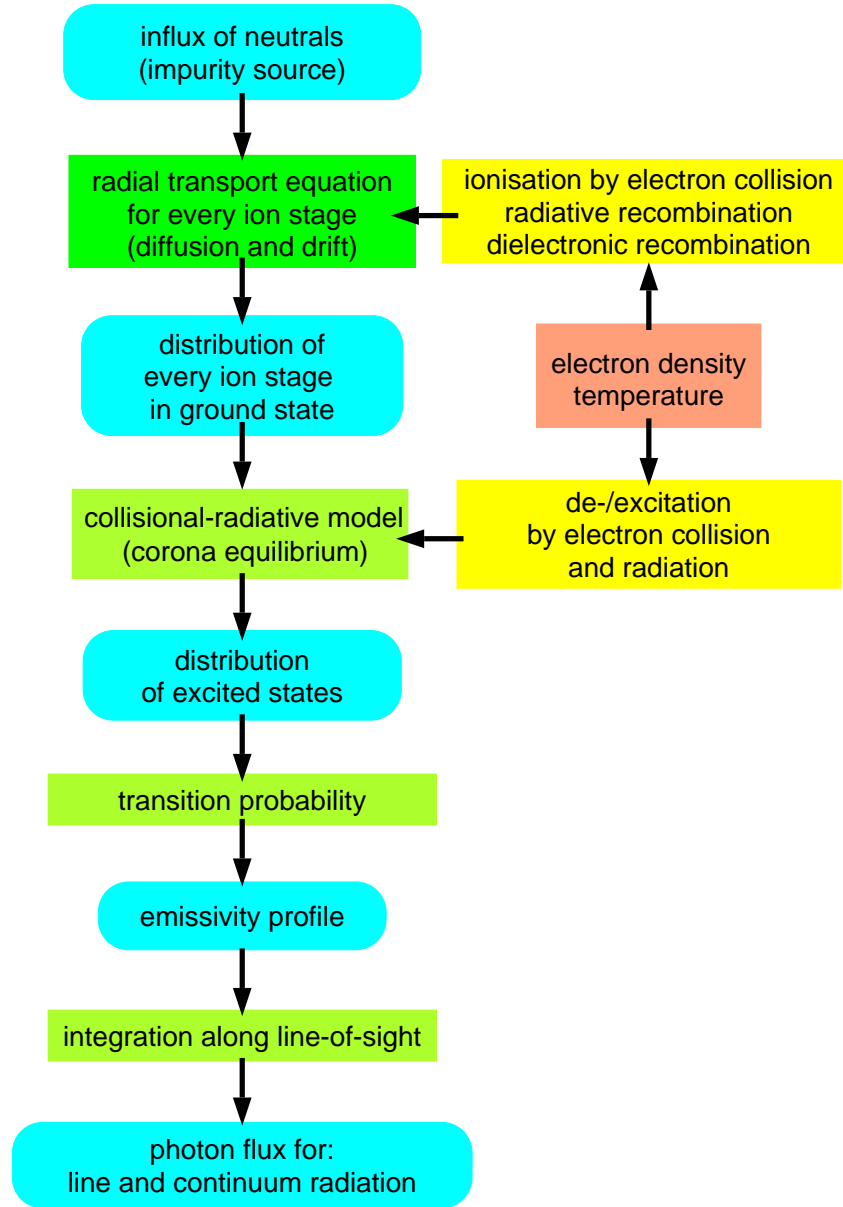


Figure A.23.: Scheme for the calculation of line and continuum radiation in the main plasma using STRAHL.

the investigated impurity.

Fast analysis of spectral measurements can be performed using the SAT code (**S**pectra **A**nalyzing **T**ool). It allows the visualization of SPRED-, Bragg- and grating-incidence-spectra and can be used to overlay the measured spectra with calculated spectra from the STRAHL code. The STRAHL spectra were calculated for a set of  $n_e$  and  $T_e$  profiles with constant form and a constant profile of the transport parameters (diffusion coefficient and drift velocity). Thus, SAT just needs the input of  $n_e$  and  $T_e$  at a specified radial position and the line averaged impurity concentration to compute the theoretical spectrum, overlay it with the measured data and give the description of the emitting ions.

### A.6.2. Spectroscopic particle influx measurements (A. Kallenbach)

Photon fluxes emerging from the plasma boundary in the vicinity of material surfaces can often be directly interpreted in terms of particle fluxes. The factor of proportionality (inverse photon efficiency) is the ratio of the ionization and excitation probabilities,  $S/XB$ , including the branching ratio  $B$ . The method is applied to visible and VUV spectroscopy to measure the influx of impurities (or to localize the impurity source) and to determine the hydrogen recycling.

The experimental situation of a particle field streaming into a high temperature plasma is considered in a simplified, 1-D geometry, where the optical viewing line is directed perpendicular to the surface where the particle source is located. The photon flux measured by an observer owing to electron impact excitation is

$$\Gamma_{ph} = \int_{x_1}^{x_2} n_i \cdot n_e \cdot X \cdot B \, dx, \quad (\text{A.23})$$

where  $n_i$  denotes the density of a particle species of ionization stage  $i$ ,  $X$  is the rate coefficient for electron impact excitation to the upper level of the observed transition with branching ratio  $B$ , and  $x_1$  is the position of a material surface where particle erosion and recycling occurs. The particles are assumed to stream into the direction of the detector at the position  $x_2$ . Since we focus on low-ionized species in the edge of a fusion plasma, recombination can be neglected (for temperatures above 2eV). Inserting the equation of continuity,

$$\frac{\partial n_i}{\partial t} + \frac{\partial}{\partial x}(v_i \cdot n_i) = S^{i-1} \cdot n_e \cdot n_{i-1} - S^i \cdot n_e \cdot n_i. \quad (\text{A.24})$$

on the right hand side of Eq. A.23 for  $n_e \cdot n_i$ , and assuming the ratio  $X/S$  to be constant in space for this analytical treatment, we obtain an expression for the observed photon flux:

$$\Gamma_{ph} = -\frac{XB}{S^i} (v_i \cdot n_i \Big|_{x_1}^{x_2} - \int_{x_1}^{x_2} S^{i-1} \cdot n_e \cdot n_{i-1} + \int_{x_1}^{x_2} \frac{\partial n_i}{\partial t} dx) \quad (\text{A.25})$$

The first two terms on the r.h.s of eq. A.25 represent the 'fuelling' of stage  $i$

$$\Gamma_i = -v_i \cdot n_i \Big|_{x_1}^{x_2} + \int_{x_1}^{x_2} S^{i-1} \cdot n_e \cdot n_{i-1} \, dx. \quad (\text{A.26})$$

The fuelling is the net sum of the particles entering a given volume element and ionization stage owing to transport and ionization,  $v_i$  is the macroscopic velocity of the species under consideration. For neutral particles (where  $i=0$  and  $S$  is zero), this velocity is the radial component of the flight speed. For ionized species in a magnetic field,  $v_i$  is caused by transport processes perpendicular to the magnetic field and may be described by the ansatz

$$v_i = v_{drift} + D \cdot \frac{\partial \ln n_i}{\partial x} \quad (\text{A.27})$$

with the pinch velocity  $v_{drift}$  and the diffusion coefficient  $D$ . For the typical experimental situation of neutral particles streaming into a plasma, the fuelling of the low ionized species is comparable to the corresponding neutral influx, as long as transport losses are small during the ionization time. For time-independent conditions, Eqs. A.25 and A.26 can be unified to the well-known relation

$$\Gamma_i = \frac{S}{XB} \cdot \Gamma_{phot}. \quad (\text{A.28})$$

The photon emission is assumed to occur instantaneously after excitation. This assumption is normally justified by the small value of the radiative lifetime of the upper level, which is typically of the order of  $10^{-8}$  s.

### A.6.3. Spectroscopic temperature measurements (R. Neu)

Beside of the extraction of the impurity content and the impurity influx, spectroscopic measurements can provide valuable informations on electron and ion temperatures as well as drifts and rotation velocities. Whereas the electron temperatures can be deduced from the intensity ratio of selected spectral lines, the ion temperature and velocity measurements rely on the broadening and the shift of spectral lines.

#### Electron temperatures

The principle of the electron temperature determination by spectroscopic means is the measurement of spectral lines with different temperature-dependent excitation rate coefficients. The ratio is then a monotonic function of the electron temperature (at least in a certain temperature range). Since only intensity ratios are used, no absolute calibration of the spectrometer system is required. However a detailed knowledge of temperature-dependent excitation rate coefficients is needed and, in the case of a passive diagnostic, also the knowledge or a model of the impurity distribution in the observed region has to be applied. The method can be used for the low temperatures at the plasma boundary as well as for the higher temperatures of the core.

At the plasma edge or in the divertor, the visible light or the VUV light from intrinsic low-Z impurities can be used (ASDEX-Upgrade: boundary layer spectrometer, divertor spectrometer). As an active diagnostic, which allows a more precise determination of the observed plasma region, a He-beam is injected in the edge plasma. Here the intensity ratio of the HeI singlet/triplet lines at 728.1nm/706.5nm, which is weakly density dependent, is generally used.

In the plasma center, the X-ray radiation from intrinsic medium-Z impurities can be utilized. Here the intensity ratio of dielectronic satellites in Li-like ions and the ground state transition in the He-like ions or the ratio between singlet/triplet lines is calculated. Figure A.24 shows a spectrum from chlorine ions, measured with the high resolution X-ray spectrometer (Johann-spectrometer) at ASDEX-Upgrade. The spectral lines marked with  $w$  and  $x,y,z$  denote transitions in singly excited He-like Cl (singlet and triplet system) and  $m,n,j,k$ ,  $q$  and  $r$  denote the dielectronic satellites from the doubly excited Li-like Cl. Since this kind of measurement is a passive one, it yields only a line of sight integrated result over the radial region where the corresponding ions exist. Therefore it is not used

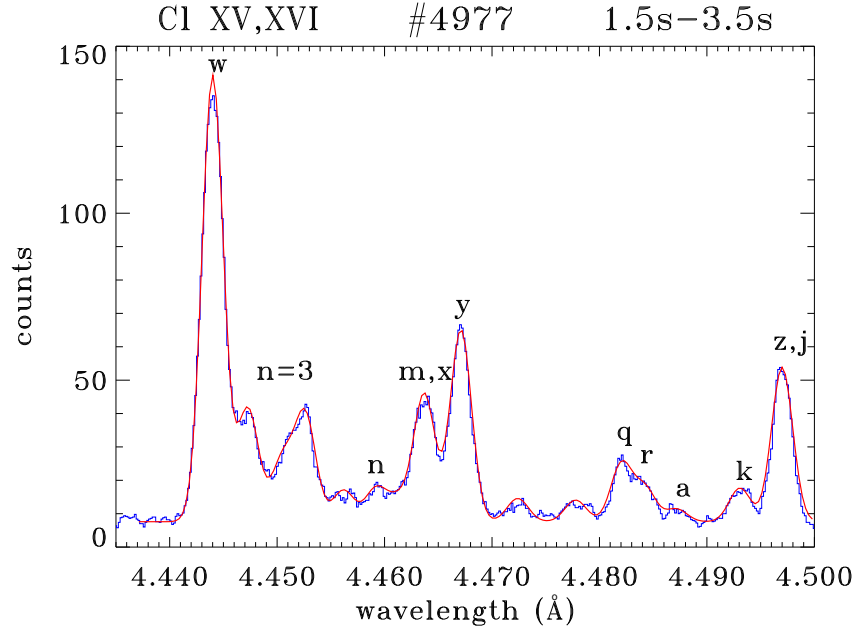


Figure A.24.: Spectrum of chlorine ions, measured with the Johann-spectrometer at ASDEX-Upgrade. The spectral lines marked with  $w$  and  $x, y, z$  denote transitions in singly excited He-like Cl (singlet and triplet system) and  $m, n, j, k$ ,  $q$  and  $r$  denote the dielectronic satellites from the doubly excited Li-like Cl.

as a standard method, nevertheless information about superthermal electrons can be extracted.

### B. Ion temperatures

The common principle of all spectroscopic techniques for extracting the ion temperatures is the measurement of the Doppler broadening of spectral lines:

$$\Delta\lambda_{1/2} = 2\lambda_0 \sqrt{\ln 2} \sqrt{2kT/mc^2} \quad \text{for} \quad \Delta\lambda_{1/2} \ll \lambda_0$$

Besides a detailed knowledge of the instrumental function, additional broadening mechanisms have to be considered:

The natural linewidth, can be omitted in most cases except for some special transitions in the X-ray region. The splitting of the spectral lines due to the fine structure and the Zeeman effect can lead to an artificial broadening, if the initial line broadening through the instrumental function or the Doppler effect is larger than the level spacing. These effects only play a role for measurements in the visible range and have to be taken into account via simulation. Figure A.25 shows the influence of the Zeeman effect on a CIII singlet line under poloidal and toroidal observation.

Under high density conditions, the Stark broadening can be much larger than the Doppler broadening, which is especially important for the measurement of spectral lines in the visible range from the divertor. High- $n$  satellite lines produce also an artificial broadening at the low energy side of spectral lines in the case of transitions in the X-ray region. For

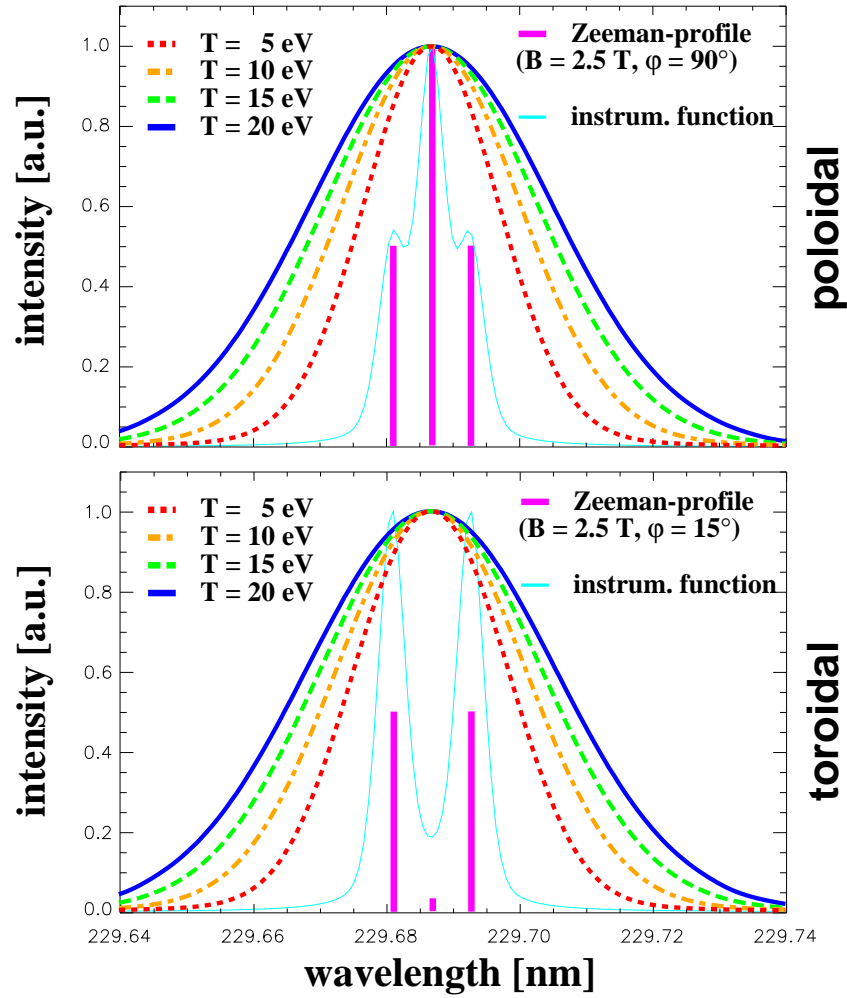


Figure A.25.: Zeeman effect of the CIII singlet line at 230 nm under poloidal and toroidal observation in the divertor of ASDEX-Upgrade.

chlorine (see Figure A.24), the  $n = 3$  satellites from Li-like Cl, in which one of the excited electrons stays in the  $n = 3$  shell, can just be separated from the resonance line ( $w$ ) in the He-like Cl, which is usually used for the  $T_i$  determination. However, satellites with  $n > 3$  can not be resolved anymore. Therefore the Doppler broadening is only extracted from the high energy side of the spectral line.

As in the case of the  $T_e$  measurements, one has to know the impurity distribution in the case of passive diagnostics. The emission is always localized through the ionization equilibrium, but if the corresponding ion exists in a rather broad temperature range, the line-of-sight integration of all the corresponding Doppler broadenings has to be considered. At ASDEX-Upgrade, passive spectroscopic  $T_i$  measurements can be performed in the divertor with the high resolution divertor spectrometer and in the central plasma with the high resolution X-ray spectrometer (Johann-spectrometer).

To eliminate the restrictions of the passive measurements, spectral lines from charge exchange reactions of low-Z intrinsic impurities with neutral hydrogen from the beam heating or a special diagnostic beam can be used. The transitions of H-like impurity ions



between states of high  $n$ -quantum numbers can be observed in the visible. By arranging several lines-of-sights perpendicular to the radial neutral beam, an almost complete radial profile of the ion temperature can be obtained. Figure A.26 shows measured and fitted sample spectra from the charge exchange spectroscopy diagnostic at ASDEX-Upgrade.

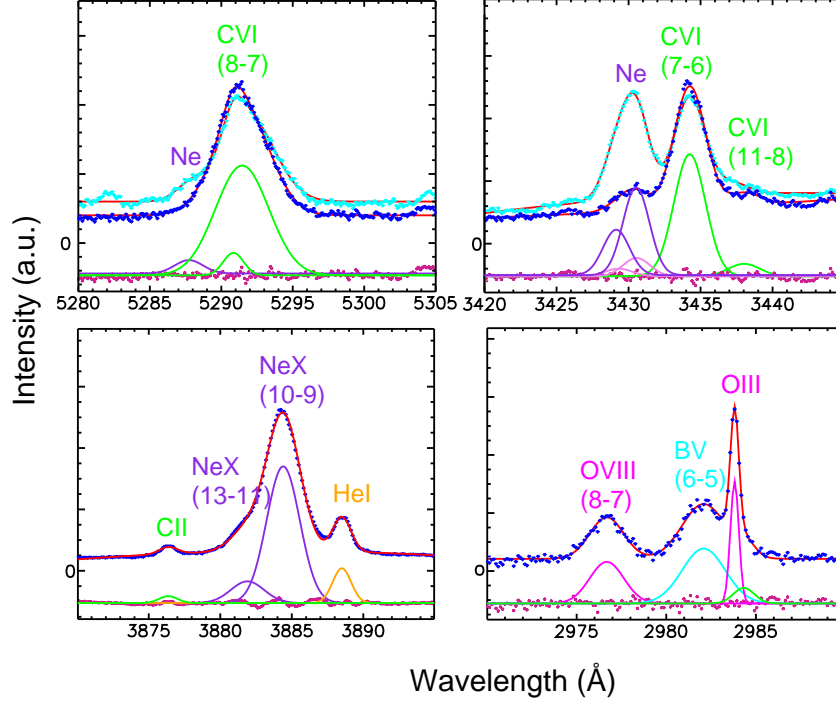


Figure A.26.: Measured and fitted sample spectra from the charge exchange spectroscopy diagnostic at ASDEX-Upgrade.

Usually the CVI (8-7) transition at 529 nm is used for the extraction of the ion temperatures, but also transitions in oxygen or neon (in the case of its injection) can be utilized. In the evaluation of the Doppler-broadened spectra, contributions from charge exchange reactions at the edge of the plasma must also be taken into account.

A common peculiarity of all the spectroscopic ion temperature measurements (except measurements using hydrogen lines at the plasma edge) is the fact that only the temperature of the impurities, but not the temperature of the hydrogen isotopes is measured. But, due to relatively small mass difference between hydrogen and the impurities and the higher charge of the impurities, the thermal equilibration is much more effective than in the case of protons and electrons.

All the measurements which extract a Doppler broadening, can also be used in principle for the determination of the drifts of the observed particles. The high resolution diverter spectrometer is therefore used to measure the ion drifts in the diverter of ASDEX-Upgrade, and the charge exchange spectroscopy routinely evaluates the toroidal rotation of the plasma.

## A.7. Neutral pressure gauges (G.Haas)

To measure the flux of neutrals with sufficient temporal and spatial resolution, pressure gauges are installed inside the vessel. They have to work under difficult conditions: strong magnetic field between 1 and 10 T with changing direction and a noisy environment. The total magnetic field inside the vessel, e.g. of a tokamak, is a superposition of the stationary toroidal field and variable poloidal fields. The poloidal fields are necessary for plasma equilibrium and control of position and shape and are typically up to an order of magnitude weaker than the toroidal field. The absolute strength of the total field is not much changed by the poloidal fields, but the direction may change by up to  $\pm 25^\circ$ .

Typical neutral flux densities are - depending on plasma operation and gauge position - of the order of  $10^{19}$  to  $5 \cdot 10^{23} D_2/(m^2 sec)$  (for room temperature these values correspond to pressures in the  $10^{-6}$  to the  $10^{-2}$  mbar-range). The assumption of a thermal velocity distribution of the neutrals, however, is not valid inside the vessel of a plasma experiment. There is always a strong component of fast neutral particles emitted by the plasma in addition to the neutrals thermalised at the wall. The fast component can represent more than the half of the total neutral particle flux.

At the MPI für Plasmaphysik, Garching, a hot cathode ionization gauge, the so called ASDEX gauge, has been developed, which can cope with these conditions, but also works without magnetic field. Without magnetic field, it behaves linearly with respect to pressure and emission current as any hot cathode ion gauge. In a magnetic field, the sensitivity rises steeply by about an order of magnitude between 0 and 1 T and stays constant at the higher fields which are normally applied in tokamaks. With magnetic field, the gauge output is linear with respect to pressure, but the sensitivity drops with increasing emission current. Such gauges are employed at several tokamaks and stellarators and are also foreseen for the planned large international fusion experiment ITER.

### A.7.1. Design of the ASDEX gauge

Because of the strong magnetic field, electrons and ions in the gauge head are restricted to a narrow ribbon like volume starting at the filament and extending parallel to the magnetic field lines. This restriction in space together with the change of the direction of the magnetic field calls for a linear arrangement of the electrodes along an axis which runs roughly parallel to the field. The electrodes - except the filament as pivot point - have to be extended perpendicular to the axis to accommodate the "ribbon" even for an oblique magnetic field (Fig. A.27).

The filament is directly heated and consists of a thoriated tungsten wire. Electrons can be emitted only if its axis and therefore the heating current runs at an angle to the magnetic field lines leading to strong  $\mathbf{j} \times \mathbf{B}$  forces. To avoid damage by these forces, a rather large filament diameter  $df$  between 0.4 and 0.8 mm has been chosen. One can show that the heating current has to be increased proportionally to  $df^{1.5}$  in order to get a certain emission current for given surface conditions (temperature and work function). The strength of the emission, however, improves as  $df^3$ .

To suppress a large background in the ion collector signal the emission current is chopped with a frequency of several kHz by means of an additional control electrode between fila-

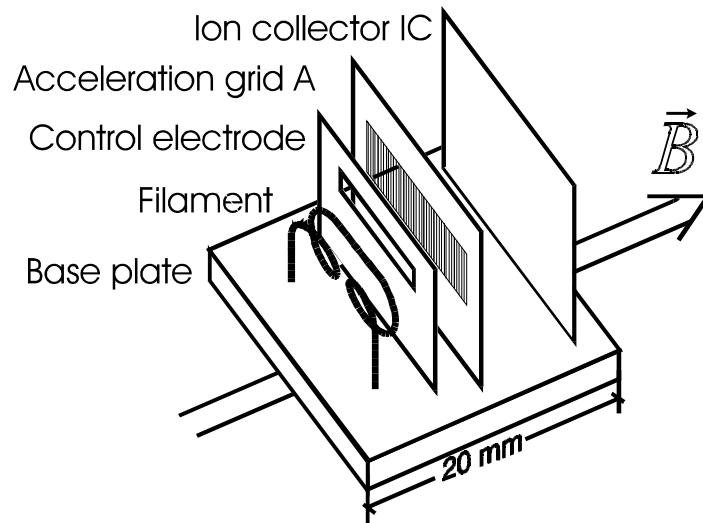


Figure A.27.: Pressure gauge setup.

ment and acceleration grid.

The DC electrode potentials are similar to those in the usual ionization gauge except for a larger potential difference between filament and ion collector. This is necessary for operation in magnetic fields. The potential of the control electrode is switched between 25 and 105 volts.

An ionization gauge measures basically the neutral particle density in the volume between the acceleration grid and the ion collector (ionization volume). It can be related to the neutral particle density or the neutral flux density outside the gauge if the conductance into the ionization volume is large or small, respectively. In the neighborhood of a plasma, a gauge has to be shielded at least against the penetration of charged particles along the magnetic field. This shield and the electrodes themselves make it nearly impossible to increase the conductance sufficiently that the neutrals inside the gauge have the same mean velocity as outside, the prerequisite for equal particle density inside and outside the gauge. It is much easier to realize the opposite case and to restrict the conductance so that the velocity distribution of the neutrals in the gauge is not influenced by the conditions outside. The gauge has to be installed in a box with a small entrance hole, i.e. particles entering the box have to undergo many wall collisions until they leave the box again. For flux equilibrium at the entrance, the incoming and outgoing flux densities have to be equal. The outgoing flux density is given by the measured particle density and the mean velocity in the box. The mean velocity may be unknown, but has to be reproducible. The gauge calibration is performed with thermal gas, i.e. the gauges are calibrated immediately in terms of particle flux density derived from the known temperature and pressure. The time resolution is given by the time constant of the box with the entrance hole, which can be made as short as 1 or 2 msec for  $D_2$ . Since the flux of neutrals hitting the plasma, the wall or a pump duct is usually of greater interest than the amount of gas staying anywhere between plasma and wall, most gauges are installed in such boxes.

### A.7.2. Operation and discussion of physical processes

To discuss physical processes in such a hot cathode ionization gauge immersed in a strong magnetic field and derive some parameters dominating the operation, we first must clarify some facts which are of basic importance for the following:

The electrons are crucial for the understanding of the processes going on in the gauge. A field is considered strong if the gyro-radii of the electrons are much smaller than the diameter of the filament or other relevant dimensions of the gauge. This is already fulfilled for the very unlikely case of an electron moving with a kinetic energy of 180 eV - the maximum it can get in the gauge - across a magnetic field of 2 T. Since electrons cannot follow an electrical field component perpendicular to a strong magnetic field, they cannot gain perpendicular momentum by the accelerating field, even if the electrical and magnetic fields are not parallel. The only source of perpendicular momentum is scattering on other particles or the emission itself. Thermionically emitted electrons from a hot filament start with an isotropic energy of a few tenths of an eV and with a wide energy spread.

The electrons are emitted by the approximately 10 mm long straight central part of the filament. Even without magnetic field, only a fraction  $\kappa$  (escape probability) of all emitted electrons can leave the filament. The rest are emitted at the back side of the filament against the electric field and are pushed back to the filament. The expected escape probability without magnetic field is about 50%. With a magnetic field,  $\kappa$  becomes smaller. A part of the electrons emitted at the front of the filament cannot leave, too, since they will hit the filament again during the first gyration orbit if the ratio between their parallel and perpendicular momenta is too small. The critical ratio depends on the angle between the filament surface and magnetic field. An estimate for a smooth cylindrical filament results in an escape probability of 35%. For a rough filament surface it can be somewhat less. The accelerating electric field does not play an important role, since the energy gain for an electron during a gyration is too small.

We have to distinguish between high and low pressures in the sense of whether the ion current collected by the ion collector is small compared with the electron current to the acceleration grid or not, respectively. Due to the higher sensitivity in a strong magnetic field, this limit is lower with field than without field. In the following discussion a low pressure case is assumed.

We will neglect the control electrode, i.e. we consider only the case with control electrode at high potential, when the electric field is not disturbed by the control electrode.

Due to the finite transparency of the acceleration grid, only part of the electrons will pass it, while the rest hit the bars of the grid directly (blocked electrons). The passing electrons are reflected by the reverse electric field in the ionization volume close to a point, where the space potential is the same as the filament potential ( $x_{max}$ , Fig. A.28).

The reflected electrons have enough energy to reach the filament again due to their finite start energy (lost electrons). Without guiding, e.g. by a strong magnetic field, however, very few electrons will be lost, because nearly all will miss the filament. Guided by the magnetic field, the electrons will miss the filament only if they undergo a collision with other particles, e.g. other electrons and lose parallel momentum or they are removed, e.g. by any particle drift perpendicular to the magnetic field out of the "shadow" of the filament. The portion of the passing electrons, which miss the filament and will survive by one of these reasons, is denoted as S (surviving probability). After a number of oscillations through the potential well, they reach finally the acceleration grid, too, by a sort

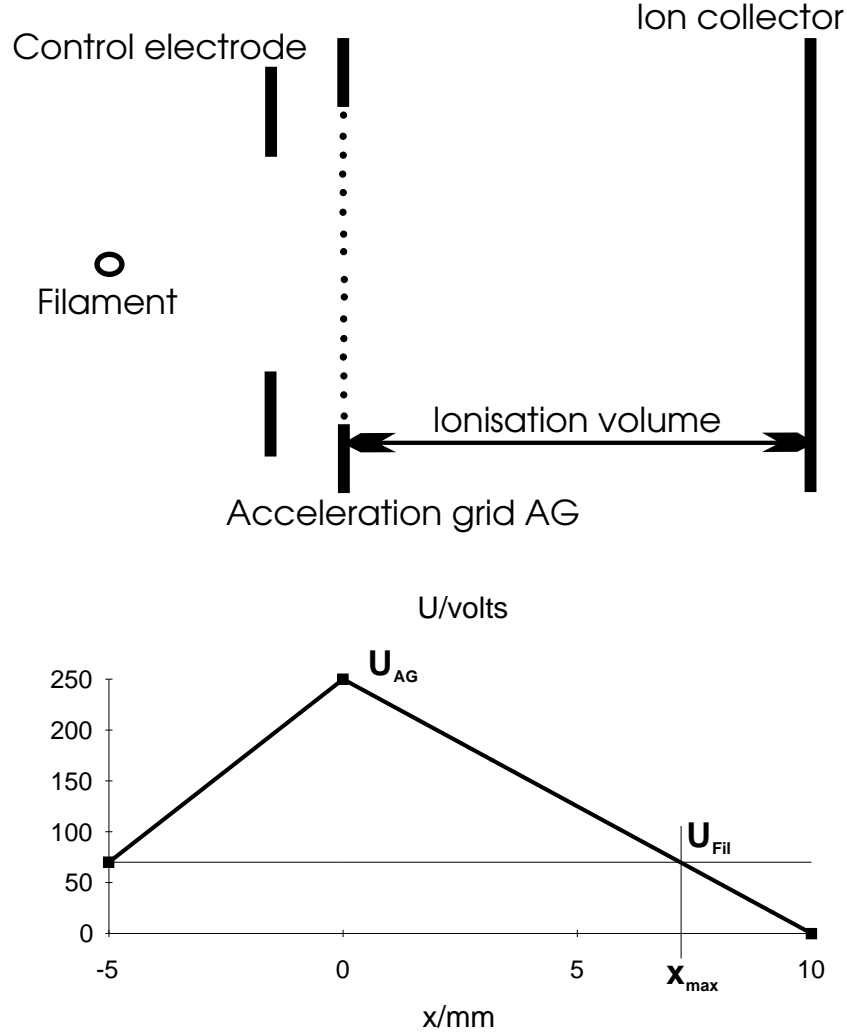


Figure A.28.: Potentials for the pressure gauge.

of cross-magnetic-field diffusion.

The total electron flux to the acceleration grid can be written as

$$\Phi_{AG}^e = \kappa \cdot \Phi_P^e \cdot ((1 - \theta) + \theta \cdot S),$$

where  $\Phi_P^e$  is the total emitted electron flux including the electrons which are immediately pushed back to the filament (primary electrons) and  $\theta$  the transparency of the acceleration grid (typically 75 to 80%). As discussed above, the escape probability  $\kappa$  and the surviving probability  $S$  depend on the magnetic field.  $\Phi_P^e$  depends only on the filament temperature and surface condition.

The ion flux to the collector can be written generally as an integral over the ionization volume  $V_{ion}$  and the energy distribution of the electrons  $f(E)$ :

$$\Phi^+ = \int_{V_{ion}} \int_0^{\inf} n_0 \cdot n_e \cdot \sigma_{ion} \cdot v_e \cdot f(E) \cdot dE \cdot dV,$$

where  $n_0$  and  $n_e$  are the neutral particle and electron density, respectively,  $\sigma_{ion}$  the ionization cross-section and  $v_e$  the electron velocity.

The shape of the energy distribution of the electrons  $f(E)$  depends crucially on electron-electron scattering in the gauge in cases with strong magnetic field. Two extreme scenarios can be distinguished depending on the electron density in the ionization volume:

First scenario:

The electron density is high and the electrons which are confined axially by the electric field and radially by the magnetic field show collective effects. They are heated and fed by the incoming electrons. Incoming and reflected electron beams running in opposite directions are supposed to excite a two-stream instability (also known as the Buneman instability) which leads to effective scattering of the electrons. Therefore  $f(E)$  becomes broad and  $S$  approaches near unity as in so called pure electron plasma devices. Such devices use a similar combination of electric and magnetic fields, but are much larger than the gauges and are rotationally symmetric.

Second scenario:

The electron density is too low, the volume too small and the symmetry too poor for effective scattering and confinement of the electrons. The electrons do not show collective effects and have to be considered as single, independent particles. In this scenario  $f(E)$  is locally a  $\delta$ -function and  $S$  is much smaller than one.

As dedicated experiments with strong magnetic field have shown most of the passing electrons reach the filament again, i.e. the surviving probability  $S$  is, despite an additional contribution from drifts, indeed rather small. Therefore, the second scenario better describes the situation in the gauges. If electron-electron scattering plays a minor role, the momentum of most electrons is nearly parallel to the field and their energy depends only on the position along the axis in the gauge and can be written in the ionization volume as:

$$E(x) = e(U(x) - U_{Fil}) = e(U_{AG} - x \cdot \frac{U_{AG}-U_{Fil}}{x_{max}} - U_{Fil}),$$

where  $e$  is the elementary charge,  $U_{Fil}$  and  $U_{AG}$  are the potentials of filament and acceleration grid respectively, and  $x$  is the coordinate along the axis with  $x = 0$  at the acceleration grid.

With this assumption and  $q$  being the cross-section of the electron beam in the ionization volume one gets:

$$\Phi^+ = n_0 \cdot \int_0^{x_{max}} \sigma_{ion}(E(x)) \cdot n_e(x) \cdot |v_e(x)| \cdot q \cdot dx.$$

If one introduces the electron flux in the ionization volume, which does not depend on  $x$ ,

$$\Phi_{ion}^e = n_e(x) \cdot |v_e(x)| \cdot q.$$

and uses the electron energy  $E(x)$ , the ion flux becomes:

$$\Phi^+ = n_0 \cdot \Phi_{ion}^e \cdot \frac{x_{max}}{e \cdot (U_{AG} - U_{Fil})} \cdot \int_0^{e \cdot (U_{AG} - U_{FIL})} \sigma_{ion}(E) dE.$$

The remaining integral can be derived from measured ionization cross-section data. For  $H_2/D_2$  and the potentials used in the ASDEX gauge it is

$$\int_0^{e \cdot (U_{AG} - U_{FIL})} \sigma_{ion}(E) dE = 1.5 \cdot 10^{-18} m^2 eV.$$

The electron flux in the ionization volume can be derived by similar considerations

$$\Phi_{ion}^e = 2 \cdot \theta \cdot \kappa \cdot \Phi_P^e \cdot ((1 - S) + f \cdot S),$$

where  $f$  is the number of oscillations which the electrons missing the filament perform before they reach the acceleration grid. The factor 2 is due to the fact that all electrons

pass the ionization volume twice during each oscillation.

The sensitivity of an ionization gauge is usually expressed as

$d = \frac{I^+}{(I^e - I^+) \cdot n_0}$ , where  $I^e$  is the current collected at the acceleration grid  $I_{AG}^e = e \cdot \Phi_{AG}^e$  and  $I^+$  the ion collector current  $I^+ = e \cdot \Phi^+$ .

$I^+$  has to be subtracted from  $I^e$  in order to correct the electron current for electrons produced by ionization and similar effects. This correction is important at high densities and can be neglected here.

Introducing  $I_{AG}^e$  and  $I^+$  one gets

$$d = \frac{3 \cdot 10^{-18} \cdot x_{max} \cdot (1 + S \cdot (f - 1))}{e \cdot (U_{AG} - U_{Fil}) \cdot ((1 - \theta) / \theta + S)}.$$

The experiments mentioned above were done under low pressure condition. They revealed an increase of the number  $f$  of oscillations which the passing and surviving electrons perform, from about 1 without field to about 6 with field. This is, however, not very important. With field, only 20% of the electrons passing the acceleration grid miss the filament after the first transit and arrive eventually after these 6 oscillations at the acceleration grid. The remaining 80% return after only one oscillation to the filament. These electrons are the main reason for the sensitivity increase under a strong magnetic field. Despite the fact that they make only one transit they contribute remarkably to the electron flux in the ionisation volume, but they do not contribute to the measured emission current.

## A.8. Bolometers (K.F. Mast, J.C. Fuchs)

In fusion research, bolometers are used as a standard diagnostic for absolute measurement of the radiation power which is emitted by the plasma. In contrast to quantum detectors, bolometers are thermal detectors which are based upon a classical thermodynamic effect. The radiation power to be measured is absorbed in a volume element of some useful material leading to a temperature elevation which is measured with a temperature dependent physical effect. Numerous types of bolometers have been developed until now but miniaturized thin-film metal resistor bolometer arrays have proved superior behavior on present large plasma experiments like JET, ASDEX-Upgrade, Tore Supra, RFX and will probably be the best choice for ITER, too.

The principle construction of a detector element of the miniaturized metal resistor bolometer array is shown in Fig. A.29.

Also, a complete ASDEX-Upgrade bolometer array with 4 detectors is shown. The plasma radiation is absorbed in a few  $\mu m$  thick gold absorber layer which is deposited on the front side of the bolometer foil. A measuring resistor layer which is deposited on the rear side of the bolometer foil changes its value proportional to the temperature rise of the foil. The variation of the resistance is measured with an AC-excited Wheatstone bridge. From the resultant bridge output voltage  $U$  the absorbed radiation power  $P_{BOL}$  can be derived with a simple differential equation

$$P_{BOL} = C \cdot \left( \frac{d\Delta U}{dt} + \frac{\Delta U}{\tau} \right),$$

where  $C$  and  $\tau$  are bolometer constants which have to be determined by calibration.

As an example the arrangement of numerous bolometer arrays in collimated pinhole cameras which are mounted inside the vacuum vessel of ASDEX-Upgrade around a poloidal circumference of the plasma is shown in Fig. A.30.

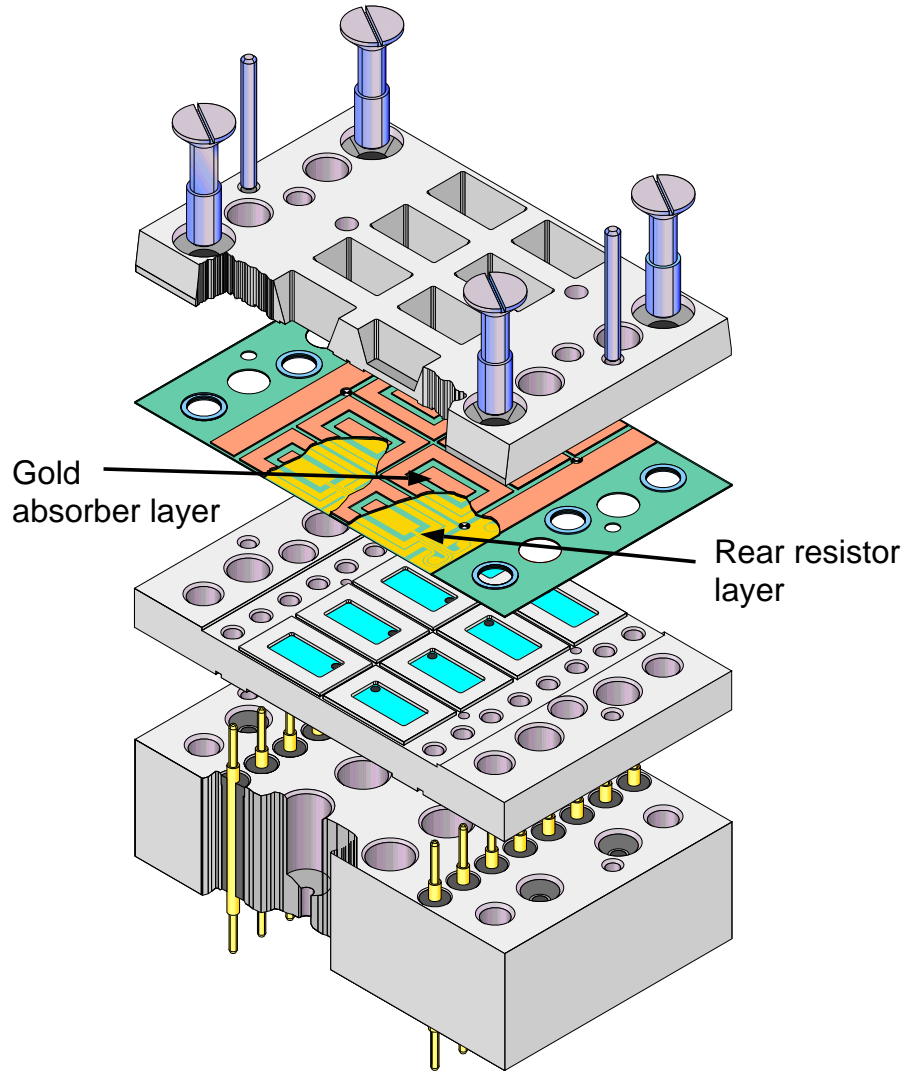


Figure A.29.: Bolometer construction scheme.

The bolometric diagnostics on the modified ASDEX-Upgrade with DivII comprises 96 bolometer channels. The majority of the lines of sight (56 channels) are arranged in such a way that they monitor mainly the plasma boundary, the SOL, the X-point region and the inner and outer divertor leg.

Two horizontal cameras HCI and HCII, each with 12 channels, register radiation with a space resolution of 3 cm from the upper and lower outer plasma boundary, the X-point region and the inner divertor leg. The top of the plasma boundary is observed with the horizontal camera HCV (8 channels, 6 cm spatial resolution) and the X-point region with the horizontal camera HCIV (8 channels, 6 cm spatial resolution). Two roof-baffle cameras, each with 8 channels, monitor the plasma in the inner (3 cm spatial resolution) and outer divertor leg (2 cm spatial resolution).

The high signal to noise ratio of the bolometers allows for a time resolution of 1 ms. In order to eliminate signal disturbances which are caused by the neutral gas pressure,



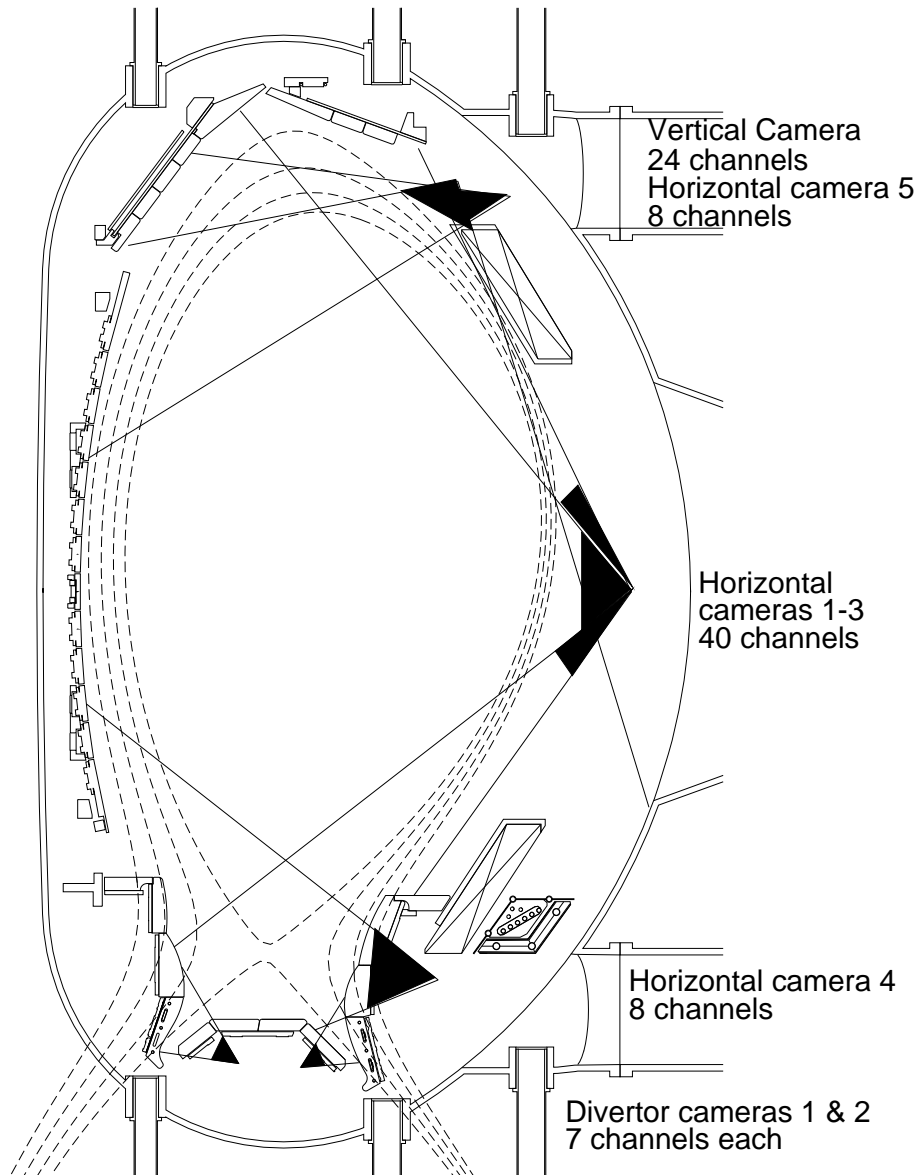


Figure A.30.: Setup of bolometer geometry for ASDEX-Upgrade.

newly developed MICA NGC(neutral gas compensated)-bolometers are installed in the two roof baffle cameras and in the HCIV. Additionally new miniaturized foil manometers are mounted in either of the roof-baffle cameras for absolute pressure measurements in order to correct the remaining offset drift of the NGC-bolometers.

## A.9. Energy-resolved neutral fluxes (J. Stober)

### Introduction

The simulation of energy-resolved neutral fluxes is a method to evaluate the radial ion-temperature profile and the neutral density along the lines of sight of the detectors. The

method presented here uses the whole information contained in the energy spectra and can treat both isotopes (H, D) simultaneously, so that it can be used for neutral beam heated plasmas as well. Since we can detect neutrals with energies down to 20 eV, the method is very sensitive to the plasma edge. After describing the method, we will present results for different scenarios and compare with the ion temperature measured by charge-exchange recombination spectroscopy.

### Idea

Since charge exchange (CX) strongly couples ions and neutrals, the energy spectrum of the neutral fluxes strongly depends on the ion temperature profile. The flux per energy unit and steradian is given by the line integral along the line of sight:

$$S(E_0) = \frac{1}{2\pi^{3/2}} \int_0^L \langle \sigma_{cx} v_{rel} \rangle(x, E_0) \cdot n_i(x) \cdot \frac{\exp(-E_0/T_i(x))}{T_i^{3/2}(x)} \cdot E_0^{\frac{1}{2}} \cdot n_0(x) \cdot \exp\left(-\int_0^x \frac{ds}{\lambda_{tot}(s)}\right) dx \quad (\text{A.29})$$

The first line of the integrand gives the birth rate of neutral particles with energy  $E_0$  via a charge exchange (CX) process between ions with energy  $E_0$  and a neutral background, assuming a Maxwellian velocity distribution for the ions. The second line describes the attenuation of the escaping neutrals along their path to the analyser. The aim is to invert the dependency function to obtain the  $T_i$  profile from the energy spectrum. Unfortunately the neutral flux spectrum does not only depend on the  $T_i$  profile but also on radial profiles of  $n_e, n_p, T_e$ , and on  $n_0$  along the lines-of-sight. The cross-sections of the main reactions between atoms, molecules, ions, and electrons have to be known as well.

Instead of “inverting” the line integral (A.29) we use a fitting procedure to simulate the measured flux data. Experimental data are used for all radial plasma profiles except for the  $T_i$  profile which is parameterized. All charged particle profiles are assumed to be constant on flux surfaces. The  $T_i$  parameters are varied such that the calculated neutral flux spectrum fits the measured one. The neutral density needed for this calculation is itself calculated from the plasma profiles using a neutral gas model and assumptions on the sources of neutrals.

### Experimental Basis

Neutral particle detectors of two different types are in operation at ASDEX-Upgrade. Their geometric position is shown in Fig. A.31: CXA I,II are gas-cell analyzers with  $E \geq 500\text{eV}$ . H and D fluxes are measured separately. CXA II is movable, also in toroidal direction. LENA is a time-of-flight analyser with  $20\text{eV} < E < 1200\text{eV}$  without isotope separation. Its interpretation in case of isotope mixtures is explained in Fig. A.32

Energy integrated neutral flux measurement is done with an  $H_\alpha$ -diode, close to the LENA line of sight and an ion gauge at the vessel wall close to the CXA-detectors.

The plasma profiles are taken from other diagnostics:  $T_e$  from Thompson scattering and ECE,  $n_e$  from a combination of interferometry and Lithium beam diagnostics,  $n_p/n_e$  is estimated from spectroscopic measurements, and the flux surfaces are obtained from magnetic measurements and function parameterization.

### Modeling of neutral density

The neutral density is not constant on flux surfaces since the neutrals are not magnetically confined. Molecules are involved in plasma-wall interactions and gas puffing. In particular, the density at the plasma edge is influenced by the vessel geometry and the

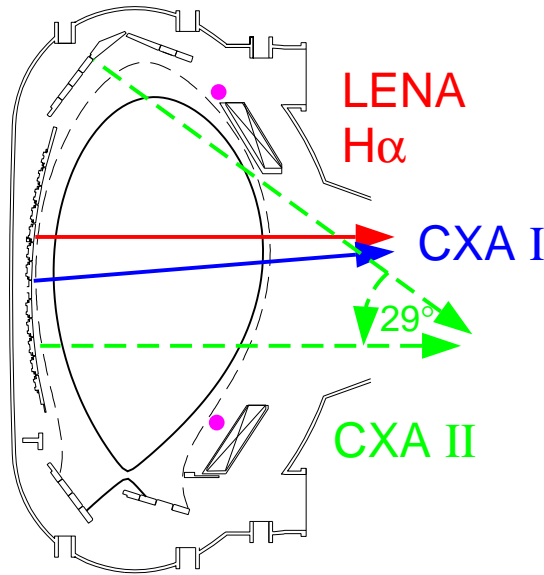


Figure A.31.: Poloidal cut of ASDEX-Upgrade with lines of sight.

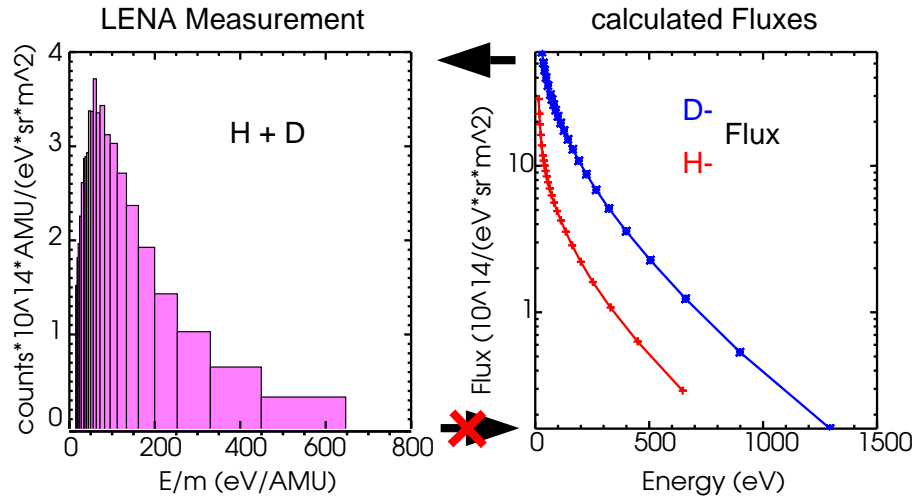


Figure A.32.: LENA measurement in the case of isotope mixture for a typical ohmic Deuterium shot. The fluxes cannot be derived from the data, but for given fluxes the corresponding data can be calculated and they can be compared to the measured data in the fitting procedure. Note the large contribution of H to the high velocity channels.

position of limiting structures and neutral sources.

The Monte-Carlo code EIRENE provides a correct solution of the neutral distribution in and around a given plasma if the important reactions are selected and the source distribution is sensible. Impurity species are not calculated, since a reduced proton density is sufficient to describe the distribution of hydrogen neutrals: the main ion-neutrals interaction is via CX, which is resonant for the reaction of hydrogen atoms and protons. An isotope mixture can be treated as one species by scaling the proton mass, if the  $\text{H}^+/\text{D}^+$  ratio is

constant in the plasma:  $E = E_H = E_D = m^* \cdot \bar{v}^2/2$  and  $\bar{v} = \sqrt{E} * (f_H * \sqrt{2} + f_D)$  implies  $m^* = 2/(f_H * \sqrt{2} + f_D)^2$  (mass unit: AMU,  $f_H, f_D$  relative concentrations,  $f_H + f_D = 1$ ). The choice of the source is, at least for LENA and CXA I, not critical. We checked different positions as indicated by pink circles in Fig. A.31 and found no differences in the CX-fluxes simulated along the lines of sight except that the source strength had to be adjusted differently. This insensitivity to the source position is due to the fact that in many cases the neutrals from volume recombination dominate the plasma center. Also, the ellipticity and the Shafranov shift enhance the influence of the sources at the outer mid-plane on the neutral density in the plasma center. Nevertheless, for low density plasmas, an influence of sources located on the inner heat shield cannot be excluded.

### Fitting procedure

To obtain the most reliable  $T_i$  and  $n_0$  profiles, the following data are fitted simultaneously: LENA, CXA I (hydrogen and deuterium or additional information on H/D-ratio),  $H_\alpha$  or ion-gauge data, CXA II (all energies or  $T_i(\text{max})$  on chord from slope), and local  $T_i$ -data from CX-recombination spectroscopy (NI only). The standard  $\chi^2$ -functional weighted with the estimated errors of the data is used as a quantitative criterion for the difference between data and simulation. For Gaussian distributed errors a good fit should result in a value in the order of the number of degrees of freedom. As parameterization for the  $T_i$  profile, a linear spline is used with a manually adjusted number of knots. The optimal knot positions can be fitted, which is very useful in regions with large curvature. i.e. at the edge. The estimated errors of the result depend on the number of knots. This number is optimized by using as few knots as possible without increasing  $\chi^2$  significantly. Further parameters are the relative concentration of deuterium and a separate source strength for each CX-chord. To avoid a differentiation of the Monte-Carlo process (MC), which is necessary for efficient minimizers, a two-step algorithm has been developed: the first step is the MC for a given parameter set and the second step is a minimization with linear constraints (monotonicity) with constant neutral densities (NAG: E04UPF). The following cycle starts at the minimum of the previous one. Empirically, convergence is observed. For reasonable start-up values ( $T_i = T_e$ ), 3 or less MCs are sufficient. Figure A.33 illustrates the accuracy and the results of the fitting procedure for an ohmic shot.

### Low Energy Cut-Off

Within the experimental errors, the energy-resolved neutral fluxes are invariant under specific one dimensional transformations of the ion-temperature profile (Fig. A.34). An analysis of eqn. A.29 together with a simplified model for the neutrals proves this hypothesis and the error of the data can be correlated with a maximum shift  $\Delta N (N = \int n \, dl)$ , which is determined by the lowest detectable energy and the corresponding experimental error. In our case,  $\Delta N$  is between  $1 \times 10^{17} m^{-2}$  and  $2 \times 10^{17} m^{-2}$ . As Fig. A.34 shows, the effect of this invariance is a high uncertainty at the separatrix due to the steep  $T_i$ -gradient. Since the fluxes at energies below the measuring range of LENA show a strong variation with the  $\Delta N$  shift, the total neutral flux changes as well. Therefore, the inclusion of  $H_\alpha$ -diode or ion-gauge data can eliminate this invariance. EIRENE can calculate the flux at the position of the ion-gauge during the Monte-Carlo process. As a post-processor, the  $H_\alpha$  intensity is obtained from the density of atoms, molecules (neutral and ionized), and plasma ions along the line of sight of the absolutely calibrated diode. A problem of the  $H_\alpha$  interpretation is the contribution of the inner heat shield, that cannot be simulated since the distribution of neutral sources is unknown. Gas puffing experiments that rise

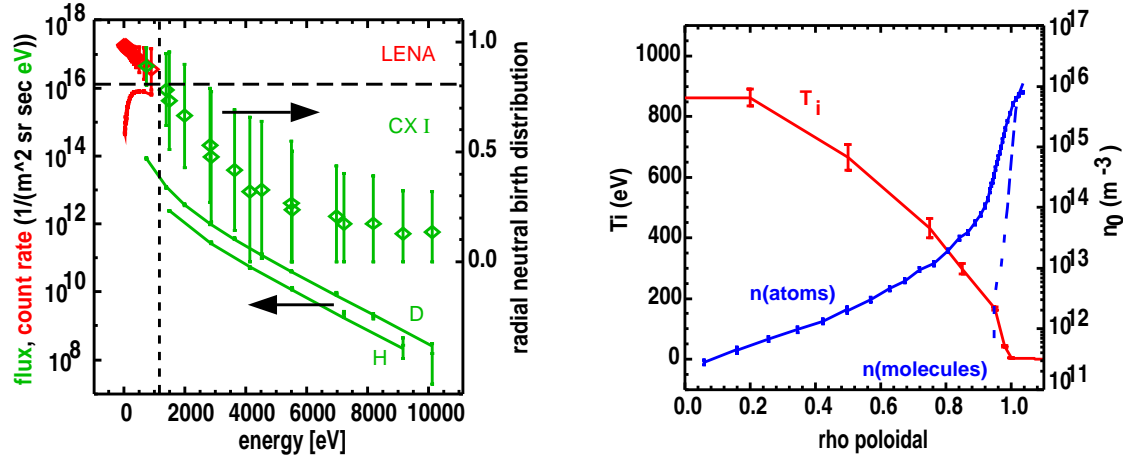


Figure A.33.: **Left:** Simulation of the CX data and birth regions of the particles. The simulated fluxes and count rates (solid lines) are within the error bars of the data. The diamonds mark the mean values of the radial birth positions of the neutrals and their error bars show the corresponding standard deviations. The radial label is the dimensionless flux-surface label  $\rho_{pol} = \sqrt{(\Psi - \Psi_{axis})/(\Psi_{sep} - \Psi_{axis})}$ ,  $\Psi$ : pol. flux. **Right:** Ion temperature and neutral densities at the minimum in parameter space. The error bars of the ion temperature parameters are determined from the curvature at that minimum. Those of the atomic (H + D) density are due to the uncertainty of the Monte-Carlo process. In the center, volume recombination dominates as atomic source. Outside the separatrix, molecules play an important role.

the neutral flux only on the outer midplane show as well as high resolution spectroscopy that in general one third of the  $H_\alpha$  intensity originates from the outer plasma boundary. The error is about 20%, which is significantly smaller than the  $H_\alpha$  variations due to  $\Delta N$ , which changes the signal by a factor of 2.

### Neutral Injection and $T_i$ from Spectroscopy

When heating the plasma with neutral injection (NI), the velocity distribution of the injected species is disturbed above 2 keV due to fast ions (Fig. A.35). The method presented here is capable of analyzing the undisturbed minority species. This requires an analyser for the CXA diagnostic with a mass separation better than 99%. In the case of NI-heating, CX-recombination spectroscopy (CXRS) can determine local ion temperatures at 14 radial positions. These have been compared with the results of the CX-particle flux simulation and they have been added to the simulation such that the deviation from the parameterized  $T_i$ -profile and the estimated error of the CXRS measurement are included in  $\chi^2$ . Figure A.35 demonstrates the results. In general, the two methods agree quite well, but differ for some scenarios, which is not yet fully understood. When the CXRS data are included, the inner  $T_i$ -profile is less oscillating, which means that more knots may be used in that case. At the plasma edge, inclusion of CXRS data does not change the result. The steep gradient zone at the separatrix can only be resolved with the CX-simulation.

### Impurities

The effect of the impurities on  $n_0, n_p$ , and the attenuation of the escaping neutrals is

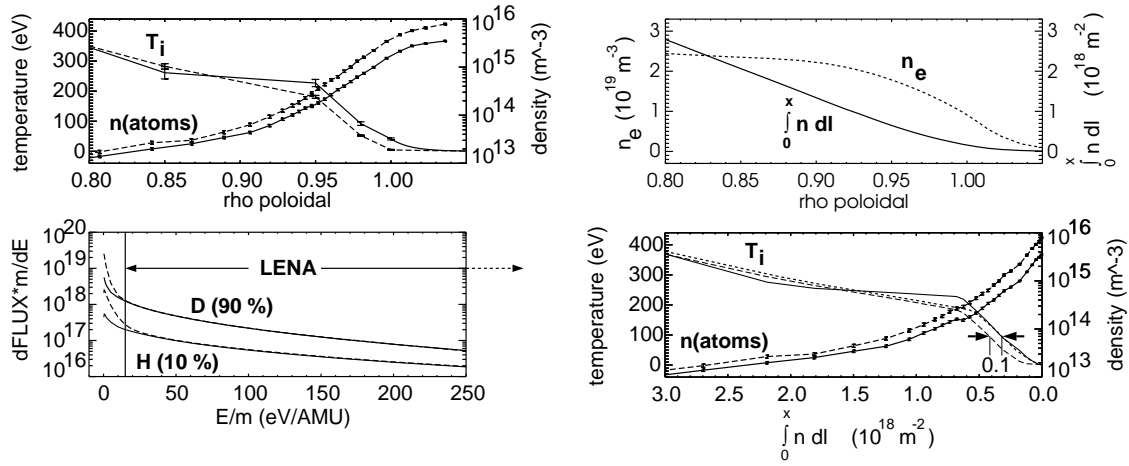


Figure A.34.: **Left:** Flux spectra and neutral densities corresponding to two different  $T_i$  profiles as calculated with the EIRENE MC-code for an ohmic ASDEX-Upgrade discharge (solid lines versus dashed lines). Fluxes are given per steradian and  $\text{m}^2$ . **Right:** Above: Illustration of the transformation from  $\rho_{pol}$  to  $\int_0^x n(l) dl$  for the ohmic shot discussed at the left. Below: Same data as upper part at the left as functions of  $\int_0^x n(l) dl$ . The short dashed  $T_i$  profile is the result of shifting the long dashed  $T_i$  profile by  $1 \cdot 10^{17} \text{ m}^{-2}$  towards the plasma edge and matches quite well the solid curve especially in the steep gradient region. This indicates, that these two  $T_i$  profiles which lead to the same flux spectra differ mainly by such a shift.

simulated with  $n_p, n_e$  according to the  $z_{eff}$  and  $\bar{z}_{imp}$  profiles, which are obtained by spectroscopic means. It turns out that without impurity puffing the corrections to the  $T_i$  profile and the absolute fluxes are within the errors of the parameters. Therefore, impurities are normally neglected for these cases. If one uses additional impurity puffing, for example to increase the radiation at the plasma edge, the error when neglecting the impurities is still within the  $\Delta N$  uncertainty (see paragraph on low energy cut-off), but to fix the position of the steep gradient correctly, the dilution of the protons/deuterons has to be taken into account.

### Multiple lines of sight

The fluxes measured with the movable CXA II analyser are thought to improve the reconstruction of the  $T_i$  profile in the intermediate radial range where the errors are large, since the additional lines of sight are tangential to intermediate flux surfaces. Two possibilities to include the additional flux spectra are examined: The first method is a complete simulation that requires a correct simulation of the neutral density over an enlarged poloidal region. The difficulties with this method are to analyse the importance of recycling sources on the upper passive stabilization loop and the fact that small differences in the calibration of the two analyzers can dominate the minimizing functional. The second method starts with the separate estimation of the maximum temperature along the additional lines of sight using the traditional method to identify the high energy logarithmic slope of the flux spectrum with the exponential factor of the Maxwell distribution (eqn. A.29) corresponding to the maximum of  $T_i$  along the line of sight. This  $T_i$  value can enter the

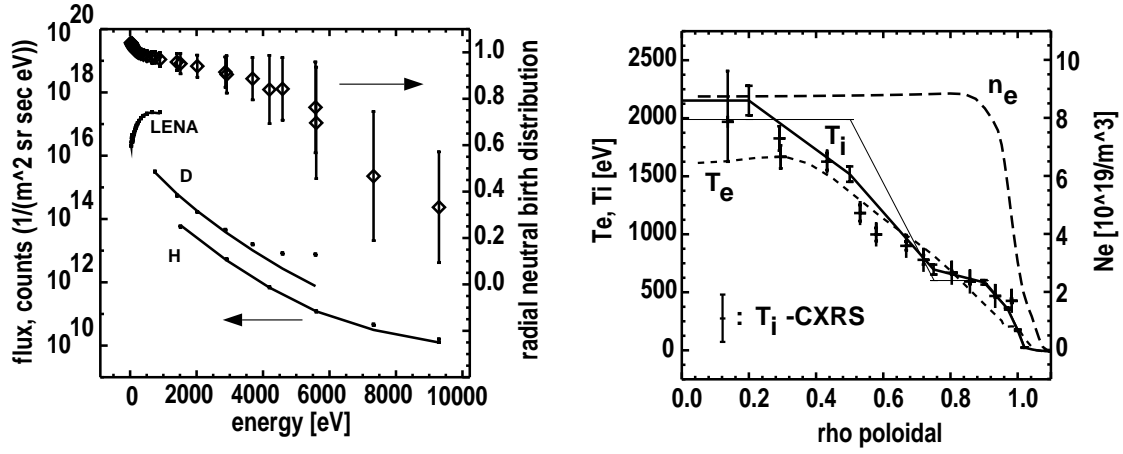


Figure A.35.: Analysis of a NBI-heated plasma ( $I_p = 1.0$  MA,  $B_t = -2.5$  T, 5 MW NBI). Left: data with errors, fit (solid lines) and birth regions of the neutrals. Since deuterium is injected, this isotope deviates from the fit at higher energies. Only the 3 lowest points are used for  $\chi^2$ . Note that LENA data are given as uncalibrated count rates  $1/(m^2 sr sec)$  since isotopes cannot be separated. Right: temperature and density profiles. The thin solid line refers to a fit of the fluxes alone. The thick solid line is the result when the deviation from the CXRS values is included in  $\chi^2$  ( $\rho_{pol} = \sqrt{\frac{\Psi - \Psi_{axis}}{\Psi_{sep} - \Psi_{axis}}}$ ,  $\Psi = pol.flux$ ).

simulation of the central line of sight (CXA I) as an additional data point, just as the CXRS values do in the case of NI heating. Here, the difficulty is to check if the logarithmic slope method is valid for the actual plasma parameters and lines of sight. The attenuation of the neutral fluxes must not change this slope. Comparison of the central  $T_i$  value obtained by the simulation of the CXA I data with the one obtained from the slope analysis of the same data indicates if the latter method is valid. Additionally, a series of similar shots can be used to measure different lines of sight with the movable analyser so that  $T_i$  values for different radial positions can be determined by slope analysis. The rise of  $\chi^2$  with the inclusion of these values into the simulation of the central line of sight is another indication of the validity of the slope analysis. Figure A.36 illustrates the results for a series of “identical” ohmic shots.

### Summary

The  $T_i$  profiles can be determined from energy resolved neutral particle fluxes for ohmic and NI heated plasmas using a central line of sight for the upper energy range (CXA) and an additional one for the low energy range (LENA). Errors generally lie between 10 and 20%. In the center, the errors might be larger due to limited information. At the separatrix, this accuracy can only be obtained by inclusion of total flux measurements in the data set to be fitted. Comparison with recombination spectroscopy (CXRS) shows fairly good agreement, but occasionally differences occur, which are not yet fully understood. Further accuracy improvement is possible when CXRS data or CX data from a movable analyser are included in the fit. Additionally the neutral-density profile is obtained along lines of sight. The H/D-isotope ratio, which is determined assuming that it is a constant for the whole plasma agrees well with the result from high resolution  $H_\alpha$  spectroscopy

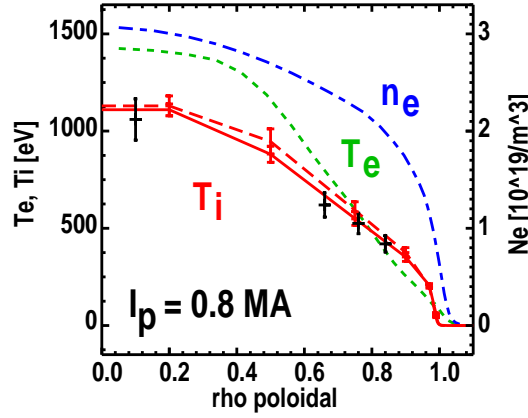


Figure A.36.: Effect of multiple lines of sight: For a series of equivalent shots different lines of sight have been chosen and the maximum  $T_i$  has been evaluated with the slope method (black crosses). These lie within the error bars of the  $T_i$  profile obtained by fitting the central curve alone (dashed curve). Inclusion of these “local” results and their errors in the fit does not significantly increase  $\chi^2$ , but decreases the uncertainties of the parameters (solid curve).

and the result of mass spectroscopy in the pump ducts.

## A.10. Microwave reflectometry (B. Kurzan)

In the following, the principles of reflectometry are presented. This includes its different possible techniques, depending on the polarisation used, the determination of electron density profiles and the measurement of the motion of the plasma layers.

### A.10.1. Principle of reflectometry

In reflectometry, microwaves are launched from an antenna into the plasma. The waves propagate inside the plasma as long as the refractive index is real. As soon as the microwaves enter a region of imaginary refractive index, where no oscillatory solution exists for the electric field, they are reflected. At this position, the plasma has a so-called cut-off. The primary quantity to be measured by reflectometry is the phase difference  $\varphi(f)$  between the wave reflected from the plasma and a reference wave. From the group delay  $\tau = d\varphi/df$ , electron density profiles, and, from the time history  $\varphi(t)$  of the phase, measured at constant microwave frequency, movements of the plasma can be determined, as shown below.

### A.10.2. Classification of the reflectometry techniques with respect to the cut-off used

For reflectometry different cut-offs of the plasma can be used. Their accessibility depends on the polarisation of the launched electromagnetic wave.

Ordinary Polarisation



If an electromagnetic wave is launched with ordinary polarisation into a magnetized plasma so that the electric field vector is parallel to the magnetic field, or into an unmagnetized plasma, then the cut-off is reached at the plasma frequency

$$f_{Ocut-off} = f_{pe} = \frac{\pi}{2} \sqrt{\frac{n_e e^2}{\varepsilon_0 m_e}}$$

( $e$ : elementary charge,  $\varepsilon_0$ : dielectric constant,  $m_e$ : electron rest mass).

An advantage of using this method for determining the electron density is that the cut-off frequency depends directly on the electron density. It is disadvantageous in that arbitrary small electron densities resulting in arbitrary small plasma frequencies need infinitely big wavelengths of the launched radiation which is not possible with the finite size of the plasma.

#### Extraordinary Polarisation

When an electromagnetic wave is being launched into a magnetized plasma with extraordinary polarisation, where the wave's electric field vector is perpendicular to the plasma's magnetic field  $B$ , there exist two possible cut-offs:

$$f_{Xcut-off,up} = \frac{f_{ce}}{2} + \sqrt{\frac{f_{ce}^2}{4} + f_{pe}^2}$$

$$f_{Xcut-off,low} = -\frac{f_{ce}}{2} + \sqrt{\frac{f_{ce}^2}{4} + f_{pe}^2}$$

( $f_{ce} = (eB)/(2\pi m_e)$ ). The upper cut-off frequency  $f_{Xcut-off,up}$  is bigger than the lower cut-off frequency  $f_{Xcut-off,low}$ . The accessibility of these cut-offs depends on the structure of the magnetic field and the form of the electron density profile. A disadvantage of using these cut-offs is that they also depend on the magnetic field  $B$  which must be known very accurately. Differences between the magnetic fields for pure vacuum and for a plasma filled volume must be taken into account. It is also advantageous that with the upper cut-off very small densities can be measured with finite frequencies, because  $f_{Xcut-off,up} \rightarrow f_{ce}$  ( $n_e \rightarrow 0$ ).

### A.10.3. Principle setup

A typical reflectometry diagnostic consists of a microwave oscillator, a launching and a receiving antenna and a detector. The phase shift of the wave running through the plasma is determined by measuring the phase difference between the wave reflected from the plasma and a reference wave. To minimize the phase shift between the two waves, the reference signal is chosen such that both waves travel approximately the same distance between the oscillator and the detector. The polarisation of the launched and the received radiation is determined by the orientation of the fundamental waveguide feeding the antennas.

### A.10.4. Measurement of electron density profiles

For determining electron density profiles, the distances to the plasma layers of density  $n_e$  must be measured for many different density values. That is why the frequency of

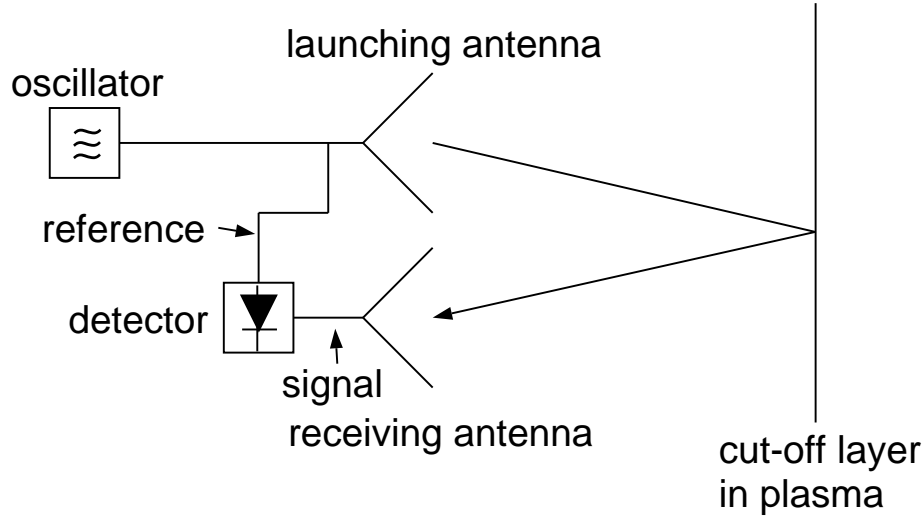


Figure A.37.: Principle setup of a typical reflectometry diagnostic.

the microwave oscillator is continuously tuned through the frequency band so that the reflecting plasma layers are probed sequentially.

With the pure frequency modulation (FM) technique, the carriers of the reference and the reflected wave are compared directly with respect to their phases. To have constructive interference, the tuning time of the oscillator must be much smaller than the time scale for macroscopic changes of the plasma, so that a “frozen” density profile is being probed. Slower tuning times are possible with the amplitude modulation (AM) technique. Here the phase of the AM which is only slowly varying compared to the phase of the carrier wave, is evaluated. With the AM technique, the amount of data to be acquired is smaller than with the FM technique.

For profile measurements the group delay  $\tau = d\varphi / df$ , meaning the phase change with frequency, is determined with both of the above mentioned techniques. In the case of ordinary polarisation, the distance of the reflection layer is

$$R(f) - R(0) = \frac{c}{2\pi^2} \int_0^f \frac{\tau(f') df'}{\sqrt{f^2 - f'^2}}$$

and the according electron density is

$$n_e(f) = \frac{4\pi^2 f^2 \varepsilon_0 m_e}{e^2}.$$

Since the group delay cannot be measured for small densities, an initialisation by a different diagnostic (e.g. Lithium beam diagnostic, or reflectometry with extraordinary polarisation), or an extrapolation of  $\tau$  to smaller frequencies is necessary.

For the extraordinary polarisation there exists no analytic inversion integral as for ordinary polarisation. In this case a numeric Abel inversion has to be used.

The space coordinates of the electron density profiles can be measured with an accuracy of a fraction of the wavelength of the used microwave radiation.

### A.10.5. Measurement of the motion of the reflecting layer

For tracking the motion of the reflecting layer, a fixed microwave frequency is launched into the plasma and the time evolution of the reflected wave's phase  $\varphi(t)$  is acquired. If  $d\varphi/dt \neq 0$ , then the reflecting layer is moving with respect to the antenna.

This kind of measurement is used e.g. to detect magnetic modes, because the motion of magnetic flux surfaces also leads to a motion of the surfaces of equal electron densities. Another application of this mode of operation is the measurement of plasma turbulence.

## A.11. Electron cyclotron emission (W. Suttrop)

### Principle of ECE diagnostics

In a hot magnetized plasma, electrons gyrate around magnetic field lines. Because of this accelerated motion electrons emit electromagnetic radiation at the cyclotron resonance angular frequency

$$\omega_c = e B / m_e \quad (\text{A.30})$$

where  $B$  is the total magnetic field,  $e$  the elementary charge and  $m_e$  the electron mass in the laboratory frame, and at low harmonics of the cyclotron frequency. Radiometry of electron cyclotron emission (ECE) can be used to determine the electron temperature of the plasma.

In a toroidal configuration, the magnetic field is inhomogeneous, so that spectral resolution of ECE measurement translates into spatial resolution. In a tokamak, for example, the major field component is the toroidal field generated by external coils  $B_t = B_t(R) \propto 1/R$ , where  $R$  is the major radius. Spectrally resolved ECE measurements along one single radial sightline yield a radial profile of  $T_e$ .

Today's fusion plasmas are in most cases optically thick for all frequencies resonant inside the plasma torus, i.e. practically all radiation is absorbed by the cyclotron resonance in a single pass of the wave through the plasma. Hence, the plasma absorbs, and, by Kirchoff's law also emits radiation as a black-body radiator. In this case, the radiation intensity depends only on the electron temperature. If the electron velocities perpendicular to the magnetic field (the orbital velocities in the gyration) have a Maxwellian velocity distribution, we can identify the apparent "radiation temperature" with the temperature of the gyration:  $T = T_{e,\perp}$  (We abbreviate  $T_{e,\perp}$  by  $T_e$  in the following).

The black-body intensity  $I_{BB}$ , radiated power per unit area and unit solid angle, is given by Planck's law

$$I_{BB} d\omega = h \frac{\omega^3}{8} \pi^3 c^3 \frac{1}{(\exp(\hbar\omega/kT_e) - 1)} d\omega$$

where  $d\omega$  denotes the observed angular frequency interval. For present day fusion plasmas ( $h\nu < 1$  meV,  $kT > 10$  eV),  $h\nu \ll kT$  and hence the Rayleigh-Jeans approximation holds:

$$I_{BB} = \frac{\omega^2}{4} \pi^2 c^3 kT_e \quad (\text{A.31})$$

Subsequently we will consider spatial and temporal resolutions and limitations of ECE measurements in fusion plasmas.

## Resolution of ECE measurements

The spatial resolution along the viewing direction of ECE radiometry is given by the relation  $\Delta R = (\partial R / \partial f) \Delta f$  and is therefore determined by the line width  $\Delta f$ , given by the spectral resolution of the detecting device (RF bandwidth) and by the relativistic shift and Doppler and relativistic broadening of the cyclotron emission from a hot plasma.

Doppler broadening results from components of the parallel electron motion along the ECE ray propagation path and can be mostly suppressed by observation perpendicular to the magnetic field direction. A finite viewing angle also results in Doppler broadening, but this effect can be reduced using an appropriate optical arrangement, e.g. Gaussian beam optics with a caustic near the region of interest.

Relativistic broadening and line shift originates from the mass increase (as seen in the laboratory frame) associated with the high electron thermal velocities in fusion plasmas and presents a fundamental resolution limit. For large optical thickness of the cyclotron resonance layer, strong re-absorption narrows the region out of which radiation can leave the plasma and reach the detector, i.e. the spatial resolution increases.

The lower detection limit, i.e. the lowest detectable electron temperature is determined by the receiver noise level. In contrast, the smallest detectable temperature *change*  $\Delta T_e$  in a hot plasma at temperature  $T_e$  is determined by the incoherent black-body fluctuations of the emitting plasma. The black body fluctuations appear as white noise (power density independent of frequency), and their magnitude in the detected receiver signal varies according to the selected RF bandwidth  $\Delta f_{RF}$  (larger signal and signal-to-noise ratio at large RF bandwidth) and video bandwidth  $\Delta f_v$  (larger noise level at large video bandwidth). The r.m.s. noise background from black-body fluctuations is described by the so-called “radiometer formula”  $\Delta T_{e,rms} / T_e = \sqrt{2 \Delta f_v / \Delta f_{RF}}$ . It should be noted that in fusion plasmas black-body fluctuations are usually much larger than fluctuations of the electron temperature related to transport-relevant plasma instabilities. For this reason, ECE measurements cannot be used to measure those plasma fluctuations unless special techniques are employed, e.g. correlation radiometry of two sightlines inclined with respect to each other by more than the black-body fluctuations decorrelation angle.

## Limitations of ECE diagnostics

The evaluation of electron temperature profiles from ECE measurements is straightforward. However, there are conditions which can modify the ECE power spectrum and restrict the applicability of the simple analysis or even inhibit the use of ECE measurements altogether.

As mentioned above, the apparent radiation temperature reflects the true electron temperature only in the case of high optical depth  $\tau = \int \alpha(r) dr$ , or high absorption  $\alpha$  over sufficient ray path length  $r$ , i.e. when the plasma is opaque at the measurement frequency. At finite optical depth  $\tau$ , the emitted intensity from a single beam pass through a slab of plasma is

$$\frac{T_{rad}}{T_e} = \frac{I}{I_{BB}} = (1 - e^{-\tau}).$$

In case of small optical depth, wall reflection and multiple passes through the plasma can increase  $T_{rad}$ . Without wall reflection, an optical depth of  $\tau > 3$  is needed to measure more than 95% of the black-body intensity. The optical depth  $\tau$  of cyclotron absorption for ordinary and extraordinary polarizations (polarization parallel and perpendicular to the magnetic field, respectively) in an inhomogeneous  $B$ -field is known. The optical depth decreases with increasing harmonic number and depends on the electron density and, in a hot plasma, on the electron temperature. In most fusion plasmas, the first harmonic in ordinary mode and the first and second harmonics in extraordinary mode are optically thick in the bulk plasma. Optical thickness quickly drops towards the plasma edge and may in some cases be insufficient for measurements in the scrape-off layer.

An upper limit to the electron density is given by the accessibility of the resonant location from the outside of the plasma. Ordinary mode waves with frequencies below the plasma frequency ( $\omega_p^2 = q^2 n_e / \epsilon_0 m_e$ ) are evanescent, i.e. cannot propagate inside the plasma. Extraordinary mode waves become evanescent when, on the ray path,  $\omega < \omega_R$ , where  $\omega_R = (\omega_c + \sqrt{\omega_c^2 + 4\omega_p^2})/2$  is the right-hand cut-off frequency, or, eliminating  $\omega_R$ ,  $\omega_p^2 > \omega^2 - \omega\omega_c$ . For the  $l$ -th harmonic ( $l \geq 2$ ) of the cyclotron frequency  $\omega = l\omega_c$ , X-mode right-hand cut-off occurs when  $\omega_p^2 > l(l-1)\omega_c^2$ , corresponding to a critical electron density  $n_{crit}^{X,l} = l(l-1)(\epsilon_0 m_e / q^2) \omega^2$ . For the X-mode second harmonic  $l = 2$ , which is optically thick in most cases, this is twice the cut-off density compared with the O-mode first harmonic. For this reason usually second harmonic X-mode waves are used for ECE measurements in order to allow for a larger range of accessible electron densities.

Deviations from a Maxwellian velocity distribution can perturb ECE measurements and may be difficult to detect under many circumstances. Non-thermal electron populations can occur, for example, in tokamaks with lower hybrid heating and at the plasma edge during H-mode confinement with steep  $T_e$  gradients at low electron density. As energetic electrons emit larger cyclotron radiation power than slow electrons, ECE measurements are sensitive to non-Maxwellian high energy tails of the distribution function. Viewing from the low-field side of a device can be favourable because down-shifted emission of tail electrons must cross a region of thermal electrons, which, if optically thick, will absorb this radiation.

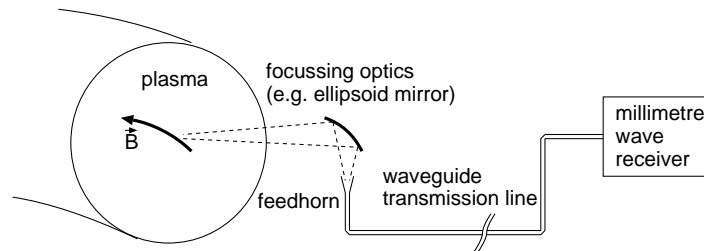


Figure A.38.: Typical ECE diagnostics setup. Millimetre wave emission from a fusion plasma is focussed quasioptically onto a waveguide horn and transmitted to a remote receiver.

## Diagnostics techniques

Confinement in a fusion plasma is achieved with a magnetic field  $B$  of several Tesla, hence the second harmonic electron cyclotron frequency  $2f = 2\omega_c/2\pi$  is in the range of millimetre waves, e.g.  $f \approx 56 \dots 280$  GHz for a magnetic field of  $B = 1 \dots 5$  T, respectively. This frequency range is accessible to RF receiver techniques (waveguide transmission, heterodyne detection with semiconductor diode mixers, etc.) as well as ‘quasi’-optical techniques (free space wave propagation, wavelength selection by diffraction and interference). Figure A.38 shows a typical ECE diagnostics setup for a toroidal confinement device. A Gaussian beam, defined by a focussing mirror or lens, views the plasma from the torus outside (low field side) and focuses the captured radiation onto an antenna feed horn. The millimetre wave radiation is transmitted by mono-mode or oversized multi-mode waveguides to a remote receiver. Polarization is selected by the waveguide orientation or by additional polarizing wire grids in the free-space beam path. Subsequently we briefly describe two popular types of ECE receivers.

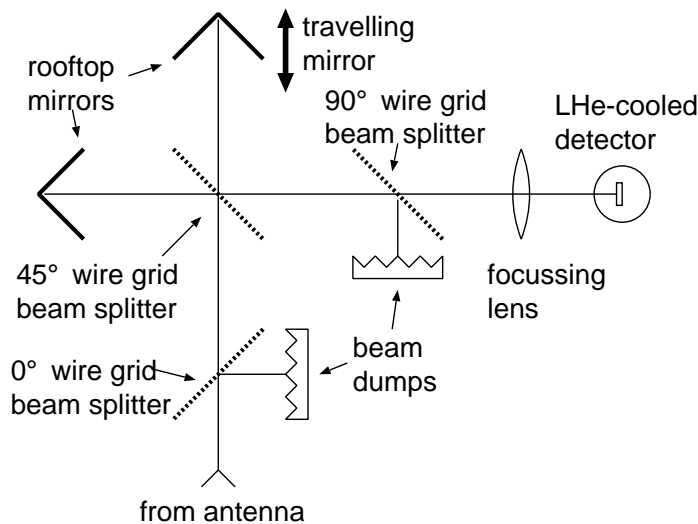


Figure A.39.: Michelson interferometer in Martin-Puplett configuration. Roof-top mirrors are used in conjunction with wire grids as polarizing beam splitters. The moving mirror is driven by an electrodynamic transducer.

A quasioptical device still in widespread use as a survey instrument for ECE diagnostics is the Michelson interferometer (see figure A.39), typically used in the Martin-Puplett configuration with polarization of the incident wave perpendicular to the  $B$ -field. The travelling mirror oscillates at highest possible speed to allow the measurement of several tens to hundreds interferograms during one plasma discharge. The ECE power spectrum is calculated from each interferogram using a fast fourier transform (FFT). A temperature profile is obtained by multiplication of the spectrum with the inverse instrument response function, which is determined by independent calibration of the instrument with a laboratory black-body source of known temperature. The time resolution of the measurement (twice the inverse mirror frequency) and spectral resolution (proportional to the mirror travel distance) are limited to several 10 profiles per second and  $\Delta f \approx 1$  GHz, respectively, due to the limited mirror velocity that can be achieved with sufficient op-

tical alignment of the interferometer. The sampling intervals of the interferogram can be made small ( $\approx 10 \mu\text{m}$ ), so that together with appropriate detectors (usually liquid helium-cooled electron bolometers) a large frequency range is covered. The poor resolution and wide frequency range renders the Michelson interferometer a typical survey instrument, capable of detecting several ECE harmonics in a single measurement. Other quasi-optical frequency selection techniques used for ECE measurements are Fabry-Perot interferometers and grating monochromators.

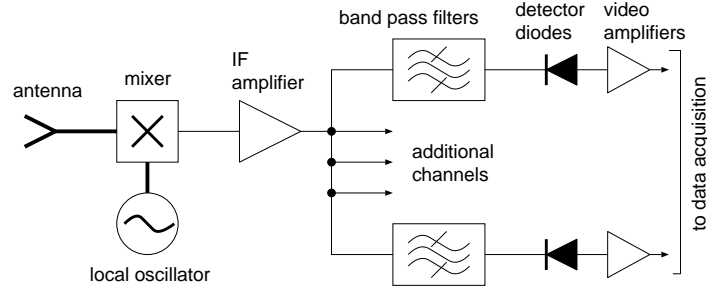


Figure A.40.: Schematics of a broadband multichannel heterodyne radiometer for ECE measurements.

The optimum combination of good temporal and frequency resolution, low noise and excellent sensitivity is obtained with heterodyne millimetre wave receivers. We briefly describe the principle of heterodyne ECE detection as illustrated in figure A.40.

The incoming ECE millimetre wave is downconverted to intermediate frequencies of  $0.1 \dots 20 \text{ GHz}$  by a broadband waveguide mixer which is pumped by a local oscillator (usually a Gunn diode). The broad-band intermediate frequency signal is amplified, split into several narrow-band channels with different center frequencies and detected by Schottky diode detectors. The output voltage of each detector is proportional to the microwave power in the corresponding channel's frequency interval. The electron temperature is obtained by multiplication of calibration factors obtained from measurement of laboratory black-body radiators. Because of signal amplification and filtering at the intermediate frequency, a heterodyne receiver combines excellent frequency selectivity and low receiver noise. RF bandwidths of  $\Delta f_{RF} \approx 100 \text{ MHz}$ , and video bandwidths of several MHz and above are readily obtained with heterodyne receivers.

## A.12. DCN-Interferometer (O. Gehre)

The index of refraction  $\mu$  of a medium can be measured by passing an electromagnetic wave of frequency  $\omega$  through it and evaluating its phase shift with respect to an external reference wave from the same source. This is the principle of interferometry.

For a magnetically confined, fully ionised, collisionless plasma, the refractive index is given by the simple relation  $\mu = (1 - (\frac{\omega_P}{\omega})^2)^{1/2}$ , if the probing beam is linearly polarized parallel to the confining magnetic field. Here,  $\omega_P^2 = \frac{n_e \cdot e^2}{\epsilon_0 \cdot m_e}$  is the square of the plasma frequency of the electron gas and linearly depends on the electron density  $n_e$ . To keep the plasma transparent, the probing wave frequency  $\omega$  has to stay well above the plasma frequency. For present fusion plasmas this means that for interferometry probing wavelengths in the

infrared to sub-mm range are necessary, where only a few laser sources exist.

The phase difference measured under these conditions is directly proportional to the integral of the electron density, taken along the line of sight of the plasma chord.

Probing the plasma along different chords of its cross-section introduces a more stringent requirement than that of simply choosing a wavelength for which  $\omega > \omega_P$ . The density profile introduces a gradient along the plasma diameter and leads to a refractive effect, which means that beams outside the midplane do not propagate along a straight line. To keep the optical arrangement of an interferometer for large scale experiments, the probing frequency has to be chosen even further above  $\omega_P$ , as refraction effects increase with the square of the wavelength. On the other hand, mechanical stability is reduced in this range due to vibrations entering the interferometers.

For the AUG plasma, a multi-channel DCN-laser interferometer is routinely used for electron density measurements and feedback control. For the plasma size and density range of AUG, the wavelength  $\lambda = 195\mu\text{m}$  is a good compromise between mechanical stability of the interferometer and plasma refraction effects, increasing with  $\lambda^2$ .

The source for the interferometer is a waveguide DCN-laser, delivering an output power of approximately 200 mW in linear polarization. The interferometer, which is of modulated Mach-Zehnder type, includes 8 probing beams through the plasma and a reference and modulation beam outside the vessel.

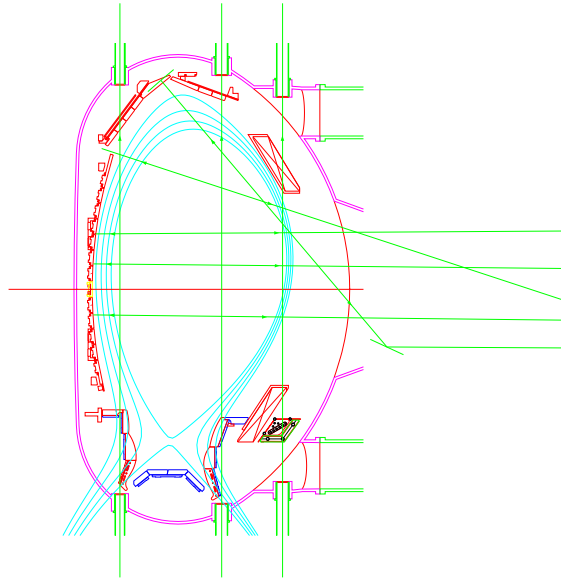


Figure A.41.: Schematic drawing of the chords of the AUG DCN laser interferometer.

In the vertical direction, 3 beams close to the plasma center and to the inner and outer separatrix are possible. In addition, nearly horizontal channels exist for which a double plasma pass with reflection from internal mirrors is necessary. A small angle between in and outgoing beams allows their separation outside the vessel necessary for the Mach-Zehnder arrangement. Due to the high mechanical stability of the experiment, no mea-



surable movement of the internal mirrors occurred during discharges and a compensating interferometer is not necessary.

The interferometer uses a 10 kHz phase modulation technique, employing the Doppler effect with reflection from a Veron rotating cylindrical grating. The phase differences between signals and reference are stored by a digital counter, which allows an on-line measurement of the total phase shift as a function of time in a continuous way within a dynamic range of  $128 \cdot 2\pi$ .

Measurements were made during about 9000 AUG discharges, covering line integral densities between  $10^{18} - 2 \cdot 10^{20} m^{-3}$  with standard plasma life times of 5 sec. Measured performance values are an accuracy of 2%, a phase resolution better than 1/50 fringe, (corresponding to a minimum resolvable density variation  $\Delta n_e = 2 \cdot 10^{17} m^{-3}$ ) and a time resolution of up to  $100 \mu s$ .

Results from the different channels are directly stored as line densities versus time in the AUG computer system. The limited number of channels prevents a reconstruction of density profiles by direct Abel inversion. Nevertheless a good profile fit is possible by including data from other diagnostics, which measure density close to the periphery of the plasma, e.g. Li-beam.

### A.13. Thomson scattering (H. Salzmann)

Due to the great difference in mass between ions and electrons, scattering of electromagnetic radiation in a plasma is dominated by scattering from electrons. The scattering of monochromatic radiation from the hot electrons leads to a spectral broadening of the scattered radiation due to the Doppler effect. First, a single, fast moving electron sees the incident radiation wavelength-shifted with respect to the wavelength of the radiation in the laboratory frame. Second, the wavelength of the radiation scattered from this electron in its rest frame is once more Doppler-shifted when observed in the laboratory frame. Summing up the radiation scattered from all the electrons moving at different velocities in different directions leads to the mentioned broad spectrum. The width of this spectrum increases with the temperature of the electrons. This is the basis for measuring the electron temperature by Thomson scattering.

When lasers with wavelengths in the visible spectrum are used, the scattering geometry is not extreme forward scattering, and the electron density is not too high, then the phases of the wavelets scattered from different electrons are not correlated and simply the scattered power can be added. For practical set-ups the conditions for this 'incoherent' Thomson scattering are fulfilled for all occurring plasma scenarios. Thus the intensity of the scattered radiation is proportional to the total number of electrons contained in the 'scattering volume' defined as the intersection of the laser beam and the fictitious 'beam' of the observation optics. This is the basis for measuring the electron density by Thomson scattering.

As pointed out, the interpretation of the measured spectrum of the scattered light does not depend on the plasma parameters. It is, however, governed by the finite signal-to-noise ratio (SNR) of the measurements (see later). In principle, the measurements should allow to infer the electron energy distribution function, yielding information on suprathermal electrons and electron drift velocities (current density). But, to do this, the

spectral measurements would have to be unfolded since the measurement of the power of the scattered radiation at a single wavelength yields a sum over the contribution of electrons moving at different energies in different directions, related by the requirement that momentum and energy are conserved for the scattering process. The attainable SNR does not allow this evaluation. Therefore, theoretical scattering spectra are calculated for Maxwellian velocity distributions and the electron temperature is determined by fitting against the measured spectra. This weakness of the diagnostic on the other hand is also its strength: it allows to measure the temperature of the bulk of the electrons without being disturbed by the presence of small fraction of suprathermal electrons. Thus the Thomson scattering diagnostic is somewhat complementary to ECE measurements.

In practice, two schemes for performing the measurements have evolved: the 'conventional' scheme, where an approximately  $90^\circ$  scattering geometry is used (existing practically on every current fusion device), and a time-of-flight scheme based on backward scattering (in use on the JET tokamak), where the required spatial resolution is achieved using sub-nanosecond laser pulses and high-speed detection. Both systems have their specific merits and disadvantages: the conventional scheme which uses simpler laser systems can be operated at higher repetition rates (typically 100 Hz) but requires an elaborate, space consuming collection optics to obtain spatial profiles. The time-of-flight method avoids the latter difficulty but has not been operated at high repetition rates yet.

The physical limitations in the measuring capability, however, are the same for both systems: the signal-to-noise ratio of the measurement limits the accuracy even in the absence of any systematic errors in calibration. The SNR is given by

$$SNR = n_{pe}^{scatt} / \sqrt{n_{pe}^{scatt} + n_{pe}^{background} + n_{pe}^{noise}},$$

where  $n_{pe}^{scatt}$  is the number of photoelectrons due to Thomson scattering (the signal),  $n_{pe}^{background}$  is the number of photoelectrons due to the background plasma radiation collected during the measurement, and  $n_{pe}^{noise}$  is the equivalent number of photoelectrons describing the detector noise current, also summed up during the measurement. The total number of signal photoelectrons (integrated over the scattered spectrum) is given by

$$n_e^{scatt} = \frac{E_{Laser}}{h\nu_{Laser}} \cdot \sigma_{Thomson} \cdot n_e \cdot \Delta L \cdot d\Omega \cdot Trans \cdot \eta,$$

where  $E_{Laser}$  is the laser energy,  $h\nu_{Laser}$  is the energy of the laser photons,  $\sigma_{Thomson}$  is the Thomson cross-section,  $n_e$  is the electron density,  $\Delta L$  is the length of the scattering volume,  $d\Omega$  is the solid angle of the collection optics,  $Trans$  is the optical transmissivity of the collection optics, and  $\eta$  is the quantum efficiency of the detector.

From these two relations all the design criteria for a Thomson scattering diagnostic can be inferred. The laser energy and the 'quality' of the collection and detection system should be as high as possible. On the other hand, it is obvious that the spatial resolution  $\Delta L$  cannot be improved without increasing the statistical error bars of the measurement. Typical values of  $\Delta L$  achieved at a statistical error of the temperature measurement of about 5% are in the range of 1 to a few cm's (for  $n_e \approx 3 \cdot 10^{13} cm^{-3}$ ,  $E_{Laser} \approx 1 J$ ). The spatial resolution, however, is crucial when the steep profiles at the plasma edge have to be measured. There is a remedy to this problem: at locations where the laser beam passes tangentially to the magnetic flux surfaces, the plasma parameters vary only slowly along the laser chord and the length of the scattering volume  $\Delta L$  can be made long. The attainable spatial resolution normal to the flux surfaces is the given by the laser beam diameter, typically of the order of one millimeter. This scheme is used on ASDEX-Upgrade to diagnose the plasma boundary: six Nd:YAG lasers ( $\lambda = 1064 nm$ ,  $E_{Laser} =$

1 J), each one operating at 20 Hz repetition rate are passed vertically through the plasma boundary, yielding measurements at 120 Hz, effectively. The laser beams are not colinear but arranged as a fan: the six laser beams intersect at the focusing lens located on top of the tokamak. Thus, in the midplane six slightly diverging beams (diameter less than 2 mm) are formed, which are displaced in radial direction by 2 mm each. These beams are viewed by a collection optics looking radially inwards through a radial port. Thus, in essence every 50 ms a grid of 42 measuring points is scanned.

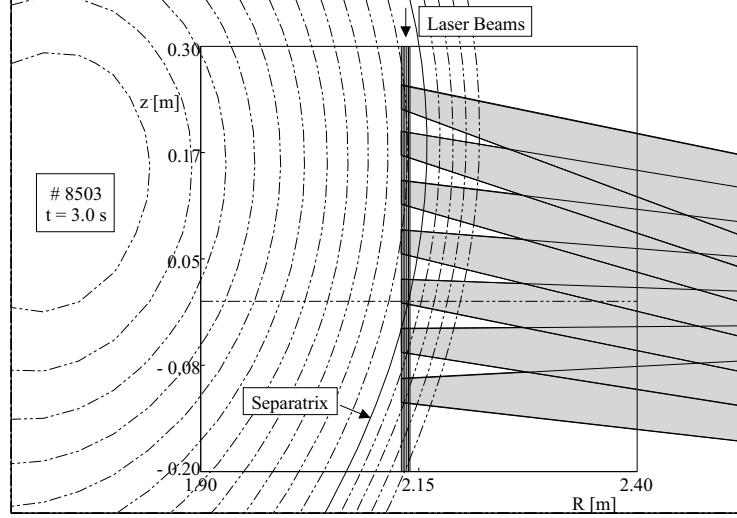


Figure A.42.: Scattering geometry on ASDEX-Upgrade for the low field plasma boundary. Shown are the six vertical laser beams (solid lines), the 'beams' of the collection optics (grey areas), and the flux contour lines.

Fig. A.43 shows a result from such edge measurements. All measurements during a quasi-stationary H-mode phase with periodic type I ELM's are depicted.

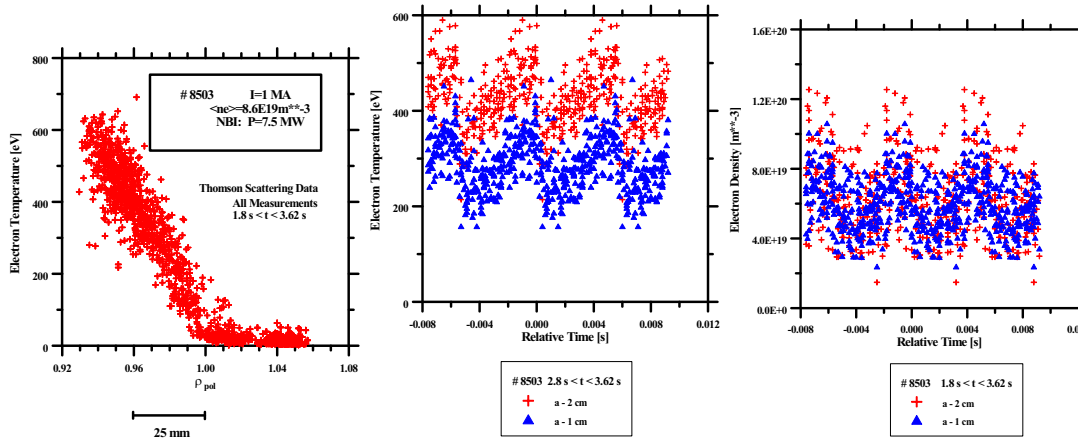


Figure A.43.: Electron temperature profiles (left) and temporal evolution of the electron temperature (middle) and electron density (right) 2 and 1 cm inside the separatrix during ELMs, respectively (middle). The measurements are time-correlated to the maximum of the  $D_\alpha$  emission in the divertor region.

Since the type I ELM's are nearly periodic during the measurement interval, the signals can be correlated to them. Fig. A.43 shows how the electron temperature at two radii varies over the ELM period (note that several, artificially created periods containing the same data are shown).

Fig. A.43 shows the corresponding results for the electron density measurements. Note that one of the great merits of the Thomson scattering diagnostic is that it measures undisputably temperature and density at exactly the same location in space and time. Thus pressure profiles can be inferred without possible additional errors introduced by mapping two independent diagnostics onto each other with the help of the reconstructed magnetic flux surfaces.



# Bibliography

- [1] J. A. Wesson, *Tokamaks*, Clarendon Press, Oxford, 1987.
- [2] ITER physics base editors, ITER physics expert groups, JCT, Nucl. Fusion 39 (1999) 2137.
- [3] F. Sardei, Y. Feng, P. Grigull, G. Herre, D. Hildebrandt, et al., J. Nucl. Mater. 241–243 (1997) 135.
- [4] P. Ghendrih, A. Grosman, and H. Capes, Plasma Phys. Controlled Fusion 38 (1996) 1653.
- [5] R. Chodura, in *Physics of Plasma Wall Interaction in Controlled Fusion (Proc. NATO Workshop Val-Morin, Quebec, Canada)*, edited by D. E. Post and R. Behrisch, pages 99–134, New York, 1984, Plenum Press.
- [6] M. F. A. Harrison, Technical Report CLM-P746, Culham Laboratory, Abingdon, Oxfordshire, 1985.
- [7] D. Reiter, Neutral Gas Transport in Fusion Devices: Atomic and Surface Data Aspects, in *Atomic and Plasma-Material Interaction Processes in Controlled Thermonuclear Fusion*, pages 243–266, Elsevier Science Publishers B.V., 1993.
- [8] D. Bohm, The Characteristics of Electrical Discharges in Magnetic Fields, Guthrie, Wakerling (eds), 1949.
- [9] P. Stangeby, Phys. Plasmas 2 (1995), 702.
- [10] K. Reinmüller, Technical Report IPP 5/79, Max-Planck-Institut für Plasmaphysik, 1998.
- [11] G. D. Hobbs and J. A. Wesson, Plasma Physics 9 (1967), 85.
- [12] N. W. Ashcroft and N. D. Mermin, *Solid State Physics*, Holt-Saunders, New York, 1976.
- [13] Y. P. Raizer, *Gas Discharge Physics*, Springer, Berlin, 1991.
- [14] L. N. Dobretsov and M. V. Gomoyunova, *Emission Electronics*, Israel Program for Scientific Translations, Jerusalem, 1971.
- [15] J. M. Pedgley et al., J. Nucl. Mater. 196-198 (1992) 1053.

- [16] R. Behrisch, in *Physics of Plasma Wall Interaction in Controlled Fusion (Proc. NATO Workshop ValMorin, Quebec, Canada)*, edited by D. E. Post and R. Behrisch, New York, 1984, Plenum Press.
- [17] F. Schwirzke, J. Nucl. Mater. 128–129 (1984) 609.
- [18] S. I. Braginskii, Transport Processes in a Plasma, in *Reviews of Plasma Physics, Vol. 1*, Consultants Bureau, New York, 1965.
- [19] M. Baelmans, Technical Report Jül-2891, KFA Jülich, Germany, 1994.
- [20] B. J. Braams, NET Report No. 68, January 1987 (EUR-FU/XII-80/87/68).
- [21] J. Neuhauser, W. Schneider, and R. Wunderlich, Nucl. Fusion 26 (1986) 1679.
- [22] LLE 48 (1991), 178.
- [23] S. Krasheninnikov and O. Bakunin, Contrib. Plasma Physics 32 (1992) 255, 3rd Workshop on Plasma Edge Theory, June 1992, Bad Honnef, FRG.
- [24] Y. Igitkhanov and A. Runov, Contrib. Plasma Physics 32 (1992) 308, 3rd Workshop on Plasma Edge Theory, June 1992, Bad Honnef, FRG.
- [25] Z. Abou-Assaleh, J. Matte, T. Johnston, and R. Marchand, Contrib. Plasma Physics 32 (1992) 456, 3rd Workshop on Plasma Edge Theory, June 1992, Bad Honnef, FRG.
- [26] M. Prasad and D. Kershaw, Stable solutions of nonlocal heat transport equations, Phys. Fluids B3(11) (1991), 3087.
- [27] H.-S. Bosch, D. Coster, S. Deschka, W. Engelhardt, C. García-Rosales, et al., Technical Report 1/281a, IPP, Garching, Germany, 1994.
- [28] D. Reiter, Technical Report Jül-1947, KFA Jülich, Germany, 1984.
- [29] D. Reiter, P. Boerner, B. Kueppers, M. Baelmans, and G. Maddison, Technical Report 428/90-8/FU-D, NET, EURATOM, 1990.
- [30] D. Reiter, Technical Report Jül-2599, KFA Jülich, Germany, 1992.
- [31] W. Eckstein, *Computer Simulation of Ion-Solid Interactions in Springer Series in Materials Science, Vol.10*, Springer, Berlin, 1991.
- [32] F. Wising, D. A. Knoll, S. I. Krashennnikov, T. D. Rognlien, and D. J. Sigmar, Contrib. Plasma Physics 36 (1996) 309.
- [33] F. Wagner et al., Phys. Rev. Lett. 53 (1984) 1453.
- [34] K. Borrass, Nucl. Fusion 31 (1991) 1035.
- [35] B. LaBombard et al., Phys. Plasmas 2 (1995) 2242.

- 
- [36] J. Schweinzer, W. Sandmann, G. Haas, J. Neuhauser, H. Murmann, et al., in *Europhysics Conference Abstracts (Proc. of the 24th EPS Conference on Controlled Fusion and Plasma Physics, Berchtesgaden, 1997)*, edited by M. Schittenhelm, R. Bartiromo, and F. Wagner, volume 21A, part IV, pages 1449–1452, Petit-Lancy, 1997, EPS.
- [37] C. S. Pitcher and P. C. Stangeby, *Plasma Phys. Controlled Fusion* 39 (1997) 779.
- [38] S. Self and H. Ewald, *Phys. Fluids* 9 (1966), 2486.
- [39] K. Borrass, D. Coster, D. Reiter, and R. Schneider, *J. Nucl. Mater.* 241–243 (1997) 250.
- [40] B. Napiontek, U. Wenzel, K. Behringer, D. Coster, J. Gafert, et al., in *Europhysics Conference Abstracts (Proc. of the 24th EPS Conference on Controlled Fusion and Plasma Physics, Berchtesgaden, 1997)*, edited by M. Schittenhelm, R. Bartiromo, and F. Wagner, volume 21A, part IV, pages 1413–1416, Petit-Lancy, 1997, EPS.
- [41] S. L. Allen, D. N. Hill, T. N. Carlstrom, D. G. Nilson, R. Stockdale, et al., *J. Nucl. Mater.* 241–243 (1997) 595.
- [42] U. Fantz, K. Behringer, J. Gafert, D. Coster, and ASDEX Upgrade Team, *J. Nucl. Mater.* 266–269 (1999) 490.
- [43] U. Fantz, K. Behringer, D. Coster, R. Schneider, D. Reiter, et al., in *Europhysics Conference Abstracts (CD-ROM), Proc. of the 26th EPS Conference on Controlled Fusion and Plasma Physics, Maastricht, 1999*, edited by C. Bastian and C. Nieswand, volume 23J, pages 1549–1552, Geneva, 1999, EPS.
- [44] U. Fantz, D. Reiter, . Heger, and D. Coster, Hydrogen Molecules in the Divertor of ASDEX Upgrade, submitted to *Journal of Nuclear Materials*.
- [45] M. Keilhacker, K. Lackner, et al., *Physica Scripta* Vol. T2/2 (1982) 443.
- [46] K. Lackner, R. Chodura, M. Kaufmann, J. Neuhauser, K. G. Rauh, et al., *Plasma Phys. Controlled Fusion* 26 (1984) 105.
- [47] R. Schneider, H.-S. Bosch, J. Neuhauser, D. Coster, K. Lackner, et al., *J. Nucl. Mater.* 241–243 (1997) 701.
- [48] J. Neuhauser and R. Wunderlich, *J. Nucl. Mater.* 145–147 (1987) 877.
- [49] K. Borrass, D. Coster, and R. Schneider, in *Europhysics Conference Abstracts (Proc. of the 24th EPS Conference on Controlled Fusion and Plasma Physics, Berchtesgaden, 1997)*, edited by M. Schittenhelm, R. Bartiromo, and F. Wagner, volume 21A, part IV, pages 1461–1464, Petit-Lancy, 1997, EPS.
- [50] H. Zohm, *Plasma Phys. Controlled Fusion* 38 (1996) 105.
- [51] H. Zohm, W. Suttrop, H. J. de Blank, R. J. Buttery, D. Gates, et al., in *Plasma Physics and Controlled Nuclear Fusion Research 1996*, volume 1, pages 439–451, Vienna, 1997, IAEA.



- [52] P. T. Lang, H. Zohm, K. Büchl, J. C. Fuchs, O. Gehre, et al., Nucl. Fusion 36 (1996) 1531, Corrigendum in Nucl. Fus. 36 (1996) 153.
- [53] D. P. Coster, R. Schneider, J. Neuhauser, H.-S. Bosch, R. Wunderlich, et al., J. Nucl. Mater. 241–243 (1997) 690.
- [54] R. Buttery, D. Gates, A. Colton, H. de Blank, S. Fielding, et al., in *European Physical Society Conference on Controlled Fusion and Plasma Physics*, volume 19C III, pages 273–276, Bournemouth, 1995.
- [55] D. Coster, B. Braams, J. Neuhauser, D. Reiter, R. Schneider, et al., in *Proc. of the 21th European Conference on Controlled Fusion and Plasma Physics, Montpellier, 1994*, edited by E. Joffrin, P. Platz, and P. Stott, volume 18B, part II, pages 846–849, Geneva, 1994, EPS.
- [56] D. Sigmar, A. A. Batishcheva, O. V. Batishchev, S. I. Krashennikov, and P. Catto, Contrib. Plasma Physics 36 (1996) 230, 5th Workshop on Plasma Edge Theory, December 1995, Asilomar, USA.
- [57] O. V. Batishchev, X. Q. Xu, J. A. Byers, R. H. Cohen, S. I. Krashennikov, et al., Contrib. Plasma Physics 36 (1996) 225, 5th Workshop on Plasma Edge Theory, December 1995, Asilomar, USA.
- [58] R. Schneider, D. P. Coster, K. Borrass, H.-S. Bosch, J. Neuhauser, et al., in *Plasma Physics and Controlled Nuclear Fusion Research 1996*, volume 2, pages 465–476, Vienna, 1997, IAEA.
- [59] D. Naujoks, J. Roth, K. Krieger, G. Lieder, and M. Laux, J. Nucl. Mater. 210 (1994) 43.
- [60] C. García-Rosales, R. Behrisch, D. Hildebrandt, B. Jüttner, W. Schneider, et al., in *Europhysics Conference Abstracts (Proc. of the 21th EPS Conference on Controlled Fusion and Plasma Physics, Montpellier, 1994)*, edited by E. Joffrin, P. Platz, and P. Stott, volume 18B, part II, pages 718–721, Geneva, 1994, EPS.
- [61] J. Roth and C. Garcia-Rosales, Nucl. Fusion 36 (1996) 1647.
- [62] A. Horn, A. Schenk, J. Biener, B. Winter, C. Lutterloh, et al., Chemical Physics Letters 231 (1994) 193.
- [63] J. Küppers, Surface Science Reports 22 (1995) 249.
- [64] R. Behrisch, *Sputtering by Particle Bombardment I, Topics in Applied Physics, Vol 47*, Springer, Berlin, 1981.
- [65] R. Behrisch, *Sputtering by Particle Bombardment II, Topics in Applied Physics, Vol 52*, Springer, Berlin, 1983.
- [66] W. O. Hofer and J. e. Roth, *Physical Processes of the Interaction of Fusion Plasmas with Solids*, Academic Press, London, 1996.
- [67] L. L. Lengyel, Technical Report IPP-1/191, IPP, Garching, Germany, 1981.

- 
- [68] ITER JCT and Home Teams, Plasma Phys. Controlled Fusion 37 (1995) 19.
- [69] S. Krasheninnikov and D. A. Knoll, Contrib. Plasma Physics 36 (1996) 266, 5th Workshop on Plasma Edge Theory, December 1995, Asilomar, USA.
- [70] K. Borrass, R. Farengo, and G. C. Vlasses, Nucl. Fusion 36 (1996) 1389.
- [71] K. Borrass, R. Schneider, and R. Farengo, Nucl. Fusion 37 (1997) 523.
- [72] V. Mertens, P. T. Lang, K. Büchl, R. Dux, C. Fuchs, et al., in *Europhysics Conference Abstracts (Proc. of the 23rd EPS Conference on Controlled Fusion and Plasma Physics, Kiev, 1996)*, edited by D. Gresillon, A. Sitenko, and A. Zagorodony, volume 20C, part I, pages 15–18, Geneva, 1996, EPS.
- [73] A. Bergmann, Y. Igitkhanov, B. J. Braams, D. P. Coster, and R. Schneider, Contrib. Plasma Phys. 36 (1996) 192, 5th Workshop on Plasma Edge Theory, December 1995, Asilomar, USA.
- [74] C. Chapman, Proc. Phys. Soc. 72 (1958), 353.
- [75] J. Neuhauser, W. Schneider, R. Wunderlich, and K. Lackner, Nucl. Fusion 24 (1984) 39.
- [76] J. Luciani, P. Mora, and J. Virmont, Phys. Rev. Lett. 51 (1989) 1664.
- [77] H.-S. Bosch, R. Dux, G. Haas, A. Kallenbach, M. Kaufmann, et al., Phys. Rev. Lett. 76 (1996) 2499.
- [78] M. J. Schaffer, M. R. Wade, R. Maingi, P. Monier-Garbet, W. P. West, et al., J. Nucl. Mater. 241–243 (1997) 585.
- [79] J. Gafert, D. Coster, C. Dorn, B. Napióntek, U. Schumacher, et al., in *Europhysics Conference Abstracts (Proc. of the 24th EPS Conference on Controlled Fusion and Plasma Physics, Berchtesgaden, 1997)*, edited by M. Schittenhelm, R. Bartiromo, and F. Wagner, volume 21A, part IV, pages 1397–1400, Petit-Lancy, 1997, EPS.
- [80] R. Dux, A. Kallenbach, M. Bessenrodt-Weberpals, K. Behringer, H.-S. Bosch, et al., Plasma Phys. Controlled Fusion 38 (1996) 989, preprint in IPP 10/1, February 1996.
- [81] D. Reiter, G. Wolf, and H. Kever, Nucl. Fusion 30 (1990) 2141.
- [82] R. Behrisch and V. Prozesky, Nucl. Fusion 30 (1990) 2166.
- [83] D. P. Coster, R. Schneider, J. Neuhauser, B. Braams, and D. Reiter, Contrib. Plasma Phys. 36 (1996) 150, 5th Workshop on Plasma Edge Theory, December 1995, Asilomar, USA.
- [84] R. Schneider, D. Reiter, D. Coster, J. Neuhauser, K. Lackner, et al., J. Nucl. Mater. 220–222 (1995) 1076.

- [85] R. Schneider, D. P. Coster, J. Neuhauser, H.-S. Bosch, J. C. Fuchs, et al., in *Europhysics Conference Abstracts (Proc. of the 22th EPS Conference on Controlled Fusion and Plasma Physics, Bournemouth, 1995)*, edited by B. Keen, P. Stott, and J. Winter, volume 19C, part IV, pages 285–288, Geneva, 1995, EPS.
- [86] O. Gruber, A. Kallenbach, M. Kaufmann, K. Lackner, V. Mertens, et al., *Phys. Rev. Lett.* 74 (1995) 4217.
- [87] A. Kukushkin, H. D. Pacher, V. Abramov, M. Baelmans, S. Bosch, et al., in *Plasma Physics and Controlled Nuclear Fusion Research 1996*, volume 2, pages 987–993, Vienna, 1997, IAEA.
- [88] M. Kaufmann, J. Schweinzer, M. Albrecht, M. Alexander, K. Asmussen, et al., in *Plasma Physics and Controlled Nuclear Fusion Research 1996*, volume 1, pages 79–94, Vienna, 1997, IAEA.
- [89] W. Suttrop, H. J. de Blank, G. Haas, H. Murmann, O. Gehre, et al., in *Europhysics Conference Abstracts (Proc. of the 23rd EPS Conference on Controlled Fusion and Plasma Physics, Kiev, 1996)*, edited by D. Gresillon, A. Sitenko, and A. Zagorodony, volume 20C, part I, pages 47–50, Geneva, 1996, EPS.
- [90] W. Suttrop, M. Kaufmann, H. J. de Blank, B. Brüsehaber, K. Lackner, et al., *Plasma Phys. Controlled Fusion* 39 (1997) 2051.
- [91] J. F. Drake, *Phys. Fluids* 30 (1987), 2429.
- [92] D. P. Coster, H. Kastelewicz, R. Schneider, and ASDEX Upgrade Team, in *Europhysics Conference Abstracts (Proc. of the 24th EPS Conference on Controlled Fusion and Plasma Physics, Berchtesgaden, 1997)*, edited by M. Schittenhelm, R. Bartiromo, and F. Wagner, volume 21A, part IV, pages 1437–1440, Petit-Lancy, 1997, EPS.
- [93] H. Kastelewicz, R. Schneider, J. Neuhauser, D. Reiter, B. Braams, et al., in *Europhysics Conference Abstracts (Proc. of the 20th EPS Conference on Controlled Fusion and Plasma Physics, Lisbon, 1993)*, edited by J. A. Costa Cabral, M. E. Manso, F. M. Serra, and F. C. Schüller, volume 17C, part II, pages 807–810, Petit-Lancy, 1993, EPS.
- [94] H. Kastelewicz et al., *Plasma Phys. Controlled Fusion* 37 (1995) 723.
- [95] W. Suttrop, V. Mertens, H. Murmann, J. Neuhauser, J. Schweinzer, et al., *J. Nucl. Mater.* 266–269 (1999) 118.
- [96] B. Lipschultz et al., IAEA (1996) F1-CN-64/A4-5.
- [97] R. D. Monk et al., *ECA* (1997) Part I, 117–120.
- [98] U. Wenzel, K. Behringer, K. Büchl, A. Herrmann, and K. Schmidtman, *J. Nucl. Mater.* 266–269 (1999) 1252.
- [99] N. Tsois, C. Dorn, G. Kyriakakis, M. Markoulaki, M. Pflug, et al., *J. Nucl. Mater.* 266–269 (1999) 1230.

- 
- [100] J. Gafert, K. Behringer, D. Coster, C. Dorn, A. Kallenbach, et al., J. Nucl. Mater. 266–269 (1999) 365.
- [101] A. Herrmann, J. C. Fuchs, V. Rohde, M. Weinlich, and ASDEX Upgrade Team, J. Nucl. Mater. 266–269 (1999) 291.
- [102] J. Schweinzer, W. Sandmann, G. Haas, J. Neuhauser, H. Murmann, et al., J. Nucl. Mater. 266–269 (1999) 934.
- [103] A. W. Leonard, M. A. Mahdavi, S. L. Allen, N. H. Brooks, M. E. Fenstermacher, et al., Phys. Rev. Lett. 78 (1997) 4769.
- [104] H. P. Summers, Technical Report Jet-IR(94)06, JET Joint Undertaking, Culham, 1994.
- [105] H.-S. Bosch, W. Ullrich, A. Bard, D. Coster, G. Haas, et al., J. Nucl. Mater. 266–269 (1999) 462.
- [106] H.-S. Bosch, J. Neuhauser, R. Schneider, A. Field, A. Herrmann, et al., J. Nucl. Mater. 220–222 (1995) 558.
- [107] H.-S. Bosch, D. Coster, R. Dux, C. Fuchs, G. Haas, et al., J. Nucl. Mater. 241–243 (1997) 82.
- [108] M. Kaufmann, H.-S. Bosch, A. Herrmann, A. Kallenbach, K. Borrass, et al., in *Fusion Energy 1998*, volume 1, pages 317–324, Vienna, 1999, IAEA.
- [109] A. Kallenbach, M. Kaufmann, D. P. Coster, J. C. Fuchs, A. Herrmann, et al., Nucl. Fusion 39 (1999) 901.
- [110] R. Schneider, D. Reiter, H. P. Zehrfeld, B. Braams, M. Baelmans, et al., J. Nucl. Mater. 196–198 (1992) 810.
- [111] D. Reiter, J. Nucl. Mater. 196–198 (1992) 80.
- [112] D. P. Coster, K. Borrass, R. Schneider, and ASDEX Upgrade Team, J. Nucl. Mater. 266–269 (1999) 804.
- [113] J. Roth, J. Nucl. Mater. 266–269 (1999) 51.
- [114] M. Laux, A. Herrmann, R. Neu, M. Weinlich, S. C. Pitcher, et al., in *Europhysics Conference Abstracts (Proc. of the 22th EPS Conference on Controlled Fusion and Plasma Physics, Bournemouth, 1995)*, edited by B. Keen, P. Stott, and J. Winter, volume 19C, part III, pages 97–100, Geneva, 1995, EPS.
- [115] A. V. Chankin, S. Clement, K. Erements, P. J. Harbour, G. Janeschitz, et al., Plasma Phys. Controlled Fusion 36 (1994) 1853.
- [116] B. Braams et al., Contrib. Plasma Phys. 36 (1996) 276.
- [117] V. Rozhansky, S. Voskoboinikov, E. Kovaltsova, D. Coster, and R. Schneider, Contrib. Plasma Physics 40 (2000) 423, 7th Workshop on Plasma Edge Theory, October 1999, Tajimi, Japan.

- [118] R. Schneider, D. Coster, B. Braams, P. Xantopoulos, V. Rozhansky, et al., Contrib. Plasma Physics 40 (2000) 328, 7th Workshop on Plasma Edge Theory, October 1999, Tajimi, Japan.
- [119] G. J. Radford, A. V. Chankin, G. Corrigan, R. Simonini, J. Spence, et al., Contrib. Plasma Physics 36 (1996) 187, 5th Workshop on Plasma Edge Theory, December 1995, Asilomar, USA.
- [120] V. Rozhansky and M. Tendler, in Rev. Plasma Phys., ed. by B.B. Kadomtsev, Consultants Bureau N.Y. v. 19 (1996) 147.
- [121] M. Tendler and V. Rozhansky, Comments Plasma Phys. Contr. Fusion 13 (1990) 191.
- [122] I. Hutchinson et al., Plasma Phys. Controlled Fusion 37 (1995) 389.
- [123] J. Boedo et al., ECA (1999) P3.063.
- [124] T. Rognlien and D. Ryutov, Contrib. Plasma Physics 38 (1998) 152.
- [125] T. Rognlien, D. Ryutov, and N. Mattor, Chzech. Journ. Phys. 48 Suppl. S2 (1998), 201.
- [126] T. Rognlien, D. Ryutov, N. Mattor, and G. Porter, Phys. Plasmas 6 (1999), 1851.
- [127] F. Hinton and Y.-B. Kim, Nucl. Fusion (1994) 899.
- [128] A. Mihailovskii and V. Tsypin, Beitr. Plasmaphys. 24 (1984) 335.
- [129] C. Rhie and W. Chow, AIAA J. 21 (1983), 1525.
- [130] S. P. Hirshman and D. J. Sigmar, Nucl. Fusion 21 (1981) 1079.
- [131] V. Rozhansky, A. Ushakov, and S. Voskoboinikov, Nucl. Fusion 39 (1999) 613.
- [132] E. McDaniel and E. Mason, *The mobility and diffusion of ions in gases*, Wiley, New York, 1973.
- [133] V. Rozhansky and L. Tsendin, *Collisional transport in partially ionised plasma*, Energoatomizdat, Moscow, 1988.
- [134] M. Rosenbluth, R. Hazeltine, and F. Hinton, Phys. Fluids 15 (1972), 116.
- [135] R. Zagorski, H. Gerhauser, and C. H.A., Contrib. Plasma Physics 38 (1998) 61.
- [136] P. Stangeby and A. Chankin, Phys. Plasmas 2 (1995), 707.
- [137] Y. Feng, F. Sardei, and J. Kisslinger, J. Nucl. Mater. 266–269 (1999) 812.
- [138] A. V. Chankin and P. C. Stangeby, Plasma Phys. Controlled Fusion 36 (1994) 1485, Preprint in JET-P(94)18, 1994.

- [139] U. Wenzel, D. Coster, A. Kallenbach, H. Kastelewicz, M. Laux, et al., in *Europhysics Conference Abstracts (CD-ROM), Proc. of the 26th EPS Conference on Controlled Fusion and Plasma Physics, Maastricht, 1999*, edited by C. Bastian and C. Nieswand, volume 23J, pages 1537–1540, Geneva, 1999, EPS.
- [140] K. Ertl and the ASDEX team, J. Nucl. Mater. 128–129 (1984) 163.
- [141] K. Burrell, Phys. Plasmas 4 (1997) 1499.
- [142] V. Rozhansky and M. Tendler, Phys. Plasmas 1 (1994) 2711.
- [143] J. L. Lachambre et al., Nucl. Fusion 34 (1994) 1431.
- [144] A. Komori, N. Ohyabu, and S. Masuzaki, J. Nucl. Mater. 241–243 (1997) 967.
- [145] G. Herre, R. Schneider, D. Coster, F. Sardei, D. Reiter, et al., J. Nucl. Mater. 241 (1997) 941.
- [146] M. Borchardt, J. Riemann, R. Schneider, et al., PSI-14, to be published.
- [147] Y. Feng, G. Herre, P. Grigull, et al., Plasma Phys. Controlled Fusion 40 (1998) 371.
- [148] G. Herre, , P. Grigull, and R. Schneider, J. Nucl. Mater. 266–269 (1999) 1015.
- [149] B. Scott, to be published.
- [150] X. Xu et al., Phys. Plasmas 7 (2000).
- [151] S. Krashennikov, to be published.
- [152] J. Neuhauser, D. P. Coster, V. Dose, J. W. Kim, B. Kurzan, et al., in *Europhysics Conference Abstracts (CD-ROM), Proc. of the 26th EPS Conference on Controlled Fusion and Plasma Physics, Maastricht, 1999*, edited by C. Bastian and C. Nieswand, volume 23J, pages 1521–1524, Geneva, 1999, EPS.
- [153] D. Coster, J. Kim, G. Haas, B. Kurzan, H. Murmann, et al., Contrib. Plasma Physics 40 (2000) 334, 7th Workshop on Plasma Edge Theory, October 1999, Tajimi, Japan.
- [154] J.-W. Kim, ASDEX Upgrade Edge Transport Scalings from the 2-dim Interpretation Code B2.5-I, submitted to Journal of Nuclear Materials.
- [155] A. Loarte, S. Bosch, A. Chankin, S. Clement, A. Herrmann, et al., J. Nucl. Mater. 266–269 (1999) 587.
- [156] W. Fundamenski, P. Stangeby, and J. Elder, J. Nucl. Mater. 266–269 (1999) 1045.
- [157] W. Ullrich, Helium Transport in ASDEX Upgrade, Laborbericht 1/321, IPP Garching – Doktorarbeit Universität Augsburg, Juli 1999.
- [158] B. Scott, in *Europhysics Conference Abstracts (Proc. of the 23rd EPS Conference on Controlled Fusion and Plasma Physics, Kiev, 1996)*, edited by D. Gresillon, A. Sitenko, and A. Zagorodony, volume 20C, part I, pages 51–54, Geneva, 1996, EPS.

- [159] B. Scott, S. Camargo, and F. Jenko, in *Plasma Physics and Controlled Nuclear Fusion Research 1996*, volume 2, pages 649–654, Vienna, 1997, IAEA.
- [160] A. Zeiler, D. Biskamp, J. F. Drake, and B. N. Rogers, in *Plasma Physics and Controlled Nuclear Fusion Research 1996*, volume 2, pages 657–663, Vienna, 1997, IAEA.
- [161] A. Zeiler, D. Biskamp, and J. F. Drake, *Phys. Plasmas* 3 (1996) 3947.
- [162] A. Zeiler, J. Bowman, and D. Biskamp, in *Europhysics Conference Abstracts (Proc. of the 24th EPS Conference on Controlled Fusion and Plasma Physics, Berchtesgaden, 1997)*, edited by M. Schittenhelm, R. Bartiromo, and F. Wagner, volume 21A, part IV, pages 1541–1544, Petit-Lancy, 1997, EPS.
- [163] M. Weinlich and A. Carlson, *Physics of Plasmas* 4 (1997) 2151.

Diesen Abschnitt widme ich all denen, die direkt oder indirekt am Entstehen dieser Arbeit Anteil genommen haben.

Dr. David Coster war über fast 10 Jahre ein Freund und Kollege mit dem es einfach Spass gemacht hat als Team zu arbeiten. Seine Detailkenntnis, nicht nur am Computer, war für mich immer verblüffend.

Dr. Josef Neuhauser hat mir die Begeisterung für dieses Arbeitsgebiet vermittelt und mir den Übergang in dieses Fachgebiet sehr leicht gemacht.

Dr. Bas Braams hat mir die speziellen Geheimnisse der Numerik für unser Arbeitsgebiet nahegebracht und war die ganzen Jahre ein zuverlässiger Wegbegleiter.

Dr. Kurt Borrass war die letzten Jahre eine echte Bereicherung der Randschichtgruppe, v.a. wegen seiner systematischen und theoretisch strukturierten Arbeitsweise.

Prof. Karl Lackner und Prof. Michael Kaufmann haben ein Team an ASDEX-Upgrade geformt, das das Zusammenspiel von Theorie und Experiment in geradezu idealer Weise gefördert hat.

Dr. Hans-Stephan Bosch hat als Experimentator erfolgreich den Spagat zur Modellierung gewagt und war stets für Diskussionen offen. Die gemeinsame Organisation der IPP-Sommerschule war eine sehr angenehme Erfahrung.

Viele Experimentatoren (stellvertretend seien hier Dr. Jürgen Gafert, Dr. Günter Haas, Dr. Henning Verbeek, Dr. Arne Kallenbach, Dr. Otto Gruber und Dr. Peter Grigull genannt) wollten zum Glück nie ganz glauben, daß wir ja eigentlich schon alles mit B2-Eirene verstanden hatten.

Dr. Hans-Peter Zehrfeld, Dr. Roland Chodura, Dr. Winfried Feneberg, Dr. Wolfgang Schneider und Dr. Lajos Lengyel, sowie alle anderen Mitarbeitern des Bereichs Tokamakphysik haben es geschafft eine Atmosphäre zu schaffen, in der es mir immer Spass gemacht hat zu arbeiten.

Dr. Bruce Scott hat etwas Turbulenz ins Spiel gebracht und ist in jeder Hinsicht ein kompetenter Diskussionspartner gewesen (auch bzgl. des FC Bayern).

Prof. Detlev Reiter, Prof. Akiyoshi Hatayama, Dr. Hans Kastelewicz und Dr. Yuri Ighitkhanov zeigten mir in unserer langen Zusammenarbeit, daß berufliche Kontakte auch zu privater Freundschaft führen können.

Die Arbeit in der ITER Expert Group (speziell seien hier Prof. Sergei Krasheninnikov, Dr. Tom Rognlien, Dr. Gary Porter, Dr. Bruce Lipschultz, Dr. Doug Post, Dr. Michiya Shimada genannt) hat mir gezeigt, wozu am Ende unsere Arbeit dienen soll. Die Diskussionen (speziell mit Dr. Günter Janeschitz) waren immer eine echte Härteprüfung.



Viele Zusammenarbeiten in anderen Gebieten (Dr. Paraskevas Lalousis, Dr. Wolfgang Eckstein, Dr. Ira Veselova) hielten mir (hoffentlich) den Blick offen.

Die gesamte B2-Eirene Gemeinschaft (Prof. Detlev Reiter, Prof. Martine Baelmans, Dr. Geoff Maddison, Dr. Andrei Kukushkin, Dr. Alberto Loarte, Dr. Richard Marchand, Prof. Volodja Rozhansky, Dr. Sergei Voskoboinikov, Dr. Xavier Bonnin, ...) hat ein echtes internationales Projekt entstehen lassen.

Die Stellaratorrandschichtgruppe (Dr. Xavier Bonnin, Dr. Mathias Borchardt, Dr. Jörg Riemann, Dr. Andreas Mutzke, Dr. Stefan Weber) garantiert weiterhin viel Spass an der Arbeit und keinen Anlaß zur Langeweile.

Der Bereich Stellaratortheorie (v.a. Prof. Jürgen Nührenberg) schafft ein tolles Umfeld mit allen Möglichkeiten.

Alle Sekretärinnen (Jutta Gauger, Petra Jordan, Sylvia Seitz, Margot Heilmair, Anja Wischke, ...) haben perfekt bei den vielen lästigen administrativen Aufgaben (Reiseplanungen, Verwaltungsanträge, ...) mitgeholfen.

Die Rechnergruppen des IPP haben (hier seien stellvertretend Dr. Karl Behler, Dr. Reinhard Drube, Roland Merkel, Stefan Heinzl, Dr. Hermann Lederer, Andreas Schott und Dr. Renate Dohmen genannt) viele der Arbeiten überhaupt erst möglich gemacht.

Eine besonders angenehme Erfahrung, in einer internationalen Gemeinschaft eingebunden zu sein, wobei sich die meisten Kontakte über die Zeit zu echten Freundschaften entwickelt haben. Viele Ideen entstanden durch offene wissenschaftliche Diskussionen mit Kollegen, daher war der persönliche Austausch für mich immer sehr wichtig.

Prof. Volker Dose hat mich die ganzen Jahre begleitet und mir bei allen wichtigen Fragen als Ratgeber weitergeholfen. Ohne ihn wäre diese Arbeit wohl auch nie entstanden.

Meine Familie hat es immer wieder geschafft, mir das eigentlich Wichtige im Leben zu zeigen und viele Unannehmlichkeiten durch meine Tätigkeit hingenommen.